Strål
säkerhets
myndigheten
Swedish Radiation Safety Authority

Research

Effects of additives on UO2 fuel behavior: expanded edition

2021:20

Author: Ali R. Massih, Lars O. Jernkvist
Quantum Technologies AB Uppsala Science Park
Report number: 2021:20
ISSN: 2000-0456
Available at: www.ssm.se

SSM perspective

Background

The Swedish Radiation Safety Authority (SSM) follows the development of nuclear fuel closely. Fuel with additives like chromia and gadolinia is used in Swedish reactors and fuel with even better thermal and mechanical properties is under development. This project is an in-depth study of data and models regarding the impact of additives on the properties of uranium dioxide fuel for light water reactors. The report is an update and expansion of the study of additives for uranium dioxide pellets that Quantum Technologies AB conducted for SSM in 2013 (SSM report 2014:21).

Results

The project constituted a review of recently completed and published experiments and studies as well as a review of computational models that describe the properties of (uranium dioxide) nuclear fuel with additives. This report summarizes openly published information from tests and experiments, and mathematical theories that have been draw from the tests. The review has included fuel behaviour in normal operation and in transients as well as impact of irradiation. The report also discusses which data that are available and where information is missing.

Furthermore, mathematical models that can be used to analyse the behaviour and their physical explanations are described. Models and their description in this report are a starting point for possible implementation in computational programs such as the version of FRAPTRAN developed by Quantum Technologies AB.

Relevance

The relevance for SSM lies in gaining in-depth knowledge about nuclear fuel with additives: how these substances affect the properties of nuclear fuel, how the new variants have been tested and how they are modelled in different analysis programs.

Need for further research

The development of nuclear fuel is continuing with more variants and additives. Hence, there is a need to understand the behaviour of the new products in all situations that they can be exposed to during their operation and the margins that are necessary to impose for accident conditions. Tests will continue, for example in the research program SCIP-IV. At regular intervals, it is appropriate with a thorough and critical review of all that is done, like this one.

Project information

Contact person SSM: Anna Alvestav
Reference: SSM2018-4298 / 7030348-00

Strål
säkerhets
myndigheten
Swedish Radiation Safety Authority

Author: Ali R. Massih, Lars O. Jernkvist
Quantum Technologies AB Uppsala Science Park

2021:20

Effects of additives on UO2 fuel behavior: expanded edition

Date: July 2021
Report number: 2021:20 **ISSN:** 2000-0456
Available at www.stralsakerhetsmyndigheten.se

This report concerns a study which has been conducted for the Swedish Radiation Safety Authority, SSM. The conclusions and viewpoints presented in the report are those of the author/authors and do not necessarily coincide with those of the SSM.

Contents

Abstract III

Sammanfattning IV

1 Introduction 1

2 Fuel chemistry 3
- 2.1 Normal fuel . . . 3
- 2.2 Burnable absorber fuel . . . 15
  - 2.2.1 Gd-U-O . . . 15
  - 2.2.2 U-Er-O . . . 18
  - 2.2.3 U-Eu-O . . . 21
- 2.3 Enhanced conductivity UO_2 fuel . . . 23
  - 2.3.1 UO_2–BeO . . . 24
  - 2.3.2 UO_2–SiC . . . 24
  - 2.3.3 UO_2–Diamond . . . 26
  - 2.3.4 UO_2–Carbon plus . . . 27

3 Thermophysical properties 29
- 3.1 Normal fuel . . . 29
  - 3.1.1 Enthalpy and heat capacity . . . 29
  - 3.1.2 Thermal expansion . . . 33
  - 3.1.3 Thermal conductivity . . . 34
- 3.2 Burnable absorber fuel . . . 36
  - 3.2.1 Gd-U-O . . . 36
  - 3.2.2 U-Er-O . . . 39
  - 3.2.3 U-Eu-O . . . 41
- 3.3 Enhanced conductivity UO_2 fuel . . . 41
  - 3.3.1 UO_2–MgO . . . 41
  - 3.3.2 UO_2–BeO . . . 42
  - 3.3.3 UO_2–SiC . . . 46
  - 3.3.4 UO_2–Diamond . . . 49
  - 3.3.5 Modeling . . . 50

4 Fission gas behavior 55
- 4.1 Fission gas diffusivity in UO_2-base fuels . . . 55
  - 4.1.1 Specimens . . . 56
  - 4.1.2 Irradiation and annealing . . . 57
  - 4.1.3 Fission gas diffusivity and release . . . 58
- 4.2 Computations . . . 61
  - 4.2.1 Fission gas release . . . 61
  - 4.2.2 Fuel gaseous swelling . . . 64
- 4.3 Discussion . . . 66
  - 4.3.1 Gas release and fuel swelling . . . 66
  - 4.3.2 Doping factors on gas diffusivity . . . 69
- 4.4 Case of BA fuel . . . 70

5 Mechanical properties **77**
5.1 Fuel creep studies . . . 77
5.2 Modeling fuel creep . . . 86
5.3 Composite fuel mechanical properties . . . 87

6 Operating experience, tests and modeling **93**
6.1 Operating experience . . . 93
6.1.1 Burnable absorber UO_2 fuel . . . 93
6.1.2 Chromia/alumina doped UO_2 fuel . . . 94
6.1.3 UO_2 fuel with other dopants . . . 97
6.2 Integral tests . . . 99
6.2.1 Power ramp tests . . . 99
6.2.2 RIA simulation tests . . . 105
6.2.3 LOCA simulation tests . . . 107
6.3 Computer simulations and models . . . 108
6.3.1 Burnable absorber UO_2 fuel . . . 109
6.3.2 Chromia/alumina doped UO_2 fuel . . . 110
6.3.3 Enhanced conductivity UO_2 fuel . . . 112
6.3.4 UO_2 fuel with other dopants . . . 117

7 Summary and conclusions **121**

Appendix A Thermophysical correlations **125**

Appendix B Thermal diffusivity versus thermal conductivity **127**

Appendix C Thermal boundary conductance **128**

Appendix D Fission gas release equations **131**

References **133**

Abstract

The report reviews the effects of various additives on UO_2 fuel behavior. Three categories of UO_2 fuel with additives for light water reactors (LWRs) are appraised: (i) Standard UO_2 fuel containing a small amount of metal oxide (≤ 0.2 wt%) to improve fuel performance; (ii) UO_2 with burnable neutron absorbers, intended to control reactor power early during irradiation, when fuel reactivity is high; (iii) UO_2 fuel mixed with a high-thermal conductivity additive to enhance the effective thermal conductivity of the composite fuel material, thereby reducing its operating temperature. The first two categories of fuel are in commercial use, but the third has not yet been utilized in LWRs.

In the first fuel category, the main incentive to dope UO_2 fuel with a small amount of metal oxides, such as Cr_2O_3, is to enlarge fuel grain size, increase fuel density and possibly make softer fuel pellets. Enlarging fuel grain size (> 30 μm) will extend the diffusion path for fission product gases to grain boundaries, through which most of the gas is released from the fuel pellet. Hence, the outcome would be a delay in thermal-activated gas release at a given fuel temperature. Increasing fuel density puts more ^{235}U mass per fuel assembly, while leading to less fuel densification during irradiation. Softer pellets, i.e. fuel with a higher creep rate and/or lower yield strength can reduce the intensity of pellet-cladding mechanical interaction during reactor power ramps, alleviating the risk of cladding failure. Additives may also affect the thermophysical properties of UO_2 fuel, such as heat capacity, thermal expansion and thermal conductivity. However, experimental data and theoretical analysis indicate that if the concentration of the additive is low (e.g. for Cr_2O_3 dopant < 0.2 wt%), these properties are hardly affected. In the second category, the burnable absorber additive Gd_2O_3 in UO_2 fuel has been widely utilized in LWRs over the years. Here, the chemical attributes, thermal properties and fission gas release behavior of (U,Gd)O_2 fuel are discussed. In the third category, the fuel thermal conductivity is enhanced by introducing certain additives with significantly higher thermal conductivity than UO_2 into its matrix. The objective is to achieve a higher effective fuel thermal conductivity with the aim of improving fuel performance during irradiation. A review of non-metallic crystals with high thermal conductivity and sufficient chemical compatibility with UO_2, stability in aqueous environments, compatibility with zirconium base cladding materials, suitable neutronics and irradiation performance, has narrowed the choice of additives to include BeO, SiC, synthetic diamonds or carbon-base materials.

The aim of this report is to assess data and models for some important properties of UO_2-base fuel containing additives. The additives considered are those investigated and reported in the literature. The results of selected in-reactor irradiation programs and integral tests on additive fuels are briefly reviewed. We also present and discuss computational studies on different types of additive UO_2 fuels for LWRs. An overview of these studies is given in the form of tables, which summarize published computer methods and simulations pertaining to fuel behavior under normal reactor operation, transients, and design basis accidents.

Sammanfattning

I rapporten granskas hur olika tillsatsämnen påverkar beteendet hos UO_2-bränsle avsett för lättvattenreaktorer. Granskningen omfattar tre kategorier av UO_2-bränsle med tillsatsämnen: (i) Standardbränsle med små mängder ($\leq$0.2 viktprocent) metalloxider, avsedda att förbättra bränslebeteendet; (ii) bränsle med brännbara neutronabsorbenter, avsedda att kontrollera reaktoreffekten i färska reaktorhärdar med hög reaktivitet hos bränslet; (iii) UO_2 blandat med tillsatsmaterial med hög värmeledningsförmåga. De senare är avsedda att förbättra den effektiva värmeledningsförmågan hos kompositmaterialet och därmed sänka dess driftstemperatur. De två första bränslekategorierna används kommersiellt, men den tredje har ännu ej använts i lättvattenreaktorer.

I den första kategorin dopas UO_2 med små mängder av metalloxider, exempelvis Cr_2O_3, huvudsakligen för att öka materialets kornstorlek och densitet, samt om möjligt göra bränslekutsarna mjukare. En ökning av bränslets kornstorlek (> 30 μm) ökar diffusionslängden för gasformiga fissionsprodukter till materialets korngränser, genom vilka den största delen gas avges från bränslekutsen. Resultatet torde vara en fördröjning av termiskt aktiverad gasavgivning från bränslet vid en given temperatur. En ökning av bränslets densitet ger större mängd ^{235}U per bränsleknippe och leder till mindre bränsleförtätning under bestrålning. Mjukare kutsar, det vill säga bränsle med en högre kryptöjningshastighet och/eller lägre plastisk flytgräns, kan mildra mekanisk växelverkan mellan kuts och kapsling under effekthöjningar (ramper) vid reaktordrift, vilket skulle minska risken för kapslingsbrott. Tillsatser kan också påverka UO_2-bränslets termofysikaliska egenskaper, såsom värmekapacitet, termisk längdutvidgning och värmeledningsförmåga. Experimentella data och teoretisk analys antyder emellertid att om koncentrationen av tillsatserna är låg (t.ex. < 0.2 viktprocent av tillsatsämnet Cr_2O_3), så påverkas dessa egenskaper endast marginellt. I den andra kategorin är den brännbara neutronabsorbatorn Gd_2O_3 vanligt förekommande som tillsats i UO_2-bränsle för lättvattenreaktorer sedan många år. I rapporten diskuteras kemiska och termiska egenskaper hos (U,Gd)O_2-bränsle, liksom dess fissionsgasfrigörelse. I den tredje kategorin förbättras bränslets värmeledningsförmåga genom tillsatsämnen med avsevärt bättre värmeledning än UO_2. Målet är att uppnå en högre effektiv ledningsförmåga och därmed förbättra bränslebeteendet under bestrålning. En genomgång av ickemetalliska kristaller med hög värmeledningsförmåga och tillräcklig kemisk kompatibilitet med UO_2, stabilitet i vattenmiljö, kompatibilitet med zirconiumbaserade kappslingsmaterial, lämpliga neutron- och bestrålningsegenskaper, har begränsat urvalet av tillsatsämnen till BeO, SiC, syntetiska diamanter eller kolbaserade material.

Målet med denna rapport är att utvärdera data och modeller för viktiga egenskaper hos UO_2-baserat bränsle innehållande tillsatser. Tillsatserna som beaktas är de för vilka studier finns rapporterade i öppen litteratur. Resultat från utvalda reaktorbestrålningsprogram och integrala prov på bränsle med tillsatser granskas översiktligt. Vi presenterar och diskuterar även beräkningsbaserade studier av olika typer av UO_2-bränsle med tillsatsämnen för lättvattenreaktorer. Dessa studier sammanfattas i form av tabeller, där publicerade beräkningsmetoder och simuleringar av bränslebeteendet under normal reaktordrift, transienter och konstruktionsgrundande olycksscenarier summeras.

1 Introduction

Three categories of UO_2 fuel with additives for light water reactors (LWRs) are discussed in this report: (i) Standard UO_2 fuel containing a small amount of metal oxide (≤ 0.2 wt%) to improve fuel mechanical performance, (ii) UO_2 with burnable absorber (BA), where an additive is used to control reactor power early during irradiation, when fuel reactivity is high, (iii) composite UO_2 fuel, where the uranium dioxide is mixed with a material of high thermal conductivity to enhance the effective thermal conductivity of the composite, thereby improving its performance.

In the first category, addition of small amounts of certain metal oxides, such as Cr_2O_3 and/or Al_2O_3, to UO_2 fuel enlarges the fuel grain size, increases fuel density and possibly makes the fuel pellets softer. Enlarging fuel grain size (> 30 μm) will extend the length of the diffusion path for fission product gases to grain boundaries, through which most of the gas is released from the fuel pellet. Hence, the outcome would be a delay in thermal-activated fission gas release at a given fuel temperature. In like manner, the main gaseous swelling contribution in UO_2 emanates from grain boundary gas bubbles, which would reduce as a results of larger grain size [1]. Increasing fuel density puts more ^{235}U mass per fuel assembly while generating more fission products per fuel volume and also leading to less fuel densification during irradiation. Softer pellets, i.e. fuel with a higher creep rate and/or lower yield strength can reduce the intensity of pellet-cladding mechanical interaction during reactor power ramps, thus lessening the risk of cladding failure. Additives may also affect the thermophysical properties of UO_2 fuel. These comprise enthalpy, heat capacity, thermal expansion and thermal conductivity, if the dopant level is sufficiently high, say ≥ 0.5 wt%. The additive oxides experimented with since the 1960s, both in laboratory and in-reactor, include TiO_2 [2–5], Nb_2O_5 [5–9], Cr_2O_3 [10, 11], V_2O_5 [3], La_2O_3 [2, 6], MgO [12, 13], Al-Si-O [14–16]. Cr_2O_3-doped UO_2 fuels have also been irradiated in commercial boiling water and pressurized water reactors (BWR and PWR), while MgO doped UO_2 fuels have been irradiated in an advanced gas cooled reactor (AGR) as reported in the literature [17–19] and [20, 21].

The specific dopants influence the trapping and diffusion of fission product gases xenon and krypton, and also the self diffusion of U^{4+} ions in UO_2. The prevailing defects in UO_2 are oxygen vacancies and interstitials. Additions of, e.g., trivalent chromium, aluminium, or gadolinium as Cr_2O_3, Al_2O_3 and Gd_2O_3 should, in general, increase the concentration of vacancies in UO_2, thereby decreasing the concentration of uranium vacancies via the equilibrium between cation and anion vacancies [22]. Hence, the rate of uranium diffusion is expected to be reduced by introduction of trivalent atoms in UO_2. On the other hand, an addition of pentavalent niobium ions, e.g., Nb_2O_5, should enhance cation diffusion. These effects, in turn, affect the diffusion and release of fission product gases produced during reactor operation in and from fuel pellets. An important factor is the state of oxygen in the fuel, namely the chemical potential of oxygen, which itself is controlled by the oxygen-to-uranium ratio of the compound and the temperature.

The second category of additives, such as Gd_2O_3 [23], Er_2O_3 [24–26] and Eu_2O_3 [27], are used as BAs in UO_2. These additives are utilized for in-core fuel management schemes and their neutronic characteristics are subjects of separate studies, which will not be discussed here. However, for Gd_2O_3, extensive thermophysical data and models are available in the

literature and we may take advantage of those to use them as analogy (as a trivalent oxide) to assess the properties of Cr_2O_3 or Al_2O_3 in UO_2, if applicable.

Nevertheless, there are also appreciable differences between the various trivalent compounds or so-called sesquioxides. For example, the ionic radii for Al^{+3}, Cr^{3+}, and Gd^{3+} are 0.5, 0.64 and 0.94 Å, respectively [28]. The corresponding solid solubility limits for Al_2O_3 and Cr_2O_3 in UO_2 at 1700°C are 70 and 700 weight parts per million (wppm), respectively [29], while for Gd_2O_3 it is substantially higher than that for Cr_2O_3 [30]. The former two dopants are grain enlarger while Gd_2O_3 is not. Atomic scale computations suggest that the trivalent oxides comprising Cr_2O_3 and Gd_2O_3 preferentially enter UO_2 by associating the substitutional ion with an oxygen vacancy [31]. The larger cation ions, e.g., Gd^{3+}, tend to form oxygen vacancy clusters, whereas the smaller ones, e.g., Cr^{3+} generate preferentially isolated defects. Middleburgh et al.'s results [31] indicate that the solubility limit of the smaller cation containing trivalent oxides, such as Cr_2O_3, is controlled by the oxidation state of the uranium dioxide, that is, the amount of Cr^{3+} that can enter solution is highly dependent on the degree of hyperstoichiometry. On the other hand, larger cations, such as Gd^{3+}, which already are highly soluble in UO_2, would not be much more stable in UO_{2+x}, and hence, their solubility is not greatly affected by the degree of hyperstoichiometry.

The third category of additives are the high thermal conductivity compounds. UO_2 base fuels being insulators have relatively low thermal conductivities while possessing high melting points. However, over the years, attempts have been made to enhance the thermal conductivity of UO_2 by introducing certain additives into its matrix to achieve a higher thermal conductivity with the aim of improving fuel thermal performance during irradiation [32, 33]. These compounds should posses sufficient chemical compatibility with UO_2, stability in aqueous environments, compatibility with zirconium alloy cladding materials, suitable neutronics, and irradiation performance. The additives include BeO, SiC, synthetic diamonds or carbon-base additives [34, 35].

The objective of this report is to assess data and models for some important properties of UO_2-base fuel containing the aforementioned additives. The report also intends to appraise a basis for model implementation in computer programs for fuel rod performance analysis. It is an updated and expanded version of the report issued in 2014 [36].

The plan of this report is as follows. Section 2 reviews some chemical and material characteristics of UO_2 with dopants. Appropriate models for thermophysical properties, comprising enthalpy, heat capacity, thermal expansion and thermal conductivity, are assessed in section 3. In section 4, fission gas diffusivity data and correlations available for some doped UO_2 materials are assessed and used in a standard model for fission gas release and gaseous swelling, to evaluate these quantities as a function of temperature and irradiation time. Moreover, the effects of grain size on gas release and swelling are evaluated in this section. Section 5 briefly reviews available data and correlations for thermal creep of Nb_2O_5- and Cr_2O_3-doped fuels. These are evaluated critically, and possible creep mechanisms are delineated. In addition, data on the effects of additives Cr_2O_3 and Al-Si-O on the yield strength of UO_2 at high temperatures are briefed. The results of selected in-reactor irradiation programs and integral type tests on additive fuels are briefly reviewed in section 6. In this section, we also review fuel rod modeling efforts reported in the literature for the considered fuels. Section 7 concludes the report with a summary and some remarks. Some technical details on thermophysical properties and the fission gas release model are placed in the appendices.

2 Fuel chemistry

In this section, we survey the chemistry of three categories of UO_2–doped fuel pellets. In subsection 2.1, we discuss "normal" UO_2–doped fuels, where the fuel is doped with an additive (an oxide) that increases fuel density and enlarges its grain size. In subsection 2.2, burnable absorber fuels are reviewed. These comprise a widely used UO_2–Gd_2O_3 fuel in light water reactors, and also UO_2–Er_2O_3 and UO_2–Eu_2O_3 fuels in which the respective additives have the role of controlling reactor core power during irradiation. In subsection 2.3, we briefly survey fuels with enhanced thermal conductivity, where nonmetallic crystals with high thermal conductivity are added to UO_2 to enhance its conductivity.

2.1 Normal fuel

As noted in the preceding section, the main impetus for introducing additives in standard UO_2 fuel is to improve fuel performance by enlarging fuel grain size, increasing fuel density, minimizing fuel densification during irradiation and possibly making a softer fuel. Of course, large grain size (> 30 μm) or higher density may also be achieved in undoped UO_2, but that would require higher sintering temperatures and longer sintering times than vendors usually apply to fabricate standard light-water reactor fuel pellets (1600-1750°C/5-10 h [37]). Minimizing the sintering time and temperature could result in appreciable economic benefits, both by reducing fabrication costs and increased production rates [38].

One way of achieving the same results is by addition of small amounts of appropriate metal oxides to UO_2 powder during manufacturing. For example, Arborelius et al. [17] report that, in order to produce high density, large grain size LWR fuel, AUC (ammonium uranyl carbonate) converted UO_2 powder is mixed with small quantities of additives in the form of oxides for about one hour to obtain full homogeneity. In case of a Cr_2O_3-dopant, e.g. 1000 wppm (weight parts per million) of Cr_2O_3-dopant was mixed with UO_2 powder, then the powder was pressed to green pellets with a force of about 50 kN. The green pellets were sintered in a H_2/CO_2 atmosphere at a maximum temperature of 1800°C for 14 h to a solid UO_2 pellet. The mean fuel grain size and density obtained for the Cr_2O_3-doped UO_2 were 44 μm and 10.62 g/cm^3, respectively, as compared to 11 μm and 10.52 g/cm^3 of the standard Westinghouse Sweden undoped UO_2 fuel [17]. In case of Cr_2O_3-Al_2O_3-doped UO_2 with 500 wppm Cr_2O_3 and 200 wppm Al_2O_3, fabricated with a similar procedure, the mean fuel grain size and density obtained were 52 μm and 10.68 g/cm^3, respectively [17].

Industrial groups in France led by AREVA NP (now: Framatome) have utilized and doped UO_2 fuels for LWRs over the years [18, 19, 39, 40]. In particular, chromium oxide with a concentration of 0.16 wt% has been used as an additive with grain size varying in the range of 50 to 70 μm, figure 1. These materials, which have densities in the range of 96 to 97 %TD (theoretical density), have exhibited less in-reactor densification than standard UO_2 fuel. Increasing the fuel density also gives an increase in the ^{235}U mass per fuel assembly for employing fuel utilization schemes with longer reactor cycles, considering that Cr_2O_3 has a very small impact on thermal neutron absorption. Factors governing microstructure development of Cr_2O_3-doped UO_2 during sintering were investigated by Bourgeois et al. [41] and Leenaers et al. [42], whereas the lattice parameter and theoretical density of this

fuel have been determined by Cardinaels et al. [43]. Solid solubility of Cr_2O_3 in UO_2 is discussed in [29, 41, 43].

In table 1, we have listed some metal oxides used or experimented with as fuel additives in thermal reactors. A combination of these oxides, e.g. Al_2O_3-Cr_2O_3 also have been used in UO_2. Included in the table are the values for the thermal neutron capture cross-section ($\sigma_{\rm ab}^{\rm th}$) for the additive elements. It is seen that Al and Mg will have the best neutronic performance (i.e. lowest $\sigma_{\rm ab}^{\rm th}$), whereas La, Ti and V are the poorest in this respect. Table 2 gives typical fuel elemental composition for a 0.16 wt% Cr_2O_3-doped UO_2 and that of two variants of "pure" or standard UO_2 fuel.

Table 1: Oxides and their base metals used as additives in UO_2 fuel [28].

Base element	Al	Ca	Cr	La	Mg	Nb	Si	Ti	V
Atomic mass	26.98	40.08	51.996	138.91	24.31	92.91	28.09	47.88	50.94
$\sigma_{\rm ab}^{\rm th}$(barns)	0.23	0.43	3.1	8.9	0.064	1.15	0.16	6.1	5.06
Major oxide	Al_2O_3	CaO	Cr_2O_3	La_2O_3	MgO	Nb_2O_5	SiO_2	TiO_2	V_2O_5

$\sigma_{\rm ab}^{\rm th}$: Thermal neutron capture cross-section.

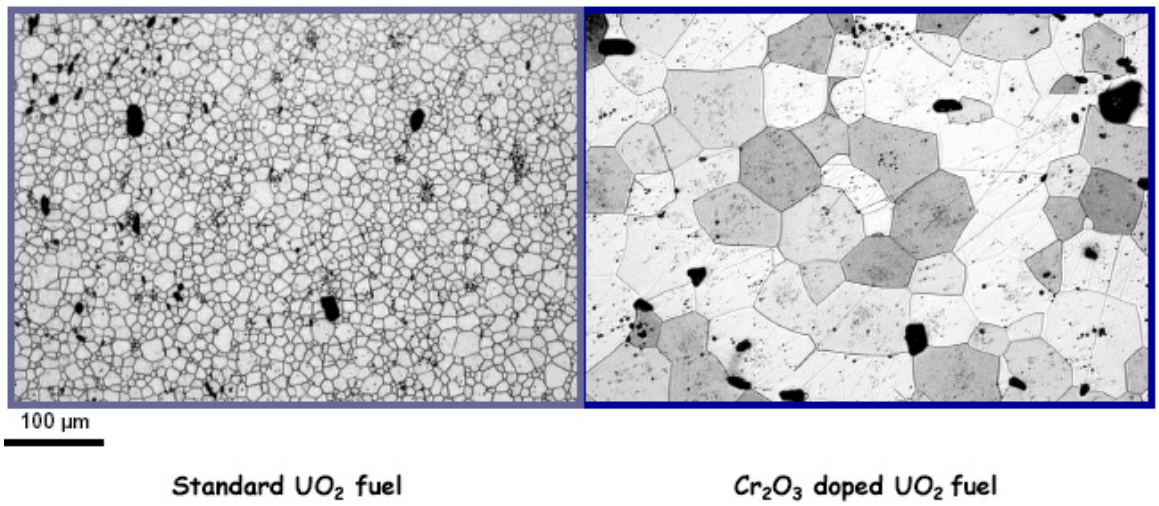

Figure 1: Micrographs of AREVA NP Cr_2O_3-doped (grain size 60 μm) and standard UO_2 (grain size 8 μm) fuels; from Delafoy et al. [18, 40].

Radford and Pope [38] compared the effect of addition of oxides of titanium, niobium, vanadium, barium and Ti-Ba at different levels, ranging from 0.05 to 1.66 mol% metal, to the UO_2 powder characterized in the far right column of table 2. These elements all suppressed the density during the initial sintering below about 1200°C followed by enhancing the density at intermediate temperatures (1200-1400°C). At higher levels of concentrations, especially for Ti and Ca-Ti, a pronounced sweeping of the fine pores ($< 2\mu$m) was observed [38]. The grain size was increased with the level of the additives, figure 2.

So, additives affect physical properties of UO_2. They influence fuel thermodynamics and the kinetic processes involved during fabrication and reactor operation. This is due to restructuring of point defects and defect processes in UO_2. Uranium dioxide has a face-centered cubic (fcc) crystal with fluorite structure named after the compound CaF_2. The unit cell contains four molecules of UO_2. It is face-centered with respect to the uranium

Table 2: Typical UO_2-base fuel elemental composition (wppm).

Dopant [Ref.]	Cr_2O_3 [44]	Undoped [44]	Undoped [38]
Grain size (μm)	70	11	8
Fuel density (%TD)	95.97	96.26	97.83
Al	6	8	<10
B	0.1	0.1	0.15
C	5	5	200
Ca	5	5	<5
Cd	0.2	0.2	<0.2
Cr	**1079**	5	<5
Cl	3	3	...
F	3	3	<5
Fe	10	10	40
Mg	0.5	0.5	<1
N	10	10	...
Ni	2	2	10
Si	4	4	<10
W	0.5	0.5	...

TD: Theoretical density of UO_2 = 10.97 g/cm^3 [28].

ions, which occupy the octahedral positions (0,0,0), (1/2,1/2,0), (1/2,0,1/2) and (0,1/2,1/2), whereas the oxygen ions occupy the (1/4,1/4,1/4) and its equivalent positions (tetrahedrally coordinated by uranium); see figure 3. Interstitial ions may be accommodated at octahedral vacant sites [45].

The UO_2 fuel can also readily take up oxygen interstitially to form hyperstoichiometric UO_{2+x}, where x can range as high as 0.25 at high temperatures; U_4O_9 will precipitate out as the temperature is lowered. Hypostoichiometric uranium dioxides UO_{2-x} form under low partial pressures of oxygen at high temperatures. They revert to stoichiometric UO_2 and precipitate metallic U upon cooling [37]. The properties of the uranium dioxide phase strongly vary as a function of the oxygen to metal uranium atom ratio (O/U); see figure 4. The variation of the chemical potential of oxygen μ_{O_2} with the O/U ratio is very distinct. It reflects the equilibrium between oxygen in the crystal lattice and the gas phase. In the hypostoichiometric domain, μ_{O_2} is relatively low, that is, the oxygen is strongly bonded in the lattice. Whereas in the hyperstoichiometric domain, μ_{O_2} is much higher, since the bonding of the O^{2-} ions in the interstitial sites is relatively weak. The variation of μ_{O_2} data as a function of O/U ratio and temperature is related to the evolution of the defect concentration in the crystal. Various suggestions for the defect chemistry in $UO_{2\pm x}$ have been presented, but are still subject of dispute [45].

In addition to point defects, such as cation and anion vacancies and interstitials, the combination of these point defects is also of importance, especially under irradiation. Such defects include the oxygen Frenkel pair, uranium Frenkel pair, the uranium-oxygen divacancy pair, Schottky defect (one U and two O vacancies separated), and the bound-Schottky trivacancy; see Liu et al. for illustrations [48].[1]

Regarding the effect of additive Nb_2O_5 on the point defect structure of UO_2, Matsui and Naito's experimental results [49] indicate that for the same μ_{O_2}, the O/M ratio for Nb_2O_5-

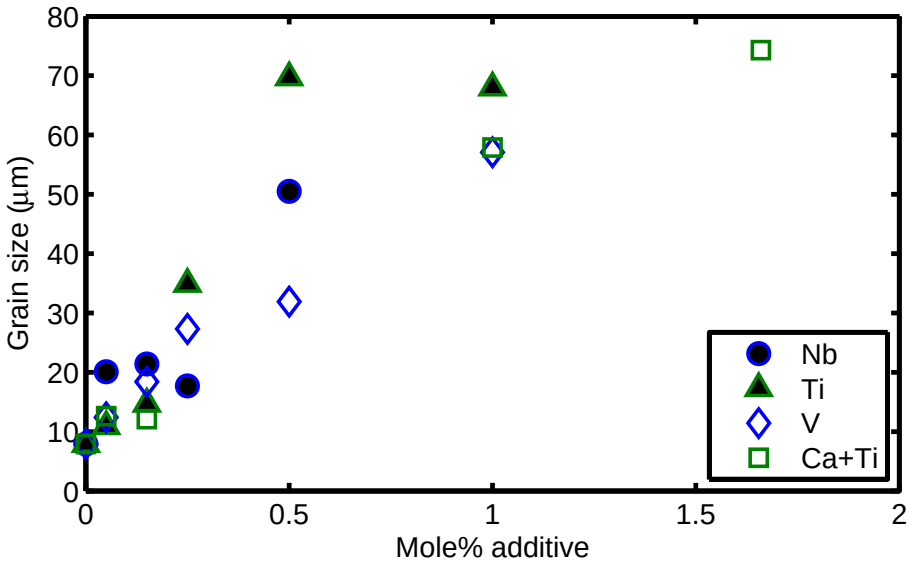

Figure 2: Grain size versus concentration level of additive metal after Radford and Pope [38]; Nb and Ti more strongly affect grain size than V or Ca+Ti.

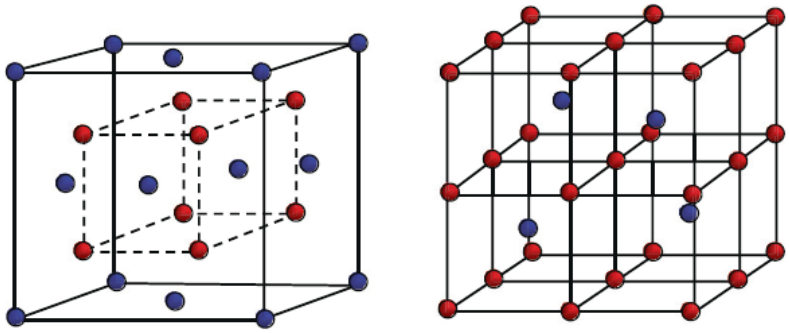

Figure 3: Fluorite fcc structure of UO_2. The unit cell (left) and the oxygen lattice (right) with the uranium atoms shown in blue and the oxygen atoms in red; from [45].

doped UO_2 is larger than that for undoped, implying that the concentrations of oxygen interstitials and cation (U) vacancies are increased by Nb_2O_5 addition. This nonstoichiometric effect on defect structure may be responsible for the augmentations of the diffusion coefficients of cations and fission gas (see section 4) due to Nb_2O_5 doping. The enhancement of the cation diffusion by addition of Nb_2O_5 is generally explained by the following defect structure [50]: Higher valent Nb^{5+} ions, substituting for the U^{4+} ions in the UO_2 lattice, impart an effective positive charge to the lattice. This should increase the concentration of oxygen interstitials and decrease that of oxygen vacancies, thereby increasing the concentration of cation vacancies through the Schottky defects in equilibrium. The increase in the concentrations of cation vacancies and oxygen interstitials is expected to increase the diffusivities of cation and fission gas. Moreover, the enhanced cation diffusion would increase the creep and grain growth rates.

It has been known for a long time that relatively small additions of TiO_2 (titania) increase both the rate of densification and the final bulk density, which can be attained during the sintering of UO_2 [2]. Amato et al. [3] have also shown the rate of UO_2 equiaxed grain growth to be greatly increased if small quantities of titania, e.g. UO_2 with 0.5 wt% TiO_2,

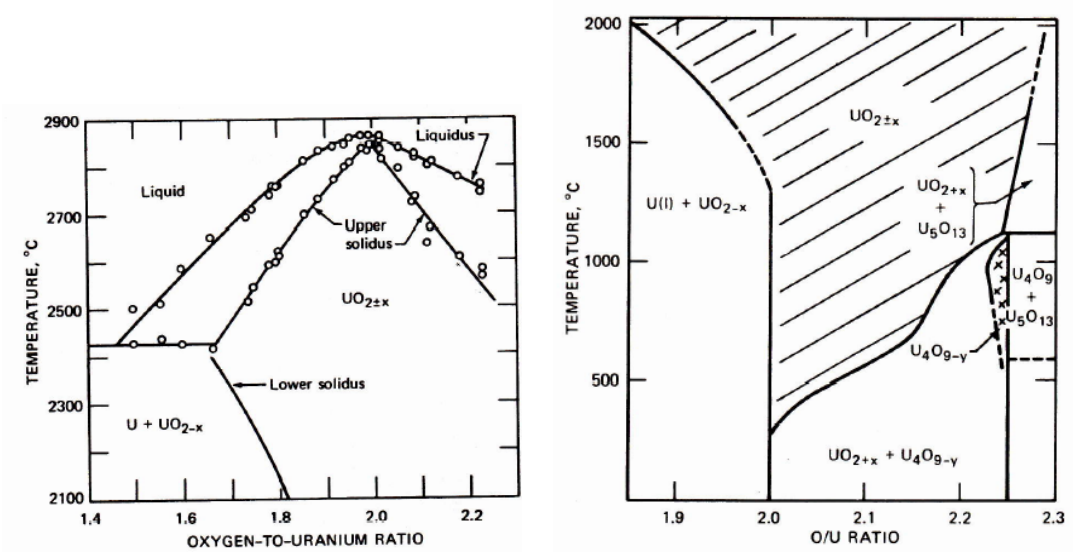

(a) (b)

Figure 4: (a) Phase diagram of urania from $UO_{1.5}$ to $UO_{2.23}$, where circles are measured values from [46]. A more detailed portion of the phase diagram; from D. R. Olander [47].

are present. Ainscough and coworkers [4] studied the effect of additions of up to 0.33 wt% titania on the grain growth and densification of UO_2. They showed that the solubility of titania in UO_2 lies between 0.07 and 0.13 wt% at 1923 K in hydrogen, and that the grain growth rate is proportional to the concentration of added titania up to the solublity limit and remains constant afterwards. They noted that titania in excess of the solubility limit forms a liquid eutectic with UO_2. This eutectic, which has a solidification temperature in the range of 1873–1893 K, inhibits grain growth at temperatures below 1873 K, but can enhance it at higher temperatures [4].

More recently, investigators at the Rensselaer Polytechnic Institute, USA [51] have applied a special sintering method to consolidate TiO_2–doped UO_2 fuel pellets with 0.5 wt% dopant concentration, above its solubility, to induce eutectic phase formation and promote sintering kinetics. Their study shows that the grain size can reach 80 μm by sintering at 1973 K for 20 min., and liquid U–Ti–O eutectic phase occurs at the triple junction of grain boundaries, which greatly improves grain growth during sintering. They observed that oxide additive also impedes the reduction of the initial hyperstoichiometric fuel powders to more stoichiometric fuel pellets upon the utilized sintering process. Their measurements indicate that these TiO_2–doped UO_2 fuel pellets have comparable thermal conductivity with the standard UO_2 fuel pellets. The doped pellet densities varied from 97.17 to 98.40 %TD depending on sintering temperature (1773, 1873 or 1973 K) and sintering time (5 or 20 min.). Pellets sintered at 1873 K for 20 min. reached 98.40 %TD.

Uranium dioxide doped with magnesium is expected to improve fuel performance during irradiation up to moderate exposures, say ≤ 30 MWd/kgU. It is argued that the dissolved Mg would reduce the oxygen chemical potential change during irradiation, leading to a more thermodynamically stable fuel. Moreover, an addition of small amount of MgO in UO_2 during fabrication increases the grain size of the fuel pellet, yielding longer diffusion paths for fission product gases to grain boundaries, through which they can escape from the fuel pellets [52]. In fact, Ingleby and Hand [20] experimentally showed that magnesia

dissolved in UO_2 under oxidation produces a solid solution of the form $UO_{2+x}MgO$, which at sintering temperature of 1700°C enhances material self–diffusion rate, and within two hours at that temperature, would yield grain sizes around 40 μm. More specifically, Ingleby and Hand tests indicated that UO_2– 0.7wt%MgO fuel pellet annealed at 1650°C in 50 vol% CO/CO_2 atmosphere would achieve grain sizes around 20–21 μm from the initial grain size of $\approx$ 10 μm within 15 min. Plus that virtually no further increase would occur at longer times. By comparison, they note that achieving a similar 20–21 μm grain size in undoped UO_2 would require anneals in hydrogen of either 150 h at 1650°C or 40 h at 1700°C.

Thermodynamic properties of a solid solution, $U_{1-y}Mg_yO_{2\pm x}$, at low magnesium concentrations have been investigated by Tateno, Fujino, and Tagawa [53] using the solid galvanic cell technique. They measured electromotive force (emf) values for samples of $y = 0, y = 0.002, y = 0.02$ and $y = 0.05$, in the temperature range 1123–1373 K, from which the temperature dependence of the oxygen chemical potential or the partial molar free energy of oxygen versus x in $U_{1-y}Mg_yO_{2\pm x}$ was determined. Figure 5 shows their measurements (markers) at $T = 1273$ K for $y = 0.02$ and $y = 0.05$. The lines in this figure are computations using a formula derived by Fujino and Sato [54]. It is seen that increasing the concentration of magnesium (y) elevates the oxygen chemical potential of the fuel and shifts its initial rise to a lower value of $x < 0$. The Fujino-Sato formula, which has a thermodynamic basis, reads

$$\mu_{O_2} = -165500 + 4bRT \ln \frac{2y + 2x - ay}{1 - 3y - 2x}, \tag{1}$$

where μ_{O_2} is the oxygen chemical potential in Jmol^{-1}, $R = 8.314$ Jmol^{-1}K^{-1}, T in kelvin and a, b are empirical constants obtained by fitting to data. In the literature, μ_{O_2} is also represented as $\Delta\bar{G}_{O_2}$. In our computations for figure 5, we used $a = 1.5$, and $b = 0.4$ for $y = 0.02$ and $b = 0.3$ for $y = 0.05$; for more details see [54].

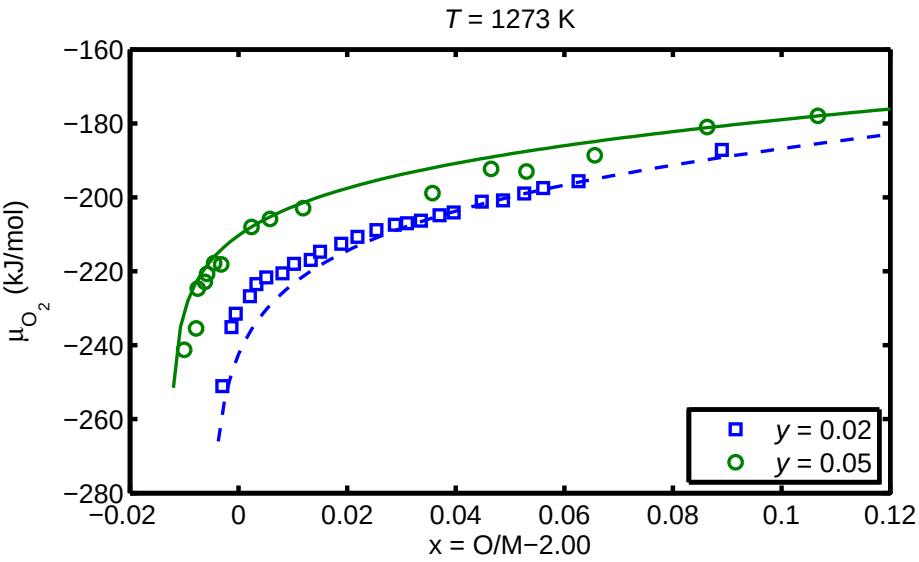

Figure 5: Oxygen chemical potential μ_{O_2} as a function of x in $U_{1-y}Mg_yO_{2\pm x}$ at $T = 1273$ K for $y = 0.02$ and $y = 0.05$. The markers represent measurements adapted from [53] and lines are computations according to the Fujino-Sato formula, relation (1).

The phase equilibria for the UO_2–MgO system have been assessed in a number of studies in the past [55–57]. The phase diagram reported in [55] was constructed from meager

experimental data of the 1950s. It indicates that the eutectic occurs at about 2220°C (2493 K) around 0.32 mole fraction MgO. In [57], however, the eutectic is reported to occur at 2553 K at ≈ 0.5 mole fraction MgO. Moreover, Sugisaki et al. [56], by means of X-ray diffraction, have studied the variation of the lattice parameter of the fluorite structure of $U_{1-y}Mg_yO_{2+x}$ containing various amounts of MgO, and the solubility of MgO in UO_{2+x}. They report a maximum solubility of 0.39 MgO mole fraction in the temperature region from 1473 K to 1873 K.

Another composite UO_2 fuel with potential LWR utilization is MnO-Al_2O_3-doped UO_2 as described by a Korean group in [58]. According to Kang et al. [58], the dopant MnO-Al_2O_3 forms a liquid phase near the conventional sintering temperature of the UO_2 pellet, enhancing the densification and increasing the grain size of UO_2 fuel. In addition, the high-temperature creep deformation rate of the fuel can be increased markedly if an appropriate amount of MnO-Al_2O_3 dopant is used in UO_2, thereby improving (soften) pellet cladding mechanical interaction (PCMI) performance of the fuel at high temperatures. As an example, figure 6 from workers in KEPCO Nuclear Fuel and Korea Atomic Energy Research Institute (KAERI) [59] shows the development of UO_2 microstructure with addition of MnO-Al_2O_3. According to Jung et al. [59], an additive concentration over 2300 wppm resulting in 40.1 μm in 2D grain size image should be applied to make UO_2 more resistant to PCMI. The density of sintered pellets has been estimated to be over 98 %TD, which is acceptable for production standard. Figure 7 shows the linear dependence of grain size as a function of MnO-Al_2O_3 concentration.

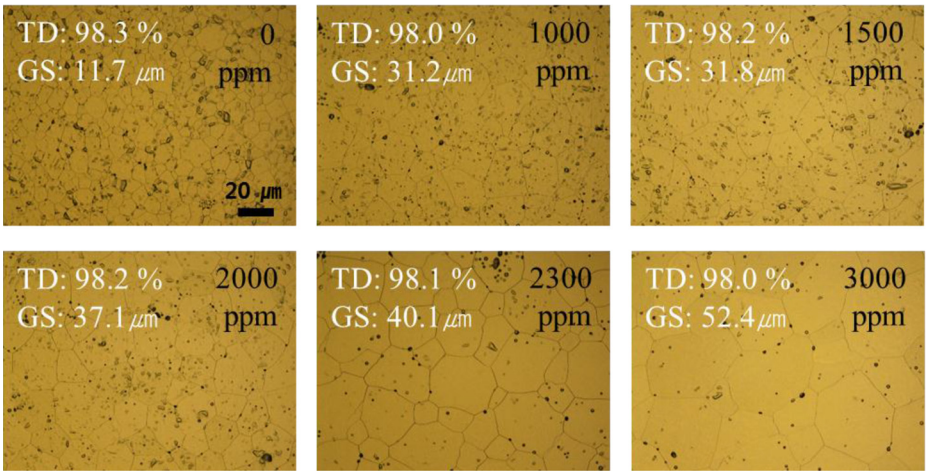

Figure 6: Grain size (GS) development by increasing the MnO-Al_2O_3 content (wppm) of UO_2 fuel with fuel theoretical density (TD) specified; from [59].

As has been reported in [60], KAERI workers have studied two types of additive-doped UO_2 fuel as potential candidate pellets for PCI remedy: MnO-Al_2O_3-doped UO_2 and Cr_2O_3-doped UO_2. The fabrication processes for these fuel pellets are briefly described in [60]. The composition of MnO-Al_2O_3 is set as 95MnO-5Al_2O_3(mol%) and the contents of Cr_2O_3 and MnO-Al_2O_3 in fuel are put as 1500 wppm and (Mn+Al)/U 1000 wppm, respectively. The microstructures of undoped UO_2 and 1000 wppm 95MnO-5Al_2O_3(mol%)-doped UO_2 pellets sintered at 1730°C for 4h in hydrogen atmosphere are shown in figure 8, reproduced here from [60]. It is seen that the grain size is markedly enlarged in the MnO-Al_2O_3-doped UO_2 pellet, for which, the average grain size is measured to be about 50 μm as compared to about 10 μm for the undoped UO_2 pellet. The thermal creep behavior of

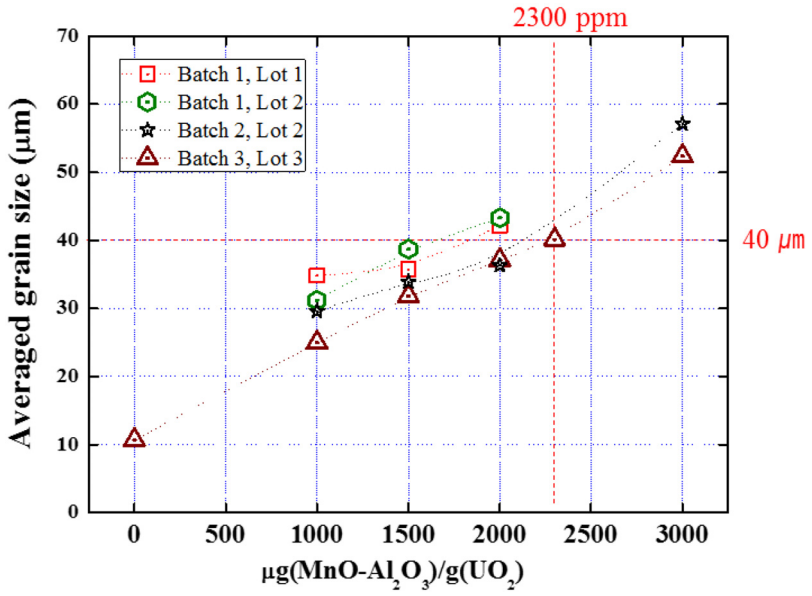

Figure 7: Grain size versus concentration level of additive MnO-Al_2O_3 in UO_2 fuel; from [59].

the aforementioned fuels is discussed in section 5.

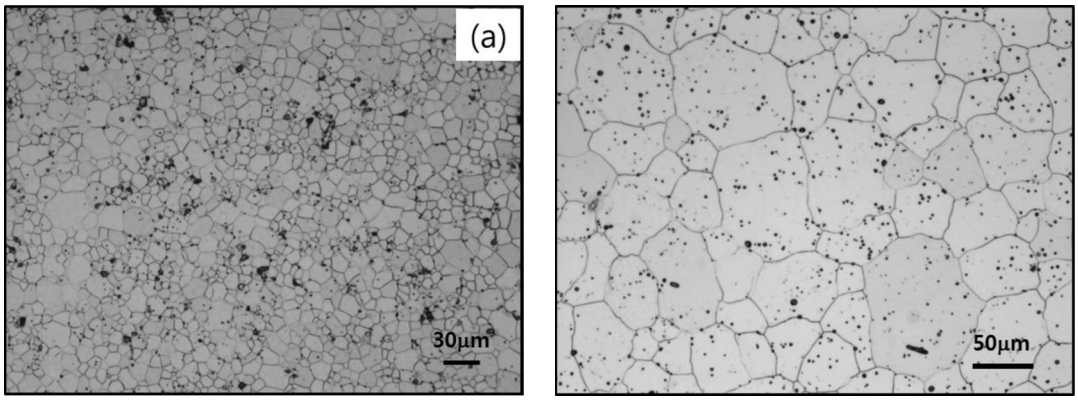

(a) (b)

Figure 8: Microstructure of (a) undoped UO_2, (b)1000 wppm 95MnO-5Al_2O_3(mol%)-doped UO_2. Fuel pellets are sintered at 1730°C for 4h in H_2; from [60].

Regarding the effect of Cr_2O_3 dopant on the point defect structure of UO_2, Kashibe and Une [11] assumed that Cr atoms enter interstitial sites in the UO_2 lattice and are ionized to a trivalency of +3. Their thermodynamic analysis [11] shows that for slightly hyper-stoichiometric $(U,Cr)O_{1+x}$, in equilibrium, the uranium vacancy concentration is proportional to the square of Cr^{3+} concentration. Thus, by dissolving Cr^{3+} ions into the UO_2 lattice, it is expected that the concentrations of cation vacancies and oxygen interstitials increase, thereby both cation and fission gas diffusivity would increase. However, generic thermodynamic calculations for trivalent dopants (M_2O_3) show that for hypostoichiometric $(U,M)O_{1-x}$, when M^{3+} ions substitute for U^{4+} ions in UO_2, it has an opposite effect [61]. That is, oxygen vacancies increase while oxygen interstitials decrease with M_2O_3 concentration [61]; see section 4.3 for concrete examples.

In a 2013 study [62], Hong and colleagues, by means of atomistic (density functional theory) computations, discuss that Cr prefers to reside in a U substitutional site and segregate

to the grain boundary. They conclude that Cr forms bonds with neighboring O atoms that weaken the ionic nature of adjacent U-O bonds, especially when it occupies U substitutional site at the grain boundary. The neighboring O atoms move towards the Cr and form Cr-O bonds with bond lengths comparable to those in Cr_2O_3 compound. This will increase electron density between U and O atoms around the Cr-O bonds, however, the absolute values of their effective charges are smaller than those of atoms in the bulk, which is primarily due to the less coordinated configuration of the grain boundary than in the bulk. Thus the ionic nature of those U-O bonds gets weaker, which enhances cation mobility that would promote UO_2 grain growth. However, when Cr resides in the interstitial site in the bulk or the free space at the grain boundary, it donates charges to the surroundings without further change of the electronic milieu according to Hong and colleagues [62].

We should note that for a dopant to be an effective grain growth promoter, i.e. to enhance self diffusion, it should be in solid solution at the applicable sintering condition. For example, for the dopant Nb_2O_5 in UO_2 at the sintering temperature of 1700°C and μ_{O_2} between -420 and -470 kJ/molO_2, the solubility limit is estimated to be about 0.4 wt% [63]. Beyond that limit, the second phase with composition close to Nb_2UO_6 has been observed at grain boundaries of the fuel [63].

For Cr_2O_3 in UO_2, Leenaers et al. [42], using electron probe microanalysis (EPMA), have found that for specimens sintered at 1600°C ($\mu_{O_2} = -370$ kJ/molO_2), 1660°C ($\mu_{O_2} = -370$ kJ/molO_2), 1760°C ($\mu_{O_2} = -360$, $\mu_{O_2} = -390$ kJ/molO_2), the solid solubility limits for Cr_2O_3 are 0.095, 0.126 and 0.149 wt%, respectively. Cardinaels et al's 2012 EPMA measurement [43] resulted in a solubility limit of 990 ± 50 μg/g for Cr in the UO_2 matrix at 1750°C, which corresponds to 0.144 wt% Cr_2O_3 solubility limit.

Clearly, the solid solubility limit of dopant depends not only on temperature, but also on the oxygen chemical potential of the fuel, which in turn is a function of temperature and the water-to-hydrogen ratio in the sintering atmosphere. The oxygen chemical potential μ_{O_2} of UO_2 as a function of temperature and p_{H_2O}/p_{H_2} may be estimated from the Wheeler-Jones empirical relation as described in [42, 64]

$$\mu_{O_2} = -479070 + 4.184T\left[8.86\log_{10}(T) - 4.42 + 9.152\log_{10}\left(\frac{p_{H_2O}}{p_{H_2}}\right)\right], \qquad (2)$$

with $\mu_{O_2} = RT\ln p_{O_2}$ in Jmol^{-1}, $R = 8.314$ Jmol^{-1}K^{-1}, T in kelvin and p_X denotes the partial pressure of X. Figure 9 depicts this relation as a function of temperature for several values of p_{H_2O}/p_{H_2}.

A detailed thermodynamic computation of the temperature dependence of oxygen chemical potential of Cr_2O_3-doped (1 mol%) UO_2 fuel has been reported in [65]. Curti and Kulik's computations [65] include the effects of of irradiation exposure (fission products) and accounts for the Zr-alloy cladding oxidation surrounding the fuel. Their computations over the temperature range of 773 - 1673 K and irradiation exposure of 1 to 60 MWd/kgU, indicate no significant effect of Cr-doping on the oxygen chemical potential, except at a very low exposure and at temperatures above 1473 K. In addition, their computations show that oxidation of zirconium alloy at the inner surface of the cladding could lower the oxygen chemical potential of the fuel considerably [65].

Riglet-Martial and colleagues, in their 2014 paper [64], have made a summary of experimental solubility data on chromium in UO_2 reported in the literature, which need not be

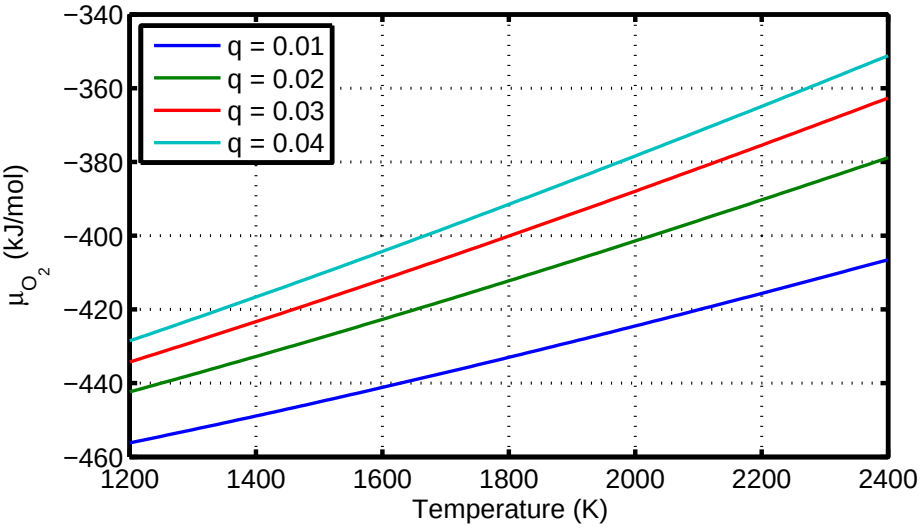

Figure 9: Oxygen chemical potential of UO_2-base fuels versus temperature at several values of the water-to-hydrogen ratio or $q = p_{H_2O}/p_{H_2}$, calculated per relation (2).

reproduced here. Besides, they have made own EMPA measurements as a function of temperature (1655-1744°C) for several values of p_{H_2O}/p_{H_2} with consistent results. In addition, the authors of [64] calculated the solid solubility of chromium or Cr_2O_3 by assuming thermodynamic equilibrium and using the mass balance law. The solubility designated by y is expressed as $\log_{10}(y) = k \log_{10}(p_{O_2}) + A + B/T$, where y in mole fraction, p_{O_2} in bar, T in kelvin, and k, A, and B are fitting parameters tabulated in [64]. Figure 10 shows the solid solubility of Cr_2O_3 in UO_2 versus temperature using this relation, where $k \approx 0$ for temperatures 1773 to 2273 according to [64]. The calculated line fits the experimental data quite well with 7% uncertainty. Here, we have only included six data points in our figure from refs. [42, 43, 64]. For solubility of CrO and Cr in UO_2, $k = 1/4$ and $k = 3/4$, respectively, with a different set of A and B values [64].

The solubility limits of chromium and its stable oxides in UO_2 as a function of oxygen partial pressure p_{O_2} at temperatures $T = 1973$ K and $T = 2013$ K are shown figure 11. The lines in the figure are calculations based on empirical correlations given in [64] with some modifications. And the markers are the measured data in [64]. As can be seen from the figure, increasing p_{O_2}, or the chemical potential, increases the solubility; recall that the oxygen chemical potential is related to p_{O_2} as $\mu_{O_2} = RT \ln(p_{O2})$. Furthermore, the solubility limit at higher pressures flattens out, i.e. becomes independent of pressure in the region of Cr_2O_3 according to the present model. Obviously, the calculated lines go through the measured data, however, the used piecewise correlations are fit to do so, rather than having a theoretical or phenomenological foundation. Hence, the predictive capability of the putative model for solid solubility to a wider parameter range is yet unresolved.

More recently, Cooper and colleagues [66] studied the role of dopant charge state on defect chemistry and grain growth of doped UO_2 by means of atomistic simulations. They computed the defect chemistry of UO_2 doped with Cr, Al, Mn, Fe, V, Ti, and Mg. Their computations show that a common mechanism for dopant solution is as positively charged interstitials in UO_2. At temperatures pertinent to sintering, all dopants studied in [66] (except Al) were calculated to form 1^+ or 2^+ charged interstitial defects at different concentrations depending on the dopant. Vanadium-doped UO_2 was calculated to have the

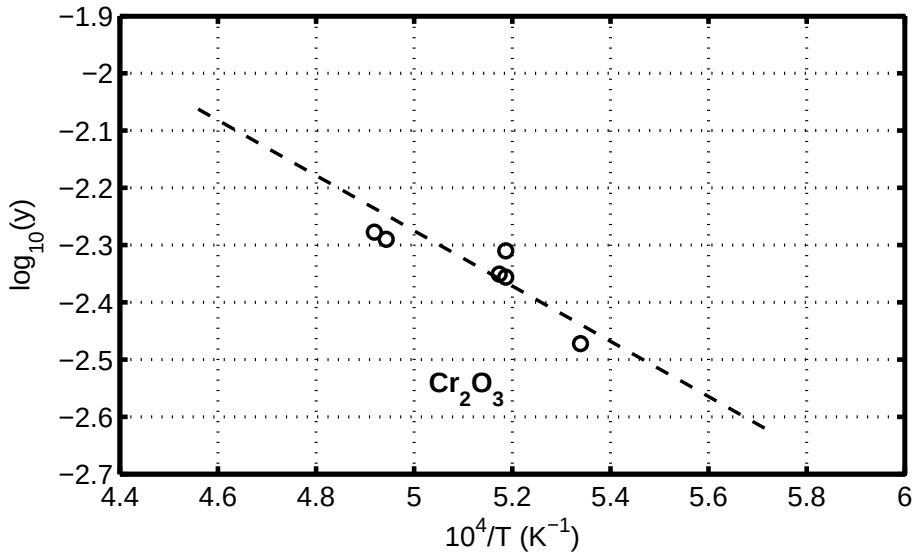

Figure 10: Solid solubility of chromia in UO_2 (y, mole fraction) as a function of inverse temperature $(1/T(\text{kelvin}))$. The dashed line is calculation according to a model in [64] and the six data points (circles) are measurements reported in [42, 43, 64]. The temperature range of dashed line is 1750-2200 K.

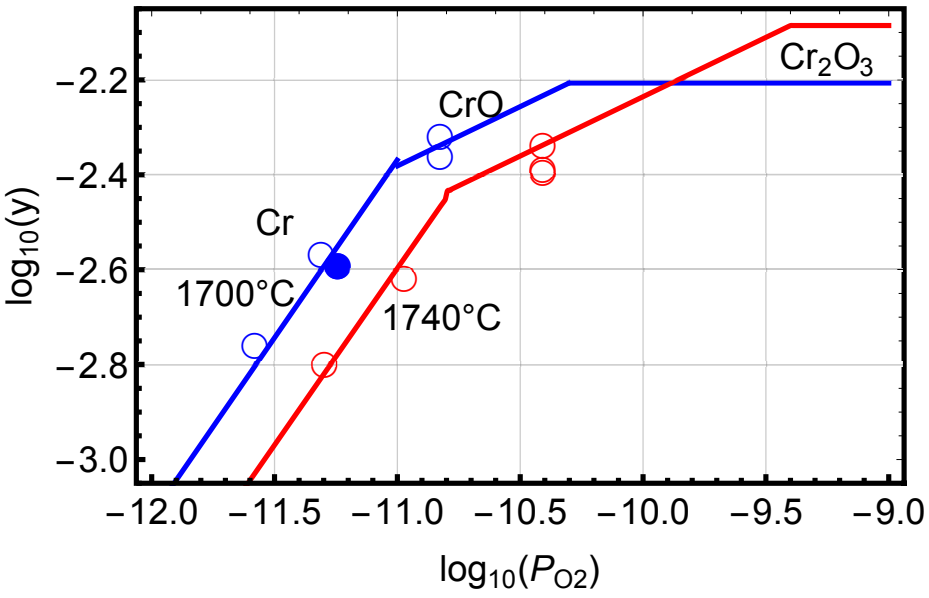

Figure 11: Solubility limits of Cr, CrO and Cr_2O_3 in UO_2 as a function of oxygen partial pressure calculated at two different temperatures (lines) and measured data (markers) based on the data and relations given in [64]. The abscissa can be converted to the oxygen chemical potential via $\mu_{O_2} = RT\ln(10)\log_{10}(P_{O2})$, $R = 8.314$ JK^{-1}mol^{-1}, and T in kelvin.

highest solubility at the interstitial site followed by Mn, Ti and Cr. As a result, Ti, V, Cr, and Mn greatly enhance the charged uranium vacancy (V_U'''' in Kröger-Vink notation) concentrations compared to undoped UO_2. Also, Fe and Mg enhance the V_U'''' concentration but to a lesser extent, whereas Al has no effect.

Cooper et al. note that an apparent preference of the interstitial site for low valence cations implies that dopants with a chemistry that enables charge states of 1^+ or 2^+, namely, Cr, Mn, Fe, V, Ti, and Mg, are accommodated at sufficiently high concentrations which modify the host defect concentrations. On the other hand, the low solubility of Al at the interstitial site is attributed to its incapacity to access 1^+ or 2^+ charge states, thereby it remains in the 3^+ state. At high (sintering) temperatures, all dopants studied make transition to a positively charged interstitial defect. Furthermore, their computations indicate that a number of dopants, namely, Ti, V, Cr, and Mn, do so in sufficiently high concentrations to greatly increase the negatively charged uranium vacancy concentration. On the other hand, Al-doped UO_2 has no impact on V_U'''', i.e. comparable to undoped UO_2. This is in agreement with experiment, showing that Al does not enhance grain growth adequately in UO_2 [67].

Cooper and colleagues [66] contend that the enhanced uranium vacancy concentrations, associated with solid solution of dopants interstitially, is the mechanism accountable for the enlarging UO_2 grains observed experimentally in Ti-, V-, Cr-, or Mg-doped systems. Their computations indicate that Mn- and V-doped UO_2 have higher uranium vacancy concentrations than the widely used Cr-doped UO_2, leading to a higher grain growth and enhanced fission gas diffusivity. In more detail, they argue that the mean grain sizes of doped ($\mathfrak{S}_d$) and undoped ($\mathfrak{S}_u$) UO_2 can be related to the corresponding vacancy contents via

$$\frac{\mathfrak{S}_d}{\mathfrak{S}_u} = \left(\frac{[V_U]_d}{[V_U]_u} \right)^{1/2}, \tag{3}$$

where $[V_U]_d$ and $[V_U]_u$ stand for the uranium vacancy concentrations for doped and undoped UO_2, respectively. Figure 12, taken from [66], illustrates this relationship as a function of temperature. It is seen that vanadium-doped UO_2 provides the largest grain size, followed by Mn-doped and Cr-doped, etc. [66].

The basic difference between Cr and Al stems from their ground state electronic configurations. Chromium is a transition metal (group 4B column of the periodic table), which means it can form stable ions with only a partially filled d-shell. Whereas, aluminium is group 3A column with three electrons beyond a stable noble gas configuration. Aluminum has a strong preference to lose all the 3 electrons in its outer shell and rendering the transition to charge states below 3^+ state unfavorable; see ref. [66].

Cooper et al.'s computations suggest that the dopant Cr can also be in 1^+ oxidation state in UO_2. However, later atomistic computations made by Sun, Stackhouse and Kowalski [68] indicate that Cr in UO_2 only exists as Cr^{2+} species rather than as Cr^{1+} or Cr^{3+}. In particular, their thermodynamic evaluation shows that the favorable structural arrangement of Cr in UO_2 is given by a pair of Cr^{2+} ions and oxygen vacancy. In this configuration, Cr atom will be shifted towards cations sublattice vacant site, which will result in a pseudo sixfold coordination, instead of the eightfold coordinated uranium site in UO_2 [68].

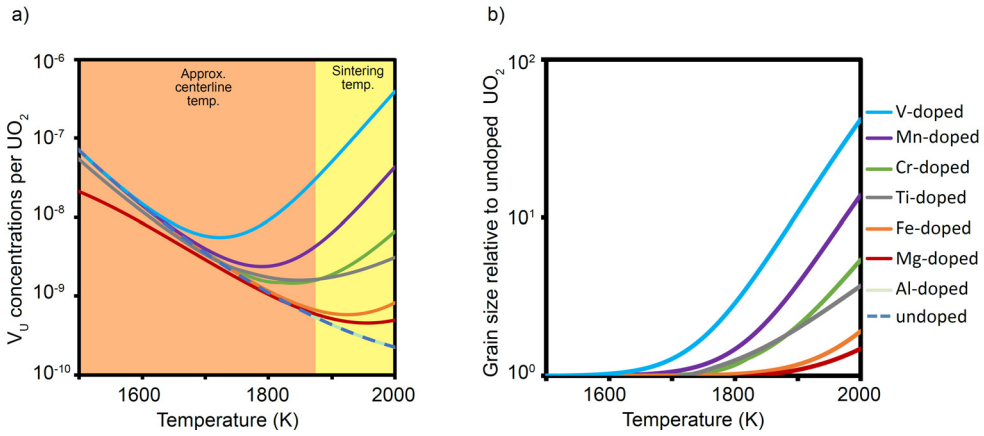

Figure 12: Cooper et al.'s analysis showing the relationship between uranium vacancy concentration (V_U) as a result of doping UO_2 with various elements and the resulting grain size as a function of temperature: (a) Comparison of the V_U concentrations in undoped and (Mg/Al/Ti/V/Cr/Mn/Fe)-doped UO_2 at temperatures pertinent to the fuel central region and for sintering with an oxygen partial pressure of 10^{-20} (atm). (b) The grain size increase with respect to undoped UO_2 assuming diffusion dominated grain growth; from [66].

2.2 Burnable absorber fuel

Uranium dioxide fuel with burnable neutron absorber (BA) material is commonly used to control or depress reactor power early in the irradiation [69–71]. Small amount (a few wt%) of gadolinium, and to some extent erbium [24, 72–74] and even europium [27, 75], mixed with UO_2 are currently the materials used or the latter considered in power nuclear reactor operation as BAs. These BA elements are classed as heavy rare earths, which range from atomic number 62 (Sm) to 71 (Lu). The fuel chemistry of these BA fuels are fairly well studied in the literature especially the former types. The neutronic merits of these BAs for PWRs have been assessed and compared in [76]. Here, we briefly review the chemical thermodynamics of these compounds.

62	63	64	65	66	67	68	69	70	71
Sm	Eu	Gd	Tb	Dy	Ho	Er	Tm	Yb	Lu

2.2.1 Gd-U-O

Gadolinium in UO_2 fuel provides an effective BA, utilized widely over the years in LWRs [77–80]. For a BA fuel, e.g. (U,Gd)O_2, to be fully neutronic effective, the additive (Gd_2O_3) should form an ideal solid solution in the UO_2 fuel matrix. The standard technique of dry milling and blending of UO_2 and Gd_2O_3 powders followed by sintering, described in [78], does not yield an ideal homogeneous UO_2-Gd_2O_3 fuel pellet. A photomicrograph of the sintered matrix fuel matrix from ref. [78] is shown in figure 13. This micrograph reveals the free UO_2 (blue-green), free Gd_2O_3 (light-tan) and UO_2-Gd_2O_3 solid solution (brown) regions. The blue-green UO_2 particle in the lower left corner of the micrograph is ≈ 230 μm.

One fabrication technique used to achieve maximum fuel pellet homogeneity is to add a small amount of $Al(OH)_3$ and/or TiO_2 to the powder blends of Gd_2O_3 and UO_2 during fabrication [81]. These additions promote diffusion during the sintering stage of fabrication

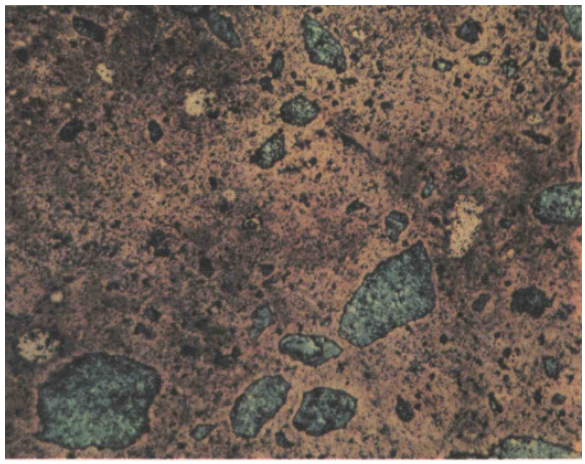

Figure 13: UO_2-Gd_2O_3 micrograph ($100\times$) of sintered matrix; from Newman et al. [78].

thereby enhancing homogeneity in fuel pellet. With the technique described in [81], the added gadolinia will primarily reside in solid solution with urania.

The phase equilibria of the U-Gd-O system determining the melting point of UO_2 as a function of Gd_2O_3 concentration have been measured and assessed by many investigators [77, 78, 82–85]. Perhaps the most accurate data are from the measurements of Kang and coworkers [83], where they determined the solidus and liquidus temperatures of UO_2-Gd_2O_3 in the Gd_2O_3 concentration of interest (up to 12 wt%). Figure 14 shows these data plus some older data. As can be seen, there is a slight decrease of the melting point from that of undoped UO_2, decreasing with Gd_2O_3 concentration.

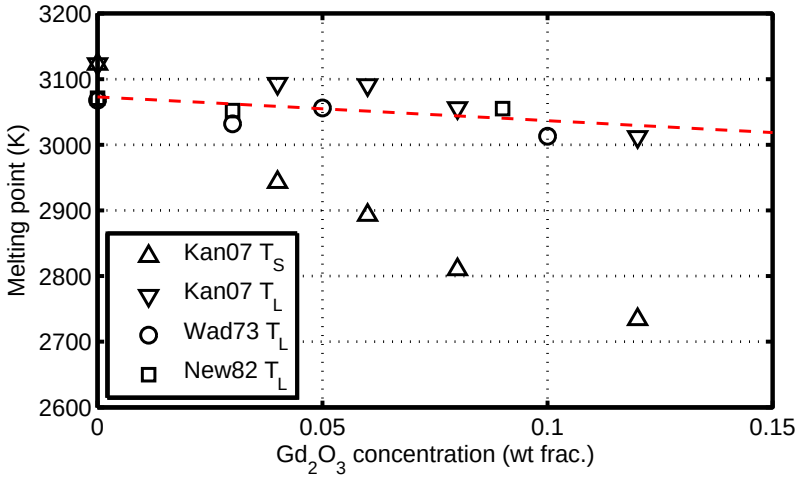

Figure 14: The melting point of UO_2-Gd_2O_3 vs. weight fraction of Gd_2O_3. The measured data (markers) are from: Kan07 [83], Wad73 [77], New82 [78], where T_L and T_S denote the liquidus and the solidus temperatures, respectively. The broken line is the melting curve from Wada et al. [77].

A systematic experimental study of the chemical thermodynamics of the U-Gd-O system was initiated with the works of Une and Oguma [86–88], followed by complementary measurements of the oxygen chemical potential of $U_{1-y}Gd_yO_{2\pm x}$ by Lindemer and Sutton [89] for an extended range of x and y at temperatures between 1273 K and 1773 K. Une and Oguma [86–88] utilized a solid electrolyte galvanic cell or/and a thermogravimetric technique to determine the oxygen partial pressure, i.e. oxygen chemical potential μ_{O_2}, at

several values of y (Gd concentration) and temperatures. Lindemer and Sutton [89] used a standard technique to measure changes in specimen weight at different applied oxygen partial pressures at various temperatures. A microbalance was used to determine mass change at temperature. The oxygen chemical potential for the solid solution increases positively with increasing Gd content.

In order to illustrate the dependence of $\mu_{O_2} = RT \ln {p_{O_2}}^2$ in $U_{1-y}Gd_yO_{2\pm x}$ on x and y, we have depicted the Lindemer-Sutton data in figure 15 at 1773 K, where O/M=$2+x$. Markers in this figure are measurements from [89], while the lines are computations according to a simplified model described in [90]. It is seen that as x increases so does oxygen partial pressure p_{O_2}. Similarly, increasing y increases p_{O_2} . The accuracy of the O/M values in figure 15 is believed to be ± 0.001 according to [89]. For computations, we have used the semi-phenomenological model of Park and Olander, described by their relations (15)-(16) in [90] with data fitting parameters. As can be seen from figure 15, the two relations (one $x > 0$ another for $x < 0$) qualitatively reproduce the data for O/M > 1.95 and $y \geq 0.1$. It is, however, poor for OM <1.95 and fails at O/M = 2.00 and $y = 0.0$ due to a logarithmic singularity. A distinctive feature of $U_{1-y}Gd_yO_{2\pm x}$ is an abrupt change in the oxygen potential at $x = 0$, which occurs even at lower temperatures than $T = 1773$ K. To illustrate this attribute, we have used the Park-Olander model to calculate p_{O_2} versus x for different values of y at several temperatures with the results shown in figure 16.

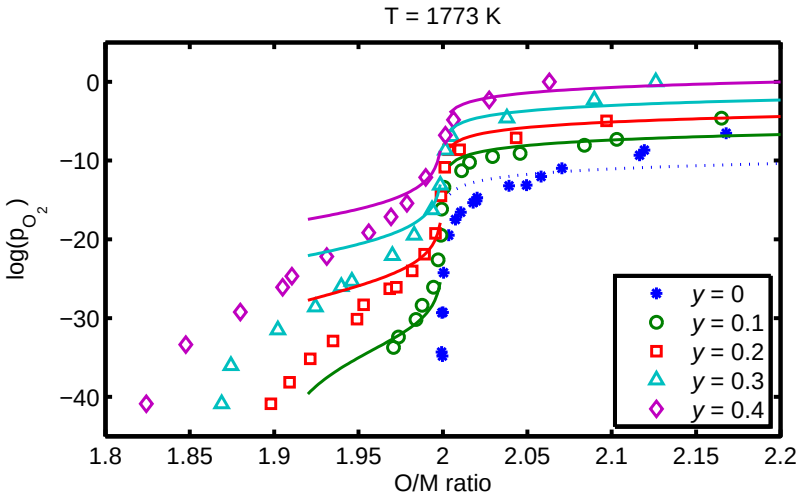

Figure 15: Oxygen partial pressure of $U_{1-y}Gd_yO_{2\pm x}$ at 1773 K with where O/M=$2+x$. Markers indicate measurements from [89] while the lines are computations according to a simplified model described in [90].

A comprehensive thermochemical assessment of the U-Gd-O system, comprising modeling, computations and comparison with measured data, has been made by McMurray and coworkers in [84, 85]. Their work includes extensive computations of the oxygen chemical potential in form of $\ln p_{O_2}$ as a function of the O/M ratio versus experimental data in a wide temperature range, through which the phase equilibria for the system are established.

In a $U_{1-y}Gd_yO_{2\pm x}$ compound, the trivalent Gd resides in the oxide as an isolated defect on uranium sublattice (Gd'_U) unless anion vacancies pre-exist. Due to its negative charge, this cation repels nearby double-charged interstitials, by coulomb force, thereby effectively eliminating some interstitial sites for oxygen from the lattice. This effect would not appear

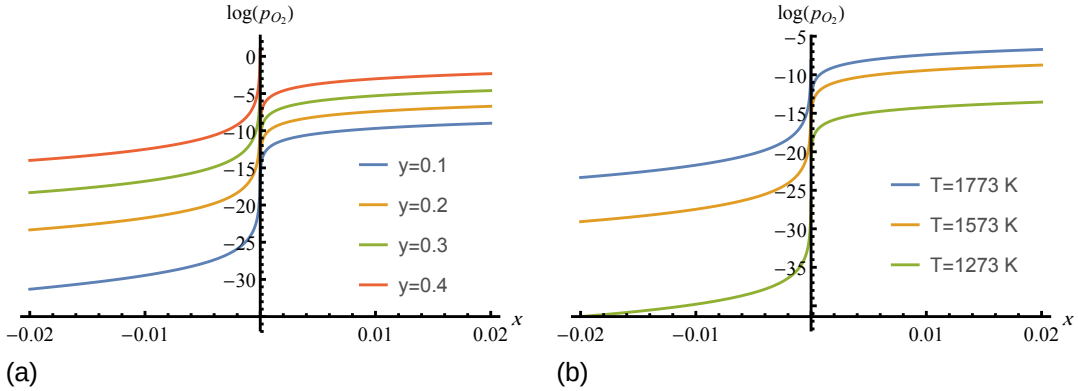

Figure 16: Calculation results by using the Park-Olander approximative model for the oxygen partial pressure in $U_{1-y}Gd_yO_{2\pm x}$ as a function of $x = O/M - 2.00$. (a) At $T = 1773$ K for several values of y, (b) for $y = 0.2$ at several temperatures.

in pure urania since in UO_{2+x}, in which oxygen interstitials can be prevalent, the concentration U'_U (in Kröger-Vink notation) is small or negligible [90]. Because Gd dopant ions are negatively charged, they attract positive anion vacancies and form dopant-vacancy clusters. According to analysis in [90], out of many possible clusters, the following reactions provide the best outcome:

$$V_O^{\cdot\cdot} + U_U{}^x + 2Gd'_U + U_U^{\cdot} \rightleftharpoons (2U : V : 2Gd)^{\cdot} \tag{4}$$

where $(2U : V : 2Gd)^{\cdot}$ is the dopant-vacancy cluster and here the Kröger-Vink notation is used, see Table 3. The presence of dopant-vacancy clusters in $UO_{1-y}Gd_yO_{2-x}$ fuel is expected to affect (reduce) fission product gas diffusivity and thereby fission gas release during irradiation; see section 4.3.

Table 3: Notation used for point defects in UO_2 crystal.

Defect type	Kröger-Vink notation	Electric charge
Oxygen interstitial	O''_i	-2
Oxygen vacancy	$V_O^{\cdot\cdot}$	+2
Uranium electron/polaron	U'	-1
Uranium hole	$U^{\cdot}$	+1
Gd atom on a U lattice site	Gd'_U	-1
U atom on a U lattice site	$U_U{}^x$	0
Vacancy-uranium dimer	$(V : U : V)^{\cdot\cdot}$	+2

2.2.2 U-Er-O

The reactor cycle length for UO_2-Gd_2O_3 fuel is currently about 12-18 months, with the Gd_2O_3 content ranging from 4 to 10 wt% depending on the cycle length design [83]. An extension of the cycle length is one method to increase the efficiency of reactor operation or reduce the fuel cycle cost. For longer operating cycles than 18 months, UO_2-Er_2O_3 is expected to be more suitable than UO_2-Gd_2O_3, because erbium provides a "weaker" neutron absorber than gadolinium. The UO_2-Er_2O_3 fuel is expected to have 1-2 wt% Er_2O_3.

Thermochemistry of $U_{1-y}Er_yO_{2\pm x}$ has not been studied as extensively as $U_{1-y}Gd_yO_{2\pm x}$ fuel in the literature. There are, however, some studies by Korean researches [25, 83, 91, 92]. H. S. Kim and coworkers [25] have measured the oxygen chemical potentials of $U_{1-y}Er_yO_{2\pm x}$ solid solutions by means of a thermogravimetric technique in the range of 1200-1500°C (1473–1773 K) and $10^{-13} \leq p_{O_2} \leq 10^{-4}$ atm. for $y = 0.06$ and $y = 0.20$, respectively. Their results show that for $U_{1-y}Er_yO_{2\pm x}$:

- The chemical potential of oxygen μ_{O_2} undergoes an abrupt increase at $x = 0.00$ in the range of $-270 \rightarrow -360$ kJ/mol for $y = 0.06$ and $-220 \rightarrow -320$ kJ/mol for $y = 0.20$, respectively, in the temperature range of 1473–1773 K.
- The difference between the μ_{O_2} values at O/M = 1.999 and 2.000 for $y = 0.06$ was about 90 kJ/mol at 1473 K, and the corresponding difference was about 40 kJ/mole at 1773 K.
- By X-ray measurement, they found that the lattice parameter of $U_{1-y}Er_yO_2$ reduces linearly with an increase in the erbium concentration. The change of lattice parameter can be described by a linear equation as $a(\text{Å}) = 5.4695 - 0.22y$ for $0 \leq y \leq 0.33$.

H. S. Kim and colleagues, in a subsequent work [91] on $U_{1-y}Er_yO_{2\pm x}$, made further experimental investigations to obtain the thermodynamic data for $y = 0.02$ and the supplementary data for $y = 0.06$ and 0.20 in the range $10^{-14} \leq p_{O_2} \leq 10^{-3}$ atm. and $T = 1473 - 1773$ K. They assumed that the trivalent Er^{3+} ions interact with the nearest positive polarons [3] and form $(Er'U)^{\cdot}$ clusters in hyperstoichiometric $U_{1-y}Er_yO_{2+x}$. In hypostoichiometric region, the charge for $V_O^{\cdot\cdot}$ was assumed to be compensated by the decomposition of $Er'^{\,x}_U$ cluster and the change of $U_U^{\cdot}$ to U_U^{x} or by electrons. They took a thermodynamic approach to study the dominant defect clusters in hyper and hypostoichiometric $U_{1-y}Er_yO_{2\pm x}$ solid solutions. In more detail, Kim et al.'s point defect-thermodynamic formulation is based on the presence of the Willis clusters [93] in the anion sublattice and the local dopant–host clusters in the cation sublattice [4]. In their model, they assumed that the $(Er'U^{\cdot})^{x}$ cluster is a predominant defect in the cation sublattice, and either so-called $(2{:}1{:}2)'$ or $(2{:}2{:}2)'$ cluster is a prevailing defect in the anion sublattice for the hyperstoichiometric solid solution. Upon these assumptions, by applying the mass action law for possible defect clusters in $U_{1-y}Er_yO_{2\pm x}$, they derived equilibrium equations relating the p_{O_2} to x and y, which fit their experimental data for given temperatures [91]. The liquidus temperature of UO_2-Er_2O_3 decreases with the Er_2O_3 content, and the solidus temperatures are about 180-270 K lower than the liquidus temperatures; cf. figure 17 with figure 14 for UO_2-Gd_2O_3.

Fedotov and coworkers [94], based on X-ray diffraction studies, have obtained simple formulae for calculating the theoretical density (TD) of a stoichiometric, equilibrium, solid solution for (U,Gd)O_2 and (U,Er)O_2 fuels as a function of Gd_2O_3 or Er_2O_3 concentration. We have plotted their results in figure 18. The reduction in TD of (U,Gd)O_2 is much sharper than that of (U,Er)O_2, with slopes –0.031 vs. –0.0175 per wt% of the respective additive.

In another comparison between (U,Gd)O_2 and (U,Er)O_2 fuels, in regard to their respective sintering behavior, Durazzo et al. [95] have investigated the sintering behavior of (U,Er)O_2 (in the range of 0–10 wt% Er_2O_3) and compared it with that of (U,Gd)O_2. Their study shows that the behavior of (U,Er)O_2 fuel sintering is similar to that for (U,Gd)O_2 fuel [96]; e.g. two-stage sintering with two peaks in the sample shrinkage rate (densification) vs. temperature curves. But, the peaks are less pronounced for Er_2O_3 than for Gd_2O_3. Durazzo

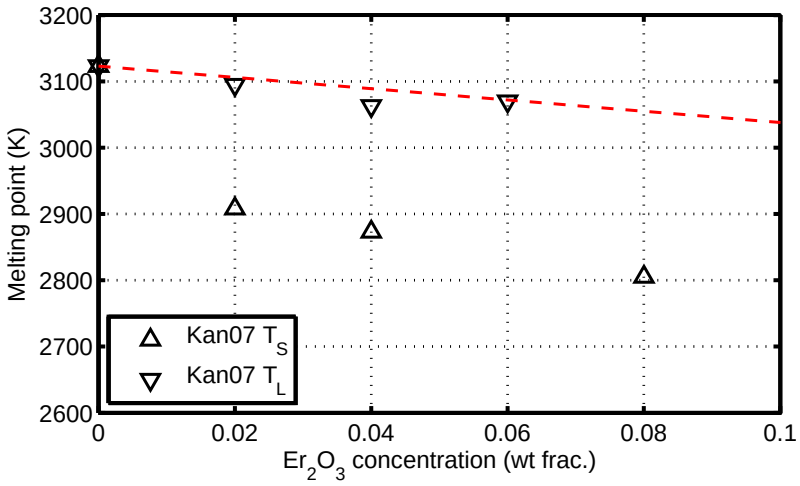

Figure 17: The melting point of UO_2-Er_2O_3 vs. weight fraction of Er_2O_3. The measured data (markers) are from Kan07 [83], where T_L and T_S denote the liquidus and the solidus temperatures, respectively. The broken line is a melting curve trend-line.

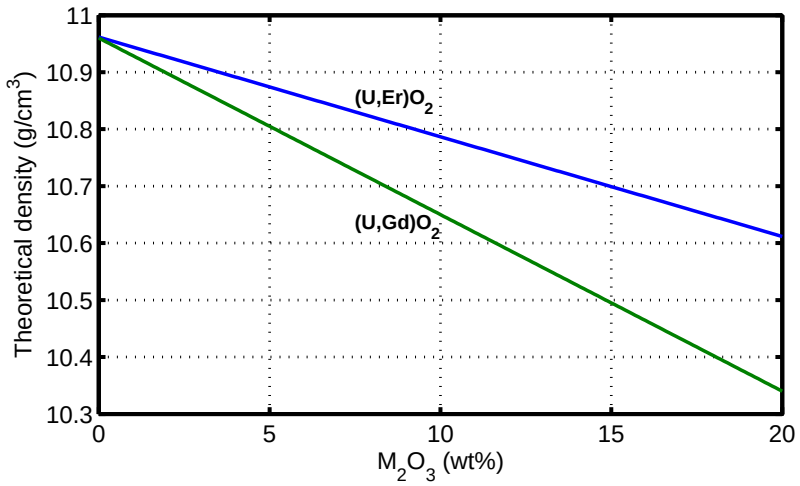

Figure 18: Theoretical density of (U,Gd)O_2 compared with that of (U,Er)O_2 versus Er_2O_3 or Gd_2O_3 concentration as calculated by the Fedotov et al. empirical formulae [94].

et al. [95] attribute this to the characteristics of the Er_2O_3 powder particles, used as raw-material, whose agglomerates are more easily broken and thereby more easily homogenized during the blending with UO_2 powder than the Gd_2O_3 powder. The (U,Er)O_2 samples were sintered to 1700°C (heating rate 5°C/min), with isothermal treatment at this temperature for 240 min. under pure hydrogen atmosphere [95].

2.2.3 U-Eu-O

As erbia-urania BA fuel, europia-urania fuel, or UO_2-Eu_2O_3, is more suitable for extended reactor cycles than gadolinia-urania BA fuel. However, its usage in LWRs has been rare. As noted in [76], although europium is a highly efficient neutron absorber, it transmutes by neutron capture and β-decay onto other neutron absorber isotopes, and it also loops onto other neutron absorbent rare earths, such as gadolinium isotopes, at the end of the chain. So, Eu introduces excessive residual neutron poisoning or even gives a poor burnup kinetics. Therefore, its usage for LWRs may be very limited or complicated [71].

Solidus and liquidus temperatures of UO_2-Eu_2O_3 versus Eu_2O_3 concentration have been determined at ambient pressure experimentally by thermal analysis, X-ray diffraction and metallography in [97], figure 19. And a ternary phase diagram of the $UO_2EuO_{1.5}O$ system at 1250°C has been determined by means of X-ray diffraction and electrochemical methods. Besides, a phase diagram for the UO_{2+x}-Eu_2O_3 system ($0 \leq x \leq 1$) at an oxygen pressure $p_{O_2} = 1$ atm. was constructed [98, 99]; see figure 20.

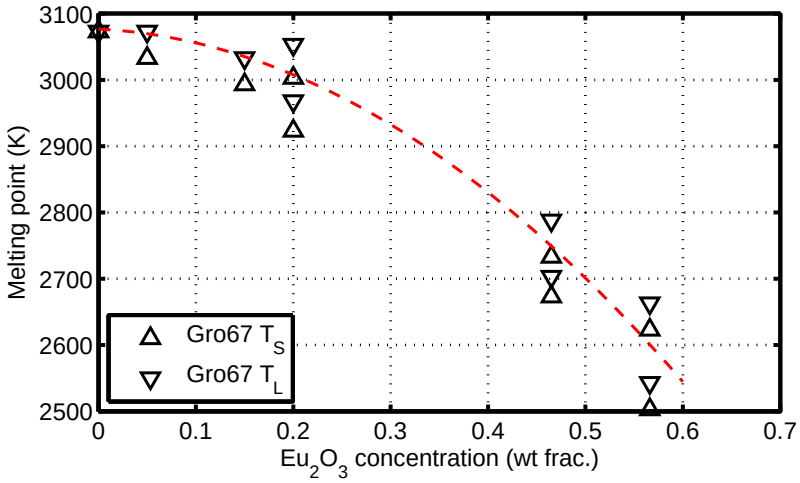

Figure 19: The melting point of UO_2-Eu_2O_3 vs. weight fraction of Eu_2O_3. The measured data (markers) are from Gro67 [97], where T_L and T_S denote the liquidus and the solidus temperatures, respectively. The broken line is a melting curve trend-line.

The oxygen chemical potential (μ_{O_2}) of europium solid solution $U_{1-y}Eu_yO_{2\pm x}$, which governs the solubility of Eu in UO_2, has been measured for $y = 0.1$ and 0.3 at 850 and 1050°C [100, 101]. It was seen in those studies that μ_{O_2} increases markedly by the addition of Eu, which is in accord with the behavior observed for most solid solutions. However, in addition to this, μ_{O_2} of $U_{1-y}Eu_yO_{2\pm x}$ was unusual in a point that the steepest change of μ_{O_2} occurred at $x < 0$, i.e. for $O/M < 2.0$, where $M = Eu + U$, and not at $x = 0$ as in the case of gadolinia-urania or erbia-urania compounds. This effect was attributed to a possible Eu^{2+} state in $U_{1-y}Eu_yO_{2\pm x}$ at high temperatures [100, 101]. The μ_{O_2} change was

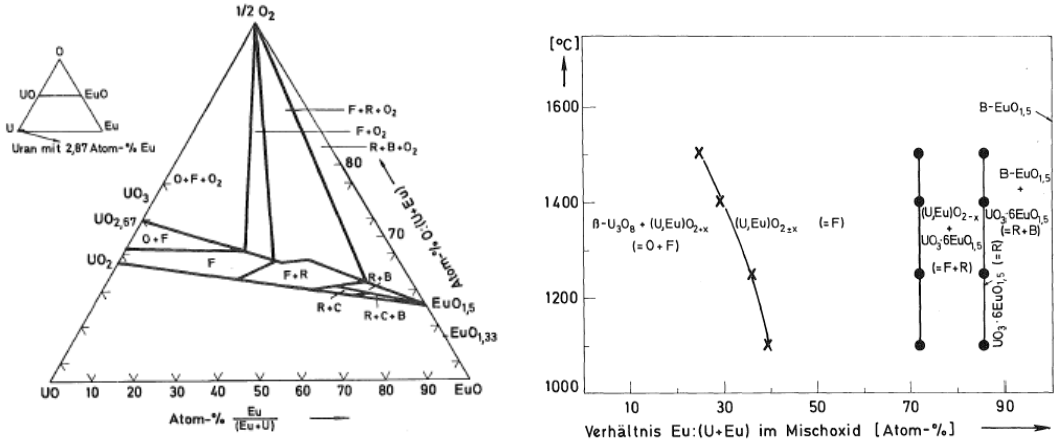

(a) (b)

Figure 20: (a) A portion of the phase diagram of the U-Eu-O system at 1250°C. (b) The pseudo-binary UO_{2+x}-$Eu_{1.5}$ for $p_{O_2} = 1$ atm.; from Tanamas [98]. Here, F=fluorite phase, O=orthorhombic U_3O_8, R=rhombohedral phase, B=monoclinic $Eu_{1.5}$,P=orthorhombic $EuUO_3$.

calculated by Fujino and collaborators [100, 101] from the entropy change in the crystal of the europium solid solution assuming the formation of (Eu^{2+}-U^{5+}) and (Eu^{2+}-$2U^{5+}$) complexes in $U_{1-y}Eu_yO_{2\pm x}$ [54, 102]. Their calculated μ_{O_2} values, based on a statistical thermodynamic model fit to the specific set of measured data, were in good agreement with the experimental data for elements La, Mg and Eu in solid solutions [102]. But the predictive ability of the model, as it stands, seems to be limited to a wider range of parameters.

Park and Olander have also modeled and computed the oxygen chemical potential of $U_{1-y}Eu_yO_{2\pm x}$ [90]. They assumed the formation of $(n\mathrm{Eu}2\mathrm{V_O})^{(n-4)'}$ and $(\mathrm{V_O UV}_O)^{\cdot\cdot}$ clusters, in the Kröger-Vink notation, together with the Willis (2:2:2) complexes in the europium solid solution. They solved the simultaneous equations of the equilibrium of the defect complexes, including the associated chemical reactions, by fitting model parameters to measured data, and found that satisfactory agreement was obtained by assuming the formation of $(6\mathrm{Eu}2\mathrm{V_O})^{2'}$. Again, the predictive capability of the Park-Olander model seems to be limited.

Additional more accurate data on $U_{1-y}Eu_yO_{2\pm x}$ regarding μ_{O_2} as a function of x value for $y = 0.05$ and $y = 0.1$ at $T = 1000$, 1100 and 1200°C were generated in [103]. With the addition of europium, again a significant increase in μ_{O_2} was observed in the hypostoichiometric region. However, its effect was almost the same for $y = 0.05$ and 0.1 in the hyperstoichiometric region. The steepest μ_{O_2} change occurred at the same O/M ratio of 1.995 at the considered temperatures and for $y = 0.05$. But the oxygen chemical potential at 1200°C was higher than that at 1000°C for the O/M ratios higher and lower than 1.995. The O/M ratio giving the steepest change of μ_{O_2} decreased with decreasing temperature in the temperature range of 1000–1400°C for $y = 0.1$, although this effect was not observed for $y = 0.05$ [103].

In order to improve the fuel performance of BA fuels during irradiation, studies have been made on the effects of addition of magnesium to $U_{1-y}Eu_yO_{2\pm x}$ and $U_{1-y}Gd_yO_{2\pm x}$ [104, 105]. The thermodynamic properties of urania solid solution doped with magnesium are markedly different from those doped with gadolinium or europium. The solubility of MgO

in UO_2 is much lower than that of Gd_2O_3 or Eu_2O_3 under low oxygen pressures, even at high temperatures ($T \geq 2273$ K). However, sintering UO_2 with MgO on pellet fabrication yields a fuel with a larger grain size, which has the effect of reducing fission product gas release during irradiation.

The oxygen chemical potential of $U_{1-y}Mg_yGd_zO_{2\pm x}$ as a function O/M ratio for several concentrations of magnesium is shown in figure 21 based on the measurements of Fujino and coworkers [105] at $T = 1523$ K. The drawn lines are qualitative representations of experimental data. It is noticed that the steepest change in μ_{O_2} occurs between -400 and -300 kJ/mol, which correspond to $p_{O_2} = 1.19 \times 10^{-9}$ and 5.1×10^{-6} Pa, respectively. The steepest change in μ_{O_2} occurs at O/M <2, where M=Mg+Gd+U, and the shift to the left gets wider as the magnesium concentration is increased, indicating that Mg is the cause of this effect. The same effect has been observed in $U_{1-y}Eu_yGd_zO_{2\pm x}$ fuel [104].

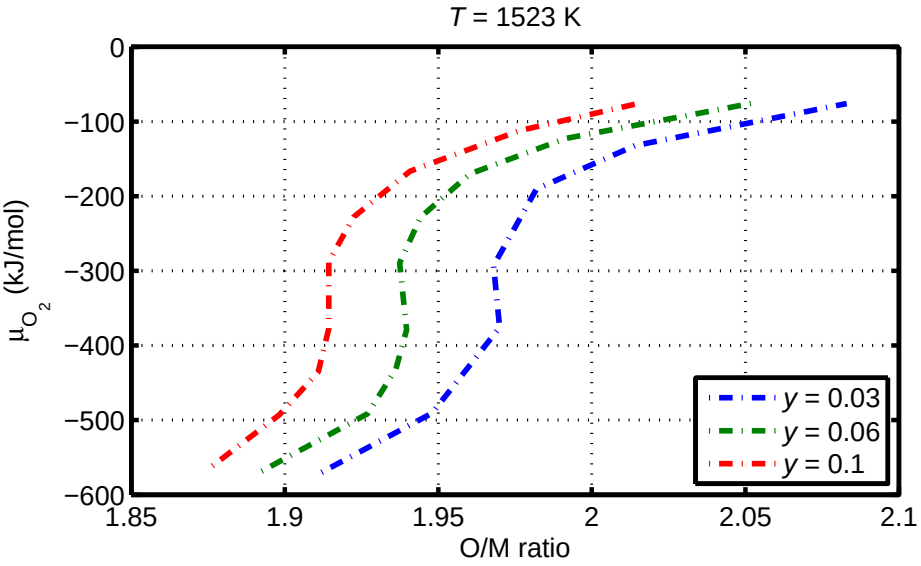

Figure 21: Oxygen chemical potential μ_{O_2} as a function of O/M ratio (M=Mg+Gd+U) in $U_{1-y}Mg_yGd_zO_{2\pm x}$ at $T = 1523$ K for $z = 0.14$, $y = 0.03$, $y = 0.06$ and $y = 0.10$. The lines are schematic, adapted from those in figure 1 of Fujino et al. [105].

2.3 Enhanced conductivity UO_2 fuel

Oxide fuels, such as UO_2 base fuels, are insulators that have relatively low thermal conductivities, while possessing high melting points. However, over the years, attempts have been made to enhance the thermal conductivity of UO_2 by introducing certain additives into its matrix to achieve a higher thermal conductivity with the aim of improving fuel performance during irradiation [32, 33]. A review of non-metallic crystals with high thermal conductivity and sufficient chemical compatibility with UO_2, stability in aqueous environments, compatibility with zirconium alloy cladding materials, suitable neutronics, and irradiation performance, has narrowed the choice of additives to include BeO, SiC, synthetic diamonds or carbon-base additives [34, 35, 106].

2.3.1 UO_2–BeO

Beryllium oxide (BeO) can be sintered at typical UO_2 fuel fabrication sintering temperatures. It is stable with UO_2 up to the eutectic point. An early constructed phase diagram for the UO_2-BeO system from Lang et al. [55] is reproduced in figure 22. These authors found that no compound or second-phase formations occurred at temperatures from 800°C to 1800°C within the compositional range 10 to 90 mol% of BeO. The eutectic of the UO_2-BeO system was found to be located at 63 ± 2 mol% of BeO and 2150 ± 10°C (2423 ± 10 K). The melting point of BeO was determined as 2450 ± 20°C (2723 ± 20 K).

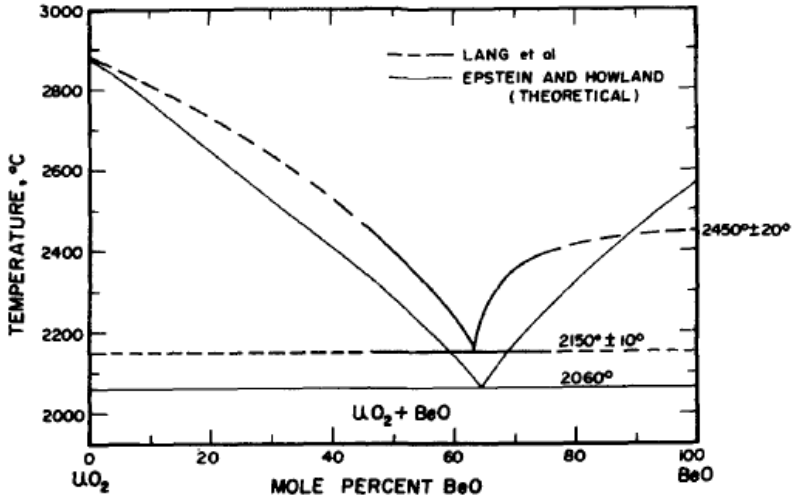

Figure 22: The U-Be-O system high-temperature phase diagram from Lang et al. [55]. See also Epstein and Howland [107].

There are several ways to fabricate UO_2-BeO pellets to obtain a continuous BeO phase in the UO_2 matrix, which can give appreciable enhancement in thermal conductivity. Ishimoto and colleagues [33] found that a 25% increase in thermal conductivity of UO_2 could be obtained at 1100 K with a nearly continuous 4.2 vol% of BeO phase at the grain boundaries (BeO continuous type). However, to attain this, the pellets required sintering above 2423 K, the eutectic temperature, for one hour. They also examined pellets with BeO dispersed phase in the matrix (dispersed type), produced at lower temperatures, which did not result in the same conductivity enhancement. Figure 23 shows images of UO_2–0.9 wt% BeO obtained by ceramography from [33].

Another method that produces a continuous high conductivity phase of BeO in UO_2, named co-sintering process, is that devised by the Purdue University group [34, 108]. This process produces a fuel structure consisting of primary UO_2 microspheres (50 to 500 μm) embedded in a mixed oxide matrix containing a continuous fine-grained BeO-rich matrix containing fine UO_2 particles; see [34] for details.

2.3.2 UO_2–SiC

Silicon carbide (SiC) is considered to be a promising additive because of its high thermal conductivity, non-toxic, benign neutronics and high stability at elevated temperature. However, the chemical compatibility between SiC and UO_2 is not satisfactory above 1643 K,

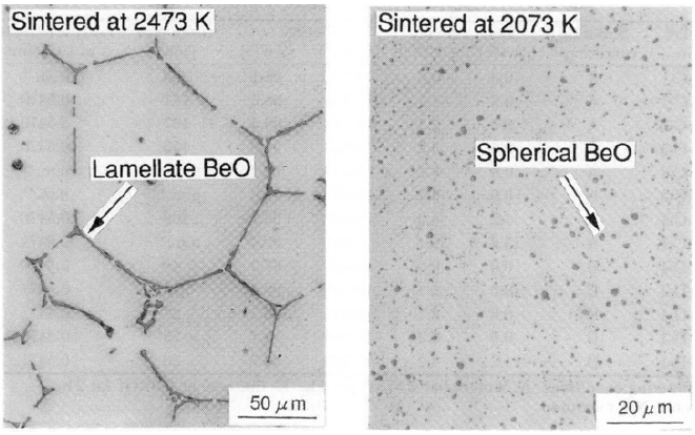

Figure 23: Photographs of UO_2–0.9 wt% BeO: (Left) BeO continuous type, (Right) BeO dispersed type. Image reprinted from [33] by permission of Informa UK Limited, trading as Taylor & Francis Group, www.tandfonline.com on behalf of Atomic Energy Society of Japan, ©Atomic Energy Society of Japan.

which may severely degrade the thermal conductivity of the composite. Sarma et al. [34] tried to produce UO_2–SiC composites at temperatures below 1643 K to bypass these reactions. Their method involved fabrication of a UO_2 pellets with open porosity followed by polymer infiltration and pyrolysis of a silicon carbide pre-ceramic polymer. However, the outcome was a pellet with degraded thermal conductivity compared to a standard UO_2 pellet. This upshot could partially be due to the higher density and crystallinity of the SiC whiskers compared to that formed by the pre-ceramic polymer.

In order to overcome these impediments with SiC additive, investigators at the University of Florida [109] produced UO_2–10 vol%SiC composite fuel pellets by oxidative sintering (OS) [110], and Spark Plasma Sintering (SPS) [111, 112] at a range of temperatures from 1673 to 1873 K. The name oxidative sintering refers to sintering of hyperstoichiometric uranium dioxide powder, in which the UO_2 powder is co-sintered with SiC powder or whiskers by increasing the O/M ratio of the starting powder to an optimum value of 2.25 [113]. The investigators employed OS over 4 h and SPS for 5 min. at the highest hold temperature [109]. SiC whiskers and SiC powder particles (mean diameter 2.4 μm) were both used. They observed that composite pellets sintered by SPS process produced smaller grain size and higher density, reduced formation of chemical products, and enhanced interfacial contact compared to the pellets produced by oxidative sintering. The density of sintered UO_2–10 vol% SiC pellets increased with increase in sintering temperature. However, the highest density among oxidative sintered pellets was as low as 88.91% relative to the UO_2 theoretical density. On the other hand, all SPS pellets sintered at a higher temperature than 1673 K had higher densities, i.e. between 91.25% and 97.78%. Moreover, in each of the sintering methods, both SiC whiskers and powder additions resulted in almost the same overall densities of the composite pellets at 1873 K. Figure 24 shows micrographs of UO_2-10 vol%SiC, which reveal the distributions of SiC whiskers and SiC particles in the composite pellets [114]. Both the whiskers and particles are seen to be uniformly distributed without any agglomeration.

The average grain size in various composite pellets sintered at 1773 K by both OS and SPS according to their composition is listed in table 4. It is seen that UO_2 with no additives has the largest grains. The grain size decreased with silicon carbide additions in both

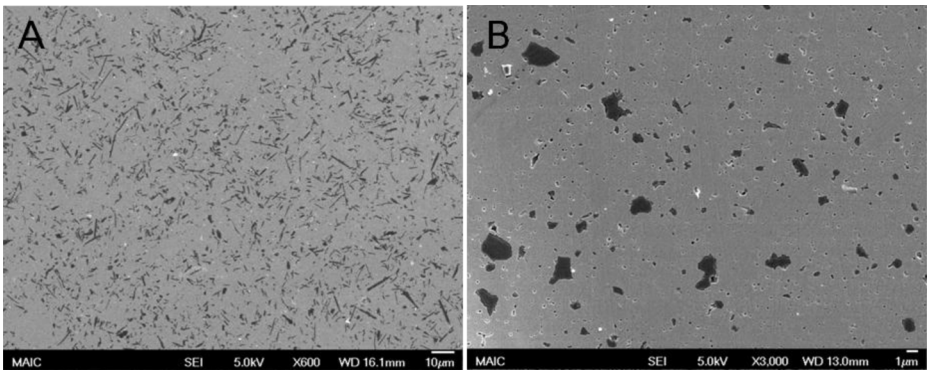

Figure 24: Micrographs of UO_2-10 vol%SiC composites, produced by SPS, showing uniform dispersion of SiC. (a) SiC whisker and (b) SiC particle; from S. Yeo's thesis [114].

sintering methods; for explanation see [109]. Hence, fission gas release behavior of this fuel deems not favorable, due to reduced diffusion path length (for fission product gases) to grain boundary despite enhancement in thermal conductivity. The desire is to maintain UO_2 grain size while enhancing its thermal conductivity.

Table 4: UO_2 grain size values (μm) in composite pellets resulting by the addition of 10 vol.% SiC powder particles (p) and SiC whiskers (w); from Yeo et al. [109].

Type	UO_2	UO_2–SiC(w)	UO_2–SiC(p)
Oxidative sintering	9.2	6.4	3.5
Spark plasma sintering	4.3	3.6	2.9

In a follow-up study [115], the University of Florida researchers examined the influence of SiC particle size and volume fraction on the thermal conductivity of spark plasma sintered UO_2–SiC composites. UO_2 powder and β–SiC particles of different sizes and of different volume fractions were mechanically mixed and sintered at 1623–1723 K for 5 min by the SPS method. They varied the SiC particle size (0.6–55 μm diameter) and SiC volume fraction (5–20%) to investigate the influence on the resulting UO_2–SiC composite fuel pellet microstructure and its thermal properties. They found that a SiC particle size less than 16.9 μm with larger volume fraction is more effective for improving the thermal conductivity of the fuel pellets. For the UO_2–SiC composite pellets containing 1 μm diameter SiC particles, the thermal conductivity increased almost linearly with volume fraction of particles. However, the addition of a larger volume fraction of SiC reduces the amount of heavy metal in the composite pellet and therefore requires a higher ^{235}U enrichment to compensate for the loss in heavy metal, which is not favorable. Another concern is the effect of long-term irradiation on the structural integrity of SiC in UO_2.

2.3.3 UO_2–Diamond

Tulenko and coworkers at the University of Florida [35, 116] have fabricated high density UO_2–5 vol% diamond composite pellets using the SPS technique. Diamond particles with mean sizes 0.25 μm, 3.0 μm, 12 μm and 25 μm were mixed with UO_2 powder and sintered using SPS at 1573–1873 K with a hold time of 5 min. Pellets containing 0.25 μm diamond particles exhibited poor mixing and inadequate densification, thereby low density. Therefore, UO_2 with 0.25 μm diamond particles was not an acceptable product. Figure

25, adapted from Z. Chen's work [116, 117], depicts the variation in the relative density of the UO_2–diamond composites as a function of sintering temperature and diamond particle size. For all the examined diamond particle sizes, the density of the sintered pellets increased with increasing sintering temperature up to 1500°C (1773 K). When the maximum sintering temperature reached 1600°C (1873 K), a slight decrease in density was noticed. The decrease was attributed to formation of microcracks and chemical reaction at high temperature. Microcracks were observed when the diamond particle size was larger than 12 μm, which adversely affected both the thermal and mechanical attributes of the composites. Fuel composites with a 3 μm diamond showed the best thermal-mechanical behavior among the samples examined, and thus, were recommended for product development. A study on the viability of spark plasma sintering for commercial fabrication of reactor fuel pellets is made in [118].

2.3.4 UO_2–Carbon plus

Other innovative carbon-base additives that enhance UO_2 thermal conductivity comprise carbon-nanotube (CNT) inclusions by 5 vol% [119], graphene-supported UO_2 [120] and graphene nanoplatelet (GNP) reinforced UO_2 [121]. UO_2–GNP composites developed at the Rensselaer Polytechnic Institute (Troy, New York) used an SPS method for fabrication, in which highly thermally-conductive and mechanically-strong graphene nanoplatelets were used as fillers to improve the thermal–mechanical properties and accident tolerance of nuclear fuels [121]. A 162% improvement of thermal conductivity in the radial direction (in-plane) is reported for the UO_2–5 wt% GNP composite fuel sintered at 1873 K for 20 min. under a uniaxial pressure of 40 MPa [121]. Furthermore, composite fuel pellets exhibited enhanced capacity to resist crack propagation. One concern, as in the case of SiC additive, is the effect of long-term irradiation on the structural integrity of CNT and GNP in UO_2 and thereby its impact on fuel thermal conductivity.

In addition, Li and colleagues [122] have recently introduced highly oriented micron–sized graphite flakes to UO_2 pellets fabricated by spark plasma sintering. Compared with UO_2, the radial thermal conductivity of UO_2–graphite improved by about 200% in the temperature range of 298–1273 K.

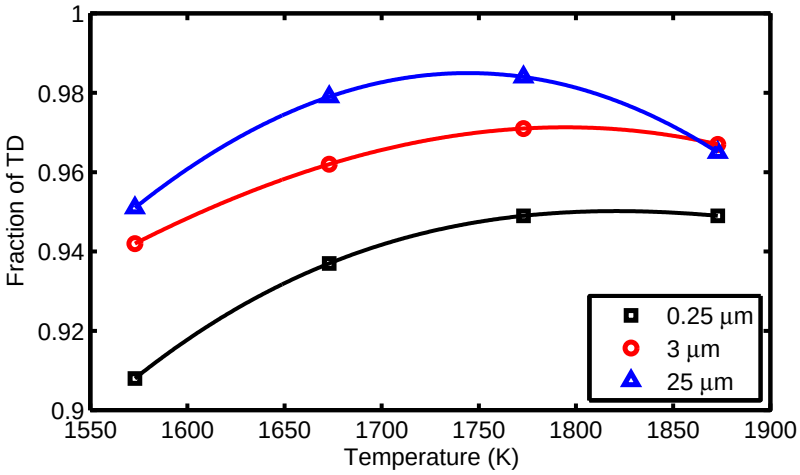

Figure 25: UO_2–5 vol% diamond composite fuel relative to theoretical density as a function of sintering temperature for several diamond particle sizes; adapted from Chen et al. [116]. Markers are measured values and lines are spline interpolations through them.

3 Thermophysical properties

In this section, some important solid-state physical properties of doped UO_2, affecting nuclear reactor fuel behavior, are appraised. The properties comprise enthalpy, heat capacity, thermal expansion, and thermal conductivity. We assess the influence of trivalent ions, e.g. Cr^{3+} added as Cr_2O_3 or generically M_2O_3 (M - metal) to UO_2, on these properties. We also review the thermal conductivity of BA fuel and that of enhanced conductivity UO_2 fuels. For a general review of thermal conductivity of various material types, see [123].

3.1 Normal fuel

We are interested in relationships or data that describe the temperature and doping concentration dependance of the aforementioned quantities. However, we could not find such relationships or data systematically, except for MgO additive, in the literature. It is usually stated that the thermophysical behavior for doped and pure UO_2 are the same or similar, and hence, the same model correlations can be used for both fuel types, irrespective of the dopant concentration [17, 40, 124]. The doping concentrations utilized by the fabricators in the form of M_2O_3 usually vary between 500 and 2000 wppm. Because, strictly speaking, such dopants, even in small amount, affect the properties of interest, we have used generic relationships for trivalent oxides added to uranium oxide to calculate its effect as a function of temperature. In particular, relationships that describe UO_2 alloyed with Gd_2O_3 are selected as our platform for M_2O_3 additives, since they are well established with ample experimental basis; however, we account and/or point out the differences between Gd_2O_3 and Cr_2O_3 or any other trivalent oxide additive compounds.

3.1.1 Enthalpy and heat capacity

Fuel enthalpy H_p and its derivative with respect to temperature, the heat capacity or specific heat, are key fuel behavior parameters for reactor safety analysis. For example, the heat capacity of fuel affects the Doppler feedback during a reactor power excursion, since it is the heat capacity that determines fuel temperature during an excursion: the higher is the temperature, the larger is the Doppler feedback and the larger reduction in the associated fuel reactivity. In fact, regarding the sensitivity of excursion yields on fuel parameters, the heat capacity, C_p, is considered to be the most important through its effect on the value of the Doppler constant [125].

From room temperature to 1000 K, the increase in heat capacity is governed by the harmonic lattice vibrations or phonons, which may be described by the Debye model [126, 127]. The Debye temperature Θ_D of UO_2 in the temperature range 300-1000 K is less than 600 K, hence, the Debye function is almost unity by $T > 1000$ K, where harmonic C_p reaches an asymptotic limit. Also, a minor contribution to heat capacity is provided by thermal excitation of localized electrons of U^{4+}, i.e. $(5f)^2$ electrons in the crystal field (CF) levels. At low temperatures, this contribution is $\propto T$, while, at high temperatures, where the concentration of U^{4+} decreases via $U^{4+} \rightarrow U^{3+} + U^{5+}$, C_p becomes virtually independent of temperature [126].

Between 1000 and 1500 K, the heat capacity increase arises from the anharmonicity of the lattice vibrations, as reflected in thermal expansion. From 1500 to 2670 K ($= T_{cr}$: the critical temperature[5]), an anomalous exponential rise in enthalpy H_p and the associated C_p is observed; see, e.g. the forthcoming figure 30. This is attributed to the formation of lattice and electronic defects. The C_p peak measured at $T_{cr} \approx 0.8T_{\rm melt}$ is similar to that observed in ionic fluorides, which exhibit a superionic second-order (or λ) phase transition to a disordered state prior to melting [128, 129]. The main contributor to this thermodynamic anomaly seems to be the buildup of Frenkel defects in the crystalline structure [130, 131]. For $T_{cr} < T < T_{\rm melt}$, the Frenkel defect concentration becomes saturated and Schottky defects become important. From T_{cr} to $T_{\rm melt}$, C_p is characterized by a steep descending wing of the transition peak, due to the rapid saturation of the defect concentration, anion disordered phase, followed by a weakly increasing stage caused by the creation of more energetic atomic defects (UO_2 Schottky trios) [126].

The question is how and to what degree the introduction of trivalent oxides in UO_2 would affect the different stages of C_p versus T curve? As noted in the foregoing section, introducing a trivalent doping element, such as Cr, Gd, La, Al, etc. in UO_2, leads to formation of Frenkel pairs of oxygen. The concentration of these Frenkel pairs (x) can be estimated from a generic formula derived years ago by Szwarc [132] by thermodynamic analysis, namely

$$x = \sqrt{2}\exp\Big(\frac{\Delta S_f}{2R}\Big)\exp\Big(-\frac{\Delta H_f}{2RT}\Big), \tag{5}$$

where ΔS_f and ΔH_f are the entropy and enthalpy of formation per Frenkel pair and other symbols have their usual meanings. Now, the anomalous increase in the heat capacity can be quantified by an excess (extra) heat capacity term accounting for the formation of the Frenkel pairs of oxygen

$$\begin{aligned} \Delta C_p &= \frac{d(x\Delta H_f)}{dT} \\ &= \frac{(\Delta H_f)^2}{\sqrt{2}RT^2}\exp\Big(\frac{\Delta S_f T - \Delta H_f}{2RT}\Big). \end{aligned} \tag{6}$$

The total heat capacity is then written

$$C_p = C_{p0} + \Delta C_p, \tag{7}$$

where C_{p0} is the heat capacity resulting from contributions of phonons (lattice vibrations), electrons and the Schottky defects.

Both ΔS_f and ΔH_f are decreasing functions of the additive concentration, as can be seen from figures 26-27. These figures are based on various experimental data put together by Matsui et al. [133], here averaged, to show the trend of the enthalpy and entropy of the Frenkel oxygen pair formation with the content of different dopants (M = Y, Gd, La, Sc, Eu) in UO_2.

From second-degree polynomial curve fits to these data (Appendix A), we have used equation (6) to calculate the excess heat capacity as a function of the cation content at several temperatures, figure 28. It is seen that the excess heat capacity is an increasing function of temperature and the cation content in UO_2, however, at high contents it levels off.

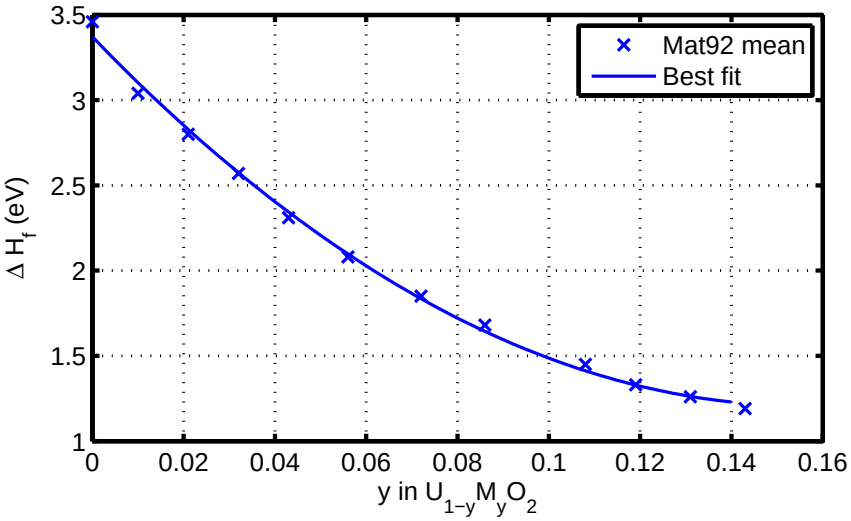

Figure 26: Enthalpy of Frenkel pair formation as a function of the dopant (M) content y in UO_2, based on data presented in Mat92 [133].

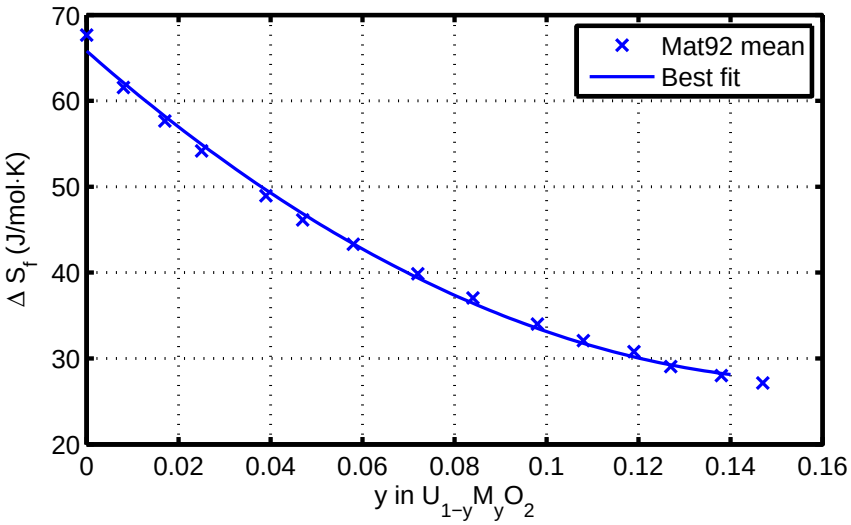

Figure 27: Entropy of Frenkel pair formation as a function of the dopant (M) content y in UO_2, based on data presented in Mat92 [133].

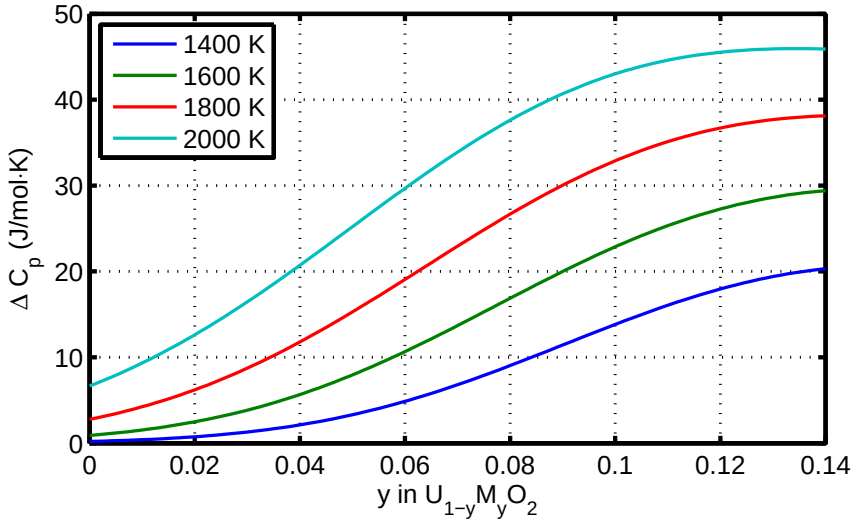

Figure 28: Excess heat capacity due to the Frenkel pair formation as a function of the dopant (M) content y in UO_2, based on data presented in figures 26-27 and equation (6).

Matsui and colleagues also found that the onset temperature of the heat capacity anomaly decreases with the dopant content. This was especially distinct for Gd dopant, as indicated in an earlier paper by Naito [134], figure 29.

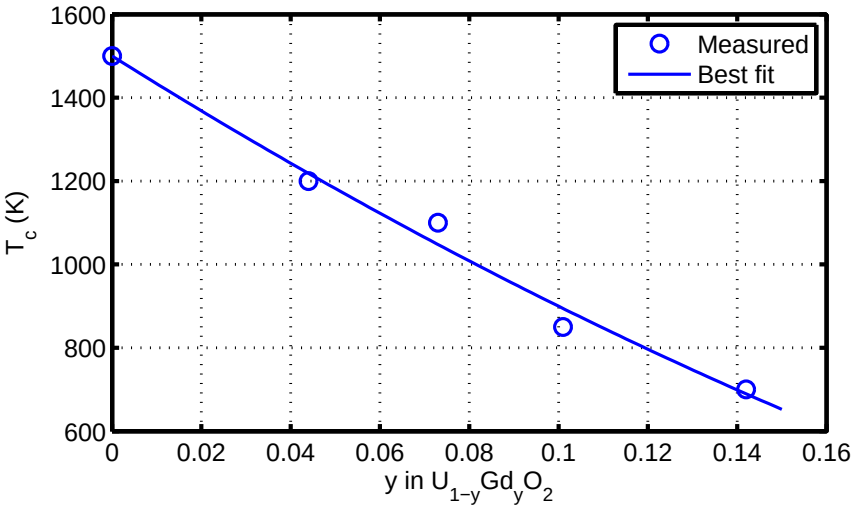

Figure 29: Temperature onset for heat capacity anomaly T_c as a function of the dopant (Gd) content y in UO_2 based on the data presented by Naito [134].

Let's next calculate the total heat capacity C_p according to equation (7) using for C_{p0} relationships based on the data by Inaba et al. [135] on $U_{1-y}Gd_yO_2$; also appraised in [136] and listed in Appendix A. The results of calculations as a function of temperature for several (low) concentrations of dopant, related to the weights of Cr_2O_3 in UO_2, are plotted in figure 30. It is seen that for temperatures less than 1600 K, the results are almost identical. For $T \geq 1600$ there is an increase in heat capacity with an increase in dopant concentration, but the deviations are insignificant in the range of concentrations considered. For example, the maximum deviation in heat capacity from "pure" UO_2 to UO_2 + 0.24 wt% additive is about 1.5% at 2200 K. Regarding fuel enthalpy, relative to the enthalpy at room temperature, for the considered dopant concentrations and temperature range, the calculated values

are practically indistinguishable from those of pure UO_2.

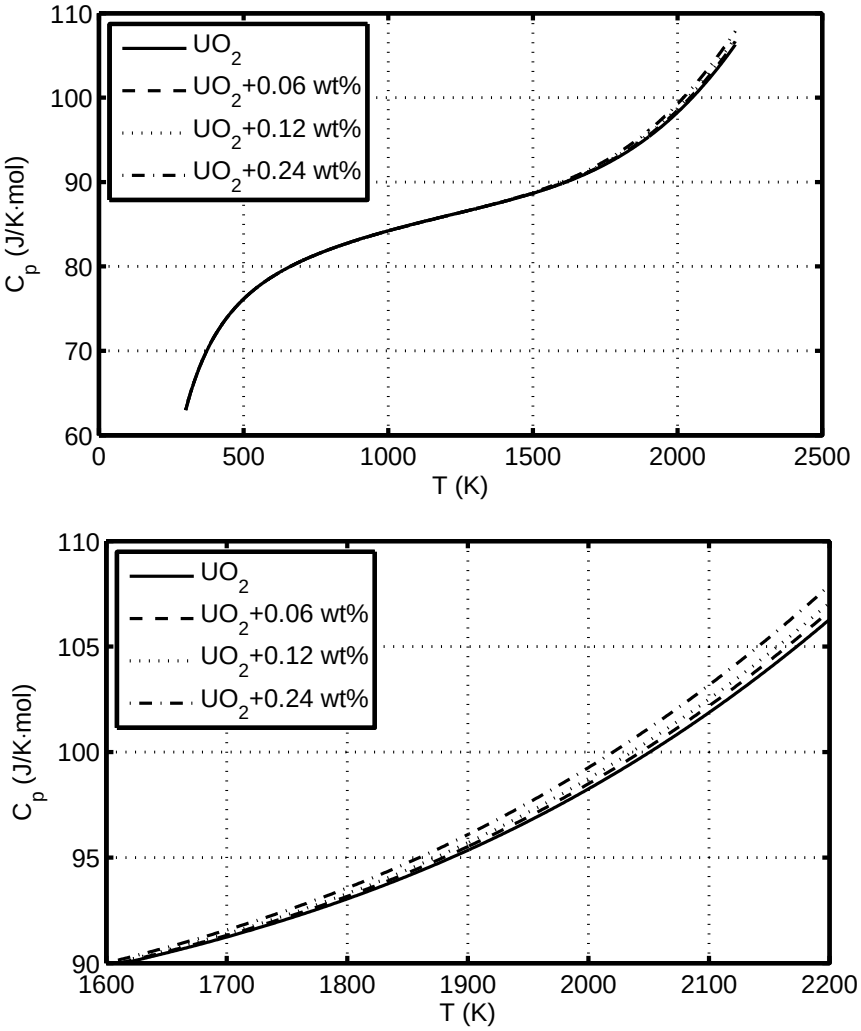

Figure 30: Heat capacity of UO_2 versus temperature as a function of the dopant (M_2O_3) mass content.

3.1.2 Thermal expansion

The coefficient of linear thermal expansion (α) for an isotropic solid, such as UO_2, is defined as

$$\alpha = \frac{1}{L}\Big(\frac{\partial L}{\partial T}\Big)_P = \frac{1}{3V}\Big(\frac{\partial V}{\partial T}\Big)_P = \frac{1}{3B}\Big(\frac{\partial P}{\partial T}\Big)_V, \tag{8}$$

where L is the linear dimension of the crystal, V its volume, and P the applied pressure. Here, $B = -V\big(\partial P/\partial V\big)_T$ is the bulk modulus.

Thermal expansion data on doped UO_2 (except mixed with Gd_2O_3) are virtually non-existent. Arborelius et al. [17] mention that UO_2 mixed with 0.1 wt% Cr_2O_3 exhibits the same behavior as UO_2 in the temperature range 293 to 1773 K. Here, we apply the empirical correlation for (U,Gd)O_2 [136] based on the data of Une [137] to the dopant contents of interest, see Appendix A. The results in the temperature range of 300 to 2400 K

indicate that up to the dopant concentration of 0.5 wt%, the deviations in thermal expansion of doped UO_2 from that of pure UO_2 is insignificant. Figure 31 shows this deviation as a function of temperature relative to 0.5 wt% dopant. In relative terms, the deviation in α is less than 0.5%; see also figure A1 in Appendix A.

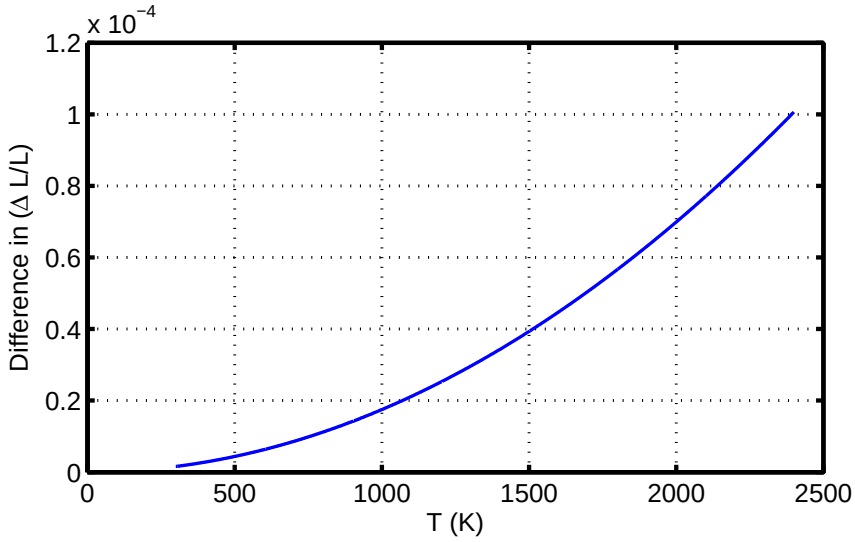

Figure 31: Calculated difference between the relative thermal expansion, $\Delta L/L \equiv [L(T) - L(273)]/L(273)$, of pure UO_2 and 0.5 wt% doped UO_2 with M_2O_3.

We should mention that there is a thermodynamic relationship between the specific heat and the thermal expansion coefficient [138], namely

$$\alpha = \frac{\gamma C_p}{3BV_m}, \tag{9}$$

where γ is the Grüneisen parameter (dimensionless) and V_m the molar volume. For UO_2, $\gamma = 2.17$, $B = 208$ GPa and $V_m = 24.62$ cm^2/mol [139]. This relationship indicates that temperature and dopant concentration dependence of the coefficient of thermal expansion follows that of the heat capacity, since B is weakly dependent on these quantities.

3.1.3 Thermal conductivity

The accommodation of trivalent oxides (M_2O_3) in UO_2 matrix distorts the lattice of the matrix locally. For example, for M = Cr, the chromium oxide, Cr_2O_3 consists of the rhombohedral primitive cell, where Cr atoms are eight-coordinated with two oxygen layers. The lattice constants at room temperature for Cr_2O_3 are $a = 4.937$ Å and $c = 3.627$ Å [140]. Conversely, UO_2 has a face-centered cubic lattice with $a = 5.458$ Å with 4 molecules per unit cell. The presence of chromium implies a strong distortion of the UO_2 lattice in its surrounding and results in an increase in the population of defects. It is expected that the number of defects increases with the chromium content, so that the thermal conductivity decreases with the increase in chromium content. But the rate of decrease gets smaller at higher temperatures. All this is expected to have an impact on the phonon-lattice and phonon-phonon interactions, leading to a decrease of the thermal conductivity of (U, M)O_{2-x}.

Klemens's thermal conductivity model [141], which is based on the relaxation-time theory when phonon-phonon scattering and phonon-point defect scattering occur simultaneously, is suitable for the aforementioned description. According to this model, the lattice or phonon thermal conductivity λ_p can be expressed by

$$\lambda_p = \frac{\lambda_0}{w}\arctan(w), \tag{10}$$

$$w = \sigma(\Gamma\lambda_0)^{1/2}, \tag{11}$$

where λ_0 is the thermal conductivity for point defect free UO_2, σ is a physical constant[6] and Γ characterizes the sum of the phonon scattering cross sections of the impurity atoms [142]; it is expressed as

$$\Gamma = \sum_i x_i\Big[\Big(\frac{\Delta M_i}{M}\Big)^2 + \xi\Big(\frac{\Delta r_i}{r}\Big)^2\Big], \tag{12}$$

where x_i is the atomic fraction of point defect i, r the average ionic radius, M the average mass, Δr_i and ΔM_i are the difference in ionic radius and mass between an impurity i and a matrix, respectively, and $\xi = 39$ according to Abeles [142], but can be taken as an adjustable parameter.

In case of mixture of two kinds of compounds A (e.g. UO_2) and B (e.g. Cr_2O_3), equation (12) becomes

$$\Gamma = x(1-x)\Big[\Big(\frac{\Delta M}{M}\Big)^2 + \xi\Big(\frac{\Delta r}{r}\Big)^2\Big], \tag{13}$$

$$\Delta M = M_A - M_B, \tag{14}$$

$$\Delta r = r_A - r_B, \tag{15}$$

$$M = xM_A + (1-x)M_B. \tag{16}$$

From these relations, we see that the larger is the mass (or the ionic radius) difference between the UO_2 and the dopant, the larger would be Γ and w, yielding smaller λ_p/λ_0. Comparison between the values for dopants Cr_2O_3 and Gd_2O_3 are listed in table 5. A usable correlation based on equation (11) is given in Appendix A for UO_2 with the additive Gd_2O_3. In addition to the phonon contribution to the thermal conductivity, there is an additive electronic term λ_e from the transport of heat by electrons, which is considered to be impurity (dopant) independent and it becomes effective at temperatures beyond 1800 K. Uranium dioxide, being classified as a Mott-Hubbard insulator, its λ_e temperature dependence is rather subtle [143, 144]. Despite this, Ronchi et al. [145], based on the theoretical analysis of Casado et al. [143] and the experimental work of Killeen [10], have obtained a usable formula for λ_e in the form

$$\lambda_{el} = \frac{A_0}{T^{3/2}}\exp(-\epsilon/k_BT) \tag{17}$$

where A_0 and ϵ are constants given in Appendix A for UO_2.

At high temperatures ($T \geq 2000$ K), there is also radiative heat transfer due to diffusion of photons, which may contribute to the thermal conductivity of fuel. This term varies with temperature as $\lambda_r \propto T^3$. However, analysis by Young [146] indicates that for UO_2 $\lambda_r << \lambda_{el}$, and hence, we ignore it here.

In figure 32, the thermal conductivity is plotted as a function of temperature for UO_2 and Gd_2O_3-doped UO_2 for several concentrations of dopants. The correlation, based on the aforementioned theory, for $(U_{1-y},Gd_y)O_2$ is used with adjusted weights for Gd_2O_3. It is seen that as the concentration of dopant is increased, the thermal conductivity is decreased for temperatures below 800 K. Nevertheless, this decrease in thermal conductivity is insignificant for dopant concentrations up to 2000 wppm. We should mention that fuel porosity (or density) also will affect the thermal conductivity. A denser, less porous fuel gives a higher thermal conductivity than a lighter one. The applied thermal conductivity correlation is listed in Appendix A; see equation (A.11).

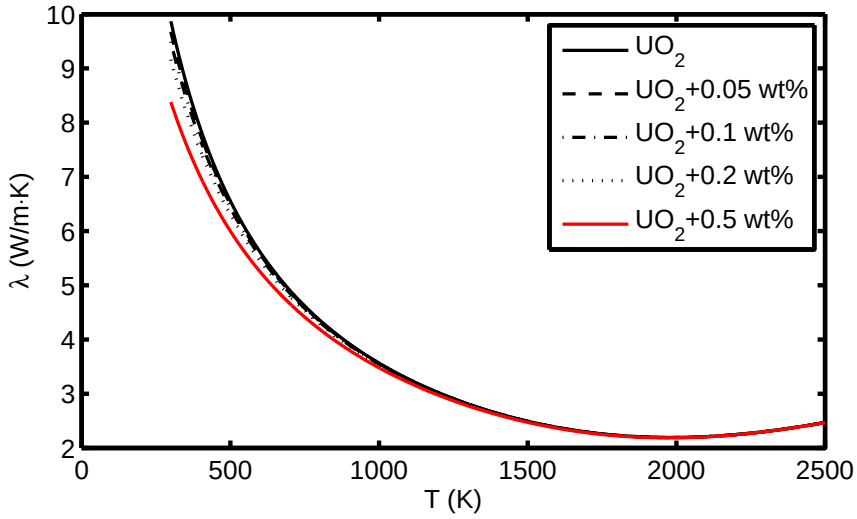

Figure 32: Calculated thermal conductivity λ of UO_2 versus temperature as a function of dopant (Gd_2O_3) mass content, see Appendix A.

Table 5: Mass and ionic radius difference between UO_2 and dopants calculated according to eqs.(14)-(16) for $x = 0.998$ (atomic fraction of UO_2), see e.g. [28].

Formula	M_i	$\Delta M/M$	Ion	r_i (Å)	$\Delta r/r$
UO_2	270.07	...	U^{4+}	0.93	...
Cr_2O_3	152.02	0.437	Cr^{3+}	0.64	0.312
Gd_2O_3	362.50	-0.342	Gd^{3+}	0.94	-0.011

3.2 Burnable absorber fuel

3.2.1 Gd-U-O

An extensive amount of data on $(U,Gd)O_2$ thermal-physical properties have been reported in the literature over the years [78, 80, 147–151] including irradiated $(U,Gd)O_2$ [152–155]. Most of these works use standard techniques to measure the heat capacity and thermal diffusivity of the compound, then combining them to determine thermal conductivity of $U_{1-y}Gd_yO_2$ as a function of temperature for several values of Gd concentration (y). All, or majority of these measurements, do cover temperatures up to around 2000 K, which are

adequate for application during normal LWR service. However, under certain types of transients, e.g. reactivity induced power surges, the fuel pellet temperature may go above 2000 K and get close to fuel's melting point. For pure (undoped) UO_2, such high temperature data amply exist, see e.g. [145]. As mentioned earlier, a UO_2 crystal transports heat primarily by lattice (phonons) from below room temperature up to around 1800 K. Beyond this temperature, electrons contribute to transport of heat and become the dominant means of heat transport beyond 2000 K, where thermal conductivity becomes an increasing function of temperature. In a recent paper [156], attempts were made to model this phenomenon for $U_{1-y}Gd_yO_2$. In [156], a set of data produced by Hirai and Ishimoto [150], which covers the temperature range of 289 to 2023 K for UO_2 doped with 3, 5, 7, 10, wt.% Gd_2O_3 was considered.

The measurements by Hirai and Ishimoto [150] were done on disk-like specimens with diameters around 10 mm and thicknesses from 0.5 to 1.2 mm. The density of the samples varied between 0.94 and 0.97 of theoretical density (TD); see table 1 in [150] for details. They only measured thermal diffusivity of the samples by a laser-flash method [150]. Thermal conductivity was calculated by the formula $\lambda = \rho C_p D_{th}$, where λ is the thermal conductivity of the sample, ρ is the density of the sample, C_p the heat capacity, and D_{th} is the measured thermal diffusivity. Heat capacity data from the literature were used in the aforementioned formula [150]. The thermal conductivity data were normalized to 0.95 TD by a standard procedure [150]. Measured data of Hirai and Ishimoto are presented in figure 33(a) (markers) together with computations (lines) which extend to 3000 K [156].

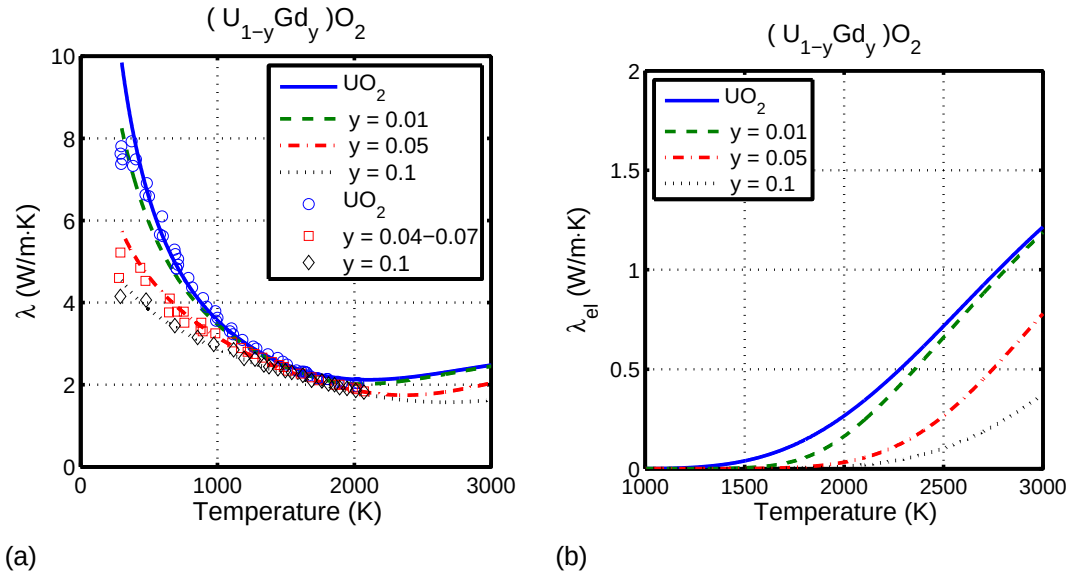

Figure 33: (a) Thermal conductivity λ as a function of temperature for $(U_{1-y}Gd_y)O_2$, calculated (lines) and measured data (markers) of Hirai-Ishimoto [150]. (b) The electronic component of thermal conductivity $\lambda_{\rm el}$ vs. temperatures; adapted from [156].

The lines in figure 33(a) are the results of calculations using the electronic model described in [156] (equations (76)-(77) of [156]) superposed to the $\lambda_{ph} \equiv \lambda_{\rm latt}$ suggested by Hirai-Ishimoto. As noted in [150], for temperatures up to about 2000 K, phonon-phonon (*Umklapp* process) and/or phonon-impurity scattering dominate the thermal conductivity of UO_2 and the UO_2-Gd_2O_3 system. To this end, Hirai-Ishimoto adopted Klemen's theory [141],

which treats phonon-phonon and phonon-impurity scattering simultaneously. The contributions of the electronic component of the thermal conductivity $\lambda_{\rm el}$ for temperatures above 1000 K are depicted in figure 33(b). As can be seen from this figure, $\lambda_{\rm el}$ is an increasing function of temperature for UO_2 and the dopant gadolinia reduces this increase with the level of doping.

In a recent numerical study [157], the effects of Gd accommodation mechanisms and concentration on the thermal conductivity of UO_2 doped with Gd_2O_3 are investigated using molecular dynamics simulations for several types of Gd doping mechanisms. More precisely, in (U,Gd)O_{2-x}, isolated Gd^{3+} substitutional defects, charge compensated by isolated oxygen vacancies (oxygen vacancy clusters), and in (U,Gd)O_2, isolated Gd^{3+} substitutional defects, charge compensated by U^{5+} or U^{5+}-induced clusters. Qin et al.'s simulations [157] indicate that thermal conductivity degradation is primarily due to isolated defects rather than defect or vacancy clusters in the compound.

Irradiation reduces thermal conductivity of fuel. The reduction, however, can be attributable not only to the dissolution of solid fission products (FPs), but also to microstructural changes, such as the O/M ratio change, precipitation of insoluble FPs, cracking, gas bubble formation and irradiation damage accumulation. The effects of FPs on thermal conductivity of (U,Gd)O_2 fuel have been investigated in [152]. Ishimoto and colleagues simulated high burnup UO_2 and (U,Gd)O_2 pellets by doping the pellets with soluble fission product elements (Sr, Zr, Y, La, Ce, Nd). They measured pellet thermal diffusivities by a laser-flash method and their thermal conductivities were evaluated in the temperature range of 300 K to 1873 K. Thermal conductivities decreased with an increase in the total amount of soluble elements at lower temperatures ($300 < T < 1400$) K, while they were almost independent of soluble element content at higher temperatures ($T \geq 1500$ K).

The effects of oxidation on the thermal conductivity of (U,Gd)O_2 fuel have been studied by Amaya and Hiarai [153]. They prepared 10 wt% Gd_2O_3 doped UO_{2+x} samples with x between 0 and 0.15 and simulated soluble FPs doped UO_{2+x}, (simulating fuel burnups: 30 and 60 GWd/tU), with $x \approx 0 - 0.02$ with an oxidation method. By using a laser-flash method, they measured the thermal diffusivities of the samples from 300 to 1400 K, from which thermal conductivities were evaluated by multiplying the thermal diffusivities by the samples' densities and the specific heat capacities obtained from the literature. Thermal conductivities of (U, Gd)O_{2+x} decreased as the hyperstoichiometry, x, increased.

Thermal conductivities of irradiated UO_2 and (U,Gd)O_2 have been measured and reported in [154]. Minato and colleagues [154] prepared disk-shaped UO_2 and 10 wt% Gd_2O_3 samples and irradiated to about 4%FIMA (Fissions per Initial Metal Atom ≈ 40 MWd/kgM) in a research reactor and measured thermal diffusivities by the laser-flash method from room temperature to about 1800 K. The thermal conductivity was determined from the thermal diffusivity, density and the specific heat capacity in a usual way. The thermal conductivity decreased by irradiation, while it partly recovered after the thermal diffusivity measurement at temperatures up to about 1800 K. The recovery of the thermal conductivity was attributed to the recovery of the irradiation-induced point defects during the measurement. The reduction in thermal conductivity assignable to the irradiation-induced point defects was small in the samples, which experienced higher temperature than 1273 K during the temperature rise.

In a subsequent study [155], Amaya and colleagues measured thermal diffusivities of

UO_2 and (U,Gd)O_2 pellets, irradiated in a commercial reactor to maximum burnups of 60 MWd/kgU for UO_2 and 50 MWd/kgU for (U,Gd)O_2, up to about 2000 K by using a laser-flash method. The irradiated (U,Gd)O_2 fuel samples examined had 4.5 wt% Gd_2O_3. Their thermal conductivities were evaluated by multiplying the thermal diffusivities by the specific heat capacities of unirradiated UO_2 pellets and sample densities. Thermal conductivities decreased with increasing burnup at lower temperature, then began to recover above about 800 K, and fully recovered above about 1500 K. The recovery of the thermal conductivity was attributed to the recovery of the irradiation-induced point defects. Moreover, the difference in relative thermal conductivities between irradiated UO_2 and (U,Gd)O_2 pellets tended to become negligible with increasing burnups of samples [155].

3.2.2 U-Er-O

Thermal-physical data for (U,Er)O_2 fuel are rather scarce in the literature. However, there are some noted studies. Thermal expansions of $U_{1-y}Er_yO_2$ with $y = [0, 0.05, 0.1, 0.2]$ solid solutions have been investigated by a Korean team [158] between room temperature and 1673 K by using a thermal-mechanical analyzer. More specifically, S-Y. Kim and collaborators [158] measured lattice parameters of the (U,Er)O_2 pellets and found that they are lower than that of UO_2. They found that the lattice parameters decrease as the Er contents increase. The linear thermal expansion and average thermal expansion coefficients of (U,Er)O_2 were higher than that of UO_2. For the temperature range from room temperature to 1673 K, they report, among others, the average thermal expansion coefficient values for UO_2 and $U_{0.8}Er_{0.2}O_2$, which are 10.94×10^{-6} and 11.42×10^{-6} K^{-1}, respectively.

In a separate paper, S-Y. Kim and colleagues [159] reported measurements of thermal diffusivities of UO_2 and UO_2 doped with 1, 3, 5, 7 and 10 mol% $ErO_{1.5}$ in the temperature range of 298–1673 K by a laser-flash method, from which thermal conductivities were calculated from the thermal diffusivity, the measured sample density and the specific heat capacity data published in the literature. The thermal diffusivities and thermal conductivities of each sample decreased with increasing the temperature. The thermal conductivities decreased with an increasing $ErO_{1.5}$ at lower temperatures ($298 < T < 1000$ K), while at high temperatures ($1000 < T < 1673$ K) they were independent of the $ErO_{1.5}$ content.

Yamanaka and colleagues [160] in a comprehensive study examined thermal-mechanical properties of $U_{1-y}Er_yO_2$ fuel ($0 \leq y \leq 0.1$). In their study, Young's modulus of the pellets was determined from the longitudinal and shear sound velocities measured by an ultrasonic pulse-echo method at room temperature in air. The thermal expansion was measured by using a thermal dilatometer from room temperature to 1500 K. The heat capacity was measured by a differential scanning calorimeter (DSC), in the temperature range from room temperature to 1500 K in an Ar flow atmosphere. The thermal diffusivity was measured by the laser-flash method from room temperature to 1500 K in a vacuum (10^4 Pa). The thermal conductivity (λ) was calculated from the heat capacity (C_p), thermal diffusivity (D_{th}), and density (ρ) using the formula $\lambda = D_{\text{th}} C_p \rho$. From their measurements, they obtained the following empirical relations for the lattice parameter (a), Young's modulus (E), and

thermal conductivity of $U_{1-y}Er_yO_2$ fuel as a function of the Er content y:

$$a(\text{nm}) = 0.5471 - 0.0364y \quad (0 \le y \le 0.1), \tag{18}$$

$$E(\text{GPa}) = 227 - 297y \quad (0 \le y \le 0.1), \tag{19}$$

$$\lambda(\text{Wm}^{-1}\text{K}^{-1}) = \left[6.44 \times 10^{-2} + 1.02y + (1.55 - 4.63y) \times 10^{-4}T\right]^{-1}, \quad (0 \le y \le 0.1, \quad 298 < T < 1473 \text{ K}). \tag{20}$$

Figure 34 illustrates the temperature and the erbium concentration dependence of the thermal conductivity through relation (20), where increasing Er concentration reduces the thermal conductivity, but at higher temperatures, the effect becomes small.

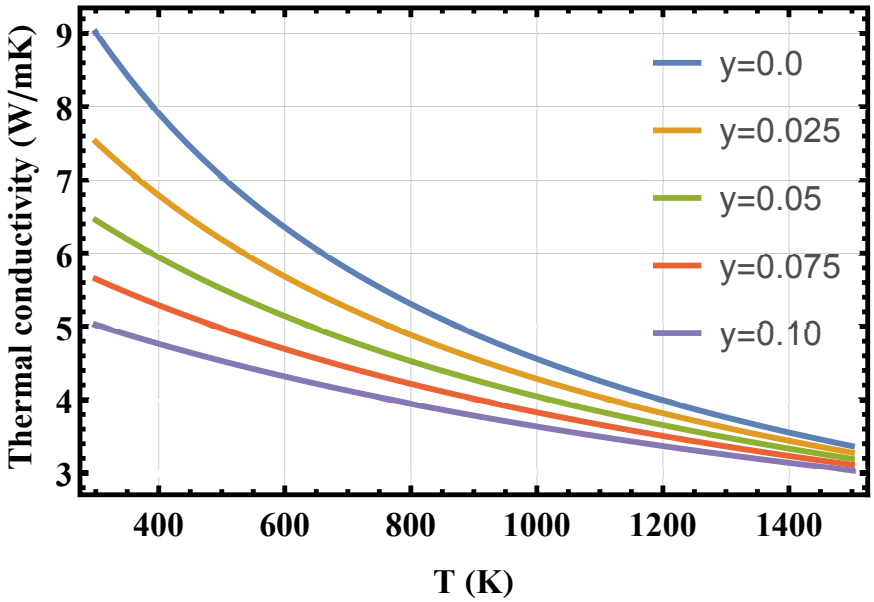

Figure 34: Calculated thermal conductivity of $U_{1-y}Er_yO_2$ versus temperature for several concentrations of Er (y) using relation (20).

Thermophysical properties of unirradiated Er_2O_3-doped UO_2 fuel pellets, containing 0, 5, 10 and 15 wt% Er_2O_3, have recently been reexamined in [161]. Xiao et al. [161] laboratory measurements show that the lattice parameter of the doped UO_2 decreases linearly with the Er_2O_3 content, implying the formation of a complete solid solution between the Er_2O_3 and UO_2 up to 15 wt% of Er_2O_3 concentration. The mean grain size, specific heat capacity and thermal expansion coefficient of doped UO_2 pellets were increased by the addition of Er_2O_3. However, the thermal conductivity duly decreased with the Er_2O_3 doping content as in the foregoing studies. In addition, the authors quantitatively discuss the effect of lattice defects, such as substitutional atoms and oxygen vacancies, on the thermal conductivity and formulate a phonon scattering Debye-type model for thermal conductivity. As an example, the authors calculate the thermal conductivity of Er_2O_3-doped UO_2 solid solutions at 1073 K as a function of Er_2O_3 concentration. They show that the model calculations agree well with their measurements when the point defect of substitutional atoms and vacancies are taken into account concurrently.

3.2.3 U-Eu-O

Only few studies on thermal-physical behavior of (U,Eu)O_2 fuel have been reported in the literature [162–164]. Matsui and colleagues in [162] report measurements of heat capacities and electrical conductivities of $U_{1-y}Eu_yO_2$ ($y = 0.044$ and $y = 0.09$). The measurements were performed by means of direct heating pulse calorimetry over the temperature range from 300 to 1550 K. They observed an anomalous increase in the heat capacity data of each sample of $U_{1-y}Eu_yO_2$. The anomalous increase occurred around 1100 K for the $y = 0.044$ samples and around 950 K for $y = 0.09$ samples. On the other hand, no anomaly was observed in the electrical conductivity curve around the onset temperature of the anomalous increase in the heat capacity. They concluded that the occurrence of the excess heat capacity of $U_{1-y}Eu_yO_2$ emanates from the predominant contribution of the formation of Frenkel pair–like defects of oxygen; cf. section 3.1.1.

Krishnan and colleagues [163] at the Indira Gandhi Centre for Atomic Research, India, prepared samples of uranium–europium mixed oxides $U_{1-y}Eu_yO_{2-x}$ with $y = 0.2 - 0.8$ by so-called citrate gel-combustion synthesis and characterized them by using X-ray diffraction (XRD). The terminal solid solubility of $EuO_{1.5}$ in UO_2 was in the composition range 60–65 mol% $EuO_{1.5}$. They measured the coefficients of thermal expansion at 1973 K for ($U_{1-y}Eu_y$)O_{2-x} ($y = 0.2, 0.4, 0.6$) by using high-temperature X–ray diffraction (HTXRD) and found them to be $\alpha = [15.80, 14.81, 14.30] \times 10^{-6}$ K^{-1}, respectively. In a separate paper, Krishnan and colleagues [164] report specific heat capacity and enthalpy measurements of ($U_{1-y}Eu_y$)O_{2-x} ($y = 0.2, 0.4, 0.6$) by using DSC and drop calorimeter in the temperature range 298–800 K and 800–1800 K, respectively. They observed the anomalous increase in the heat capacity in all of the solid solutions at around 950 K. They attributed this anomaly to the contribution from the Frenkel pair oxygen defects. And from the excess heat capacity data, they computed the enthalpy for the formation of these defects and found it to be in the range of 2.10 ± 0.02 eV. To our knowledge, no thermal diffusivity measurements for (U,Eu)O_2 have been reported in the literature.

3.3 Enhanced conductivity UO_2 fuel

There already exists a 2018 article [165] reviewing thermal-physical properties, i.e. data and models, of enhanced thermal conductivity UO_2 base fuels together with other innovative fuel pellet materials. In this section, we intend to be complementary to [165] and also by citing new articles that have appeared since then. However, we focus our treatment to oxide fuels, which we discussed in the foregoing section regarding their chemical behavior.

3.3.1 UO_2–MgO

In section 2.1, we considered the additive MgO as a grain size promotor for UO_2 rather than thermal conductivity enhancer. However, experimental data indicate that if UO_2 is doped sufficiently with MgO, its thermal conductivity would be enhanced [166].

Thermal conductivity of magnesium doped UO_2 has been determined by Fujino and colleagues [166] as a function of temperature for Mg concentrations of 0, 5, and 15 at%.

Fujino et al. [166], within a large program on irradiation behavior of Mg doped (and also Mg-Nb doped and Ti doped) UO_2, made thermal diffusivity measurements on unirradiated and irradiated fuel pellets. They used laser-flash method for that purpose. The temperature was measured by an infrared detector. Measurements were made at every 200 K from 473 to 1673 K.

Fujino et al.'s [166] Mg–doped samples for testing were prepared by mixing various amounts of MgO with UO_2 in an agate mortar to obtain UO_2 samples containing magnesium concentrations of 2.5, 5, 10, and 15 at%. The mixtures, in form of powder, were pressed into pellets, 3 mm in diameter and about 1 mm in thickness. The pellets in crucibles were heated in a furnace in a steam H_2–He gas at 1710°C (1983 K) for 5 h, upon which the sintered pellets shrank in diameter to about 2.5 mm. Those pellets with Mg concentrations 0, 5, and 15 at% were tested for thermal diffusivity.

The thermal conductivity was determined through $\lambda = \rho D_{\rm th} C_p$, where $D_{\rm th}$ is thermal diffusivity, ρ the bulk density and C_p the heat capacity of the specimen. The heat capacity was not measured by Fujino and colleagues but calculated (approximately) by combining that of MgO and UO_2 using a mixing rule

$$C_p(\mathrm{Mg}_y\mathrm{U}_{1-y}\mathrm{O}_{2-y}) = yC_p(\mathrm{MgO}) + (1-y)C_p(\mathrm{UO}_2), \tag{21}$$

where separate heat capacity data for MgO and UO_2 were used from the literature [166]. Based on these measurements and calculations, a relationship for thermal conductivity (phonon contribution) as a function of temperature and Mg concentration in UO_2 was established (Appendix A). Figure 35 depicts this correlation for unirradiated samples (UO_2 with 96%TD) for several Mg concentrations. It is seen that the conductivity first decreases slightly with Mg concentrations up to 5 at% Mg-UO_2, then raises again and exceeds that of UO_2 at 15 at% Mg-UO_2. The irradiation (burnup) reduces the thermal conductivity in a usual way, e.g. see [167]. It can be argued that at low Mg concentrations, the thermal conductivity is reduced by phonon-impurity scattering, while at higher Mg concentrations, samples are largely composed of MgO precipitates and UO_2, and the former compound has a higher thermal conductivity than the latter; see e.g. [57].

In recent work [168], Shamanin and colleagues at the Tomsk Polytechnic University in Russia have fabricated UO_2-MgO fuel with different concentrations of MgO by plasma-chemical synthesis of the compound from water–organic nitrate solutions or WONS. Their objective in [168] was to examine the impact of MgO concentration on the thermal conductivity of such fuel compounds. The experimental data reported in [168], presumably based on Russian sources which we could not verify, are displayed in figure 36. The impact of MgO concentration on compound's thermal conductivity is manifest from these data.

3.3.2 UO_2–BeO

Perhaps the first systematic study of thermal conductivity of UO_2–BeO fuel was published by Ishimoto et al. [33]. They fabricated beryllium oxide (BeO)–doped (0.3, 0.6, 0.9, 1.2 and 13.6 wt%) UO_2 pellets to evaluate the effects of BeO precipitate shape on thermal conductivity. Two types of fuel pellets with different precipitate distributions were fabricated: pellets containing BeO precipitates that almost continuously formed along grain

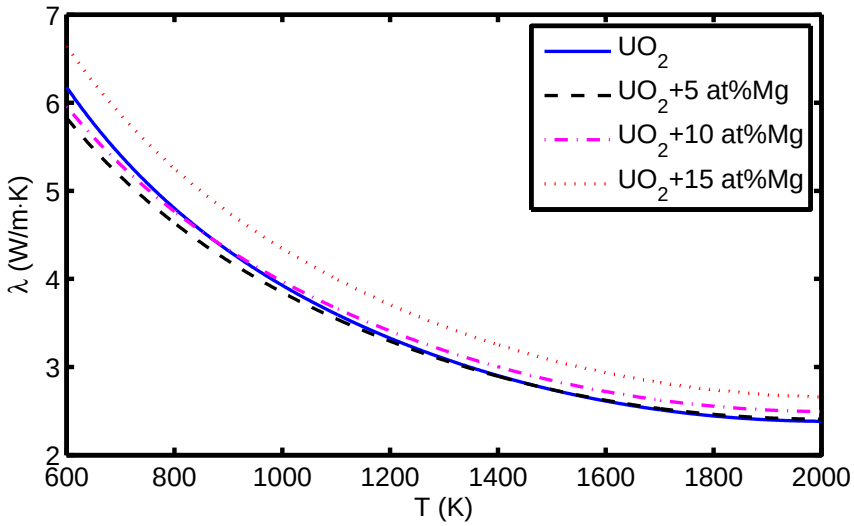

Figure 35: Calculated thermal conductivity λ versus temperature of UO_2 as a function of dopant (Mg) content, using an empirical relationship dscribed in Appendix A.

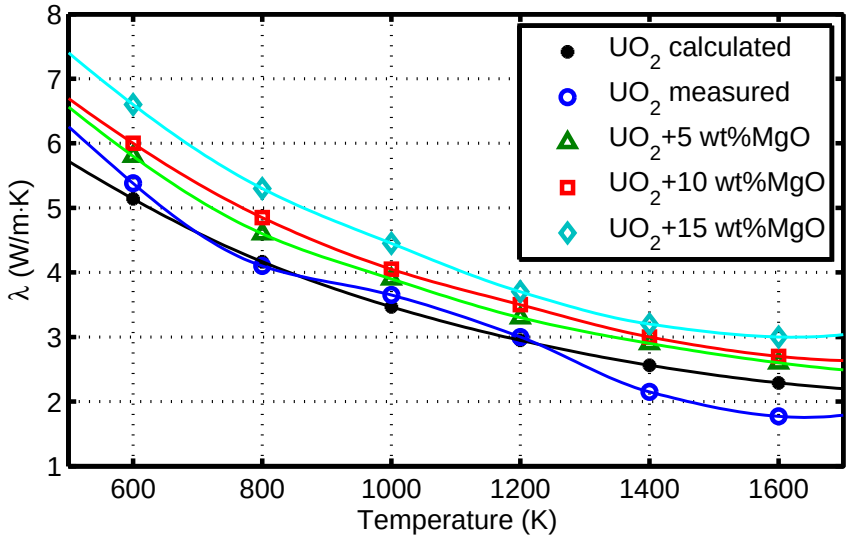

Figure 36: Measured data (markers) on thermal conductivity λ versus temperature of UO_2-MgO compounds from [168]. The black dots are calculated values according to a relationship given by Ronchi et al. [145, 169] for standard UO_2 fuel. The lines are interpolations through the data points.

boundaries, designated as BeO continuous type, and pellets with spherical BeO precipitates, which were randomly dispersed within the fuel matrix, designated as BeO dispersed type; see figure 23. Thermal diffusivity of fuel samples was measured by a laser-flash method at temperatures of about 300 to 1900 K, and thermal conductivity was evaluated from the heat capacity data for UO_2 and BeO, reported in the literature, and sample densities. The heat capacity of the UO_2–BeO compound was calculated by the Kopp-Neumann law of mixture

$$C_p = fC_p(\mathrm{BeO}) + (1-f)C_p(\mathrm{UO_2}). \tag{22}$$

Here, f denotes the mass fraction of BeO in the UO_2–BeO compound. It should be noted that the value of $C_p(\mathrm{BeO})$ is about six times larger than that of $C_p(\mathrm{UO_2})$, therefore the effective C_p increases with BeO content.

The measurements by Ishimoto et al. [33] show that thermal diffusivities of the BeO continuous type increase remarkably with BeO doping at lower temperatures, whereas the magnitude of the increase becomes smaller with increasing temperature. On the other hand, thermal diffusivities of the BeO dispersed type are only slightly higher than those of UO_2, and the magnitude of the increase is smaller than that of the BeO continuous type, especially at lower temperatures. Likewise, thermal conductivities of UO_2–BeO increased with BeO contents, and thermal conductivities of the BeO continuous type were higher than those of the BeO dispersed type, especially at lower temperature. For example, for UO_2–1.2 wt% BeO at 1100 K, the thermal conductivity was higher than that of UO_2 by 25% for the BeO continuous type and by 10% for BeO dispersed type [33]. Figure 37 shows Ishimoto et al.'s thermal conductivity data on the continuous type UO_2–BeO pellets with BeO concentrations 0.6 and 1.2 wt% as compared with that of UO_2.

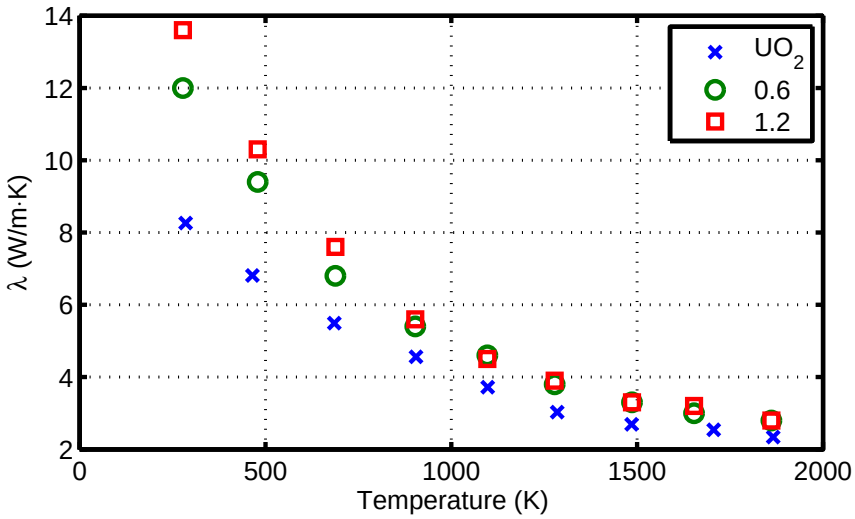

Figure 37: Thermal conductivity data obtained by Ishimoto et al. for continuous type UO_2–BeO pellets versus temperature for two concentrations (wt%) of BeO compared to that of pure UO_2 fuel; adapted from [33].

Solomon and colleagues [108, 170] prepared and examined two kinds of UO_2–BeO fuels: The green-granule process and slug-bisque processes, each with 10 vol% BeO, designated as GUB and SUB, respectively. These two samples were prepared to examine differences in their thermal conductivities. Standard laser-flash technique was employed to measure the thermal diffusivity of the samples as a function of temperature in the range 400 to 1400

K [108]. The thermal conductivity of the UO_2–BeO fuel was then calculated from these thermal diffusivity measurements, their densities, and specific heats. The data show no distinct differences between the thermal conductivities produced from either of the fabrication processes. Figure 38 depicts these data for the reference UO_2 and UO_2–BeO with 10 vol% BeO. The UO_2–10vol%BeO shows about 50% enhancement of the thermal conductivity at lower temperatures.

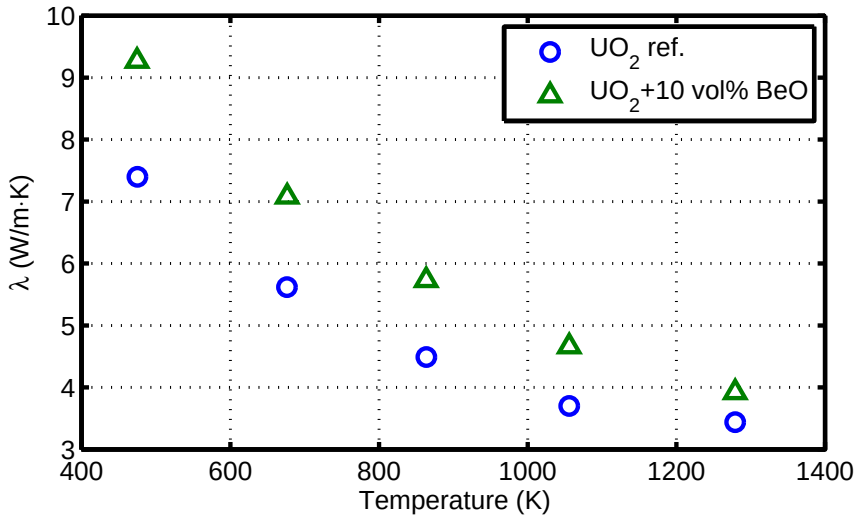

Figure 38: Thermal conductivity data obtained by Solomon et al. for continuous type UO_2–BeO pellets versus temperature for 10 vol% BeO compared to that of pure UO_2 fuel; adapted from [108].

In a related study, Li and collaborators [171] investigated the thermal physical behavior of 10 vol% BeO–UO_2 composites fabricated by spark plasma sintering (SPS). In [171], they present data for the coefficient of thermal expansion (α) and thermal conductivity (λ) as a function of temperature from room temperature up to 2000°C (2273 K) for the former and up to 1600°C for the latter quantity. Their measured data show that α increases slowly from 9.06×10^{-6}/K to 10.95×10^{-6}/K as the temperature is raised from 373 K to 1773 K. However, with further increase in temperature, it rapidly drops to 1.35×10^{-6}/K at 2273 K. The increase in α is linear with temperature from 298 K to 1623 K then a rapid increase to maximum at 1863 K followed by the drop. This anomalous thermal expansion behavior perhaps is caused by the mismatch between UO_2 and BeO thermal behavior at high temperatures, which needs explanation; see [171]. Regarding measurements of λ, Li et al. do not provide sufficient information in [171] to indicate how they obtained their results. They state that thermal conductivity of BeO/UO_2 was measured by a laser-flash apparatus. But the common method is to measure thermal diffusivity with laser-flash and then combine that with heat capacity and density data to determine thermal conductivity. Their thermal conductivity for UO_2–10vol%BeO lies over that of UO_2 as a function of temperature, but has an erratic behavior above 1273 K. In particular, the conductivity of UO_2–10vol%BeO raises from 1673 K to 1873 K, which is in contrast with the behavior of UO_2. Surely, more clarification and independent measurements are needed to make a definite conclusion about this behavior.

3.3.3 UO_2–SiC

According to the review of Slack [106], the thermal conductivity of single crystal SiC at room temperature (300 K) is 490 W/mK and at 1300 K is 50 W/mK, whereas at the corresponding temperatures, those for UO_2 are ≈ 8 and ≈ 3 W/mK, respectively. Moreover, silicon carbide also has the benefit of a low thermal neutron absorption cross section, high melting point (≈ 2973 K), good chemical stability, e.g., strong resistance to oxidation in air and air–moisture atmospheres, and no unacceptable phase changes [172].

Tulenko and collaborators [109, 115] at the University of Florida have investigated the effect of silicon carbide particle addition on thermal conductivity of UO_2–SiC composite pellets. Uranium oxide powder and β-SiC [173] particles of different sizes (0.6–50 μm) and different volume fractions (5–20%) were mechanically mixed and sintered at 1350–1450°C for 5 min. by SPS method to obtain sample pellets. They measured thermal conductivity of the pellets using an Anter Flashline 3000 Thermal Properties Analyser. In this method, the data on thermal diffusivity, $D_{\rm th}$, and the specific heat capacity, C_p, were obtained by measurement of the rising temperature on the back surface of a sample caused by a pulsed laser beam on the sample's front surface. They performed the measurements three times each at 100°C (373 K), 500°C (773 K), and 900°C (1173 K) from which they calculated the mean conductivity at each temperature. In more detail, the thermal diffusivity was given as $D_{\rm th} = 0.1388L^2/t_{1/2}$, where L is the thickness of the specimen and $t_{1/2}$ is the time for the back surface temperature to reach 50% of its maximum value. The specific heat capacity is $C_p = Q/(\Delta T m)$, where Q represents the energy of the pulsed laser beam, determined by comparing the maximum value of the temperature rise with that of a reference, m is the mass of the specimen, and ΔT is the maximum value of the temperature rise. By multiplying density with $D_{\rm th}$ and C_p, thermal conductivity was determined.

Figure 39 shows some of Yeo et al.'s measurements [109] of the thermal conductivity of UO_2–SiC pellets, fabricated at two sintering temperatures by SPS (1400°C and 1600°C), 10 vol% SiC powder particles (p), in comparison with that of standard UO_2. The SPS fabricated UO_2–SiC composite pellets have higher measured thermal conductivity than UO_2 pellets. In general, the higher the SPS temperature, the higher the measured thermal conductivity. A maximum thermal conductivity enhancement was observed in UO_2–SiC composites sintered by SPS at 1600°C, and the data in figure 39 show that the increases are ≈ 45%, 40%, 50% at 373, 773 and 1173 K, respectively, compared to the standard UO_2 value. Pellet densities, with 10 vol% SiC(p), were 96.06 and 96.97 %TD/UO_2 for 1400°C SPS and 1600°C SPS respectively; for details see [109].

We have also evaluated the thermal conductivity λ of UO_2–5 vol%SiC composite from the data of the thermal diffusivity and heat capacity shown in figures 8 and 9 in [115]; see table 6. To calculate the composite density, we have used the usual rule of mixture:

$$\rho = \rho_{\rm UO_2}(1 - v_p) + \rho_{\rm SiC} v_p, \tag{23}$$

where $\rho_{\rm UO_2}$, $\rho_{\rm SiC}$ and v_p are densities of UO_2, SiC, and the SiC volume fraction, respectively. We have assumed the theoretical densities of 10966 kg/m^3 and 3220 kg/m^3 for UO_2 and SiC, respectively, and the fraction of TD for the UO_2–5 vol%SiC is taken as 0.9681 [115].

High temperature thermal physical performance of SiC–UO_2 composites up to 1600°C has been studied by researchers at the China Academy of Engineering Physics and the China

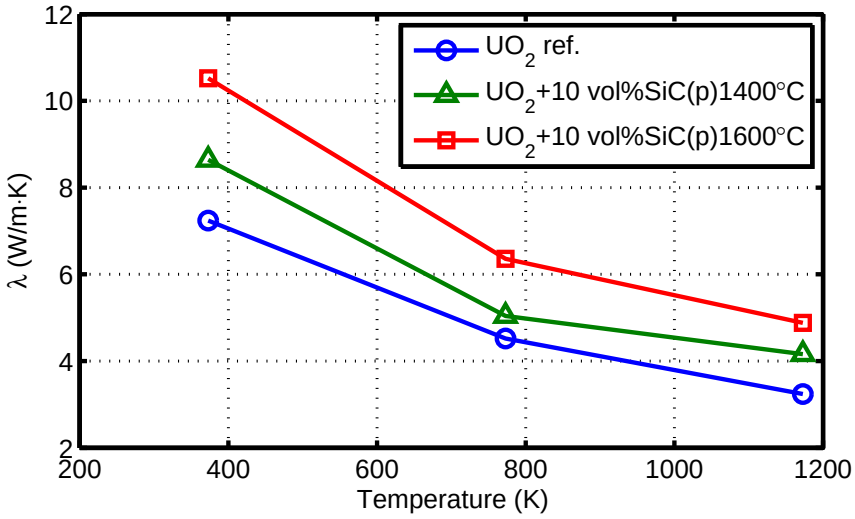

Figure 39: Measured thermal conductivity values of UO_2 and UO_2–SiC composite pellets sintered by SPS technique at 1400°C and 1600°C; adapted from [109]. Pellet densities of 10 vol% SiC(p) are 96.06 and 96.97%TD/UO_2 for 1400°C SPS and 1600°C SPS.

Table 6: The thermal conductivity λ of UO_2–5 vol%SiC calculated via $\lambda = \rho D_{\rm th} C_p$; data for $D_{\rm th}$ and C_p are taken from figures 8 and 9 in [115] and density ρ is calculated through the mixture rule.

Temperature	°C	100	500	900
ρ	kg/m^3	10241	10241	10241
$D_{\rm th}$	m^2/s	2.88×10^{-6}	1.53×10^{-6}	1.00×10^{-7}
C_p	J/kgK	266.5	317.5	328.5
λ	W/mK	7.86	4.97	3.36

Nuclear Power Technology Research Institute [174]. Li et al. [174] prepared SiC–UO_2 SPS composites by mixing UO_2 powders (99.9% purity) with SiC powders (4–10 vol%) with a mean diameter of about 2 μm. The sintering temperatures used for the mixture in their experiments were 640°C, 1200°C, 1300°C, 1400°C and 1500°C under an applied pressure of 25 MPa with a holding time 10 min. at the sintering temperature. They measured the thermal diffusivity by a laser-flash apparatus (Netzsch, Germany). The specimens tested were about 12.7 mm in diameter and 3 mm in thickness. The test temperature range reported in [174] is from 25 to 1600°C in an interval of 200°C. They determined the thermal conductivity λ through the usual formula $\lambda = D_{\rm th} C_p \rho$, mentioned before. The density ρ was measured by the Archimedes method and the specific heat C_p was calculated through the Kopp-Neumann law of mixture as in equation (22).

Figure 40 shows some of Li et al's thermal conductivity data on SiC–UO_2 composites with 6 vol% SiC(p) and 10 vol% SiC(p) along a calculation using a standard thermal conductivity relationship for 0.95TD dense UO_2 [169]. Figure 40 shows that the increases in thermal conductivity for 10 vol% SiC(p) specimen are $\approx$ 28%, 25% and 33% at 873 K, 1273 K and 1873 K, respectively, over that of standard UO_2 fuel.

Li et al. [174] also measured the coefficient of thermal expansion α by a dilatometer (DIL-402E, Netzsch, Germany) in the temperature range from room temperature to 1400°C (1673 K). The size of the specimen was 8×15 mm^2. The employed heating rate was 5 K/min. Figure 41 shows Li et al's measured data on α for SiC–UO_2 composites plus calcu-

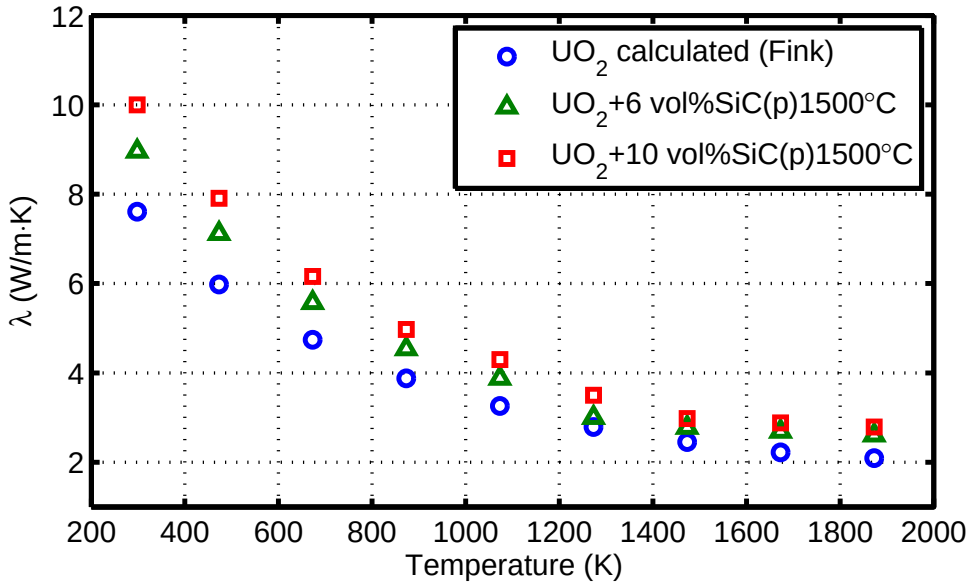

Figure 40: Li et al. [174] thermal conductivity data for UO_2–SiC composite pellets sintered by SPS technique at 1500°C; adapted from supplementary data provided in [174]. Pellet densities of 6 vol% SiC(p) and 10 vol% SiC(p) are 98 and 97%TD/UO_2, respectively.

lated values for UO_2, where the latter is evaluated using a standard relation given in [169]. It is seen that α of SiC–UO_2 increases with temperature and decreases with SiC addition. Similar to UO_2, the rate of increase of α is slow below 1073 K, but accelerates at higher temperature. After the addition of SiC, α exhibits a quasi-linear dependence on temperature. Furthermore, the coefficients of thermal expansion for 6 vol% SiC and 10 vol% SiC remain almost parallel over the entire temperature range.

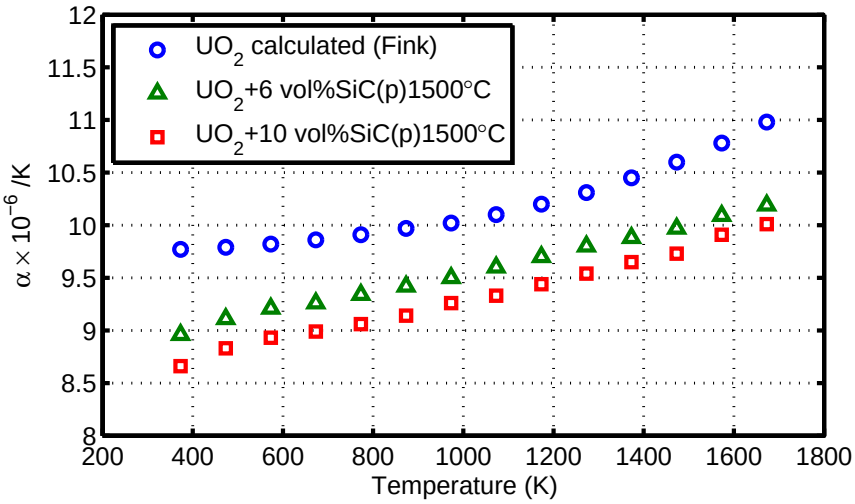

Figure 41: Coefficient of thermal expansion α measurements for UO_2–SiC composite pellets sintered by SPS technique at 1500°C; adapted from supplementary data provided in [174].

3.3.4 UO_2–Diamond

Limited information is available in the literature regarding UO_2–diamond thermal-physical properties. Tulenko and colleagues [35, 116] have investigated the microstructure and thermal properties of UO_2–diamond fuel pellets fabricated via SPS, using different diamond particle sizes ranging from 0.25 μm to 25 μm, as mentioned in section 2.3. They measured the thermal diffusivity at three different temperatures, i.e. at 100°C, 500°C and 900°C, using a laser-flash method (Anter Flashline–3000). Specific heat was calculated through the Kopp-Neumann law of mixture as in equation (22) and the values shown in table 7. The thermal conductivity was then determined as the product of thermal diffusivity, specific heat and pellet density.

Table 7: Properties of UO_2, diamond and UO_2–diamond; data from refs. [116, 169, 175].

Material	Density (kg/m^3)	Specific heat (J/kgK)		
		100°C	500°C	900°C
UO_2	10.96	258	305	314
Diamond	3.52	757	1687	1849
UO_2–5vol% diamond	10.59	266	328	340

A comparison is made between thermal conductivities of the UO_2–diamond composite and several UO_2–based composites published in the literature in figure 42, at temperatures: 100°C (373 K), 500°C (773 K) and 900°C (1173 K). In this figure, data for UO_2–5 vol% diamond come from [35, 116], UO_2–4.2 vol% BeO (continuous type) from [33], UO_2–5 vol% SiC data are evaluated according to table 6, and those for UO_2 (0.95 dense) are calculated according to a relationship given by Ronchi et al. [145, 169]. As can be seen, among these fuels, UO_2–BeO continuous manifests the highest thermal conductivity at the measured temperatures 373 K and 773 K. At 1173 K, the thermal conductivities of the UO_2–BeO continuous and the UO_2–diamond converge. For the UO_2–diamond composite pellets, the maximum increase in thermal conductivity relative to UO_2 (calculated) is about 42%, 40% and 35% at 100°C, 500°C and 900°C, respectively [35, 116].

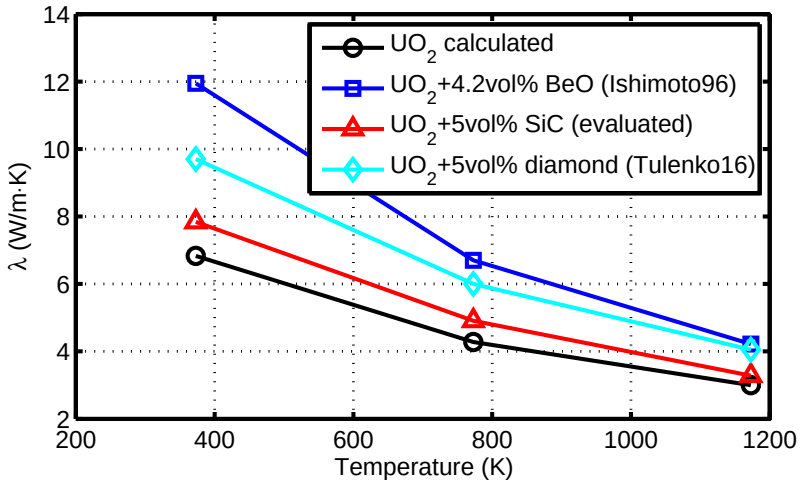

Figure 42: Comparison of thermal conductivity of UO_2–diamond and that of various UO_2–based fuels. In the legend: Ishimoto et al. [33], Tulenko16 [35, 116], UO_2 calculated [145, 169] and data for UO_2–SiC are evaluated in table 6.

As mentioned in section 2.3, related enhanced thermal conductivity UO_2-base fuels with potential applications include graphene-nanoplatelet [121] and micron–sized graphite–flake crystal [122] additives. In [121], UO_2 composite fuel pellets with various graphene nano–platelet inclusions from 1 wt% to 5 wt% were consolidated into dense fuel pellets by SPS, forming a lamellar interconnection along in–plane direction (with the 2D graphene nanosheets aligned along the radial direction of the sintered fuel pellets), which enhanced thermal diffusivity/conductivity along the radial direction of the fuel matrix. Yao et al. [121] measured thermal diffusivity of the sintered pellets by a laser-flash apparatus. The measurement was conducted in argon inert atmosphere at room temperature. They calculated thermal conductivity as the product of density, thermal diffusivity, and specific heat capacity. The densities of the sintered fuel pellets were measured based on Archimedes principle at room temperature and the specific heat capacities of pristine UO_2, UO_2–1 wt%G, and UO_2–5wt% pellets were calculated using the usual rule of mixture. A value of 0.237 J/g·K was used for UO_2 and the value of 0.711 J/g·K for graphene at room temperature from Pop et al. [176]. An enhancement in thermal conductivity by 162% in the radial direction (in-plane) was achieved for the UO_2–5wt% composite fuel relative to UO_2 at room temperature for pellets sintered at 1600°C for 20 minutes under a uniaxial pressure of 40 MPa. To our knowledge, however, no thermal conductivity data in operating temperatures of reactor have been reported for this type of fuel in the literature.

In a recent study, Li and colleagues [122] introduced highly oriented micron–sized graphite flakes to UO_2 pellets fabricated by SPS. Similar type of measurements, as the forgoing study, indicate that relative to UO_2, the radial thermal conductivity of UO_2–5wt% graphite increased by about 200% in the temperature range 298–1273 K.

3.3.5 Modeling

The measured data on fuel thermal conductivity discussed in the foregoing sections were obtained by first measuring thermal diffusivity by laser-flash technique then combining that with fuel density and heat capacity data to determine the conductivity. Thermal conductivity of a solid material λ is related to thermal diffusivity, heat capacity and density, through the Debye formula, namely

$$\lambda = \rho D_{\mathrm{th}} C_p, \tag{24}$$

where D_{th} is thermal diffusivity, ρ the bulk density and C_p the heat capacity of the tested specimen. A simple derivation of this important formula is provided in Appendix B.

Furthermore, the enhanced thermal conductivity of composite fuels discussed in this section are two-component type entities, meaning that, a high thermal conductivity material, usually nonmetallic, embedded in UO_2 fuel with a low thermal conductivity. We have already used a rule of mixture, referred to as the Kopp–Neumann rule, for combining the heat capacities and densities of binary composites in the foregoing subsections, see equations (22) and (23). Here, we shall recount some rules for combining the sole thermal conductivities of the binary or two-phase fuel to obtain the effective thermal conductivity of the composite fuel. Some conventional thermal conductivity mixing rules for two-phase composites are listed in table 8.

Authors of various reports in the literature have selected different mixing rules even for the same compound. For the UO_2-MgO fuel, Fujino and colleagues [166] have used a single-

Table 8: Conventional models of effective thermal conductivity of two-component UO_2+additive. Effective thermal conductivity of composite λ, thermal conductivity of matrix (UO_2) λ_m, thermal conductivity of particle λ_p, thermal conductivity ratio $\alpha = \lambda_p/\lambda_m$, $\beta = \lambda_p/ah_c$, particle radius a, interfacial thermal conductance h_c, particle shape factor n, particle volume fraction v, $S = \pi t/8a$, t flake thickness, and $\lambda_r = \lambda_p/(1+\beta)$.

Model	Expression/Method	Remarks
Maxwell [177]	$\frac{\lambda}{\lambda_m} = 1 + \frac{3(\alpha-1)v}{(\alpha+2)-(\alpha-1)v}$	Spherical dispersion
Hasselman-Johnson I [178]	$\frac{\lambda}{\lambda_m} = \frac{2(\alpha-\beta-1)v+\alpha+2\beta+2}{(1+\alpha+\beta)v+\alpha+2\beta+2}$	Spherical dispersion
Hasselman-Johnson II [178]	$\frac{\lambda}{\lambda_m} = \frac{(\alpha-\beta-1)v+1+\alpha+\beta}{(1-\alpha+\beta)v+1+\alpha+\beta}$	Circular cylinder $\perp$ to heat flow
Hamilton-Crosser [179]	$\frac{\lambda}{\lambda_m} = \frac{\alpha+(n-1)-(n-1)(1-\alpha)v}{\alpha+(n-1)+(1-\alpha)v}$	Spherical ($n=3$), nonspherical ($n=6$) particle
Lichtenecker [180]	$\frac{\lambda}{\lambda_m} = \left(\frac{\lambda_p}{\lambda_m}\right)^v$	Parallel orientation of plates
Hatta-Taya [181, 182]	$\frac{\lambda}{\lambda_m} = 1 + \frac{v(\lambda_r/\lambda_m-1)}{1+S(1-v)(\lambda_r/\lambda_m-1)}$	Flakes in $x-y$ plane
Latta et al. [170]	Numerical simulation	Finite element analysis (FEA)
Badry et al. [183]	Numerical simulation	FEA with interface thermal resistance

phase thermal conductivity expression (Appendix A), whereas Shamanin et al. [168] have used Lichtenecker's rule as described in table 8. For the UO_2-BeO fuel, Ishimoto et al. [33] have used a cumbersome relation, which require numerical solution, attributed to B. Schulz [184], with satisfactory outcome, where they have derived different model parameter values for dispersed type versus continuous type BeO. Morrison and coworkers [185] and Spencer et al. [186] utilize Maxwell type relations for thermal conductivity of UO_2-BeO fuel, while Chandramouli and Revankar [187] developed and used a single-phase thermal conductivity relationship based on correlations implemented in the FRAPTRAN computer program [188]. Shamanin et al. in [189] employed a Lichtenecker rule for computing the thermal conductivity of UO_2-BeO fuel. Latta et al. [170] have used the finite element analysis computer program ANSYS to develop composite fuel geometries with set boundary conditions to produce effective thermal conductivity for UO_2-BeO fuel. They have simulated the measurements of Ishimoto et al. [33] with good agreement. Moreover, in [170], they used the same method to simulate the thermal conductivity of UO_2-SiC fuel, albeit with no experimental verification.

A combination of a mechanical contact or poor chemical adherence at the interface, plus a possible thermal expansion mismatch between different constituent phases in a composite, can give rise to an interfacial thermal contact resistance. Nan et al. [190] have derived algebraic relations for calculating the effective thermal conductivity of arbitrary particulate composites with interfacial thermal resistance in terms of an effective medium approach combined with the notion of Kapitza thermal contact resistance. Their method somewhat generalizes the Hasselman-Johnson relations [178] for computing the effective thermal conductivity of two-component composites containing particles of various shapes.

Latta et al. [170] compared their computations (FEA) of UO_2-BeO thermal conductivity against experimental data [33] within the error of the measurement but not explicitly accounting for the Kapitza resistance. Badry et al. [183] have further explored the relationship of microstructure and thermal conductivity and have quantified the influence of the thermal boundary resistance on the effective thermal conductivity. They validated their numerical model (FEA) against experimental data on thermal conductivity of a dispersed

UO_2-BeO microstructure up to 10 vol% in the temperature range 50 to 300°C. The authors in [183] also simulated a continuous UO_2-BeO microstructure. They devised that structure by constructing Voronoi diagrams, employing multiple order parameters, akin to a phase-field model of grain growth. Contrary to the dispersed type, the UO_2 was represented as second-phase particles (grains) and the BeO was represented as the matrix, in the sense that it is the continuous phase. Badry et al. compared their BeO continuous type model calculations with experimental data [191] for 6 vol% and 10 vol% BeO in the temperature range from 50 to 250°C with agreeable results. An extended and refined version of the model is presented in [192]. Surely, an extension of measurements and numerical simulations presented in [183] to higher temperatures covering normal reactor operation and even operational transients would be valuable.

In a numerical simulation study, Li, Garmestani, and Schwartz [193] have computed the thermal conductivity of UO_2–BeO composites using a statistical continuum mechanics approach that characterizes the anisotropy of the composite microstructure. Their results indicate that the addition of BeO within UO_2 matrix can markedly enhance the thermal conductivity of the composite fuel in a preferred direction, if anisotropy is engineered into the microstructure through processing.

In a recent publication [194], Hilty and Tonks present a finite element based model for the UO_2 fuel microstructure containing high thermal conductivity additives, namely BeO and SiC, without introducing the Kapitza thermal resistance concept in the model. Instead, a thermal resistor model is developed for estimating the effective thermal conductivity of a composite. The authors validate their model against experimental data from the literature on four types of experimental fuels, namely UO_2-BeO pellets with BeO dispersed and continuous type (cf. figure 23) and UO_2-SiC pellets, with SiC whiskered or powdered additive (cf. figure 24). The secondary constituent volume fractions in their simulations for continuous BeO, dispersed BeO, whiskered SiC, and powdered SiC were 3.48 vol%, 3.19 vol%, 10.01 vol% and 9.92 vol%, respectively. The temperature ranges that the calculated effective conductivity was compared with experimental data were 300-1500 K for the UO_2-BeO specimens and 300-1200 K for the UO_2-SiC specimens.

For UO_2–SiC fuel, Yeo et al. [115] have used the Hasselman-Johnson I rule (cf. table 8) to compute the effective thermal conductivity of the UO_2-SiC composite. A salient feature of this model is the entry of the interfacial thermal conductance parameter h_c in the mixing rule, accounting for the UO_2-SiC interface contribution described by a separate expression; see Appendix C. The interfacial thermal conductance between matrix and second phase particles is related to the density, specific heat and phonon velocity of the two materials. Yeo et al. compute h_c and thereafter λ at several temperatures then compare their model calculations with their measurements at those temperatures (373, 773, 1173 K) as a function of SiC volume fraction (up to 20%) with good accordance [115]. Recently, Zhu et al. [195] have evaluated the UO_2/BeO interfacial thermal conductance based on the so-called diffusive mismatch model with full band phonon dispersions computed by density functional theory. They examine and elucidate the principal mechanisms for attenuating the heat flux through the UO_2/BeO interface; see Appendix C.

For UO_2– diamond fuel, Chen et al. [116] suggest the Hasselman-Johnson I thermal conductivity mixing rule. They do not, however, apply this rule to compute the effective thermal conductivity as a function of temperature against their measurements. Regarding UO_2-graphene, in the review article [165], it is stated that the Hamilton-Crosser rule

is used to compute the effective conductivity, which we could not verify. Recently, Li and colleagues [122] have reported results on thermal conductivity of UO_2-graphite flakes fuel pellets. They determined the thermal conductivity through thermal diffusivity measurement in the radial direction. They also calculated the conductivity of the composite fuel using the Hatta-Taya mixing rule (table 8) plus the acoustic mismatch formula from [196] for h_c. The separate thermal conductivity data for UO_2 and graphite used in their Hatta-Taya relation are taken from the literature. Their computations match their measurements for $v = 0.1$ (10 vol% graphite) in the temperature range from room temperature to 1000°C. In table 9, we list some references to material correlations and data for UO_2 and its specific thermal conductivity enhancer material discussed here. Together with the rules outlined in table 8, the information in these references can be used to compute, e.g., the effective thermal conductivity of the composite UO_2 fuel as a function of temperature.

Table 9: Sources to thermal property data and models for UO_2 and the additive. Here, ρ is the density at room temperature, T_M the melting point and property data include thermal expansion coefficient, specific heat, thermal diffusivity or/and thermal conductivity.

Material	ρ (kg/m^3)	T_M (K)	Property data reference
UO_2	10966	3120	[169, 197–199]
MgO	3650	3110	[57, 200–203]
BeO	3010	2823	[200, 202–204]
SiC	3215	3103	[106, 173, 201]
Diamond	3513	3820	[35, 106, 175, 205–208]
Graphite/Graphene	2266	4890*	[176, 204, 209–215]

* See also refs. [216, 217]

Integral fuel rod modeling studies of composite type UO_2-base fuels reported in the literature have been surveyed in [165], which will also be discussed in section 6.3.

Sample computation Let's compute the effect of adding graphite to UO_2 on its thermal conductivity. To this end, we use the Hamilton-Cross mixing rule given in table 8 with $n = 6$. For UO_2, we select the standard thermal conductivity correlation [145], while for graphite (type G-348), we use that developed in [214]. The thermal conductivity data and correlation for the graphite as a function temperature are depicted in figure 43(a). Figure 43(b) shows the graphite/UO_2 thermal conductivity ratio as a function of temperature. Finally, figure 44 shows plots of the effective thermal conductivity of UO_2-graphite for various levels of graphite volume fraction, as computed using the Hamilton-Cross rule. Hence, our model calculation indicates that for this graphite (G-348) to be an effective thermal conductivity enhancer, one should have $v \geq 0.05$.

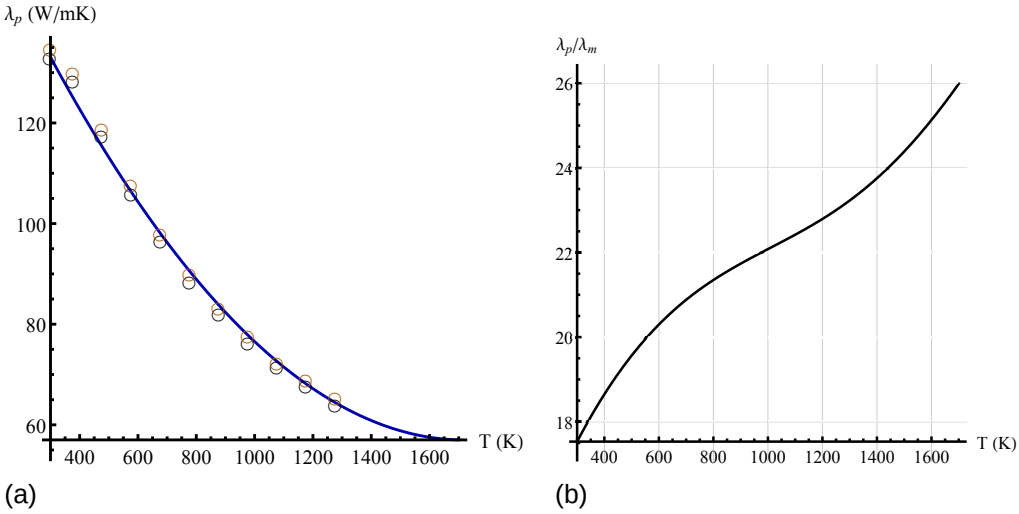

Figure 43: (a) Thermal conductivity of G-348 graphite as a function of temperature, based on the data (markers) of Swank et al. [214]. (b) The graphite/UO_2 thermal conductivity ratio (λ_p/λ_m) as a function of temperature.

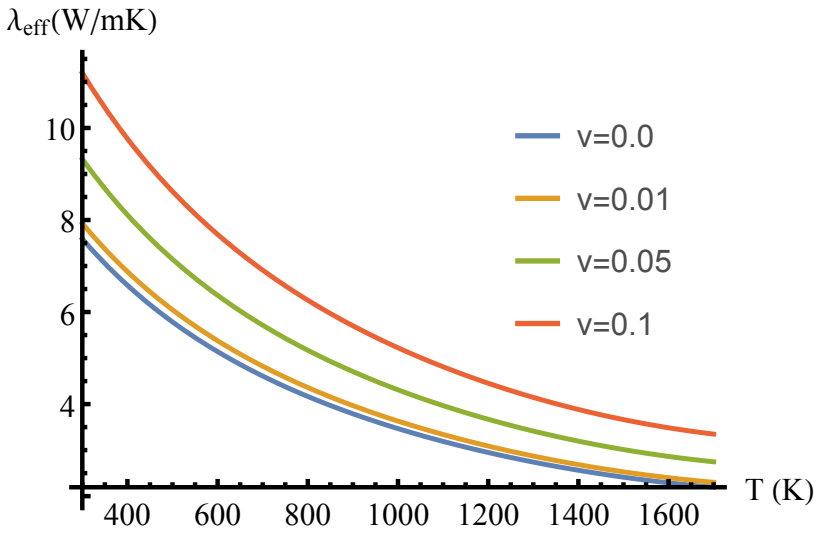

Figure 44: Calculated thermal conductivity of UO_2-graphite composite as a function of temperature for several volume fractions of graphite v.

4 Fission gas behavior

Fission product gases Xe and Kr comprise roughly 13% of the fission products, and are insoluble in UO_2 fuel [37, 218]. At reactor operating temperatures, the gases migrate to fuel grain boundaries, dislocation loops or preexisting pores where they aggregate into bubbles. A portion of these gases, primarily through the grain boundary gas bubble inter-linkage, escapes to free surfaces of the fuel [219]. The amount of fission gas released depends crucially on the operating conditions (linear power density and fuel burnup) and is a subtle and important part of the fuel rod design. Nevertheless, due to modest power ratings and restriction on linear heat generation rate (LHGR) versus fuel burnup (thermal-mechanical operating limit), most UO_2 fuel in LWR cores retains 95% and more of its gas. As pointed out by Lassmann and Benk [220], the fission gas behavior needs to be embraced in fuel rod analysis, because:

- The fission gases xenon and krypton degrade the thermal conductivity of the backed-filled helium gas inside the fuel rod, decreasing the gap conductance and thereby elevating fuel temperatures. Enhanced fuel temperatures may further increase fission gas release and may even initiate an unstable process called "thermal feedback."
- The release of fission gases increases the rod internal pressure. This pressure increase may limit the design life of a fuel rod, since the inner pressure should not exceed a prescribed pressure.
- The swelling due to gaseous fission products may lead to enhanced pellet-cladding mechanical interaction, especially during anticipated or postulated reactor transients, which may cause fuel cladding failure.
- The release of radioactive gases from UO_2 to the free volume of fuel rod would decrease the safety margin of a nuclear plant. In this regard, the nuclear fuel matrix is considered as the first barrier to the release of radioactive fission products [221].

Hence, an assessment of fission gas behavior in various UO_2 doped fuels is prudent and indispensable. Since the concentrations of dopants are usually quite low in UO_2, the main effect of additives is on the fission gas diffusivity and the fuel grain size, which in turn affect gas release [6].

In this section, we first assess fission gas diffusivity data reported in the literature for some UO_2 doped fuels, where appropriate correlations are compared against those for undoped UO_2 as a function of temperature. Next, these correlations are used in a fission gas release and a gaseous swelling model to evaluate gas release and fuel swelling as functions of irradiation time at different constant fuel temperatures. Moreover, the effect of grain size is studied. The considered additives include Cr_2O_3, Al_2O_3, Nb_2O_5, and Gd_2O_3.

4.1 Fission gas diffusivity in UO_2-base fuels

As noted in section 3, additives alter the stoichiometry (oxygen to uranium ratio) of UO_2 fuel. The effect of the O/U ratio on the fission gas diffusion has been studied and assessed by a number of investigators in the past, see e.g. [22, 222–224] and references therein. They indicated that the fission gas release rate from hyperstoichiometric UO_{2+x} is higher than

that from stoichiometric UO_2. On the other hand, the gas diffusion coefficient is lowered in hypostoichiometric UO_{2-x} relative to UO_2.

The effect of additives on diffusion coefficient of xenon has been investigated by Matzke [2, 22, 225] and Long et al. [226]. Matzke obtained gas release curves of radioactive xenon from UO_2, doped with 0.1 mole% Nb_2O_5, Y_2O_3, La_2O_3 or TiO_2. The xenon was introduced by ion bombardment technique and reactor irradiation. Also, he obtained the uranium self-diffusion coefficients in the same specimens. The fission gas release data were obtained following a short reactor irradiation at elevated temperatures after a fast release (burst) within the first few minutes. The cumulative gas release fraction increased linearly with the square-root of time or $t^{1/2}$. This part of the release was used to evaluate the diffusion coefficients (see below). Matzke's results are summarized in table 10. From the fact that the doping did not affect appreciably the xenon release in the specimens at low doses, 5×10^{20} fissions/m^3, whereas it greatly enhanced the uranium diffusion, Matzke concluded that xenon does not diffuse in uranium or oxygen vacancies.

Table 10: Ratio of Xe diffusivity in fuel containing 0.1 mol% additives to that for pure UO_2, determined upon irradiation to low dose; from Matzke [225].

Fuel	Fission density	Temperature	
Oxide	fissions/m^3	1400°C	1550°C
UO_2+Nb_2O_5	5×10^{20}	0.32	1.29
UO_2+Y_2O_3	5×10^{20}	0.79	1.00
UO_2+La_2O_3	5×10^{20}	0.37	0.93

Experiments by Long et al. [226] indicated that the diffusion coefficient of xenon from UO_2 doped with 10-30 mol% Y_2O_3 appeared to be about 20-50 times larger than that of undoped UO_2. MacDonald [227] and Killeen [6, 228] indicated no reduction in the fission gas release rate for the large grain UO_2 fuels (grain size: 50-100 μm) doped with 0.1 wt% TiO_2, 0.4 wt% Nb_2O_5, or 0.5 wt% Cr_2O_3, when compared to undoped fuels (grain size: $< 10\,\mu$m). To clarify these results, these workers suggested enhanced fission gas diffusions in the doped fuels. Nevertheless, it is believed that at higher fuel burnups, the diffusion coefficient of the fission gases in additive fuel may become similar to that in undoped UO_2, since solid fission products soluble in the UO_2 lattice, such as rare earth elements and zirconium, are accumulated in higher concentrations than in initial additive concentrations.

Nonetheless, since none of these past experiments were conducted at controlled oxygen potentials, no definite conclusions on the effect of additives on fission gas behavior could be drawn. For this reason, a new set of more careful experiments were conducted in Japan by Une and his coworkers to quantify the effect of additives and the oxygen potential on fission gas diffusion and release in and from UO_2 fuel [5, 11, 50].

4.1.1 Specimens

In the first series of ^{133}Xe diffusivity measurements (1987), Une and company [50] prepared specimens by mixing 0.5 wt% Nb_2O_5 and 0.20 wt% TiO_2 with UO_2 powder, followed by pressing and sintering in hydrogen gas at 1750°C for 8 h for the Nb_2O_5 mixture and at 1700°C for 2 h for the TiO_2 mixture. Undoped UO_2 pellets were sintered in H_2 at 1700°C

for 2 h. In the subsequent 1998 tests, Kashibe and Une [11] studied the effect of additives, Cr_2O_3, Al_2O_3, SiO_2 and MgO, on diffusive release of ^{133}Xe from UO_2 fuel. In these studies, Kashibe and Une sintered the undoped and (Cr_2O_3, Al_2O_3 or SiO_2)-mixed UO_2 compacts in hydrogen at 1750°C for 2 h. Whereas, they sintered the MgO-mixed UO_2 compact in argon at 1660°C for 2 h to form a (U,Mg)O_2 solid solution with good homogeneity. Then they annealed it in a slightly oxidizing atmosphere of wet N_2+8%H_2 at 1660°C for 2 h and finally, in a reducing atmosphere of dry N_2+8%H_2 at 1660°C for 2 h to precipitate MgO particles of nanometer size in the UO_2 matrix. In table 11, we summarize the basic material characteristics of these specimens, including their Booth equivalent sphere radius a_e; cf. Sec. 4.1.3. More details can be found in the original papers [11, 50].

Table 11: Nominal values of the specimens basic characteristics used by Une et al. for fission gas diffusivity and release measurements, where a_e is the Booth equivalent sphere radius.

Fuel pellet	Content	Grain size	Density	O/M ratio	a_e	Ref.
-	wt%	μm	g/cm^3	-	μm	-
UO_2	...	15	10.71	2.001,2.004	1.88	[11]
+ Nb_2O_5	0.5	NA[a]	10.41	NA	2.03	[50]
+ TiO_2	0.2	NA[b]	10.68	NA	2.62	[50]
+ Cr_2O_3	0.065	15	10.73	2.002	1.63	[11]
+ Al_2O_3	0.076	30	10.75	2.002	1.73	[11]
+ SiO_2	0.085	17	10.75	2.002	1.28	[11]
+ MgO	0.50	26	10.46	1.999	3.75	[11]

[a] 110 μm with density 10.8 g/cm^3 in ref. [5]; [b] 85 μm with density 10.8 g/cm^3 [5].

4.1.2 Irradiation and annealing

Une and colleagues [11, 50] irradiated the specimens in evacuated quartz capsules for 6 h at a thermal neutron flux of 5.5×10^{13} neutrons/cm^{2}s in the Japan Atomic Energy Research Institute (JAERI) test reactor JRR-4, yielding a total dose of 1.2×10^{23} fissions/m^3 (4 MWd/tU). After irradiation, the specimens were cooled for a period of 7-10 days to allow short-lived nuclides to decay.

In the 1998 experiment, Kashibe and Une [11] used Mo capsule containing the irradiated specimen (Cr_2O_3, Al_2O_3 or SiO_2)-mixed UO_2, to heat by induction furnace in a stepwise manner from 1100-1600°C with a heating rate of 1.7°C/s, temperature step of 100°C and a holding time of 1 h. Sweep gas was a high purity He+2%H_2 mixture at a flow rate of 60 cm^3/min. The β-activity, with an energy of 346 keV and half-life of 5.27 d, of released ^{133}Xe during heating was continuously measured within an ionization chamber. After the annealing experiments, the residual ^{133}Xe in the specimen was determined upon dissolving the powder in hot nitric acid. The annealing procedure in Une et al.'s 1987 experiment (Nb_2O_5,TiO_2 with UO_2 specimens) was similar, but details were different [50]. The method used by Une and company to determine the xenon diffusivity was that used by Davies and Long [229].

4.1.3 Fission gas diffusivity and release

For post-irradiation annealing experiments, the cumulative fractional release, F, may be related to the equivalent sphere radius, a_e, and the effective gas diffusivity D by the following short time approximation of Booth's equivalent sphere model [230]

$$F(t) \approx \frac{6}{a_e}\sqrt{Dt/\pi}, \tag{25}$$

where the approximation should be valid for $F \leq 0.3$.[7] The equivalent radius is expressed as $a_e = 3/S\rho$ where S is the specific surface area and ρ the bulk density of the specimen. In experiments, initial burst release is usually observed, followed by a steady state release. Hence, D can be calculated from the steady state part of a plot of F versus the square-root of time t. The specific surface area S was determined by BET[8] measurements [11, 50].

Kashibe and Une [11] measured fractional release of ^{133}Xe gas during a ≈ 6 h stepwise heating ramp test from 1100 to 1600°C for undoped and (Cr_2O_3, Al_2O_3 or SiO_2)-doped UO_2. The total release obtained in this set of measurements was larger in the order: Cr_2O_3-UO_2 (16.5%), undoped and Al_2O_3-UO_2 (12%), and SiO_2-UO_2 (4.8%). The ^{133}Xe release of the Cr_2O_3-UO_2 at high temperatures of 1500-1600°C was clearly greater than that of undoped and Al_2O_3-UO_2 specimens. In another set of identical measurements, the ^{133}Xe release of MgO-UO_2 and undoped-UO_2 were determined. The two specimens had comparable release values. Thus, Kashibe-Une's measurements indicate that the additive Cr_2O_3 enhances the diffusive release of ^{133}Xe and the additive SiO_2 suppresses it. On the other hand, the additives Al_2O_3 and MgO have no appreciable effect on gas release.

Kashibe and Une evaluated the diffusion coefficient of ^{133}Xe for specimens annealed according to the stepwise pattern from 1100 to 1600°C from the least squares fitted gradient of $36D/(a_e^2\pi)$ obtained by the $F^2 - t$ plot of equation (25). In this fitting, Kashibe and Une precluded the 1100°C data, since they did not fit well due to a small amount of ^{133}Xe. The obtained results are in the form of Arrhenius relations with different or same coefficients listed in table 12, where we have even included Une et al.'s 1987 results [50] on UO_2-Nb_2O_5 and UO_2-TiO_2 samples. In addition, for the sake of comparison, we have also comprised in this table the Davies and Long xenon diffusivity in pure UO_2 [229], which is widely used in the literature and usually is attributed to Turnbull et al. [231].

Some remarks on the results presented in table 12 are merited. The experimentally determined diffusivities for the insoluble Al_2O_3-doped UO_2 and the soluble MgO-doped UO_2 (dissolved concentration: 0.08 wt%) are almost equivalent to that of the undoped UO_2. The diffusivities for these three specimens are approximated by the same Arrhenius relation, see table 12.

The scatter in Kashibe-Une's data from undoped UO_2 samples were within 30% relative to the corresponding Arrhenius relation. Moreover, the diffusion coefficient for the undoped UO_2 obtained by Kashibe-Une's 1998 study [11] was about three times larger than the values reported by Une et al. in 1987 [50] in the temperature range of 1473-1873 K. Compared to the 1987 activation energy of 264 kJ/mol, the 1998 value is slightly smaller, by about 30 kJ/mol. Une and Kashibe attribute this difference in diffusion coefficient for undoped UO_2 to a difference in the annealing pattern. Namely, in the 1998 Kashibe-Une experiments, a stepwise annealing pattern (annealing time 1 h) was used, whereas in the Une et al. 1987 experiments, a one-step annealing (12 h) was used. Moreover, Kashibe and

Une note that slight differences during the specimen preparation and irradiation may affect the diffusion coefficients for undoped UO_2 in the two experiments. Regarding the doped UO_2 results, Une et al.'s 1987 paper [50] does not provide data on grain size and the O/M ratio of the samples.

In figure 45, Arrhenius plots of ^{133}Xe in undoped and doped UO_2 with various additives per table 12 are compared. Note that the xenon diffusivity in (Al_2O_3 or MgO)-doped UO_2 is the same as in undoped UO_2 according to [11]. Figure 46 compares the temperature dependence of ^{133}Xe in undoped UO_2 with that in UO_2+Cr_2O_3 and UO_2+Nb_2O_5. It is seen that for temperatures below 1500 K, xenon diffusivity in UO_2 is somewhat higher than that in UO_2+Cr_2O_3, while for $T > 1600$ K it is vice versa. However, xenon diffusivity in UO_2+Nb_2O_5 is resolutely higher than in UO_2. It is worthwhile to compare Une's diffusivity for undoped UO_2 (table 12) with the corresponding ones used in the literature, figure 47. In this figure, Dav63 is the Davies and Long xenon diffusivity in UO_2 [229].

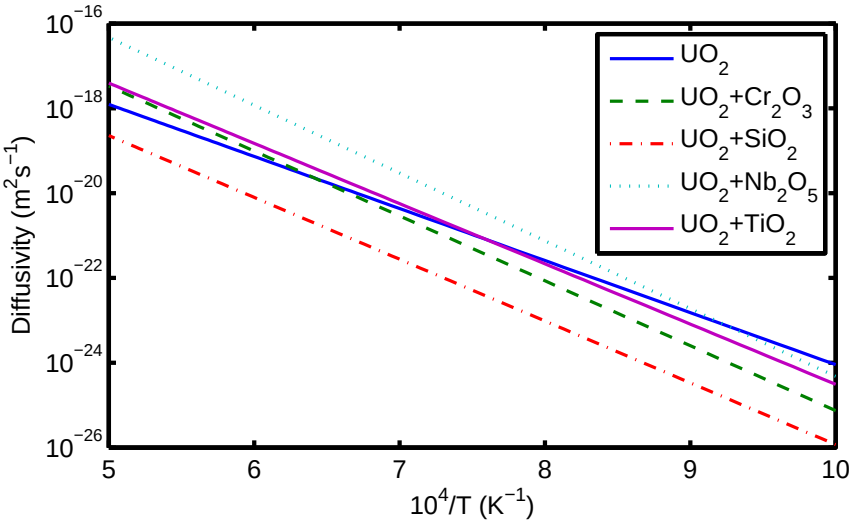

Figure 45: Effective diffusivity of ^{133}Xe versus inverse temperature in undoped and doped UO_2 with various additives in temperature range 1000 to 2000 K, see tables 11 and 12. ^{133}Xe diffusivity in (Al_2O_3 or MgO)-doped UO_2 is the same as in UO_2.

Table 12: Diffusivity of ^{133}Xe in UO_2, with and without additives, evaluated from gas release measurements, with $D = D_0 \exp(-Q_D/RT)$.

Fuel	Temperature range	D_0	Q_D	Source
-	K	m^2/s	J/mol	-
UO_2	$1273 - 1773$	7.6×10^{-10}	293060	[229]
UO_2	$1473 - 1873$	1.7×10^{-12}	235000	[11]
+ Nb_2O_5	$1273 - 1873$	4.6×10^{-9}	306000	[50]
+ TiO_2	$1273 - 1873$	5.0×10^{-11}	272000	[50]
+ Cr_2O_3	$1473 - 1873$	1.5×10^{-10}	293000	[11]
+ MgO	$1473 - 1873$	1.7×10^{-12}	235000	[11]
+ Al_2O_3	$1473 - 1873$	1.7×10^{-12}	235000	[11]
+ SiO_2	$1473 - 1873$	4.4×10^{-12}	279000	[11]

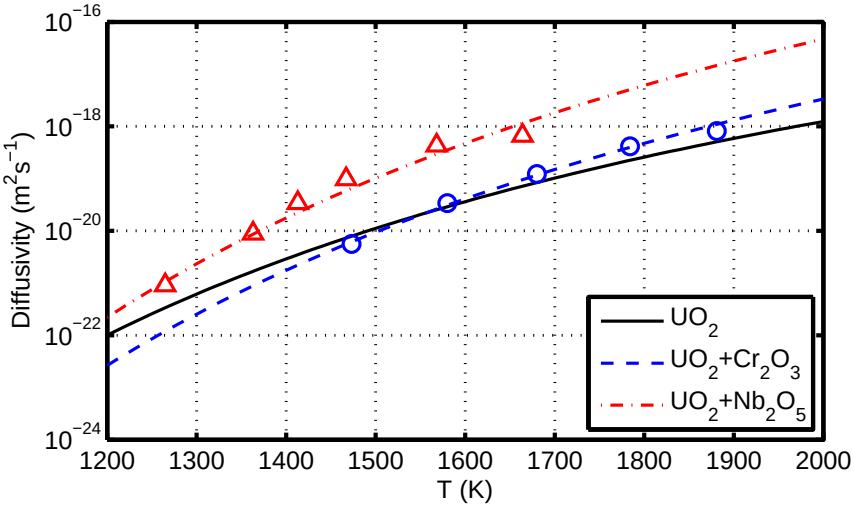

Figure 46: Effective diffusivity of ^{133}Xe as a function of temperature in UO_2 [11], UO_2+0.5wt%Nb_2O_5 [50] and UO_2+0.065wt%Cr_2O_3 [11], see tables 11 and 12.

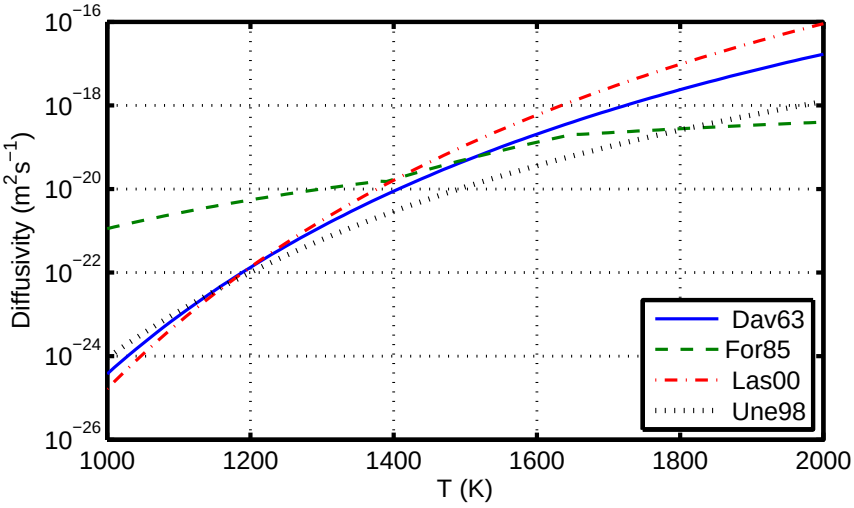

Figure 47: Comparison between various effective thermal diffusion coefficients used for fission gas in UO_2 in literature, where Dav63 [229], For85 [232], Las00 [220], Une98 [11].

4.2 Computations

In this subsection, we present the results of model computations on fission gas release (FGR) and gaseous swelling for some of the fuel types discussed in the foregoing section, including UO_2+Cr_2O_3. The standard model [232–234] for fission gas release through grain-boundary saturation and re-solution is utilized. The grain size, fuel density and gas diffusivity data listed in tables 11 and 12 are used as input to the model. These computations are considered as generic and putative rather than *bona fide*, specific to given experiments or irradiation conditions.

4.2.1 Fission gas release

The equations for the standard fission gas release model through grain boundary saturation and re-solution used in our computations are outlined in Appendix D. The input data to the model, except those for gas diffusivity, fuel density and grain size, which are given in tables 11 and 12 or otherwise specified, are listed in table D1 of Appendix D.

Let us first calculate the threshold for onset of thermal gas release, using the aforementioned model, where threshold temperature vs. irradiation time (or fuel burnup) is evaluated. We compare the behavior of undoped UO_2 and UO_2+Cr_2O_3 in figure 48. It is seen that for irradiation times less than 5000 h, the threshold temperature for UO_2+Cr_2O_3 is below that of undoped UO_2, in conformity with the diffusivity results displayed in figure 46. Here, for fission gas production rate, a linear power density (or LHGR) of 27 kW/m was used, cf. table D1, Appendix D.

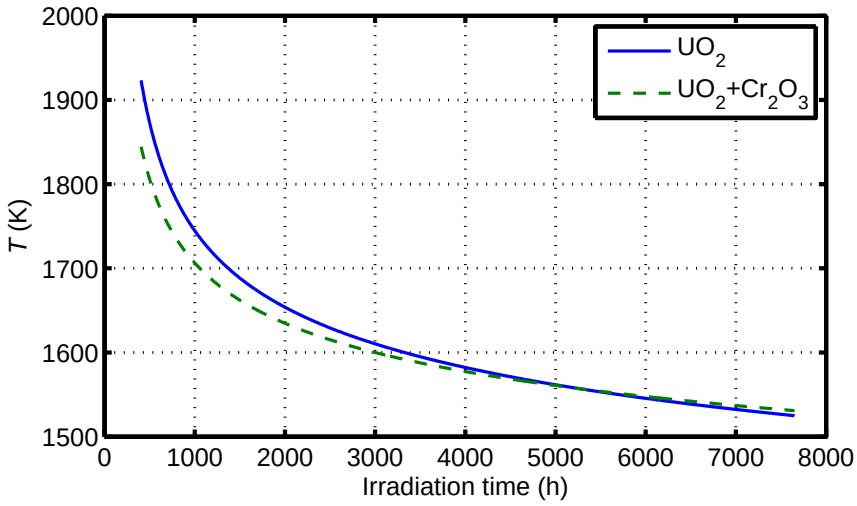

Figure 48: Calculated temperature versus irradiation time for onset of thermal gas release (grain boundary saturation) for two types of fuel, using the model outlined in Appendix D.

In a series of figures 49-51, we plot the results of our computations of thermal fission gas release versus irradiation time at several constant local fuel temperatures, 1600-2000 K, for (Cr_2O_3, Al_2O_3, Nb_2O_5)-doped and "pure" UO_2 fuels. It is seen that among these four samples, the Nb_2O_5-doped has the largest FGR while the Al_2O_3-doped has the lowest. The relative gas release from the Cr_2O_3-doped sample depends on the temperature, i.e., at 1600

K its release is in the order of that from "pure" UO_2, while at 2000 K it is close to that from Nb_2O_5-doped sample.

We recall that the grain radius for pure UO_2 and Cr_2O_3-doped sample was the same, whereas for Nb_2O_5-doped sample we used a grain radius of 55 μm in our computations, see table 11. To illustrate the impact of grain size on FGR, we have done computations on release from the Cr_2O_3-doped sample for several grain sizes. The results at 1800 K are shown in figure 52. The release rate is predicted to be inversely dependent on the fuel grain size.

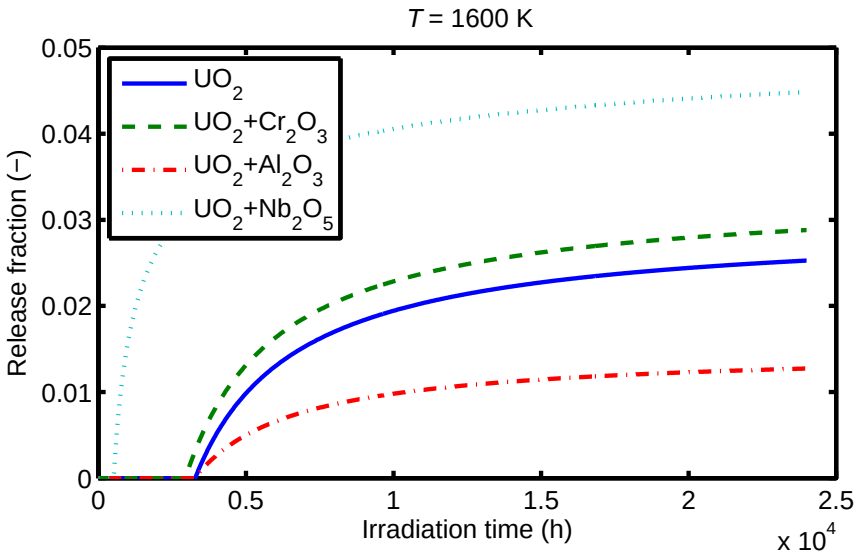

Figure 49: Calculated fractional fission gas release from different UO_2-base fuels at a constant temperature of 1600 K, using the model outlined in Appendix D.

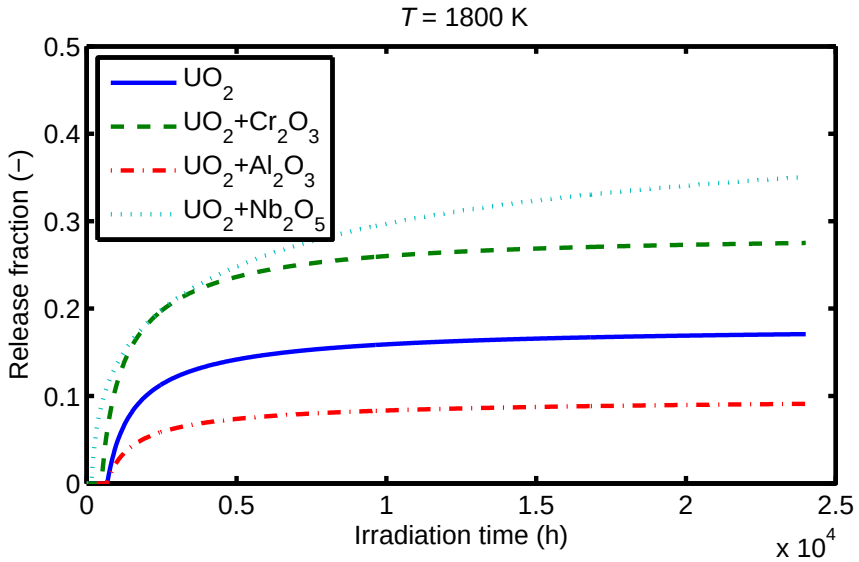

Figure 50: Calculated fractional fission gas release from different UO_2-base fuels at a constant temperature of 1800 K, using the model outlined in Appendix D.

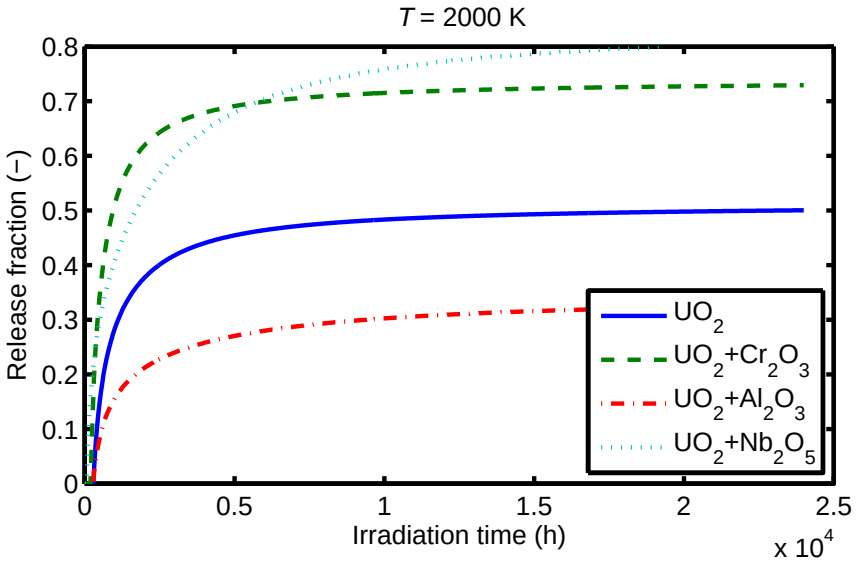

Figure 51: Calculated fractional fission gas release from different UO_2-base fuels at a constant temperature of 2000 K, using the model outlined in Appendix D.

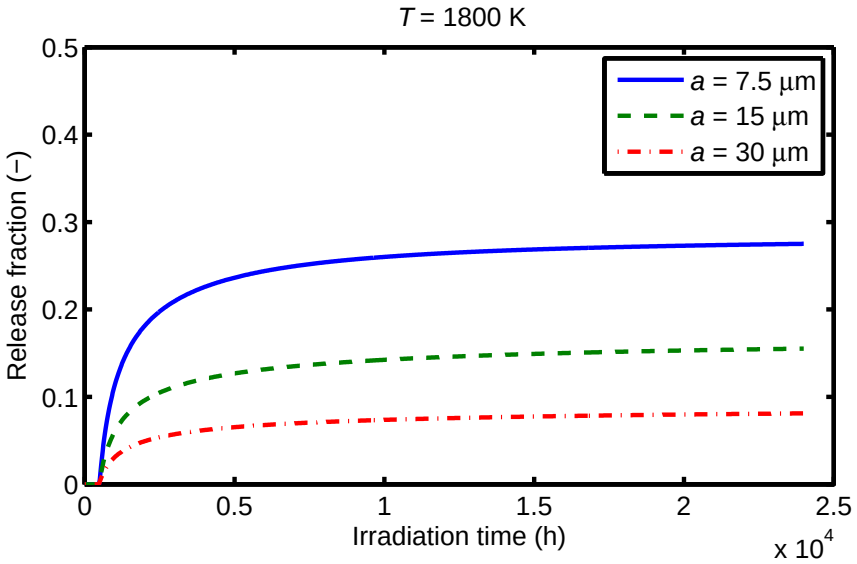

Figure 52: Calculated fractional fission gas release from a Cr_2O_3-doped UO_2 sample at a constant temperature of 1800 K for several grain radii, using the model outlined in Appendix D.

4.2.2 Fuel gaseous swelling

Fuel swelling is the increase in volume by the fission products located in the fuel. The solid fission products are theoretically predicted to contribute to fuel swelling on the average by 0.032% per MWd(kgU)$^{-1}$ [47]. The contribution of gaseous fission products to fuel swelling includes rare gases, such as krypton and xenon, in solid solution and the volume change arising from the formation of fission gas filled bubbles. For the gases in solid solution and the small intragranular gas bubbles, it is estimated that they contribute about 0.056% per MWd(kgU)$^{-1}$ to matrix swelling rate [235]. The intergranular gas bubbles can make the largest contribution to volume change depending on temperature and their amount. Large fission gas bubbles with diameters around a few microns on grain faces and also along grain edges have been observed [236]. At sufficiently high exposures and temperatures, the bubbles interlink, forming a tunnel network, which concomitantly leads to gaseous swelling and gas release [237, 238].

It is plausible that for the considered UO_2-base fuels, with low concentration of additives, the solid fission product swelling is the same as that for pure UO_2. So here we only evaluate fission gas swelling due to intergranular gas (grain face) bubbles. The model we use here rests on the fission gas release model employed in the foregoing subsection and outlined in Appendix D. The method for computation of swelling is fully described in [239], and hence, is not repeated here.

We basically repeat our FGR computations presented in section 4.2.1 for fuel swelling. Figures 53-55 show the relative increase in fuel volume $\Delta V/V$ versus irradiation time at several constant local fuel temperatures, 1600-2000 K, for (Cr_2O_3, Al_2O_3, Nb_2O_5)-doped and "pure" UO_2 fuels. As can be seen, among these four specimens, the Cr_2O_3-doped sample has the highest swelling rate, while the Nb_2O_5-doped sample has the lowest. It is a combination of gas diffusion, grain boundary saturation and grain size, which yields the present behavior.[9] Note that gaseous swelling saturation is an inverse function of grain size [239]. Figure 56 illustrates this for the Cr_2O_3-doped UO_2 sample. It is also seen that the larger is the grain size, the smaller is the swelling rate and the saturation value.

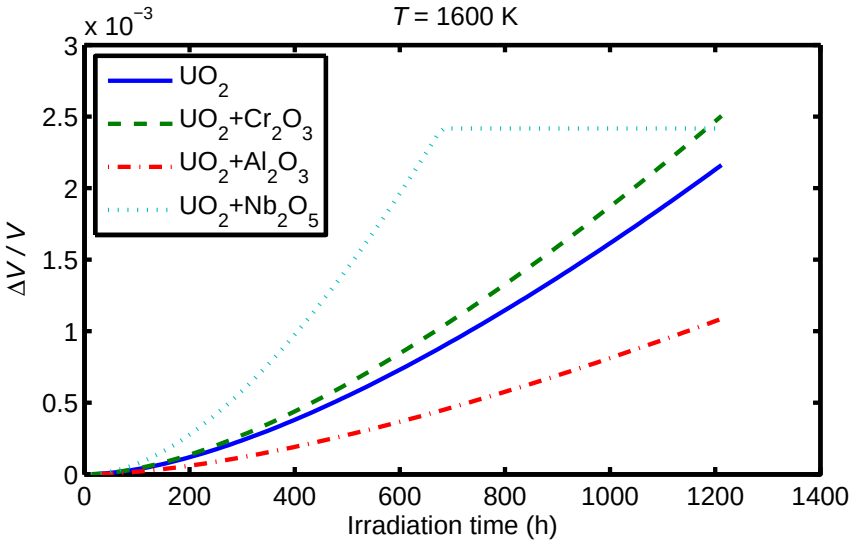

Figure 53: Calculated relative increase in fuel volume versus time for different UO_2-base fuels at a constant temperature of 1600 K, using the gaseous swelling model in [239].

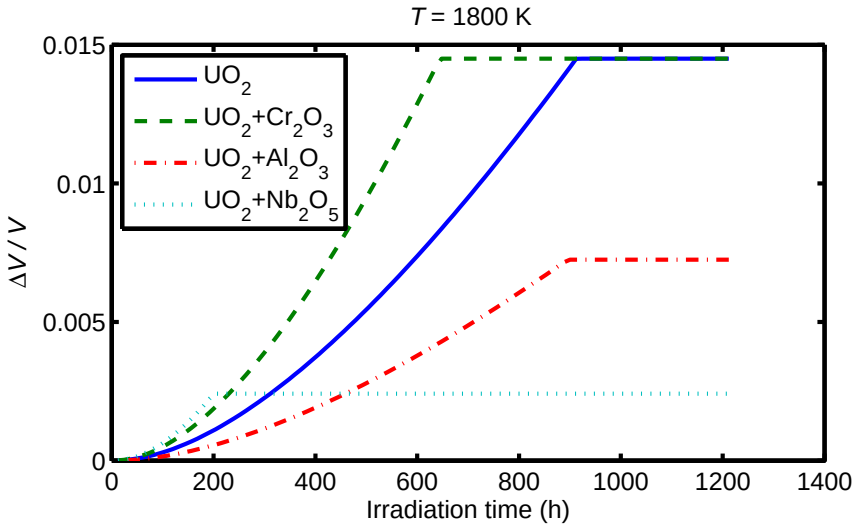

Figure 54: Calculated relative increase in fuel volume versus time for different UO_2-base fuels at a constant temperature of 1800 K, using the gaseous swelling model in [239].

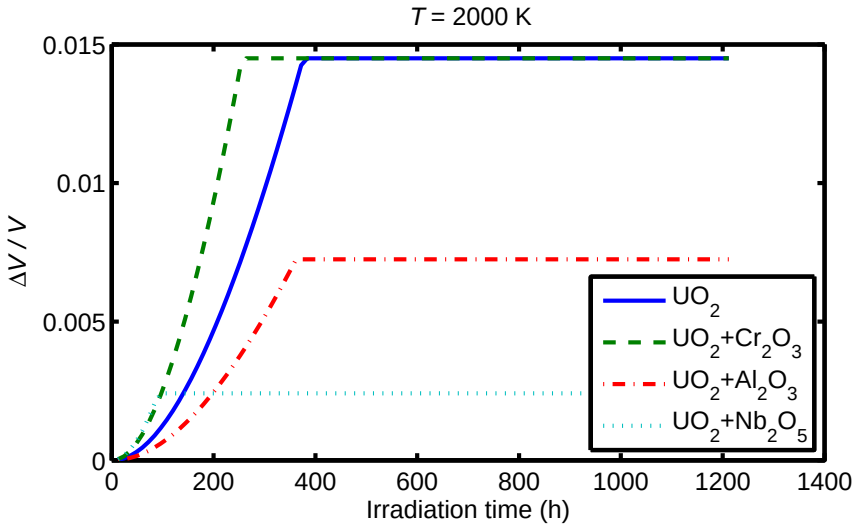

Figure 55: Calculated relative increase in fuel volume versus time for different UO_2-base fuels at a constant temperature of 2000 K, using the gaseous swelling model in [239].

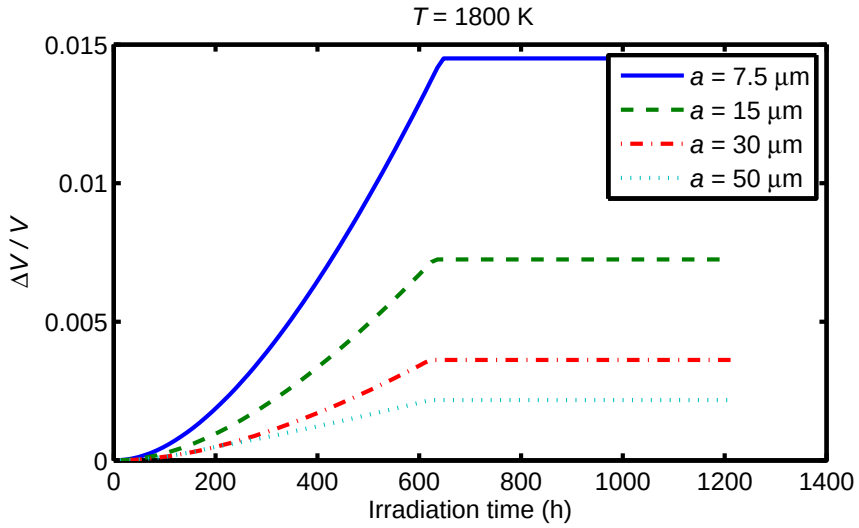

Figure 56: Calculated relative increase in fuel volume versus time for a Cr_2O_3-doped UO_2 sample at a constant temperature of 1800 K for several grain radii, using the gaseous swelling model in [239].

4.3 Discussion

4.3.1 Gas release and fuel swelling

Let us briefly draw attention to some experimental results regarding the effects of additives and grain size on UO_2 fuel FGR and swelling behavior. In a 1980 paper, Sawbridge et al. [240] report the performance of fuel from an experiment, which was loaded into the Windscale experimental AGR (advanced gas-cooled reactor) in the UK in February 1970, aimed to assess the effects of magnesia (MgO) additions to UO_2 and grain size on fission product release. The fuel elements (assemblies) were discharged unfailed after 1840 effective full power days or EFPD, where the doped fuel pellets had attained burnups between 24.5 and 28.5 MWd/kgU. The details of the fuel rod design, material characteristics and irradiation history are described in [240]. Two fuel elements contained standard UO_2 fuel and two others contained three pins (rods) of experimental fuel doped with 5 mol% MgO, sintered to a density of 10.25 g/cm^3 with a mean linear intercept grain size of about 35 μm. Pre-irradiation measurements suggested that ≈ 0.8 mol% of the MgO was in solid solution in UO_2 with the remainder present as intra- and inter-granular precipitates. The remaining pins contained 97% dense UO_2 with a grain size of about 4 μm (reference design). A number of conclusions could be drawn from this study:

(i) Post-irradiation examination of fuel pins containing large grain sized UO_2 pellets doped with magnesia and irradiated in the AGR showed that the FGR in the pins containing doped fuel was reduced by a factor of > 2.5 compared with "pure" UO_2 irradiated under identical conditions. (ii) Micro-gamma scanning indicated that there was a much greater retention of ^{137}Cs in MgO-doped fuel than in UO_2 irradiated under identical conditions. (iii) Computer modeling, assuming identical fission gas diffusivity for MgO-doped and UO_2 fuel, suggested that the improvement in gas release was largely due to differences in grain size. Recall that Kashibe-Une's 1998 experiment [11], see table 12, indicated roughly the same ^{133}Xe diffusivity in their MgO-doped and pure UO_2 samples. (iv) No inter-granular gas

bubbles were observed in the doped fuel, but in the high temperature regions, a high density of large intra-granular bubbles, ≈ 0.2 μm in diameter, was observed. Sawbridge and company suggested that these large bubbles were stabilized by interaction with the MgO precipitates.

In a related investigation, Killeen in 1994 reported [21] on a series of post-irradiation anneal tests, which had been carried out on fuels taken from an experimental stringer (fuel assembly) from the Hinkley Point B AGR. The stringer was part of an in-reactor study on the effect of large grain size fuel. Three different fuel types were present in separate pins in the stringer. One variant of large grain size fuel had been fabricated by using an MgO dopant in UO_2 with a fuel density of 10.54 g/cm^3, a second variant was fabricated by high temperature sintering of standard fuel, with a density of 10.76 g/cm^3, and the third was a reference UO_2 fuel, with 12 μm grain size and a density of 10.65 g/cm^3. Both large grain size variants had similar grain sizes, i.e. around 35 μm. The experimenters took fuel specimens from highly rated pins from the stringer with local burnups in excess of 25 MWd/kgU and annealed them to temperatures of up to 1810 K under reducing conditions to allow a comparison of fission gas behavior at high release levels. The results showed the favorable effect of large grain size on release rate of ^{85}Kr following gas bubble interlinkage. At low temperatures and release rates, there was no difference between the fuel types, but at temperatures in excess of 1673 K, the release rate was found to be inversely dependent on the fuel grain size. The experiments showed some differences between the doped and undoped large grains size fuel, such that in the former, the gas bubbles were interlinked at a lower temperature than in the latter fuel, thereby releasing fission gas at an increased rate at that temperature. At higher temperatures, the grain size effect was dominant. The temperature dependence for FGR was determined over a narrow range of temperature and found to be similar for all the three types; for both bubble pre-interlinkage and post-interlinkage releases. The difference between the release rates is then seen to be controlled by grain size. Both Killeen's and Sawbridge et al's results are in qualitative agreement with our analysis.

Finally, it is worth mentioning the 1993 work of Une and coworkers [5], who investigated fission gas behavior of UO_2 fuel pellets with controlled microstructure, irradiated to 23 MWd/kgU in the Halden boiling water test reactor in Norway, by using a post-irradiation annealing experiment. Four types of fuel pellets with or without additives were examined: (i) undoped standard grain size, (ii) undoped large grained, (iii) Nb_2O_5-doped large grained, and (iv) TiO_2-doped large grained fuels. The fuel rods tested by Une et al. had a conventional BWR design. The basic data for the fuel pellets are listed in table 13. The annealing was performed at 1873 or 2073 K for 5 h in reducing or oxidizing atmospheres.

Fission gas release and bubble swelling caused by the high temperature annealing for the two undoped fuels were reduced to about 1/3-1/2 by increasing the grain size from 16 to 43 μm, which roughly corresponded to the ratio of their respective grain size. On the contrary, the performance of the two large grained fuels doped with Nb_2O_5 or TiO_2 was roughly equivalent to, or rather inferior to that of the standard fuel, despite their large grain sizes of 110 and 85 μm. This may be attributed partly to a much higher diffusivity of fission gases in these doped fuels at high temperatures as noted in section 4.1, see figure 45. The fission gas behavior of undoped fuels was aggravated by increasing the chemical potential of oxygen in the annealing atmosphere, while that of additive doped fuels did not depend on it. Une and coworkers found that the diffusivities of undoped large grained and standard

fuels were enhanced by about three and one orders of magnitude, respectively, by changing the annealing atmosphere from reducing to oxidizing. They observed that for undoped fuels, intergranular bubble swelling was predominant, while for additive doped fuels, both coarsened inter- and intragranular bubbles contributed to larger swelling. Une et al.'s results on FGR and bubble swelling for microstructure controlled UO_2-base fuels indicate a close relationship between gas diffusion and cation vacancy diffusion [5].

Table 13: Fuel pellet data in Une et al.'s 1993 study [5].

Fuel type	Additive conc.	Grain size	Density	Pellet Ø
-	wt%	μm	g/cm^3	mm
Undoped standard	...	16	10.6	10.35
Undoped large grain	...	43	10.5	10.35
Nb_2O_5-doped	0.7	110	10.8	10.35
TiO_2-doped	0.2	85	10.8	10.35

Some words of explanation regarding our sample computations on grain boundary bubble swelling (sec. 4.2.2) are in order here. Our computations showed that both swelling rate and the threshold for swelling saturation, which is intimately related to the onset of FGR, are reciprocal functions of the grain size, using the model described in [239]. Regarding the latter quantity, the model gives the swelling saturation by

$$\left(\frac{\Delta V}{V}\right)_{\rm gs} = B_g f_{\rm b} \frac{r_{\rm bs}}{2a}, \tag{26}$$

where B_g is a gas bubble geometry factor, $f_{\rm b}$ is the fractional coverage of grain boundary by the bubbles, $r_{\rm bs}$ is the bubble radius at the onset of interlinkage, and a is the mean grain radius. In the parametric computations in section 4.2.2, we kept all these parameters except the grain radius constant. If, for that matter, $r_{\rm bs}$ is related somehow to the fuel grain size, then that empirical correlation is unknown to us. Computations presented in section 4.2.2 should be regarded as a parametric study to accentuate the influence of grain size on FGR and bubble swelling which, however, seem to conform, in general, with experimental results reported in the literature. Our analysis of gaseous swelling does not include the contribution of intragranular bubbles, which may become important in case of large grain fuel.

The effect of doping UO_2 on its crystal defect structure and its consequent impact on fission gas behavior has been discussed sporadically in the literature [2, 11, 22, 225, 241]. The conventional understanding is that, in general, adding dopants such as Nb_2O_5 should lead to hyperstoichiometric fuel UO_{2+x}, i.e. produce uranium vacancies, while adding trivalent dopants such as Cr_2O_3 or Gd_2O_3 can produce oxygen vacancies, and hence, hypostoichiometric fuel UO_{2-x}. It has also been known for a long time, based on the work of Miekeley and Felix [222], that xenon diffusivity in UO_{2+x} is much higher than in UO_2 and vice versa in UO_{2-x}. The schematic picture shown in figure 57 illustrates this effect as a log-log plot of fission gas diffusivity versus the fission density (fission/m^3). The reduction in diffusivity is attributed to the presence of the Frenkel defects (oxygen vacancy-interstitial pairs) and Schottky trivacancies (a cation vacancy and two anion vacancies) [242], which may act as traps to fission product gases [22]. Thus, it is expected that dopant concentration would affect the O/M ratio and that in turn influence the gas diffusivity [224, 243, 244].

The fission gas release rate is roughly proportional to the square root of gas diffusivity $\propto \sqrt{D}$ and inversely to the fuel grain size $\propto 1/d_g$. It has been known that xenon dif-

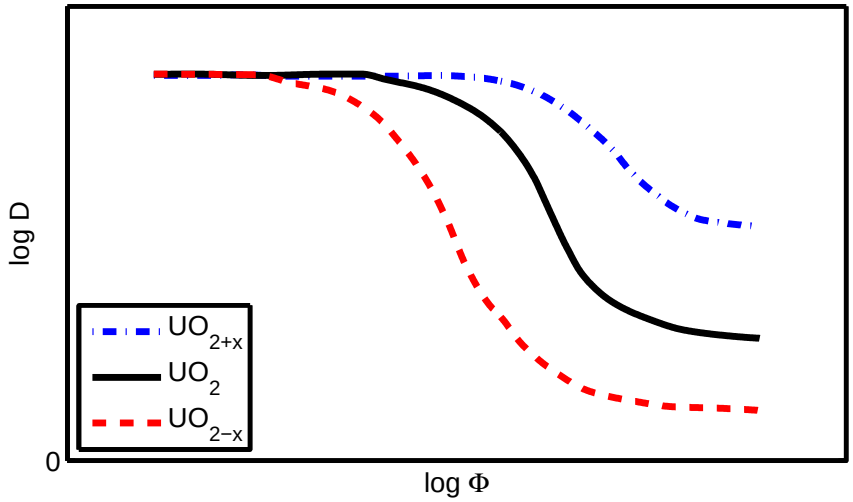

Figure 57: Schematic dependence of gas diffusivity D versus fission density (dose) Φ on the O/U-ratio at constant temperature; after Matzke [22].

fusivities in UO_2 and (Gd,U)O_2 are markedly lower in hypostoichiometric regime than in hyperstoichiometric regime [88, 222, 241] or in stoichiometric UO_2. So hypostoichiometric (Gd,U)O_2 fuel may experience lower fission gas release rate than hyperstoichiometric (Gd,U)O_2 or UO_2, even if it has a smaller grain size than the latter fuels, as noted in [88]. In the hypostoichiometric regime, the xenon atoms are considered to get trapped in the Schottky defects [242], thereby reducing the effective gas diffusivity. In hyperstoichiometry, however, the cation vacancies enhance the diffusivity of xenon in UO_{2+x} [243].

4.3.2 Doping factors on gas diffusivity

Recently, in a rich-in-content paper, Cooper and colleagues [245] have used a thermochemical method to study the oxygen chemical potential of stoichiometric UO_2 doped with 1000 wppm Cr_2O_3. Their analysis indicates that the oxygen chemical potential in the fuel is controlled by the Cr-Cr_2O_3 two–phase equilibrium below 2500 K. Based on this finding or understanding, the authors of [245] employ a method, referred to as free energy cluster dynamics, to compute the concentrations and time evolution of defects in the UO_2 system during irradiation. The method solves a set of ordinary differential (kinetic) equations that simulate a number of phenomena, comprising: production of Frenkel pairs through irradiation, mutual recombination of Frenkel pairs, interaction with sinks, and clustering of point defects. The point defect energies computed by a density functional theory (DFT) program were used within the cluster dynamics simulations to calibrate and reproduce the oxygen potential of stoichiometric UO_2 reported in the literature.

The data generated with this method were used to compute both the intrinsic diffusivity (D_1) and the irradiation enhanced thermal fission gas (Xe) diffusivity (D_2) in UO_2 fuel. Furthermore, the impact of 1000 wppm Cr_2O_3 on these quantities was evaluated [245]. However, the authors of [245] note that here are a number of uncertainties in the model relating to the kinetics of defect production and annihilation, and those emanating from the DFT computation. So, in order to examine the impact of these uncertainties on the fission gas diffusivity, the authors in [245] considered two cases: one in which minimal

changes were made to the enduring DFT data, designated as Case A, and another where the possibility that DFT overestimates the migration barrier of uranium vacancies (Case B). The two cases assume different values for the migration energy of uranium vacancy and the source and sink strengths that appear in the kinetic equation [245].

Using the cluster dynamics model, the authors [245] calculated Xe diffusivity in doped and undoped UO_2 for both the intrinsic and irradiation-enhanced regimes. The results indicate that the diffusivity of Cr_2O_3-doped UO_2 is increased markedly in the respective regimes as a result of higher concentrations of uranium and oxygen vacancies. Thereafter, they fitted the cluster dynamics diffusivity data for doped and undoped UO_2 to an exponential type (Arrhenius) function to obtain two diffusivity doping factors for D_1 and D_2, respectively, namely, $D_1^{\text{doped}} = f_1 D_1^{\text{undoped}}$ and $D_2^{\text{doped}} = f_2 D_2^{\text{undoped}}$ with[10]

$$f_i = e^{-q_i(1/T - 1/T_i)}, \quad i = 1, 2. \tag{27}$$

The obtained values for the constants q_i and T_i are given below; cf. table 3 in [245].

Parameter	Case A	Case B
$T_1 = T_2$ (K)	1773	1773
q_1 (K)	3711	3809
q_2 (K)	-3882	-8121

In figure 58, we have plotted the relations in (27) as a function of temperature in the range $1200 \leq T \leq 2000$ K for illustration. As can be seen from figure 58(a), f_1 is an increasing function of temperature, albeit $f_1 \leq 1$ up to $T = T_1 = 1773$ K. Meaning that, it suppresses the undoped D_1 up to this temperature. Moreover, the values of f_1 for cases A an B remain very close in the temperature range of interest. On the other hand f_2, figure 58(b), is a decreasing function of temperature with $f_2 \geq 1$ for up to $T = T_2 = 1773$ K, which enhances D_2 up to this temperature. In addition, the f_2 values for cases A and B differ appreciably at lower temperatures, say $T < 1600$ K. Cooper et al. [245] do not specify upper temperature limits for the applicability of equation (27), which we may put at $T = T_i = 1773$ K when $f_i = 1$. The difference resulting from Case A and Case B may be considered as the uncertainty emanating from the analysis of fission gas diffusivity in the doped UO_2.

In figure 59, we have plotted the result of applying the factor f_1 to the undoped UO_2 Davies-Long fission gas diffusivity (table 12 [229]); shown by a green dash-dot line in the figure. The figure also includes plots of gas diffusivity for the undoped UO_2 and that for the 0.065 wt% Cr_2O_3 doped UO_2 based on the Kashibe-Une measurements [11].

We should note that the obtained diffusion doping factors in [245] do not include any concentration dependent term, thereby, they are applicable to UO_2 fuel containing around 1000 wppm Cr_2O_3, with a large uncertainty in the irradiation-enhanced part f_2.

4.4 Case of BA fuel

As mentioned earlier, hypostoichiometric (Gd,U)O_{2-x} fuel may experience lower fission gas release rate than hyperstoichiometric (Gd,U)O_{2+x} or UO_2, even if it has a smaller grain size than the latter fuels [88]. There are very few analytical studies regarding fission gas release behavior of (U,Gd)O_2 fuel reported in the literature.

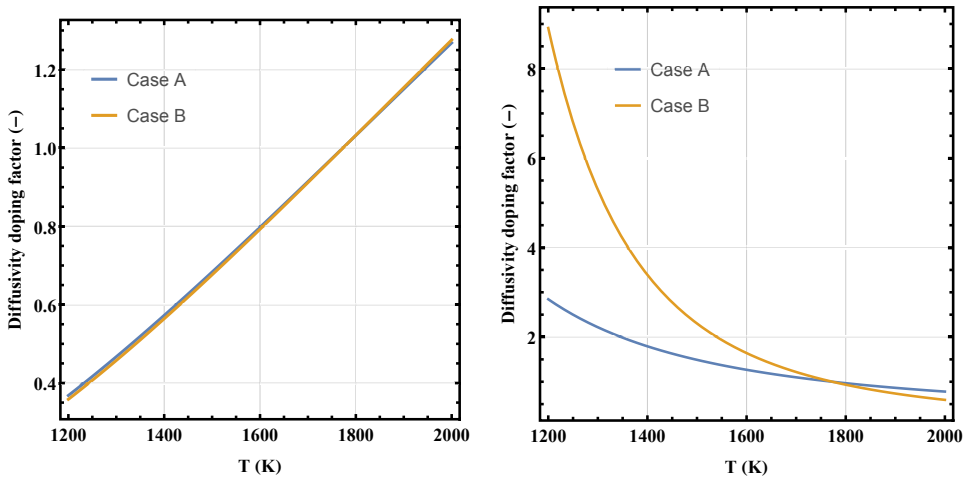

Figure 58: Diffusivity doping factors as defined by equation (27) versus temperature: (a) Factor f_1 for the intrinsic gas diffusivity D_1, (b) Factor f_2 for the irradiation enhanced thermal gas diffusivity D_2.

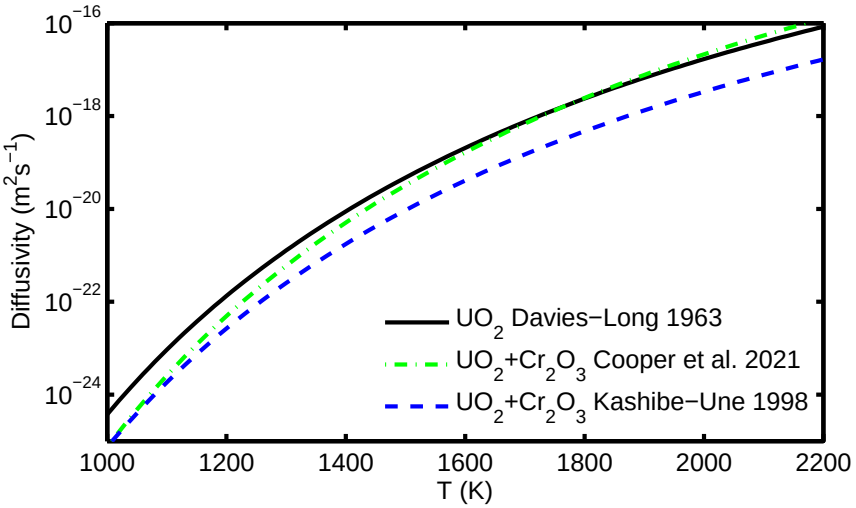

Figure 59: Comparison between the intrinsic diffusion coefficients suggested for fission gas in UO_2 and UO_2+Cr_2O_3 fuels, where the legend is explained in the text.

Some years ago, in a North European reactor fuel technology and utilization program [246], studies were made on fission gas release of such fuel which, due to its lower thermal conductivity, operates at a higher temperature than UO_2 rods at the same power. By increasing the fuel bundle average enrichment (^{235}U concentration) to achieve higher fuel burnup, the number of (U,Gd)O_2 fuel rods was increased to maintain the reactor shutdown margin.[11] Accordingly, there was a potential peaking factor penalty associated with maintaining both the power and ^{235}U enrichment low for (U,Gd)O_2 fuel rods rods.

In this program, fuel rods with relatively high gadolinia concentrations (5 wt%) at moderate burnup were thus examined non-destructively at the site pool and destructively in hot cells. The rods in 8×8 type fuel assembly were taken from a Swedish BWR, which operated in 18-month cycles with Gd-doped UO_2 and operating at relatively high powers. Two rods with about 30 MWd/kgU burnup were examined, and later, two rods with rod average exposure of 43 MWd/kgU, corresponding to 50 MWd/kgU for some UO_2 rods in the assembly, were examined. The highest fission gas release fraction measured was 8% [246].

By means of axial and radial gamma scanning on a thin sliced piece of fuel, it was confirmed that Gd-doped UO_2 pellets did in fact retain mobile fission products better than UO_2 fuel, although the Gd-doped pellet had operated at a higher temperature [246]. Figure 60, taken from [246], shows gamma scanning curves for different characteristic gamma energies typical for one mobile fission product nuclide, ^{137}Cs, and one immobile nuclide, ^{106}Ru. The sample fuel was taken from a piece of a fuel rod with axial grading of gadolinia, meaning that Gd-doped UO_2 pellets and undoped UO_2 pellets were mixed but had the same ^{235}U enrichment, i.e. experienced similar power histories after the first year of reactor operation. As can be seen from figure 60, less fission product migration took place in the Gd-doped pellet. Because gas release from the central regions of the pellets is known to be equal for volatile fission products, such as cesium, and for fission product gases, the behavior illustrated here should also be true for fission gas release [246]. For an introduction to non-destructive methods, based on high-resolution gamma-ray spectroscopy, relating to fission gas release, see [247].

In order to compare the fission gas release behavior of Gd-doped UO_2 fuel rods with undoped UO_2 fuel rods as a function of burnup, the authors of [246] provide such data in a figure, which we have reproduced here. Figure 61 shows measured fission gas release versus rod average burnup for fuel rods operated in BWRs in Sweden and Finland. The crosses indicate BA fuel, i.e. Gd-doped UO_2 rods (12 of them) and the pressures in the legend refer to the backfill helium pressures of the rods at room temperature.

The impact of Gd-doping of UO_2 on fission gas release during irradiation was also appraised in [80] by calculations with respect to measurements. In [80], the fission gas diffusivity was suppressed with temperature and Gd_2O_3 concentration (to compensate for higher fuel pellet temperatures experienced by this kind of fuel as compared to the undoped UO_2 if subjected to similar power history) to obtain agreeable results with fission gas release measurements of rods irradiated up to about 42 MWd/kgU in BWRs. However, the formulation of the diffusivity suppression factor in [80] is somewhat awkward or at least ad hoc with little materials physics justification. Perhaps a more appropriate formulation, i.e. for

$D^{\text{doped}} = fD^{\text{undoped}}$, would be

$$f = \frac{1}{1 - ax(1 - \exp(E/T)} \tag{28}$$

where x is the gadolinia concentration and a and E are some positive constants to be adjusted by measurements. This can be a type of formula for accounting the Gd-induced fission gas traps, e.g. vacancy clusters, that may affect fission gas release.

Finally, we should mention some results from the work of Hirai et al. [241] regarding fission gas diffusivity in UO_2 and (U,Gd)O_2 fuels. These workers, *inter alia*, examined the oxygen-to-metal ratio dependance of diffusion coefficient at 1673 K for these fuels. Figure 62 shows these results for three kinds of specimen, table 14. Below the stoichiometric composition, the diffusion coefficient decreases only slightly, but increases sharply with increasing O/M above and near stoichiometry. The decrease in the diffusivity for their G81 specimens is hardly visible from figure 62 due to the log scale of the ordinate. Indeed, the decrease in diffusivity in G81 from about O/M = 2.00 to O/M = 1.99 is 1.78×10^{-19} to 1.45×10^{-19} m^2/s, respectively.

Table 14: Fuel data in Hirai et al.'s study [241].

Parameter	Unit	G01	G41	G81
Gd_2O_3 content	wt%	0	4	8
Sintered density	%TD	96.2	96.1	96.1
Grain size	μm	31	29	38
Nominal O/M ratio	-	2.004	1.992	1.996

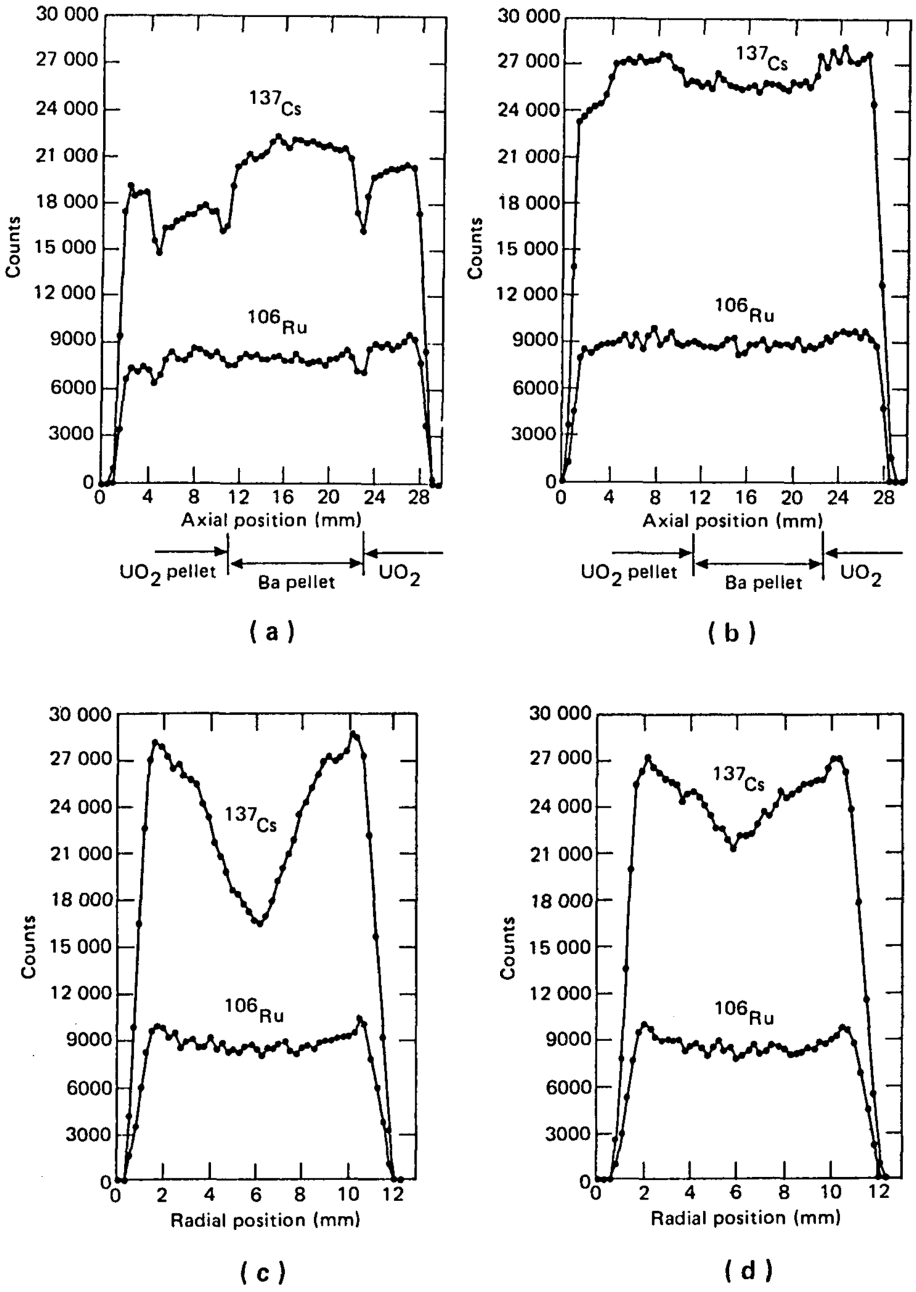

Figure 60: Microgamma scanning of a sliced piece of BA (U,Gd)O_y fuel rod showing: (a) Axial γ-scan fuel center, (b) Axial γ-scan fuel periphery, (c) Radial γ-scan UO_2 fuel pellet, (d) Radial γ-scan 5 wt% gadolina doped UO_2; from Andersson et al. [246].

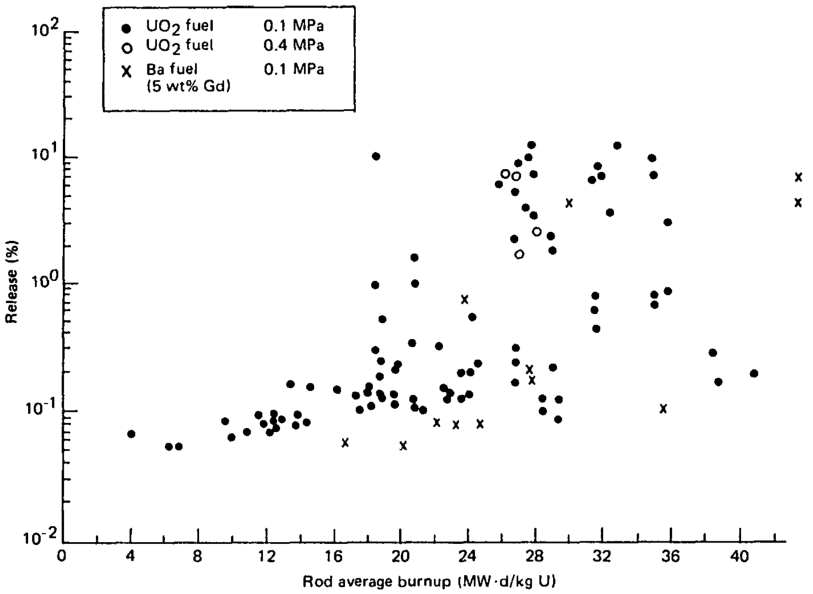

Figure 61: Measured fission gas release fraction (%) versus rod burnup (MWd/kgU) for fuel rods irradiated in commercial boiling water reactors in North Europe; from Andersson et al. [246].

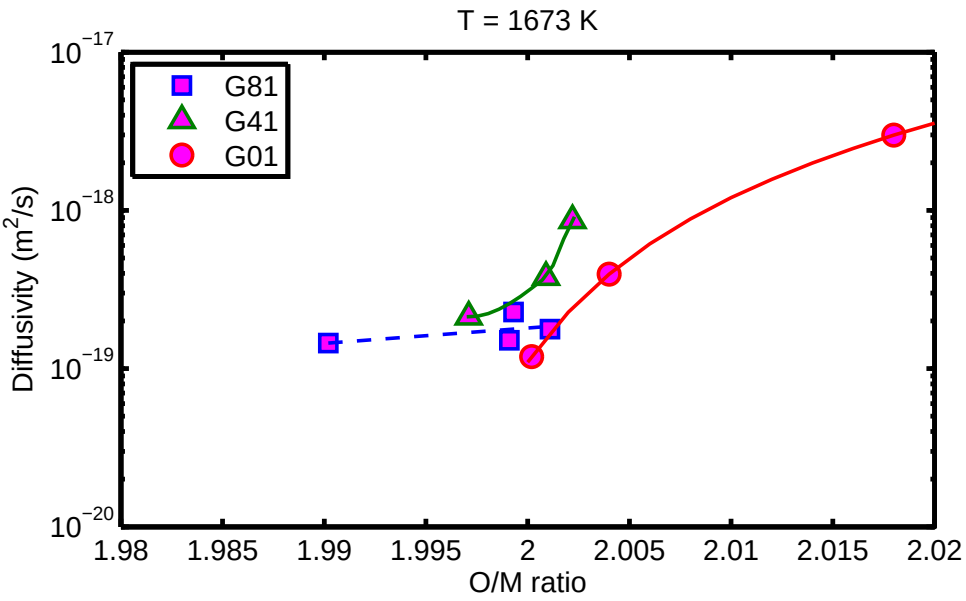

Figure 62: Oxygen-to-metal ratio (O/M) dependence of fission gas diffusivity in (U,Gd)O_2 fuel specimens (table 14), read off from figure 19 of Hirai et al. [241].

5 Mechanical properties

Doping of UO_2 fuel to improve its pellet-cladding interaction (PCI) resistance during reactor operation through enhanced fuel plasticity has been discussed in the literature over the years [8, 248]. In this section, we first provide a brief survey of the literature regarding the effect of additives on the thermal creep rate of UO_2 fuel and its yield strength/stress.[12] Next, results of modeling the creep deformation of Nb_2O_5- and Cr_2O_3-doped UO_2 are presented against experimental data. A detailed description of the model is reported elsewhere [61]. Finally, some basic mechanical properties of composite UO_2 fuels with enhanced thermal conductivity are surveyed in this section.

5.1 Fuel creep studies

A noted work among the early thermal creep studies is the 1981 paper of Sawbridge and coworkers [248], who investigated the creep of UO_2 fuel doped with Nb_2O_5. They investigated the creep of UO_2 containing small additions of Nb_2O_5 in the stress range 0.5-90 MPa at temperatures between 1422 and 1573 K in the Berkeley Nuclear Laboratories, Berkeley, UK. Compression creep tests were carried out under a constant load in atmosphere of flowing purified argon. Sawbridge et al. reported data on the creep rate of seven dopant concentrations from 0.2 mol% to 1.0 mol% Nb_2O_5. The samples examined had different mean (linear intercept) grain sizes, depicted in figure 63.

At high stresses, Sawbridge et al. found a strong dependence of creep rate on stress, typical of dislocation-controlled creep. At lower stresses (< 70 MPa), a roughly linear dependence was observed, typical of diffusion creep. It is the lower stress regions, typified by a linear stress dependence, that are the most significant creep modes under normal reactor operating conditions. Sawbridge et al. established that in all the specimens, the secondary creep rate could be represented by the equation of the form

$$\dot{\epsilon} = A\sigma^n \exp(-\frac{Q}{RT}), \tag{29}$$

where $\dot{\epsilon}$ is the steady state creep strain rate, σ the uniaxial stress, Q the activation energy, and A and n are constants for each material, and RT has its usual meaning. Sawbridge and colleagues observed that Nb_2O_5 additions can cause a dramatic increase in the steady state creep rate as long as the niobium ion is maintained in the Nb^{5+} valence state. Material containing 0.4 mol% Nb_2O_5 crept three orders of magnitude faster than the "pure" UO_2 material.

Figure 64 shows the variation of creep rate with Nb_2O_5 content, at $T = 1523$ K and $\sigma = 20$ MPa. As can be seen, the variation of creep rate with composition is not smooth. The main reason for this is that the grain size of the different batches of material is not constant, cf. figure 63. To normalize the creep rates, Sawbridge et al. plotted the data versus a quantity that they named grain size compensated viscosity, η/d_g^2, against Nb_2O_5 concentration. This smoothened the data somewhat, however, we could not reproduce it. The η/d_g^2 term arises, because it was noted that diffusional creep rate varies as the reciprocal square of the grain size d_g, which is in accordance to the Nabarro-Herring creep law [47], namely $\dot{\epsilon} \propto \sigma D_v/d_g^2$, where D_v is the uranium volume diffusivity related to the diffusivity of uranium vacancy

D_{U} and its concentration U_v, $D_v \sim D_{\mathrm{U}}\mathrm{U}_v$. The viscosity of a solid is defined as the reciprocal of the shear rate per unit shear stress. In the present case of uniaxial stress, we have $\eta \equiv \sigma/\dot{\epsilon}$.

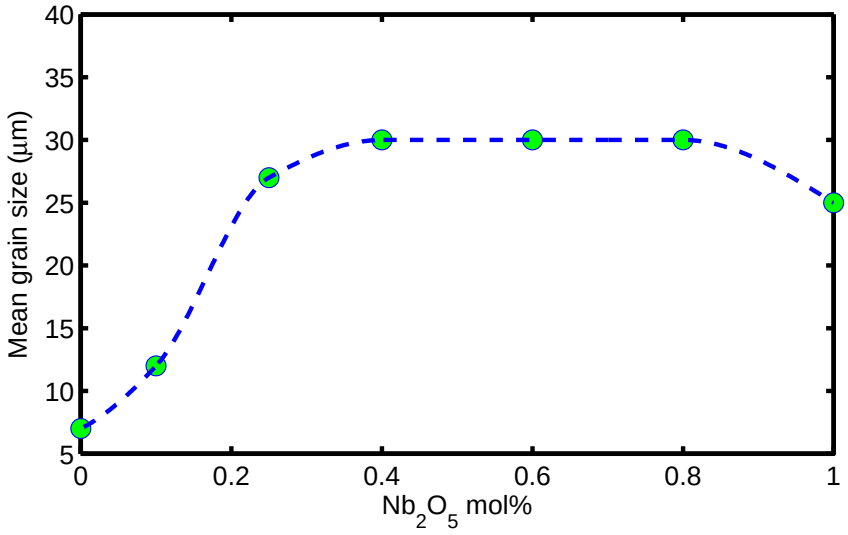

Figure 63: UO_2 fuel grain size versus Nb_2O_5 concentration in samples tested by Sawbridge et al. [248].

Instead of depicting the logarithm of fuel viscosity as a function of Nb_2O_5 concentration à la Sawbridge and co., we have scaled the creep data with d_g^2/σ and plotted the results in figure 65. To analyze further, we have considered a model outlined in [248], which utilizes the Nabarro-Herring creep model with the uranium volume diffusivity. In more detail, $D_v = D_{\mathrm{U}}U_v$, where D_{U} is the diffusion coefficient for uranium vacancies and U_v is the uranium vacancy concentration, the latter depending on the concentration (mole fraction) of dopant Nb_2O_5, here denoted by x. Sawbridge et al. derived the following relations for the thermal creep rate of Nb_2O_5-doped UO_2

$$\dot{\epsilon} = A\frac{\sigma}{d_g^2}\exp\Big(-\frac{Q_u + E_2 - E_1}{RT}\Big), \quad \text{as} \quad x \to 0, \tag{30}$$

$$\dot{\epsilon} = A\frac{\sigma x^2}{d_g^2}\exp\Big(-\frac{Q_u + E_2 - 2E_1}{RT}\Big), \ \text{for} \quad x > 0, \tag{31}$$

where Q_u is the activation energy for the diffusivity of uranium vacancies, and E_1 and E_2 are the formation energies of the Frenkel and Schottky defects, respectively. A more complete derivation is given elsewhere [61].

Unfortunately, the authors of [248] do not provide numerical values for the aforementioned energy parameters; hence, we could not use relation (31) faithfully to evaluate the creep rate data presented in figure 64. Nevertheless, we have attempted to fit the data to a relation in the form $\mathscr{S} \equiv \dot{\epsilon}d_g^2/\sigma$ versus x^2, which may be sensible at $T = 1523$ K and $\sigma = 20$ MPa. The result $\mathscr{S} = 6.65x^2$, where $\mathscr{S}$ has units of [μm^2/MPa·s], is plotted as a dashed line (Nabarro-Herring fit) along the measured data as a function of Nb_2O_5 content in figure 65. *N.B.*: Here x is in mole fraction, whereas in the figure $\mathscr{S}$ versus mol% is displayed.

The results in figure 65 clearly show that the Nabarro-Herring fit is quite proper for up to 0.5 mol% Nb_2O_5, but it overestimates the measurements for higher concentrations of Nb_2O_5.

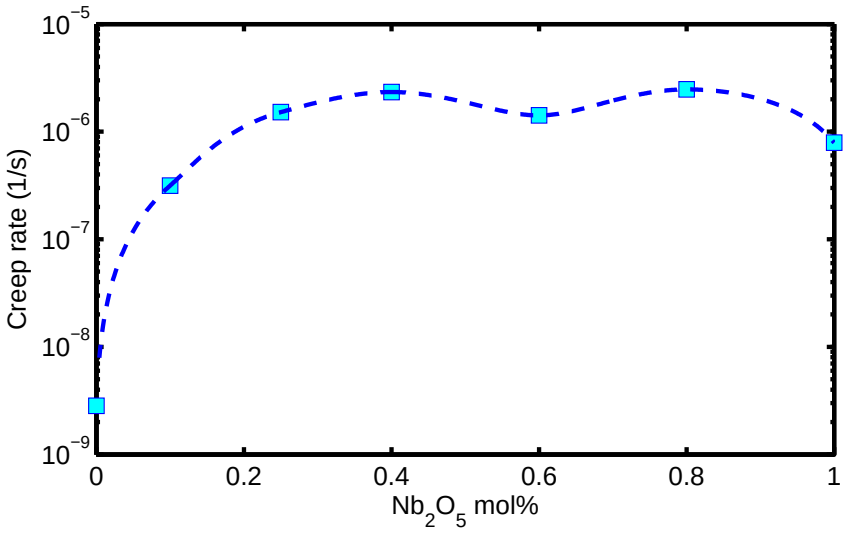

Figure 64: Thermal creep rate of UO_2-base fuel versus Nb_2O_5 concentration at 1523 K and normalized stress of 20 MPa; adapted from Sawbridge et al. [248].

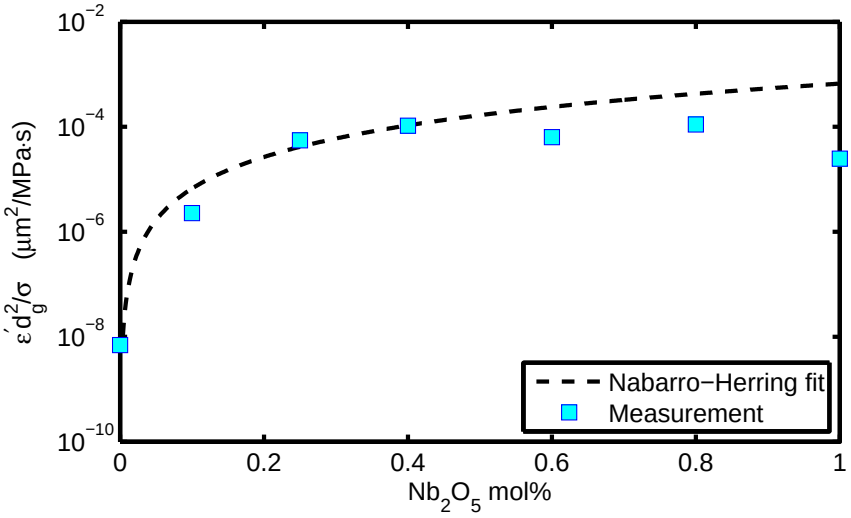

Figure 65: Scaled creep rate of UO_2, with square of grain size divided by stress (20 MPa), versus Nb_2O_5 concentration at 1523 K, based on the data in figs. 63-64.

Likewise, computation made on (logarithm of) fuel viscosity versus x by Sawbridge et al., which is presented in their figure 11 [248], indicates a similar trend.

The main conclusions of Sawbridge et al.'s paper [248] are as follows:

- In the stress range applicable to normal reactor operation, UO_2 doped with Nb_2O_5 deforms by a diffusional creep mechanism (Nabarro-Herring), and the creep rate is linearly proportional to the applied stress.
- The addition of Nb_2O_5 leads to a sharp increase in the creep rate of UO_2. This is credited to the suppression of the U^{5+} ion concentration and the modification of the crystal defect structure by the addition of Nb^{5+} ions.
- The Nb^{5+} ion can be rapidly reduced in atmospheres with a low partial molar free energy of oxygen. When this occurred by switching the test atmosphere from argon to dry hydrogen, the creep rate was reverted to that of undoped uranium dioxide.

Another relevant work on the subject detailed here is Dugay et al.'s study [249, 250] on the influence of the dopants Cr_2O_3 and Al_2O_3 on the thermal creep behavior of UO_2 and its yield (flow) stress. Here, their work on Cr_2O_3 dopant is assessed. They tested five batches of PWR-geometry fuel pellets, without dishing. One undoped batch, serving as a reference material, and four doped batches with Cr_2O_3 concentrations ranging from 0.025 to 0.2 wt% in UO_2 were prepared for testing. The mixture of powders was dry blended by ball-milling. The mixture was then sintered under H_2+1.7%H_2O atmosphere at 1700°C, thereby restricting the hyperstoichiometric range of UO_{2+x} to $x = x_{\max} = 5 \times 10^{-4}$, which promoted grain growth. The basic characteristics of the sintered materials are listed in table 15. Grain size was determined by linear intercept measurements.

Table 15: Dugay et al. UO_2-Cr_2O_3 fuel material data [250].

Cr_2O_3 conc. wt%	Fraction of T.D. -	Density[a] g/cm^3	Grain size μm
0.0	0.968	10.62	7
0.025	0.958	10.51	15
0.06	0.970	10.64	27
0.1	0.975	10.70	45
0.2	0.976	10.71	70

[a] UO_2 theoretical density (T.D.) of 10.97 g/cm^3 is used.

Dugay et al. [249, 250] conducted two kinds of tests in a CEA laboratory in Grenoble, France, namely, (i) compression tests under a constant applied strain rate, from which the stress versus strain curves were produced beyond the yield point, and (ii) compression creep tests, in which the strain rate as a function of stress level was determined.

The constant strain rate compression tests were done at 1773 K under argon gas with 4% hydrogen to maintain the stoichiometry of the specimens during the experiment. The tests were conducted at a crosshead speed of 20 μm/min. corresponding to a strain rate of 0.09/h. The stress-strain curves presented in [249, 250] show that Cr_2O_3 additions cause a decrease in the yield stress from about 85 MPa (undoped UO_2 specimen) to 70 MPa (0.1 wt% Cr_2O_3) at 1773 K. However, when the doped specimens (with 0.06 wt% Cr_2O_3) were reduced in hydrogen atmosphere at 1773 K for 12 h or 24 h, their stress-strain curves exhibited peaks

close to that of the yield stress of undoped UO_2 (≈ 85 MPa), especially the specimen that was reduced for 24 h in hydrogen; see refs. [249, 250] for more details.

All the creep tests were done by compression under argon or reducing (hydrogenated argon) milieu, comprising temperatures 1623-1923 K on unirradiated specimens. In particular, measurements of creep rate were made at 1773 K subject to applied stresses varying from 20 to 70 MPa. The Grenoble workers found that Cr_2O_3 additions starkly increase the creep rate relative to that of pure UO_2 in argon atmosphere. All the doped specimens were assumed to follow equation (29) with varying stress exponent n, which varied from 4.9 to 6.3, in contrast to the Sawbridge et al.'s measurements on Nb_2O_5-doped UO_2, which exhibited $n \approx 1$ dependence. In table 16, we have listed the creep parameters given in [250], which the authors apparently have taken from the 1773 K data. Moreover, we have included in this table the values of the creep model parameter A that we deduced from the creep-rate data presented in [250] at 1773 K and 45 MPa. We have also narrowed the stress range of applicability for the doped specimens compared to [250], which is ranged from 30-65 MPa, based on our own evaluation of data. Dugay et al. [250] also state that doping UO_2 with Al_2O_3 would lead to similar observations.

Table 16: UO_2-Cr_2O_3 creep model[a] parameters at 1773 K from [250].

Cr_2O_3 conc.	Stress range	A^b	n	Q
wt%	MPa	$(\text{MPa})^{-n}\text{s}^{-1}$	-	kJ/mol
0.0	20-45	1.176×10^{2}	2.1	410
0.025	40-65	9.129×10^{-3}	6.3	487
0.06	40-65	5.919×10^{-3}	6.1	466
0.1	40-65	3.625×10^{2}	4.9	551
0.2	40-65	1.236×10^{2}	5.2	550

[a] $\dot{\epsilon} = A\sigma^n \exp(-Q/RT)$; [b] Values are determined from measured data at $\sigma = 45$ MPa.

The parameters in table 16 are used to plot creep strain rate as a function of Cr_2O_3 concentration in UO_2 at high temperatures at 45 MPa, figure 66. It is seen that, for example at 1773 K, the creep rate of UO_2-0.1wt%Cr_2O_3 increases roughly by a factor of 5 relative to that of pure UO_2. For pure UO_2, Dugay et al. [250] found that in the stress range 45-60 MPa, $n = 4.8$. Hence, there is a shift in creep mechanism around 45 MPa at 1773 K from $n \approx 2$ to $n \approx 5$. This result is somewhat in agreement with the 1970 work of Langdon on creep mechanisms in pure UO_2 [251], which showed a transition stress of about 40 MPa at 1808 K, at which the stress exponent changed from $n \approx 1$ to $n \approx 4.5$. To compare these results with the thermal creep behavior of niobia-doped UO_2, we should mention the work of Ainscough et al. [7], which showed a transition stress of 20 MPa at 1773 K and an oxygen potential of -423 kJ/mol, where the creep rate stress exponent for UO_2-0.4wt%Nb_2O_5 changed from $n = 1.1$ to $n = 2.4$.

Different creep stress exponents imply different creep mechanisms, as classified by Langdon and others. Figure 67, taken from a paper by Langdon [252], illustrates this connection. So one may conclude that Dugay et al.'s data [250] on UO_2 creep behavior, in the stress range 20-45 MPa at 1773, with $n \approx 2$ falls into the superplasticity region, while the UO_2-Cr_2O_3 behavior (40-65 MPa) is in the dislocation climb domain, according to Langdon's classification. The various deformation mechanisms have been clarified by Langdon in [253].

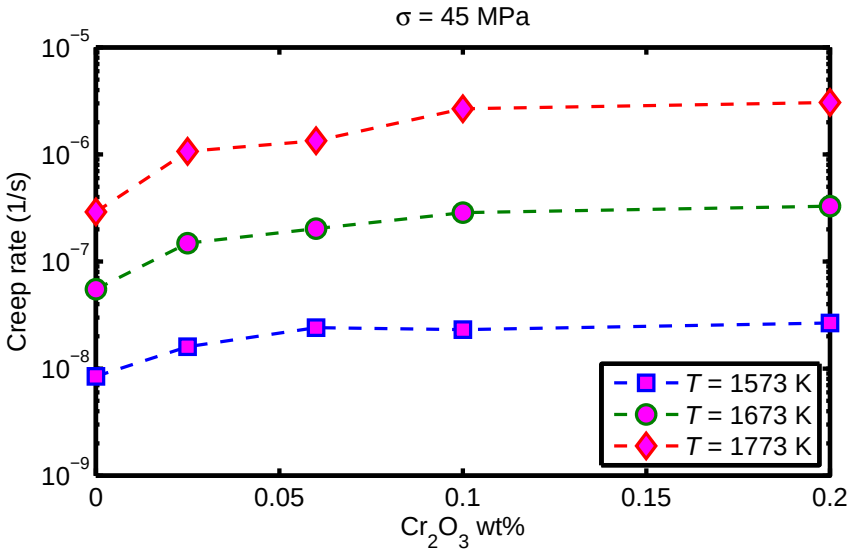

Figure 66: Thermal creep rate of UO_2-base fuel versus Cr_2O_3 concentration at a stress level of 45 MPa, using the data in table 16.

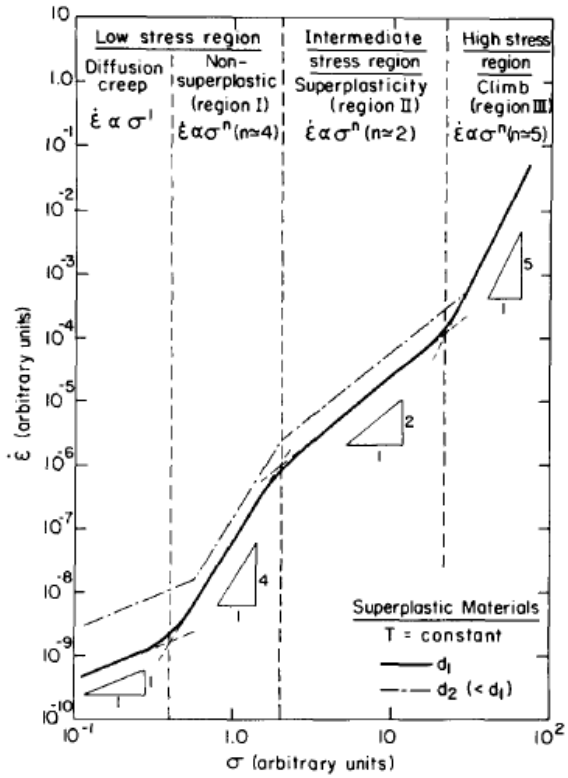

Figure 67: Langdon's schematic diagram of strain rate $\dot{\varepsilon}$ vs. stress σ, showing the partition into different regions of creep behavior at constant temperature T. It also shows the effect of grain size from d_1 to $d_2 < d_1$. The relation $\dot{\varepsilon} \propto \sigma^n$ is obtained with $n = 1$ in the diffusion creep region, $n \approx 4$ in the non-superplastic region, $n \approx 2$ in the superplasticity region, and $n \approx 5$ in the climb region; from [252].

To sum up the work of Dugay et al. [250] on Cr_2O_3-doped UO_2 thermal creep, there is a large scatter in the raw data, and hence, it is difficult to build a usable or an empirical model to describe the thermal creep behavior of this material in the wide range of applicable stress and temperature for various Cr_2O_3 concentrations. Additional and more refined measurements in a carefully controlled laboratory environment are necessary for this endeavor. Moreover, the influence of grain size on creep rate was not examined by Dugay and company, which as discussed earlier can be significant.

Thermal creep behavior of Cr_2O_3-doped UO_2 has also been examined experimentally by Nonon et al. [254], who reported on creep tests that were performed at 1743 K and 45 MPa, under a controlled atmosphere of argon with 5% hydrogen to prevent oxidation and stoichiometry changes of the samples during the experiment. They compared the creep rate under compression of an undoped UO_2 sample and different Cr_2O_3-doped samples with the dopant concentration varying from 0.075 to 0.225 wt% under identical experimental conditions. They found that addition of Cr_2O_3 increases considerably the creep rate of the material, i.e., by up to a factor of 10. However, this effect saturates at higher additive contents (≈ 0.2 wt%).

Nonon et al. [254] also examined the effect of stress on thermal creep rate. They obtained results at several applied stresses (20 to 60 MPa), under the same experimental conditions ($T = 1743$ K) in order to evaluate a creep law. As in Dugay et al.'s study [250], the steady state creep rate of UO_2 doped with Cr_2O_3 was described by an equation of the form (29). Nonon and coworkers only found a single creep regime with a stress exponent value of $n = 4$ and a creep activation energy Q close to the uranium self-diffusion energy in UO_2, which according to Matzke [255] is about 460 kJ/mol. Nonon et al.'s value of $n = 4$ is lower than those found by Dugay and co. for the same material, cf. table 16. Details of the measurements and data are not given in [254].

A series of laboratory creep tests were made on unirradiated Westinghouse ADOPT^{TM} (Advanced Doped Pellet Technology) and compared with standard UO_2 fuel pellet in [256]. ADOPT is a Cr_2O_3-Al_2O_3-doped UO_2 fuel (Cr: 300-650 μg/gU and Al: 70-150 μg/gU) currently employed as a standard fuel pellet by Westinghouse in commercial LWRs. Two different types of creep tests at temperatures 1300°C to 1700°C were reported in [256]: they were done under either constant applied stresses (30, 45 and 60 MPa), at which the strains were measured, or alternatively, under a varying stress to maintain a constant strain rate (either 0.1/h or 0.5/h) in a 95% Ar+5% H_2 milieu as described in [256].

The plots of strain as a function of time (up to 5 h) from these creep tests, shown in [256] and reproduced in figure 81, section 6.2.1, indicate that at 1300°C/60 MPa deformation behavior of the two types of fuel is alike, whereas at 1500°C/45 MPa and 1700°C/30 MPa, the doped fuel has a much higher creep rate than standard UO_2 fuel. These temperatures (≥ 1400 K), however, are much higher than what fuel experiences during normal operation and anticipated operational occurrences. For example, a typical fuel design under normal BWR operations would experience fuel temperatures below 1300 K (≤ 1000°C); see. e.g. [257].

As mentioned in section 2, the thermal creep behavior of MnO-Al_2O_3-doped UO_2 and Cr_2O_3-doped UO_2 fuels has been studied and compared by KAERI workers [60]. The KAERI creep tests were done at a temperature of 1450°C (1723 K) under an initial applied stress of 60 MPa up to about 20 h. Figure 68 displays the results of these tests as presented

in [60]. These tests show that, e.g., the deformation strains of MnO-Al_2O_3-doped UO_2 fuel after 5 h is about seven times larger than that of the pure UO_2 fuel. Furthermore, the data indicate that the (primary) creep rate of MnO-Al_2O_3-doped UO_2 is higher than that of Cr_2O_3-doped UO_2 fuel up to about 5 h, but the deformation strains for the two fuel types coincide after 20 h under the employed conditions.

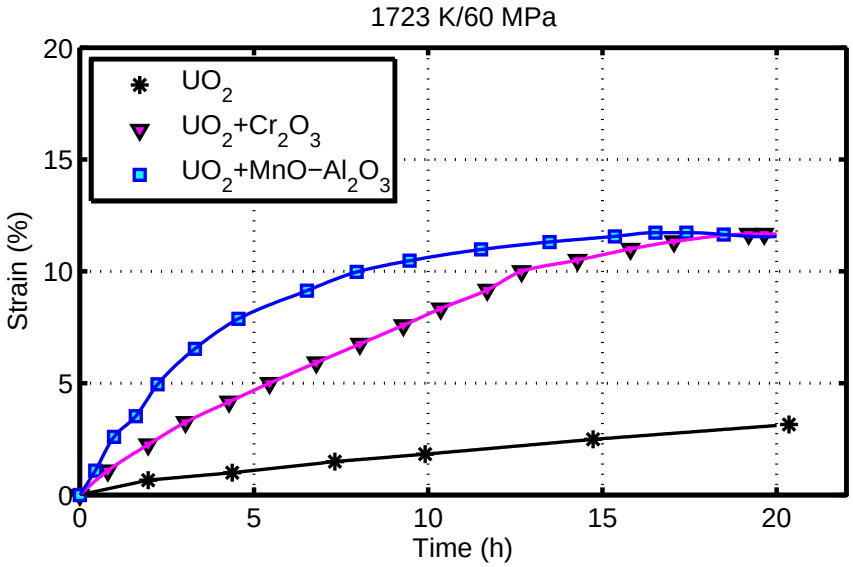

Figure 68: Measured compressive creep strain of pure UO_2, MnO-Al_2O_3-doped UO_2 and Cr_2O_3-doped UO_2 pellets; adapted from [60].

Other published works on the the creep behavior of doped UO_2 include the study by Rhee et al. [258] on the effect of SiO_2-CaO-Cr_2O_3 (SCC) additive and the investigation by Matsunaga et al. [15] on Al-Si-O additive. Rhee and coworkers conducted compressive creep tests in Ar-5%H_2 atmosphere subject to 20, 35, 50, and 65 MPa uniaxial stress at 1773 K. They observed that the creep rate of the 0.07 wt% SCC-added UO_2 was lower than that of the pure UO_2, whereas, the creep of the 0.22 wt% SCC-added UO_2 was about 3.5 times faster than that of the pure UO_2, depending on the applied stress in the lower stress range (20-35 MPa). In the case of the 0.35 wt% SCC-added UO_2, the creep rate decreased in comparison with that of the 0.22 wt% SCC-added UO_2. They suggested that the increase in the creep rate of the 0.22 wt% material could be due to the enhanced diffusivity through the amorphous intergranular phases and to the low viscosity of the second phase. Whereas, in the case of 0.35 wt% SCC-doped fuel, the creep rate decreased in comparison with the 0.22 wt% SCC-doped material, due to grain size of the former, which was three times larger than those of the pure UO_2 and that of the latter (8 μm).

Matsunaga et al.'s [15] determined the yield stress and also the steady creep rate under uniaxial compression at a constant load in dry 8%H_2+92%N_2 gas flow for (Al-Si-O)-doped UO_2 specimens with a dopant concentration of 0.025 wt%. For the creep test, the applied stresses were about 12 MPa and temperature ranged from 1723 to 1823 K. For the yield stress test, temperature ranged from 1273 to 1673 K, and the strain rate chosen was 0.1/min. Matsunaga et al. showed that the steady state creep rate of (Al-Si-O)-UO_2 fuel is higher than that of standard UO_2; whereas the yield stress of (Al-Si-O)-doped fuel is slightly lower than that of the standard UO_2 fuel and the difference gets larger with increase of temperature, figure 69. At lower temperatures, the Al-Si-O precipitation effect and grain

size effect would be balanced, hence, the difference in yield stress would be small. At higher temperatures, the precipitation effect would be reduced due to the softer Al-Si-O phase, according to Matsunaga and coworkers [15].

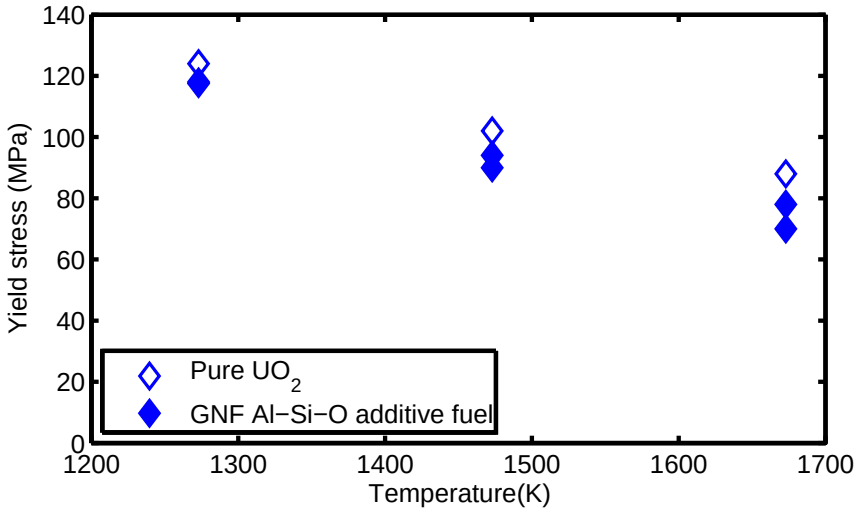

Figure 69: Effect of Al-Si-O additive (0.025 wt%) on yield stress of UO_2; adapted from Matsunaga et al. [15].

Radial cracking of the fuel pellet, which occurs during power change, especially at the pellet periphery, may contribute to a detrimental localized stress distribution in the cladding. Figure 70 compares the crack pattern of a standard UO_2 fuel pellet (cross-section) with that of a Cr_2O_3-doped UO_2 pellet for fuel rods that experienced equivalent power and holding time during a power ramp. We see that the crack patterns are similar between the two types of fuel, however, in the Cr_2O_3-doped pellet, the radial cracks in the brittle periphery are more numerous and shorter. The pellet diameter is not specified in [259], but typically in a PWR 17×17 fuel assembly design, it is around 8 mm.

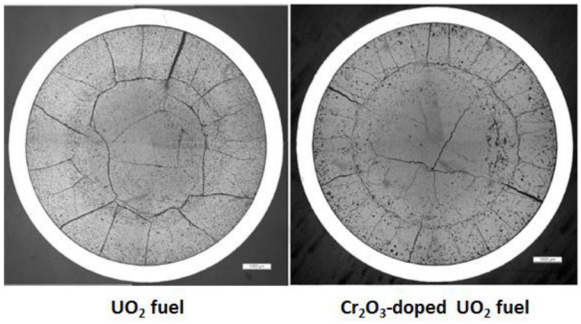

Figure 70: Comparison between standard UO_2 and Cr_2O_3–doped UO_2 fuel pellet cross sections after a power ramp; from [259].

Hence, the PCI advantage of a softer doped UO_2 fuel pellet due to its higher creep rate is only expedient under certain LWR accidents or transients, at which the fuel temperature can raise above 1500°C. Even then, the durations of such accidents are of order of minute or less, not hour, which is the time scale of UO_2 base fuel creep.

5.2 Modeling fuel creep

In a 2015 paper [61], creep deformation of UO_2 fuel doped with Nb_2O_5 and Cr_2O_3 was assessed using a point defect model based on the law of mass action and the diffusional creep according to the Nabarro-Herring mechanism, which relates the creep rate to the lattice self-diffusivity, the inverse of grain area and the applied stress. The self-diffusion coefficients of the cation uranium and the anion oxygen are directly proportional to the concentrations of ions, which in turn are functions of dopant concentrations.

To be more specific, the Lidiard point-defect model [243] of self-diffusion of uranium in UO_2 was extended to express the concentrations of oxygen and uranium vacancies as a function of trivalent and pentavalent oxide dopants. The lattice diffusion coefficients for these defects were then related to the dopant concentrations and temperature. In the case of pentavalent dopant, a hyperstoichiometric situation was assumed, whereas in the trivalent dopant, a hypostoichiometric condition was supposed. The input data to the model are the formation energies of the Frenkel pairs and the Schottky defects, and the diffusion coefficients of oxygen and uranium point defects. These data were taken from measurements reported in the literature. The model was then used to simulate (calculate) creep experiments on UO_2 doped with Nb_2O_5 and Cr_2O_3 in concentrations up to about 1 mol%, with a varying grain size at different temperatures and applied stresses. The model is said to be adequate for low concentrations of dopants, e.g. ≤ 0.01 mole fraction.

The results of creep computations versus measurements for Nb_2O_5 doped UO_2 shown in [61] are depicted in figure 71. It is seen from this figure that the calculated creep rates follow the trend of measurements from [248], with an overestimation at 1 mol% Nb_2O_5. Nevertheless, the results are comparable to, but not the same as, those calculated by Sawbridge et al. (see figure 11 of [248]). Figure 71 shows the results of calculations carried out with constant grain sizes of 15 μm and 30 μm. The inset figure shows measured grain size versus Nb_2O_5 mole fraction of UO_2 doped in samples tested in [248].

The results of creep computations for Cr_2O_3 doped UO_2 in [61] are presented in figure 72, which compares measured creep rate values from [250] with calculated ones. Considering the uncertainty in the measurements (up to about $\pm 18\%$), the agreement is fair. The measured data depicted in figure 72 are the results of direct fit to the raw data as given in [250]. The inset figure shows measured grain size versus Cr_2O_3 concentration of UO_2 doped specimens tested in [250].

Using the aforementioned model, the temperature/stress dependence of creep rate of UO_2-0.4 mol% Nb_2O_5 was also calculated in [61], for which only a few experimental data are reported in [248]. The results of the calculations, together with experimental data, are presented in figure 73. The results up to a stress of 20 MPa are fair, but beyond this stress level, only data for 1453 K are available, which the calculations overestimate. More experimental data and analysis are needed to appraise the predictive capability of the model.

Here, we have only discussed fuel thermal creep. There is also irradiation-induced (in-reactor) creep of UO_2 [260], which we haven't touched upon due to the lack, or to our knowledge, non-existence of such data for doped UO_2 fuel. A model for irradiation-induced creep of UO_2 was described in [261] and compared with experimental data. This model may be combined with the above discussed thermal creep model for doped UO_2 fuel and used as a base model for doped UO_2 fuel creep in computer programs for fuel rod

performance analysis.

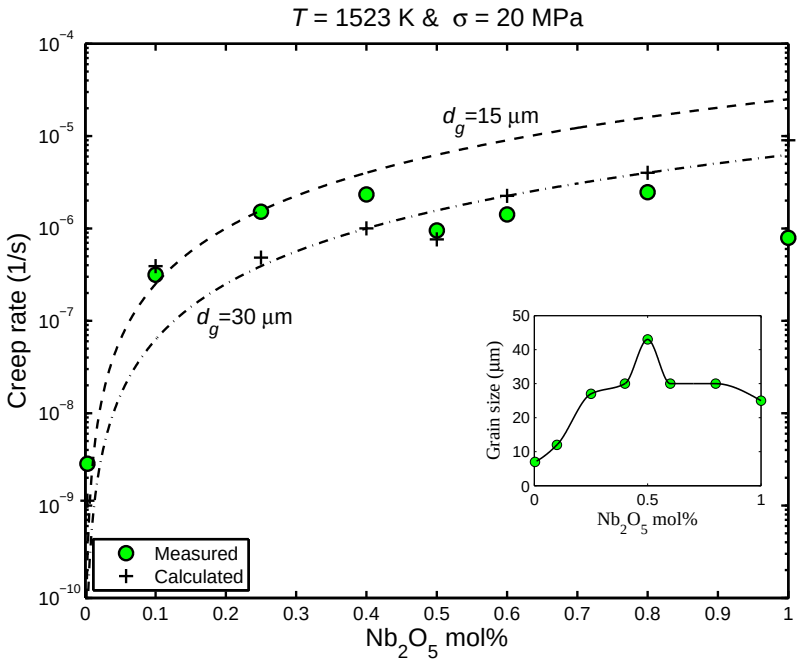

Figure 71: Measured creep rates (circles) vs. calculated values (+) as a function of Nb_2O_5 mol% in UO_2 at an applied stress of 20 MPa at 1523 K. Measurements are from [248]. The dashed and dash-dot curves show computations made at constant grain sizes. The inset shows measured grain size vs. Nb_2O_5 mole fraction of UO_2 doped in samples tested by Sawbridge et al. [248]. The line is simply an interpolation through the data points. (Adapted from ref. [61].)

5.3 Composite fuel mechanical properties

Materials mechanics properties of the fuel pellet, such as Young's modulus, Poisson's ratio, yield and ultimate tensile strength, etc., are important quantities for fuel rod modeling both during normal reactor operations and under off-normal conditions. For example, to compute fuel cladding deformation during pellet-cladding mechanical interaction, such properties, i.e. their corresponding constitutive relations, are requisite. Experimental data for the aforementioned quantities are not readily available for UO_2-base composite fuels of interest, but some quantities may be estimated from those of UO_2 and its additives by use of models.

Suppose two isotropic phases firmly bonded together to form a mixture with any concentrations. Then, a rule of mixtures can be used to compute a specific elastic property. Based on Hill's work [262, 263], the bounds for Young's modulus of the composite material "AB" can be written as

$$E_r \leq E_c \leq E_v, \tag{32}$$

where E_c is the effective Young's moduli of the composite with bounds

$$E_v = \phi_A E_A + \phi_B E_B, \tag{33}$$

$$\frac{1}{E_r} = \frac{\phi_A}{E_A} + \frac{\phi_B}{E_B}, \tag{34}$$

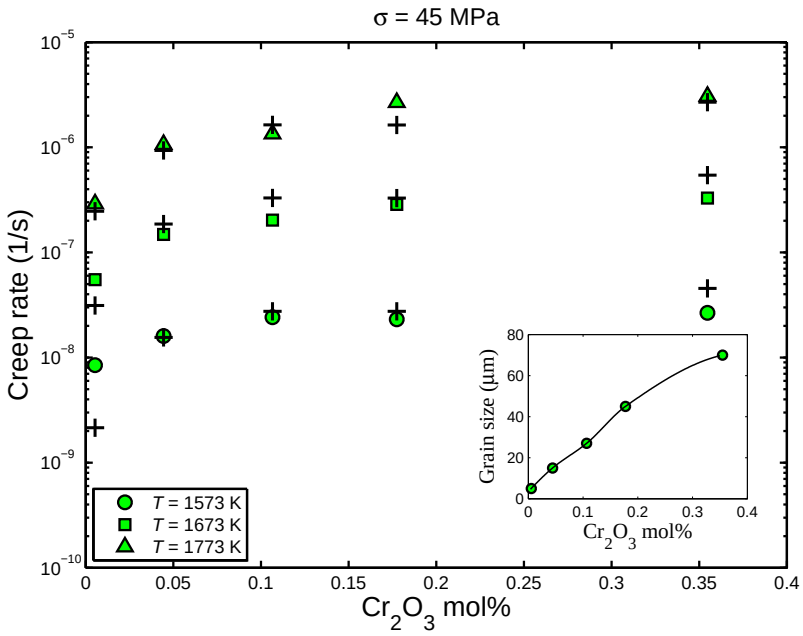

Figure 72: Measured creep rates (filled symbols) vs. calculated values (+) as a function of Cr_2O_3 mol% in UO_2 at an applied stress of 45 MPa at different temperatures. Measurements are from [250]. The inset shows measured grain size vs. Cr_2O_3 concentration of UO_2 doped specimens tested in [250]. (Adapted from ref. [61].)

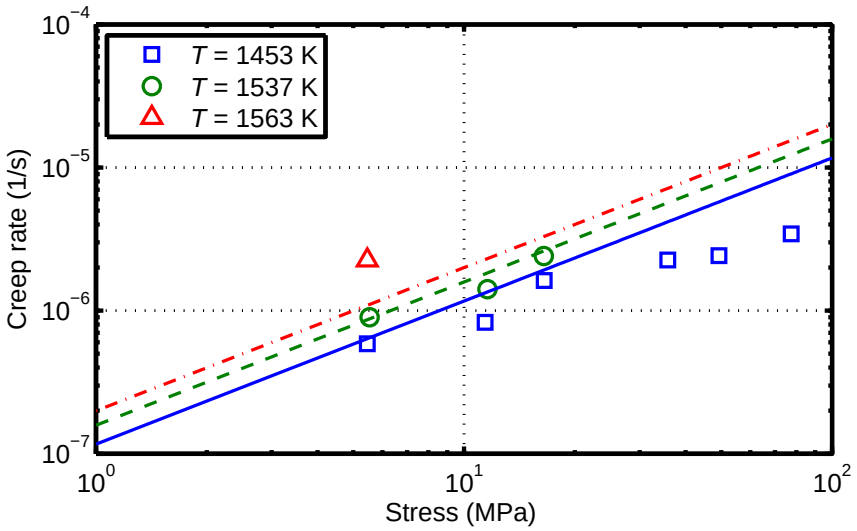

Figure 73: The log-log plot of the variation of creep rate with stress at several temperatures for UO_2 doped with 0.4 mol% Nb_2O_5. The lines are calculated, whereas the symbols are measured values reported in [248]. (Adapted from ref. [61].)

where ϕ_A and ϕ_B stand for the volume fractions of constituents A and B, respectively. Moreover, E_v and E_r are referred to as the Voigt and Reuss estimates for the effective Young modulus of the composite, respectively. Detailed derivations and limitation of this inequality, and also the associating relations for the bulk and shear (or rigidity) moduli plus Poisson's ratio are given by Hill in [263], which we do not reproduce here. We only mention that, supposing the phases in the composite have equal shear moduli, Hill derived a formula for the effective Poisson's ratio (ν) that reads

$$\nu = \frac{\phi_A \nu_A + \phi_B \nu_B - \nu_A \nu_B}{1 - \phi_A \nu_B - \phi_B \nu_A}. \tag{35}$$

UO_2–BeO Here, A $\equiv$ UO_2 and B $\equiv$ BeO. Elastic properties data and/or empirical correlations for UO_2 as a function of temperature can be found in [264–266]. Some elastic properties of BeO can be found in [267–269] and references therein. Using these data, equations (33)-(35) may be applied to estimate elastic properties of UO_2–BeO fuel.

UO_2–SiC Yeo, in his doctorate dissertation [114], has reported measurements of Young's modulus and hardness of UO_2–SiC composite fuel. The hardness of the composite specimens was measured using both Vickers and Knoop indentations, while an ultrasonic instrument was employed to measure both longitudinal and shear (transverse) velocities for determining Young's modulus of UO_2–SiC specimens (at room temperature). The specimens had SiC volume fractions: 0.0, 0.05, 0.1, 0.15, 0.2 with SiC particle sizes ranging from 0.6 μm to 55 μm. Standard relations,[13] were used to compute Young's modulus and Poisson's ratio from measured longitudinal and shear (transverse) velocities [270]. Yeo's data show that both hardness (Vickers and Knoop) and Young's modulus increase linearly with SiC volume fraction in the range tested.

Yeo also calculated Young's modulus as a function of SiC volume fraction by using separate data for UO_2 and SiC, and employing the Hashin-Shtrikman mixing formulae. Hashin and Shtrikman [271] derived expressions for calculating the effective bulk and shear moduli of a composite. They assumed that the composite material was statistically isotropic and considered a boundary value problem for homogeneous elasticity. Based on variational principles in terms of the elastic polarization tensor described in [272], they found upper and lower bounds on the effective bulk and shear moduli of a two-phase composite material. Yeo's computations are in good agreement with his experimental data. It is worthwhile to extend the computations to higher temperatures, applicable to reactor service, and compare them with measured data when the latter become available. Elastic properties data for SiC as function of temperature can be found in [173].

Yeo also carried out Raman spectroscopy on the UO_2–SiC specimens containg SiC particles of varying size [114]. The aim was to measure the internal stress induced by SiC as a function of SiC particle size. Raman spectra from a SiC particle in stress free SiC powder and the SiC particles with sizes, 0.6, 1, 9, 16.9, and 55 μm in UO_2-5vol%SiC composite pellets were analyzed. The Raman spectrum from a stress free SiC particle included a transverse optical (TO) peak at 796 cm^{-1}. The largest particle size SiC (55 μm) exhibited similar TO peak (795.7 cm^{-1}), whereas the other composites SiC particles containing 0.6, 1, 9, and 16.9 μm SiC particles showed higher number of TO peaks (800-803 cm^{-1}) than that of the stress free SiC particle. From the Raman Spectra data, after some theoretical

analyses, Yeo deduced the residual stress in the material as a function SiC particle size. Accordingly, the measured compression stress was up to 1.65 GPa in 1 μm SiC particles, which decreased rapidly to ≈ 0 GPa with increasing particle size to 55 μm due to microcracking and interfacial debonding that released the accumulated stress [114].

The performance of UO_2–SiC as light water reactor fuel has been modeled in [273]. The authors of [273] have constructed a computer model consisting of self-defined but fully coupled modules in a finite-element method platform. Within this model, they calculate the effective Young's and Poisson's ratio of UO_2–SiC fuel by using equations of type (33) for both of these quantities without any validation. This is further discussed in section 6.3.3.

UO_2–diamond Chen, Subhash and Tulenko [35, 116] have determined Young's modulus of UO_2–5vol% diamond composite fuel pellets using an ultrasonic measurement method, which provides an accurate value and is a nondestructive technique. Using a pulser/receiver system, both the longitudinal velocity v_L and the shear velocity v_S of the pellets were measured at room temperature. Young's modulus and Poisson's ratio were then calculated via standard formulae [270].

The pellet samples tested contained different diamond particle sizes. Their study showed that pellets with 3 μm diamond particle size displayed a higher Young's modulus than pure UO_2 samples, while pellets with 0.25 μm, 12 μm, and 25 μm diamond showed relative lower values. In particular, microcracks were observed when the diamond particle size was larger than 12 μm, which poorly affected both the thermal and mechanical properties of the composites.

Chen, Subhash and Tulenko [274] also utilized Raman spectroscopy to investigate the phase transformation (graphitization of diamond) in diamond particles within a UO_2-diamond composite pellet processed by spark plasma sintering. The sintered pellet had a diameter of 12.5 mm and a thickness of 3.5 mm, containing 5 vol% diamond. A Raman spectrometer with a 532 nm laser was utilized. The spectral resolution of this system was 0.1 cm^{-1}, with the spatial resolution of 0.38 mm; more details are described in [274]. Whereas pure diamond gives a sharp Raman peak at 1331.6 cm^{-1}, the graphitized diamond shows broad peaks either at 1350 cm^{-1} or 1580 cm^{-1}. The authors found that more than 20% of diamond was graphitized on the surface of the UO_2-diamond pellet, whereas around 10% of diamond was graphitized in the interior regions of the pellet. The implications of these results need to be carefully examined, comprising additional tests, before implementing UO_2-diamond composite as a reactor fuel pellet product.

UO_2–graphene Yao and colleagues [121] fabricated UO_2 composite fuel pellets with various graphene nano-platelet (GNP) concentrations, 1 wt% to 5 wt%, consolidated into dense fuel pellets by spark plasma sintering technique. The platelets formed a unique lamellar interconnection along in-plane direction and thereby improved thermal diffusivity/conductivity along the radial direction of the fuel matrix. Yao et al. investigated the hardness and the fracture toughness of sintered fuel pellets by Vickers microhardness indentation technique at room temperature. They obtained hardness values by using small loading of 100 g for 10 s holding at the peak value. Fracture toughness was estimated by a

standard fracture mechanics method. The authors found that, by increasing graphene concentration, the hardness of the composite fuel pellets decreased markedly, implying that the composite fuels may display enhanced plasticity and fracture toughness, which is favorable for reducing the PCMI intensity. Yao's data, including thermal conductivity, are listed in table below.

Sample	Thermal conductivity W/mK	Hardness GPa	Fracture toughness MPam$^{1/2}$
UO_2	7.28 ± 0.02	6.3 ± 0.2	1.4 ± 0.2
UO_2-1wt%GNP	12.7 ± 1.7	4.1 ± 0.3	3.5 ± 0.4
UO_2-3wt%GNP	...	1.96 ± 0.1	3.2 ± 0.6
UO_2-5wt%GNP	19.1 ± 1.4	1.41 ± 0.1	3.3 ± 0.1

6 Operating experience, tests and modeling

Standard (undoped) UO_2 fuel pellets have been used in LWR:s for more than 60 years, and there is an immense operating experience for this kind of fuel for a wide range of burnups and reactor operating conditions. Likewise, there is a large database of tests and experiments on standard UO_2 fuel. This operating experience and test database is essential for defining appropriate design and safety criteria, and also for verification and validation of computer programs and models that are used in licensing analyses to confirm that these criteria are met. Data are needed not only for the fuel performance under normal reactor operation, but also for transient conditions (anticipated operational occurrences - AOOs) and design basis accidents (DBAs), such as loss-of-coolant accidents (LOCAs) and reactivity initiated accidents (RIAs). These off-normal conditions require costly testing in exclusive experimental facilities, and over the years, an extensive database has been collected for standard UO_2 fuel [275, 276].

The situation is generally much different for UO_2 fuel with additives. The database from tests and experiments in transient and accident conditions is scarce, and significant operating experience exists only for (U,Gd)O_2 burnable absorber fuel and to some extent also for UO_2 fuel doped with Cr_2O_3 and Al_2O_3. In the following, results of some in-reactor irradiation programs and transient/accident tests on additive UO_2 fuels are briefly reviewed. We also review open literature sources dealing with computer simulations of various aspects of the thermal-mechanical performance of these fuels under normal reactor operating conditions, transients and accidents. The purpose is to assess the maturity of computer models and programs that are needed for design and safety analysis.

6.1 Operating experience

There have been a number of irradiation or "qualification" programs to compare in-reactor fuel performance of UO_2 fuel with additives against that of standard undoped UO_2. The results of these programs are usually presented in conferences and published in the proceedings, and hence, are not subjected to the rigorous peer review process commonly exercised for journal publications. As such, the quality of the presentations may vary considerably from one study to another. In this section, we provide a brief survey of some results from these programs as presented in the publications.

6.1.1 Burnable absorber UO_2 fuel

Gadolinium has been frequently used as a burnable absorber in BWR UO_2 fuel since the mid-1970s, and more recently, it has found its way also into PWR and VVER[14] fuel. Consequently, the operating experience for (U,Gd)O_2 fuel is extensive: the reader is referred to [23, 277] for summaries. At beginning of fuel life, the radial power distribution in (U,Gd)O_2 fuel pellets is strongly depressed by the neutron absorbing Gd isotopes, which affects the radial temperature distribution, and hence, temperature dependent phenomena. Later in life, as the absorbing isotopes are burnt, the most important effect of the gadolinia is in lowering the fuel thermal conductivity. The diffusivity of gaseous fission products is

also affected by the gadolinia. As already discussed in section 4.4, this may influence gas release from the fuel pellets.

Apropos of other types of BA fuel, not much reactor operational experience and data can be found in the open literature. Corsetti and colleagues, in a 1991 conference paper [24], after describing some neutronic advantages of erbia burnable absorber, note that four fuel assemblies containing 0.9 wt% erbia in 3.4 wt% ^{235}U enriched UO_2 pellets were fabricated in 1989 and operating in the Calvert Cliffs II PWR. Furthermore, they mention that four additional fuel assemblies with 1.5 wt% erbia in 3.65 wt% ^{235}U enriched UO_2 pellets were scheduled for insertion into the San Onofre Unit 2 PWR in the fall of 1991. These fuel assemblies were intended to confirm neutronic methods and satisfactory fuel behavior. The outcome of these experiences are unknown to us.

It is worth mentioning that fuel assemblies comprising (U,Er)O_2 rods have been loaded in RBMK (high-power channel) reactors after the Chernobyl reactor accident in Ukraine [278], e.g. at the Ignalina Atomic Power Plant, Lithuania [279]. The primary objective has been to eliminate the possibility of uncontrollable increase in reactor power, due to prompt neutrons, in case of dehydration of the active zone. It is noted that the experience with this kind of fuel has been satisfactory and burnup computations agreed well with measurements with no adverse effects [279]. Thus, the effectiveness of (U,Er)O_2 fuel for this type of reactor has been verified; for more details, see refs. [278–280].

6.1.2 Chromia/alumina doped UO_2 fuel

Operating experience has also been accumulated for UO_2 light water reactor fuel doped with chromia and/or alumina. For example, industrial groups in France, led by Framatome (formerly AREVA), have utilized UO_2 fuel doped with Cr_2O_3 in BWRs and PWRs since 1997 [18, 19, 39, 40]. In the course of developing this fuel, both separate-effect irradiation experiments in a test reactor [39, 254] and irradiation campaigns in commercial LWRs [18, 19, 40] were conducted to assess the performance of various types of doped UO_2 fuels versus standard pure UO_2 fuel.

More specifically, Valin and company [39] tested fission gas retention and release of a variety of experimental doped and undoped UO_2 fuels, irradiated in a facility at the periphery of the Siloé test reactor in Grenoble, to a fuel pellet burnup of about 10 MWd/kgU. They kept the central temperature of the annular pellets below 973 K to avoid triggering thermal fission gas release. After irradiation, the test rodlets were punctured and their gas contents were analyzed, showing very low release during the base irradiation. Then, the fission gas retention capacities of the fuel pellets were examined by post-irradiation annealing tests made in a dedicated facility. The annealing was done in a high frequency furnace at 1973 K for either 30 minutes or 5 hours, whereupon ^{85}Kr released from the fuel was measured by gamma spectrometry. In figure 74, we reproduce Valin et al.'s informative diagram, showing ^{85}Kr release after 5 h at 1973 K versus grain size for the tested samples. Note that every data point belongs to a specific kind of fuel. The samples included several variants (concentrations) of Cr_2O_3-doped UO_2 plus MgO-, SiO_2-, Al_2O_3-, ZrO_2-doped, and several alternates of non-standard UO_2.

As Valin et al. noted, the highest gas retention samples were fuels having the larger grain sizes (over 50 μm). This characteristic, however, was not sufficient, since the large-grained

UO_2 fuel release reached 30%. They pointed out that the other important feature for an improved fission gas retention is the presence of intragranular sites, which are favorable to bubble nucleation and pinning. These sites are structural defects due to the hyperstoichiometry in UO_{2+x} and second phase precipitates in fuels doped with 0.2% Cr_2O_3. According to Valin and coworkers, the fuels containing only Cr_2O_3 as a dopant showed an improved gas retention, especially those with 0.2% Cr_2O_3. This improvement in gas retention was not only attributed to a larger grain size, but also to the presence of second phase precipitates in the fuel.

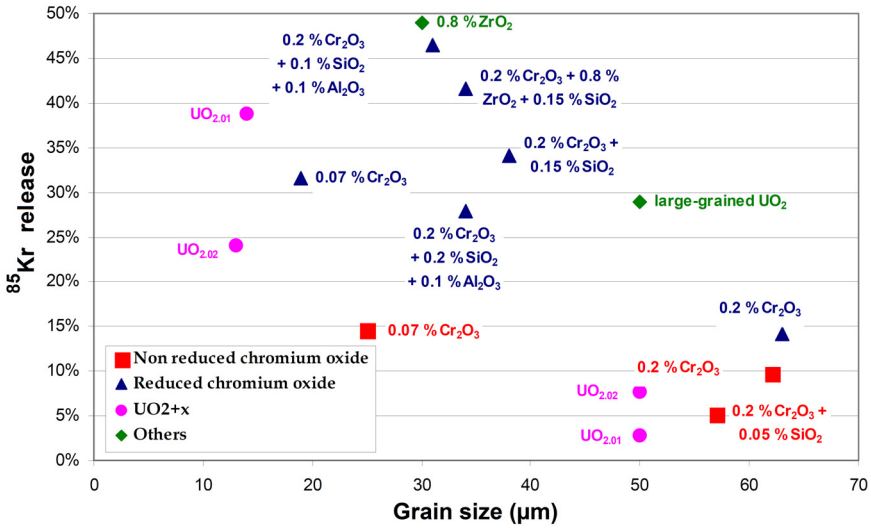

Figure 74: Valin et al. results on ^{85}Kr release after annealing tests of 5 hours at 1973 K [39].

In later publications, Delafoy and coworkers in [19, 40] concluded that the Framatome chromia-doped UO_2 fuel has an optimum Cr_2O_3 concentration of 0.16 wt%, which leads to grain sizes in the range of 50 to 60 μm and fuel densities typically in the range of 96 to 97%TD. They reported on the PWR irradiation program CONCERTO, in which extensive PIEs have been carried out with respect to this type of Cr_2O_3-doped UO_2 fuel. They pointed out that in comparison with standard Zircaloy-4 clad UO_2 rods, non-destructive examinations have revealed a slightly higher fuel rod growth and diametral rod deformation in Cr_2O_3-doped UO_2 fuel rodlets. This behavior is attributed to an earlier-in-life pellet-cladding contact, considering that the Cr_2O_3-doped fuels exhibit a lower densification. Density measurements have confirmed the higher dimensional stability of Cr_2O_3-doped fuel up to 62 MWd/kgU, with a very low early-in-life fuel densification relative to undoped UO_2. Rod puncturing of the CONCERTO rods after 5 cycles of reactor operation showed fractional FGR values below 2% for Cr_2O_3-doped fuel. Moreover, the microstructural examinations showed that precipitation of fission gases occurred in intragranular rather than intergranular bubbles, in contrast to what is observed in the undoped UO_2 fuel. The microstructural examinations also revealed a great stability of the Cr_2O_3-doped fuel, in particular that no grain growth had occurred during irradiation up to about 60 MWd/kgU. This behavior is in line with the observations made by Westinghouse in Sweden; see below. For additional data and PCI test results performed on this type of doped fuel, the reader may consult the presentations by Delafoy and co-workers [19, 40]. Finally, it should be remarked that fission gas release from chromia-doped UO_2 fuel of Framatome design has been studied under normal reactor operating conditions in the IFA-716 experiment in Halden, Norway [44, 281]. However, only part of the results from this experiment has yet

been published in the open literature; see e.g. [282].

Westinghouse Electric has developed the ADOPT^{TM} (Advanced Doped Pellet Technology) fuel pellet concept, in which both Cr_2O_3 and Al_2O_3 are used as dopants [283, 284]. The first fuel of this kind was loaded in a commercial LWR in 1999, and the concentrations of the dopants have been optimized based on operating experience from LWRs and test reactor experiments. Publications on this work are summarized below.

In 2006, Arborelius and colleagues [17] reported the outcome of a comprehensive demonstration program on doped UO_2 fuel performance. The fuel rods were first irradiated in a commercial boiling water reactor, then subjected to power ramps in a test reactor. More specifically, two segmented rods containing doped fuel pellets (table 17) were irradiated at the Barsebäck 2 BWR in Sweden. Each of the two rods consisted of five segments with five different pellet types, Std, Std Opt2 and three variants of doped fuel denoted by D1, D2 and D3 in table 17. The additive composition in the D3 pellets is close to the nominal composition in ADOPT^{TM} fuel. All fuel pellets had a diameter of 8.36 mm and a length of 10 mm. The rods had LK3 Zircaloy-2 cladding, with an internal zirconium liner.

The two rods were irradiated in a fuel assembly to a burnup of about 30 MWd/kgU under normal BWR conditions. The rod power history for the base irradiation is shown in [17]. After base irradiation, the three middle segments of each rod were examined at the Studsvik Nuclear laboratories, Nyköping, Sweden. This examination, using both the cladding profilometry and pellet-cladding gap measurement, revealed that the volume change of the pellets was -0.2% for the Std Opt2 pellets and +0.8 to +1.4% (positive sign $\equiv$ swelling) for the doped pellets D1, D2 and D3. Ceramographic examination performed at mid-pellet position on D2 pellets indicated fuel grain growth in the central part of the pellet [17].

Table 17: Fuel types used in a Swedish BWR irradiation program [17].

Specimen	UO_2 fuel composition	Density g/cm^3	Grain size μm	$^{235}U^*$ wt%
Std	UO_2	10.52	10-12	1.7, 2.8
Std Opt2	UO_2	10.60	10-12	4.2
D1	+ 0.1wt%Cr_2O_3	10.66	44	4.2
D2	+ 0.1wt%Cr_2O_3+0.01wt%MgO	10.68	42	4.2
D3	+ 0.1wt%Cr_2O_3+0.02wt%Al_2O_3	10.68	52	4.2

* Uranium-235 enrichment.

Besides the results of post-irradiation examinations (PIEs), Arborelius and company [17] also reported results from BWR pool-side measurements made on doped UO_2 fuels, with similar characteristics as the ones presented in table 17. The pool-side rod axial length measurements showed a higher fuel rod irradiation-induced growth for rods containing doped UO_2 than those holding Std fuel pellets. Subsequent data presented in [283, 285] confirm this effect. That is, the rod growth with doped UO_2 is appreciably faster than that with pure UO_2 fuel pellets. This may be attributed to a higher fuel swelling rate and/or lower fuel in-reactor densification of doped fuel, which closes the pellet-cladding gap earlier during irradiation, thereby leading to a larger rod length increase. Note that the nominal as-fabricated densities of doped fuels are larger than Std fuel (table 17), hence, there is less in-rector densification of doped fuel.

In a 2009 presentation by Backman et al. [283], fission gas release data for Westinghouse

doped UO_2 fuels obtained by reactor pool-side gamma scanning (i.e. non-destructive examination) of rods (in two fuel assemblies) which were irradiated under normal BWR operation to burnups of up to 55 MWd/kgU, and also on rods that were subjected to heavy-duty power histories in the Halden test reactor, are cursorily mentioned. The pool-side gamma scanning of Cr_2O_3-Al_2O_3 doped UO_2 fuel exhibited lower fractional FGR (2 rods with 1.3%) than undoped UO_2 fuel rods (3 rods with 1.5-2.1%) at burnups in the range of 50-55 MWd/kgU. However, since the individual power histories for these rods are not specified, it is hard to draw confident conclusions about the outcome. More data in this burnup range are needed to confirm the trend.

Additional data on fission gas release for chromia/alumina-doped UO_2 fuel at high power are available from the Halden IFA-677 experiment [286]. The fuels tested in this experiment comprised two Cr_2O_3-Al_2O_3 doped UO_2 rods and one rod with undoped UO_2, irradiated to about 24 MWd/kgU in BWR conditions at linear heat generation rates from 35 to 45 kW/m. The doped fuels had 0.09wt%Cr_2O_3-0.02wt%Al_2O_3 (rod 1) and 0.05wt%Cr_2O_3-0.02wt%Al_2O_3 (rod 5). The fuel mean grain sizes were 56 μm (rod 1), 46 μm (rod 5) and ≈ 12 μm for pure UO_2 (rod 6) [286]. The fractional FGR of the tested rods were similar, that is, 22% (rod 1), 17% (rod 5) and 19% (rod 6) [286]. From these results, one may conclude that fuel rods that are subjected to high power densities (> 35 kW/m) for sufficiently long periods would have similar FGR, whether they are doped with Cr_2O_3-Al_2O_3 or not.

6.1.3 UO_2 fuel with other dopants

The effects of high burnup at low fuel temperatures on swelling and fission gas retention capacity of UO_2 doped with various metal (Mg,Nb,Ti) oxides have been investigated by Fujino et al. [13, 166]. More precisely, fuel pellets of undoped and doped UO_2, with different ^{235}U enrichments, were irradiated in a special capsule in the JRR-3M test reactor of Japan Atomic Energy Research Institute (JAERI) to burnups ranging from 19 to 94 MWd/kgU at temperatures 820-1100 K. The addition of Mg and Ti resulted in large grain size fuel. The Mg-doped pellets included Mg concentrations: 2.5, 5, 10, and 15 mol%. To vary burnup, the samples were prepared with ^{235}U enrichments: 6, 10 and 20 wt%. The sintering for these pellets was done at 1983 K, 5 h, in a stream of 4%H_2-He. Table 18 lists the grain sizes and densities for the 10 wt% ^{235}U samples with Mg-doped UO_2.

The aim of Fujino et al.'s study was to simulate and give information on irradiation behavior of the fuel pellet periphery region (rim zone) at high burnups. Thermal conductivity of unirradiated Mg-UO_2 was higher than that of undoped UO_2 (see section 3.1.3), which apparently seemed to also hold for irradiated specimens. Limited measurements indicated that the swelling of Mg-doped and undoped UO_2 as a function of burnup was similar. By the same token, fission product gas xenon retention capacity of the doped versus undoped fuels was similar. The study by Fujino and co-workers [166] indicates that the effect of metal oxide addition on fission gas release seems to be small or subsidiary at high burnup and low burnup, at least for the considered dopant concentrations.

One test rodlet charged with UO_2-BeO fuel has been irradiated to a burnup of about 36 MWd/kgU in the Halden test reactor, Norway. The rodlet was instrumented with fuel centerline thermocouples, a fuel stack elongation sensor and a rod gas pressure transducer.

Table 18: Fuel (10% ^{235}U) data used in Fujino et al.'s study [166].

Specimen	Mg content mol%	Grain size μm	Density g/cm^3
UO_2	-	30	10.51
UO_2-2.5Mg	2.5	47	10.52
UO_2-5Mg	5.0	50	10.49
UO_2-10Mg	10.0	NA	10.49[a]
UO_2-15Mg	15.0	71	10.19

[a] Calculated from fuel swelling data.

It was part of the IFA-716 test assembly, which also contained rodlets with undoped and chromia-doped UO_2 fuel [44, 281]. The BeO-doped fuel had 4.95 wt% ^{235}U and contained 3 wt% BeO. Figure 75 shows the fuel centerline temperature measured in the UO_2-BeO test rodlet, in comparison with temperatures in undoped UO_2 [287]. The measured temperatures for the UO_2-BeO fuel were significantly lower than for undoped UO_2 fuel, and fairly well reproduced by increasing the UO_2 thermal conductivity by 30 %. Thanks to the lower fuel temperature, no thermal fission gas release was detected at LHGRs that typically lead to substantial FGR in standard UO_2 fuel [287].

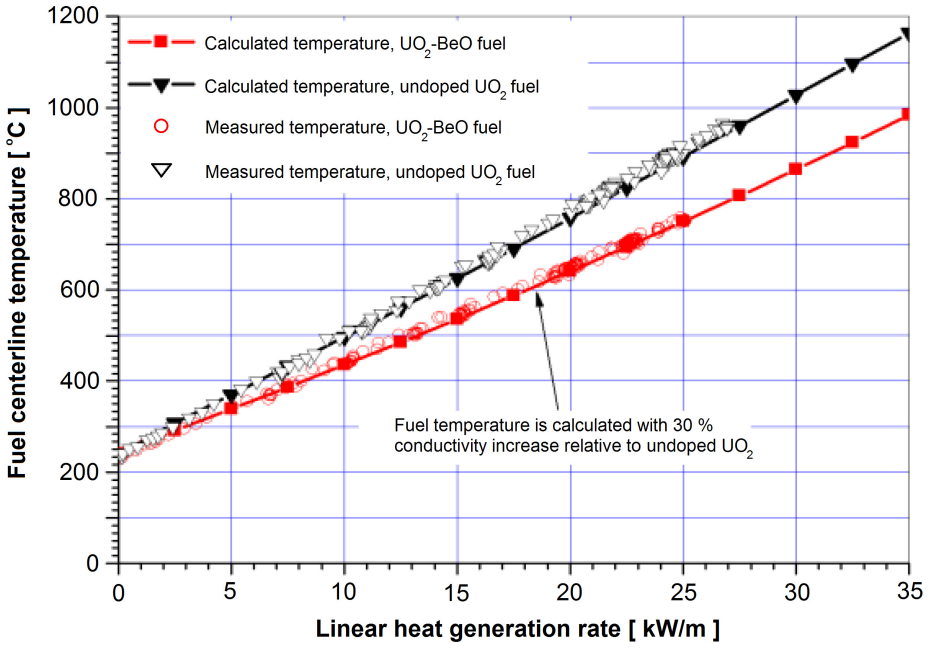

Figure 75: Fuel centerline temperatures for undoped UO_2 and UO_2 doped with 3 wt% BeO, measured during first rise to power in Halden IFA-716 [287, 288].

Also UO_2 with 0.1-0.2 wt% alumino-silicate (Al_2SiO_5) additive has been tested in the Halden reactor [287, 289]. The additive fuel had a grain size around 26 μm, in comparison with 11 μm for undoped UO_2 fuel that was included in the same test assembly for comparison. The initial porosity and density were almost identical for the two fuel materials. The large-grain doped fuel did not show any significant improvement in fission gas retention compared with the undoped fuel. This was attributed, in part, to more extensive micro-cracking of the doped fuel [290].

In this context, we should also mention a study by Une and coworkers [16] on the fuel

rim structure formation and high burnup fuel behavior of large-grained UO_2 fuel doped with 0.025-0.25 wt% alumino-silicate, with a grain-size range of 37-58 μm, versus that of standard (9-12 μm) grain-sized undoped UO_2. The fuels were irradiated in the Halden heavy water reactor up to a pellet average burnup of 86 MWd/kg. Une and colleagues examined the effect of grain size on the rim structure formation quantitatively, in terms of the average xenon depletion (or depression) in the pellet outer region, measured by electron probe microanalysis. The Xe depression in the high burnup pellets above 60 MWd/kg was proportional to: $\propto d_g^{-1/2}$ to $\propto d_g^{-1.0}$ (d_g: grain size), and the large-grained pellets exhibited noted resistance to the rim structure formation. Une et al. observed that a high density of dislocations preferentially decorated the as-fabricated grain boundaries, and the sub-divided grain structure was localized in that region. Although the swelling rate of the large-grained pellets up to the middle burnup of about 30 MWd/kg was larger than that for the standard pellet, it became smaller at higher burnups beyond 30 MWd/kg [16].

In contrast to the additives chromia and alumina, alumino-silicate is virtually insoluble in the UO_2 fluorite matrix, and it forms an intergranular glassy phase in the material. Global Nuclear Fuel (GNF) and its associated vendor companies have been developing alumino-silicate additive fuel for over 35 years, but in contrast to Framatome and Westinghouse, they have not yet introduced their additive fuel commercially in reload quantities. The alumino-silicate doped UO_2 fuel is claimed to have higher fission gas retention capacity than standard undoped fuel, as well as higher creep rate at high temperature [15, 291]. The latter attribute leads to improved fuel performance under conditions of pellet-cladding interaction; see below.

6.2 Integral tests

In the following, we summarize results from integral-type tests, conducted on fuel rods with additive UO_2 fuel pellets under simulated transient and accident conditions in dedicated test reactors.

6.2.1 Power ramp tests

Power ramp tests are essential for studying fuel rod failures caused by pellet-cladding interaction (PCI) and for establishing operational guidelines to avoid these failures in commercial power reactors. PCI-induced cladding failures may occur when there is a significant and rapid increase in the fuel linear heat generation rate [292]. Such power excursions may arise during normal power reactor operation, such as load following in PWRs and control-rod sequence exchange maneuvers in BWRs, but they are also encountered in AOO (Condition II) transients [293, 294]. Particularly challenging conditions arise when the power increase follows an extended period of low power operation, which leads to pellet-cladding gap closure by inward cladding creep.

The PCI performance of Framatomes Cr_2O_3-doped UO_2 fuel has been examined with a series of power ramp tests for both PWR and BWR fuel rods. Two common types of power ramp tests practiced for determining the PCI failure threshold are schematically shown in figure 76. Delafoy and Arimescu [259] evaluated the data from both type of ramp tests in

terms of the power ramp increment (or step to ramp terminal level, RTL), ΔP, versus the initial (or conditioning) power, P_i.

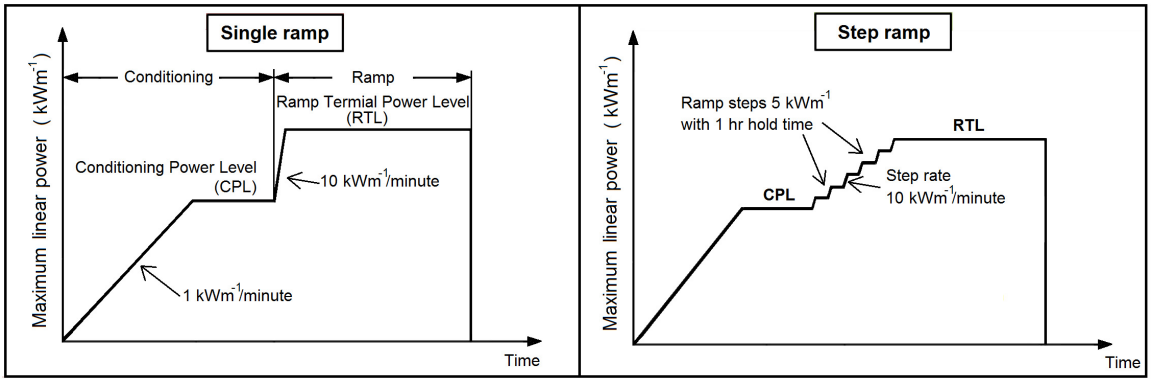

Figure 76: Power ramp test schemata; from [259].

The power ramp database of Cr_2O_3-doped UO_2 fuel, reported in [259], comprise 26 power ramps: (i) Twelve power ramps with 17×17 PWR fuel design rods, with either Zircaloy-4 or M5® cladding, (ii) Fourteen power ramp tests, of which 12 on ATRIUM™ 10 fuel rods with Zircaloy-2 non-liner cladding, which is the reference cladding configuration for Cr_2O_3-doped fuel employed in BWRs by Framatome.

The Cr_2O_3-doped UO_2 fuel ramp test results, from [259], are shown in figure 77 in terms of the aforementioned ΔP versus P_i. This figure also includes the failure threshold of the non-liner standard fuel database and the more recent Framatome liner rods power ramp results. From this data base, Delafoy and Arimescu [259] concluded that, for BWR applications, the advantage of the Cr_2O_3-doped fuel is an increase of 7 to 10 kW/m of the power increment failure threshold in comparison to that of the standard liner or non-liner non-doped fuel. For PWR usage, results with Cr_2O_3-doped UO_2 fuel rods show a power increment to failure that is 4 kW/m higher than for fuel rods with standard UO_2 pellets and M5® cladding.

The data in figure 77 indicate that the higher is the initial power P_i prior to ramp, the lower is ΔP to fuel rod failure. For undoped UO_2 fuel, the data cover up to $P_i \approx 32$ kW/m, whereas for Cr_2O_3-doped UO_2 fuel, P_i reaches at most ≈ 23 kW/m. So the failure propensity of the latter fuel up to around $P_i \approx 30$ kW/m and higher is not manifest from the data presented in figure 77. Furthermore, the authors in [259] do not specify or identify the fuel rod burnup behind the individual data points, which can have an impact on the outcome. Hence, a conclusion regarding the advantage in the ΔP value of Cr_2O_3-doped UO_2 fuel over undoped UO_2 fuel (drawn linear lines) is anticipatory rather than definite.

In addition to the aforementioned work, Nonon and colleagues [254] reported on the performance of Cr_2O_3-doped UO_2 fuels submitted to power ramps after pre-irradiation up to 30 MWd/kgU in a PWR. The power ramp tests were conducted in the OSIRIS test reactor at CEA Saclay, France. The ramp terminal power levels, after preconditioning at 20 kW/m for 12 h, were 47 and 53.5 kW/m for the doped fuel rodlets, whereas they were 40 and 44 for the standard UO_2 rodlets. The ramp rate from the preconditioning level to peak power was around 10 kW/m·min, and the ramp peak power hold time was 12 h. No fuel failures were detected after the ramps. The rodlets embracing Cr_2O_3-doped UO_2 fuel experienced a much larger cladding diameter deformation (about a factor of 2) during the ramps than the

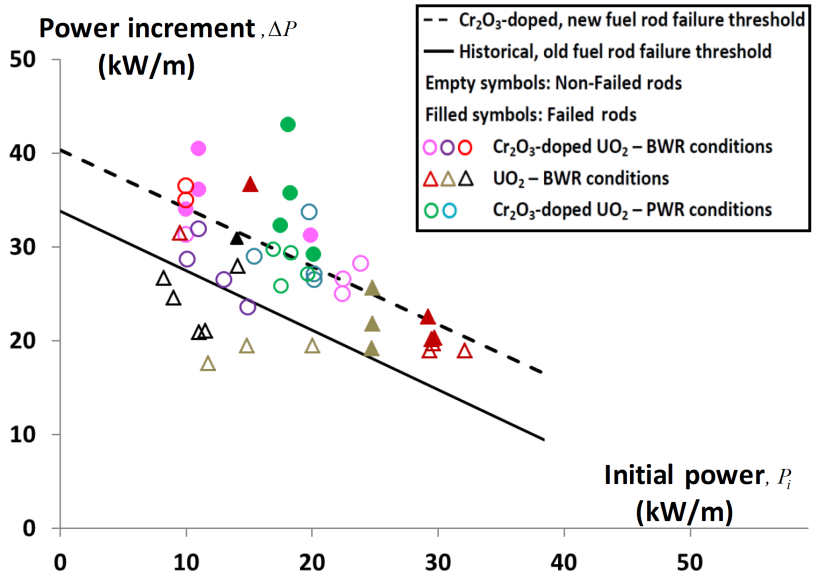

Figure 77: Ramp test results for Cr_2O_3-doped UO_2 fuel compared to standard non-doped UO_2 fuel: Power increment ΔP versus conditioning power P_i; from [259].

undoped rodlet, as we could interpret from figure 7 in [254]. The relative fission gas release from the two doped rods were 8 and 10%, which seem fairly low relative to what one has experienced from standard UO_2 fuel rodlets subjected to such ramps. Very few quantitative results regarding fuel characteristics and post-irradiation measurements are provided in [254].

The chemical thermodynamics of UO_2 fuel rods doped with Cr_2O_3 under power ramps has been studied by Riglet-Martial et al. [295]. Their work indicates that irradiated fuel, with nominal stoichiometry close to 2.0 and pellet average burnup around 30 MWd/kgU, under temperature gradients that would occur during a high-power transient, experiences a perturbation of its oxygen state, i.e. its oxygen chemical potential, μ_{O_2}. This is due to radial migration of oxygen from the hot center to the cold periphery of the pellet.

In the study by Riglet-Martial and co-workers [295], fuel rods charged with UO_2 doped with 0.2 wt% Cr_2O_3 were irradiated in commercial PWRs to a pellet burnup around 30 MWd/kgU. The rods were cut into sections and re-fabricated into rodlets that were power ramp tested in the OSIRIS reactor. A typical power ramp that the rodlets were subjected to is shown in the left panel of figure 76 (Single ramp). One of the rodlets experienced a ramp terminal power level of about 53 kW/m with a hold time of 12 h at RTL. After the ramp, sections of fuel pellets were examined by, among others, electron probe microanalysis (EPMA), which was used for measuring the concentration of chromium in solid solution across the fuel pellet radius. The recorded radial profile of soluble chromium, which is averaged over its fluctuations, for one of the power ramped pellets, is shown in figure 78(a) with the corresponding calculated pellet temperature distribution depicted in figure 78(b). These two figures are based on the data from figure 1b in [295].

In the low temperature part of the pellet, between the pellet surface ($r/a = 1$) and the radial position that reached about 1670 K ($r/a \approx 0.6$), the concentration of soluble chromium in the UO_2 matrix was measured around a constant value of 0.1 wt%, independent of temperature. The chromium fraction in excess of 0.1 wt% Cr was precipitated in UO_2 as an

oxide secondary phase. However, in the high temperature part of the pellet, between the radial position that reached ≈ 1730 K and the pellet center, the concentration of chromium in solid solution decreased down to 0.05-0.08 wt% (cf. figure 78), where the authors in [295] observed an abundant precipitation of metallic chromium as a secondary phase in the fuel.

In the low temperature part of the pellet ($T < 1730$ K), the measured concentration of soluble chromium was equivalent to that of the initial unirradiated fuel after sintering, measured to 0.102 ± 0.004 wt%, according to [295]. Moreover, as compared to the initial unirradiated fuel, the chemical form of the chromium precipitates of type Cr_2O_3 did not change during base irradiation, not even during ramp tests, irrespective of the burnup level and the speciality of the ramp, i.e. power level, duration, etc. The investigators therefore concluded that chromium in the UO_2 fuel remains in its initial condition attained after sintering in the low temperature part of a power ramp or in normal operating conditions [295].

In the high temperature part of the pellet ($T > 1730$ K), a rapid decrease of chromium dissolved in UO_2 was manifest by EPMA. This change was coupled to a massive metal chromium precipitation as secondary phase in UO_2. The authors of [295] state that "this change is an indication of a switch from a kinetically controlled chemical system to a thermodynamically controlled one." The thermal energy brought to the system beyond 1730 K exceeds the energy barrier of the transition.

Thermochemical analysis in [295] indicates that the oxygen chemical potential for an equilibrium state of a stoichiometric UO_2 fuel, irradiated to 30 MWd/kgU in temperature range of 1500 °C $\rightarrow$ 2000 °C, varies in the range of $\mu_{O_2} \approx -275 \rightarrow -200$ kJ/mol O_2. But, during the power ramp, in this temperature range and burnup, μ_{O_2} for the Cr_2O_3-doped UO_2 is reduced to $\mu_{O_2} \approx -394 \rightarrow -410$ kJ/mol O_2. The results imply that irradiated fuels, subjected to temperature gradients induced e.g. by power ramps, are exposed to strong oxidation-reduction perturbations, because of the radial migration of oxygen from the center to the periphery of the pellet. It is noted in [295], that the drop in amplitude of μ_{O_2} during a power ramp can depend on the temperature gradient across the fuel pellet, as a result of ramping, and the amount of oxygen available for migration. The latter quantity in turn is related to the initial fuel stoichiometry, fuel burnup, and the concentration of dopant in UO_2. The drop in μ_{O_2} during a power ramp clearly also occurs in undoped UO_2, but it does not lead to a massive chromium precipitation, instead to some fission product metal precipitations, such as Mo, Ru, Tc, etc.

The effect of oxygen redistribution during a power transient on irradiated fuel thermochemistry and on chemically reactive gas release from the fuel is further studied in [296]. Computations in [296] indicate that oxygen redistribution, even if moderate in magnitude, leads to reduction of metallic oxides (molybdenum dioxide, cesium molybdates, chromium oxide) in the vicinity of the fuel pellet center, and thereby, to release of a much greater quantity of fluid cesium.

Ramp test results for UO_2 fuel pellets doped with Cr_2O_3 and a combination of Cr_2O_3 and Al_2O_3 have been presented by Arborelius and co-workers [17]. These results are given for the Std Opt2, D1 and D3 type fuels, as defined in table 17, section 6.1.2. After pre-irradiation and PIE, two rod segments, Std Opt2 and D1, were refabricated into roughly 600 mm long rodlets that were power ramp tested under simulated BWR coolant conditions (9 MPa, 285°C) in the R2 test reactor at Studsvik Nuclear. The details of power ramping

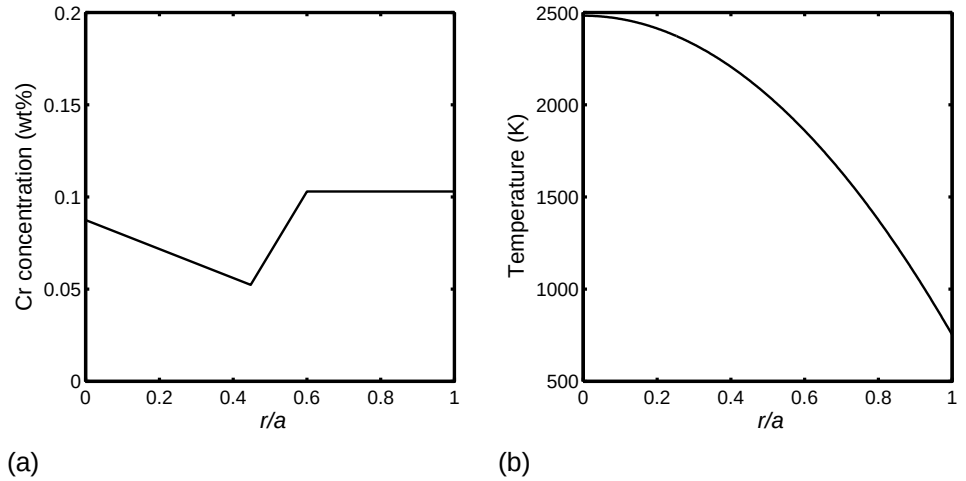

Figure 78: Radial profiles for (a) concentration of soluble chromium (averaged from EPMA data) and (b) fuel pellet temperature (calculated), corresponding to a power density of 52 kW/m. The figures are schematically drawn based on data from figure 1b in [295]. Here, r/a is the radial position, normalized with the pellet radius, a.

are described in [17]. The peak LHGRs reached for the Std Opt2 and D1 rodlets were 56.7 and 57.7 kW/m, respectively, with hold times at peak power from 7 to 12 hours. Both rodlets survived the ramp test. Post-irradiation examination after the ramp tests showed that the fractional FGR of D1 and Std Opt2 were 17.2 and 30.2%, respectively. Furthermore, ceramography of the peak power region of the rodlets revealed that the D1 pellets had formed a central hole, in contrast to the Std Opt2 pellets. This was attributed to D1's slightly higher linear power density (57.7 versus 56.7 kW/m).

In a similar experiment, referred to as a "bump test", two rodlets with Std Opt2 and D3 pellets were post-irradiated in the R2 test reactor to moderate power levels. The bump test irradiation was then initiated from a linear power density of 22 kW/m, followed by a power ramp to 46.4 and 45.1 kW/m for the Std Opt2 and the D3 rodlet, respectively, both with a hold time of 17.5 days. Following the test, the rodlets were punctured to examine fission gas release of the two pellet types. Measurements after the bump tests showed that the FGR was 29.7 and 20.5% for the Std Opt2 and D3 segment, respectively. Hence, the D3 pellets had roughly 30% lower FGR than the Std Opt2 pellets. The lower FGR measured in these doped fuels is primarily due to the much larger grains of the fuel (see table 17), as our computations on the influence of grain size on FGR in section 4.2 indicate.

In a parallel paper to that of Arborelius et al., the same group, led by Zhou [297], provided further data and computational results on the Westinghouse doped UO_2 versus undoped UO_2, subjected to the aforementioned ramp/bump tests. Here, we only refer to their profilometry measurements of the cladding outer diameter along the rodlets containing D1 and Std Opt2 pellets after the ramps; see figure 79. It is evident that the D1 fuel cladding experienced appreciably larger strains than Std Opt2.

Differences in fuel microstructure between standard and ADOPT^{TM} fuel after ramp testing are shown in figure 80 [256]. It is seen that in the standard UO_2 pellet, gas filled bubbles and pores have precipitated mainly at the grain boundaries. Fine pores can be observed within the grain at mid radius. In the ADOPT^{TM} fuel pellet, however, the pores have precipitated mainly within the grains, which are much larger than the grains of the standard

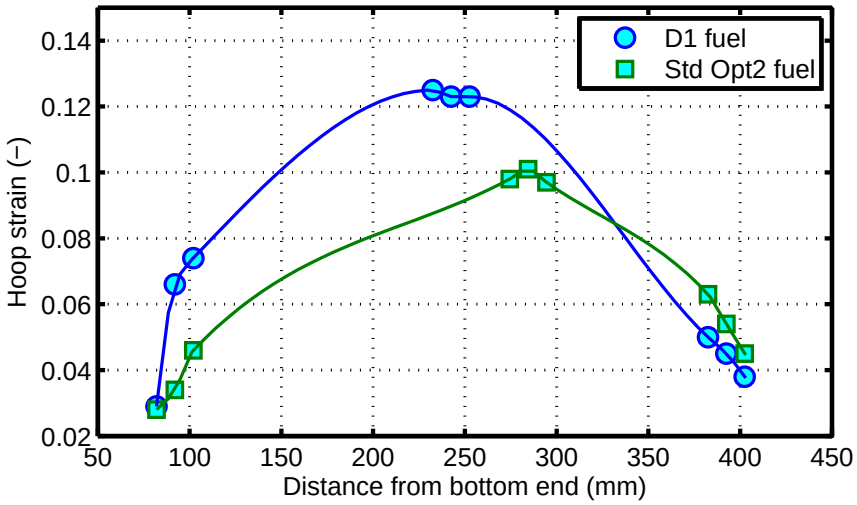

Figure 79: Cladding tube engineering hoop plastic strain after power ramp versus axial position along the rodlet. The strains are calculated based on the measured cladding outer diameter profiles and the nominal as-fabricated outer diameter of 9.63 mm; from table 2 of Zhou et al. [297]. The lines are piecewise cubic interpolations through the points; see table 17 for sample identification.

fuel. During a short-duration power excursion, this condition is availing with respect to the fission product gas release. However, no consequential difference between the standard and the doped fuel are expected during normal reactor operations [256].

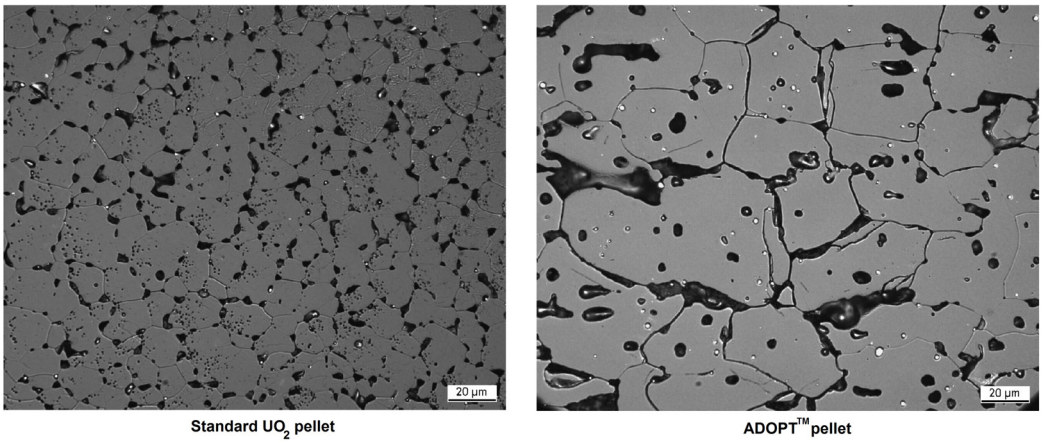

Figure 80: Micrographs of fuel about 2 mm from the pellet center, after ramp testing. The bar at the lower right corner indicates 20μm; from [256].

Wright and coauthors [256] concluded that the PCI advantage offered by doped pellets can be due primarily to the high temperature creep behavior of the material; see section 5. The "softer" pellets offer a PCI benefit, but only at the high temperatures experienced under ramp tests or postulated transients and accident scenarios in commercial LWRs. In normal reactor service, the fuel temperature is too low for PCI failure mitigation by this mechanism alone, and the ADOPT^{TM} pellet material has no advantage over undoped UO_2 fuel. This is illustrated by figure 81, which shows the results of compressive creep tests on un-irradiated UO_2 and ADOPT^{TM} fuel pellets at temperatures between 1300 and 1700 °C. In addition to the creep enhancement at high temperatures, changes of the oxygen potential and formation of modified fission product secondary phases as a result of the dopants in the pellets may

provide some protection against cladding stress corrosion cracking (an important aspect of PCI failures) at all temperatures. This effect, however, has not yet been substantiated in detail and supported by data, as can be judged from the open literature.

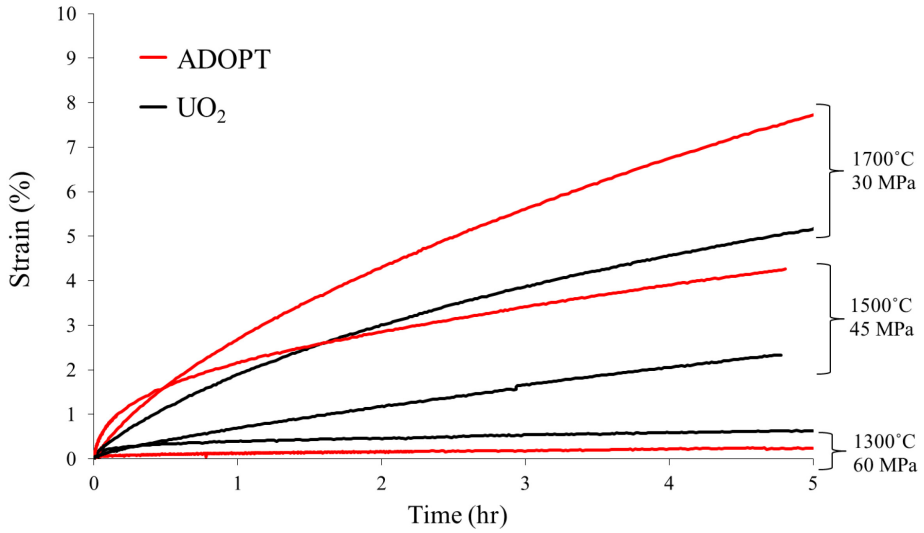

Figure 81: Comparison of undoped UO_2 and ADOPT^{TM} fuel pellets in compressive creep tests [284, 298].

Ramp test results for alumino-silicate additive UO_2 fuel, developed by GNF, have been presented by Davies and co-workers [291]. The data, which cover only moderate fuel burnups (< 25 MWd/kgU), show that the transient fission gas release was consistently lower for the doped fuel, in comparison with undoped UO_2 fuel that was ramp tested under similar conditions. This was attributed to the larger grains, typically 28-40 μm, in the alumino-silicate doped fuel [291]. Moreover, the fuel rod PCI failure threshold, in terms of peak LHGR, was reported to be significantly higher for the doped fuel. The improvement was attributed to the "softer" mechanical behavior of the alumino-silicate fuel at high temperature, e.g. the lower yield strength and the higher creep rate; see section 5.1. However, later studies [299] suggest that the alumino-silicate additive may also trap corrosive fission products, notably iodine, in the fuel grain boundaries. This would delay their diffusion to the pellet-cladding interface and mitigate stress corrosion cracking of the cladding tube.

6.2.2 RIA simulation tests

Most RIA simulation tests on UO_2 fuel with additives have been conducted on fresh (unirradiated) fuel: the only exceptions are two tests on chromia and chromia+alumina doped fuel, recently conducted in the Nuclear Safety Research Reactor (NSRR), Japan [300]. This should be borne in mind when discussing the behavior of doped versus undoped UO_2 fuel under RIA, since the behavior of fresh fuel is known to be much different from that of high-burnup fuel in this kind of accidents [276].

As a first example, we take the study of Shiozawa and co-workers, who carried out RIA simulation tests on fresh (U,Gd)O_2 fuel in the NSRR [301]. The tested fuel was of 17×17 PWR design with 6 wt% Gd_2O_3. The observed failure behavior was not notably different from that of fresh undoped UO_2 fuel of identical rod design. In particular, the failure

thresholds in terms of fuel specific energy deposition were similar: 1110-1150 J(gUO_2)$^{-1}$ for the (U,Gd)O_2 fuel versus 1055-1105 J(gUO_2)$^{-1}$ for the pure UO_2 fuel [301]. To the best of our knowledge, no RIA simulation tests have yet been performed or scheduled on pre-irradiated burnable absorber fuel.

Yanagisawa investigated the behavior of fresh Nb_2O_5-doped UO_2 fuel under RIA conditions by testing in the NSRR [302, 303]. In a 1991 paper [302], Yanagisawa reported the behavior of UO_2 fuel containing 0.29 wt% Nb_2O_5 additive, using 14×14 PWR fuel rods pre-pressurized with pure helium gas to 3.4 MPa. He found that the failure threshold, in terms of peak fuel enthalpy, of the pressurized doped fuel was equal to or greater than that of the earlier experimental data on undoped UO_2 fuel obtained from RIA simulation tests in the NSRR. The failure mechanism was ballooning of the cladding tube, followed by rupture, which was attributed mainly to the pre-pressurization. No significant differences were found in the failure mechanism between doped and undoped pre-pressurized fuels.

In a subsequent 1995 paper [303], Yanagisawa reported the results of RIA simulation tests, conducted in the NSRR on fresh un-pressurized fuel rods charged with UO_2 fuel pellets with and without Nb_2O_5 additive. More specifically, six test rods contained UO_2 fuel doped with 0.30 wt% Nb_2O_5 and four rods contained undoped UO_2 fuel pellets. The average grain size, determined by two-dimensional linear intercept method, was 29 μm for the doped fuel and 9 μm for the undoped one. All tested fuel rods, except for two doped fuel rods that had 100% He without pre-pressurization, had a gas composition of 95%He + l%Kr + 4%Xe. From the results of post-pulse irradiation examinations, such as visual inspection, dimensional measurement and metallography, the fuel failure threshold and failure mechanism were examined. The following conclusions were reached [303]:

- The failure threshold, in terms of fuel specific energy deposition, of the un-pressurized Nb_2O_5 doped fuel under RIA was almost equal to that of the previous NSRR experimental data on undoped UO_2 fuel. Moreover, no significant differences in the threshold for mechanical energy release existed between the un-pressurized Nb_2O_5 doped fuel and the previous NSRR experimental data for undoped fuel.
- The failure mechanism for both doped and undoped UO_2 fuel was cladding partial melting, followed by embrittlement of the thinned cladding wall. Bonding between fuel and cladding occurred at a lower fuel enthalpy level (1155 J(gUO_2)$^{-1}$) in the doped fuel than that (1427 J(gUO_2)$^{-1}$) in the undoped fuel. The bonding was usually accompanied by fuel pellet microstructural change at its periphery.

Similar RIA simulation tests were carried out in the NSRR on fresh 8×8 BWR fuel rods with alumino-silicates added to the UO_2 fuel pellets [304]. Four different types of additive fuels with various mixtures and concentrations of Al_2O_3 and SiO_2 were tested, in addition to undoped UO_2 fuel. The tested fuels varied with regard to grain size and density, depending on their composition; see table 19.

The tests revealed no measurable differences in failure thresholds between the fuels with alumino-silicate additives and standard UO_2 fuel. Likewise, no measurable difference was observed regarding the fuel enthalpy threshold for mechanical energy release. The permanent cladding diametral strain for the test rods with additive fuels increased with increasing energy deposition, very similar to the rods charged with standard UO_2 fuel, and the fuel rod failure mechanism appeared to be the same for both kinds of fuel: partial melting of the cladding, followed by cracking of the embrittled material [304].

Table 19: Alumino-silicate UO_2 fuels, RIA tested in the NSRR by Yanagisawa and co-workers [304].

Notation	Composition (ratio)	Concentration (vol%)	Grain size (μm)	Density (%TD)
HA	$Al_2O_3 : SiO_2 \approx 1 : 1$	≥ 1.6	25 - 27	96.3
LA	$Al_2O_3 : SiO_2 \approx 1 : 1$	≤ 1.6	23 - 25	95.7
HB	$Al_2O_3 : SiO_2 < 1 : 1$	≥ 1.6	12 - 14	96.3
LB	$Al_2O_3 : SiO_2 < 1 : 1$	≤ 1.6	10 - 13	95.7
STD	Pure UO_2	-	12 - 15	96.1

To date, only two RIA simulation tests have been conducted on pre-irradiated fuel rods with doped UO_2 fuel pellets. Both tests, LS-4 and OS-1, were recently done on 10×10-type BWR fuel in the NSRR [300]. The fuel pellet burnup was 48 and 64 MWd/kgU, respectively, in these test rods, which had been pre-irradiated in two commercial BWRs. The dopant in LS-4 was Cr_2O_3, whereas OS-1 contained Westinghouse ADOPT^{TM} fuel, e.g. UO_2 pellets doped with both Cr_2O_3 and Al_2O_3.

The LS-4 and OS-1 test rods were pulse irradiated in the NSRR with the coolant initially at ambient conditions (299 K, 0.1 MPa). While the LS-4 rod survived the test, the OS-1 rod failed with an axial crack at a fuel enthalpy increase of 160 J$(gUO_2)^{-1}$. The fuel enthalpy increase at failure for OS-1, so far evaluated, is lower than those obtained in previous tests on pre-irradiated BWR fuel rods with similar cladding hydrogen contents of about 200-300 wppm. Follow-up experimental and analytical studies have been launched to clarify dominant factors for the low failure enthalpy in OS-1. Firm conclusions have not yet been reached, but radially oriented hydride precipitates, which were observed to be dense in a specific azimuthal section of the cladding tube, are suspected to have aggravated the cladding embrittlement [300].

It is not possible to draw firm conclusions regarding possible effects of chromia/alumina dopants on the behavior of high-burnup UO_2 fuel under RIA from only two tests. Nevertheless, the outcome of OS-1 and computational analyses suggest that the doped fuel has a higher swelling rate late in life during base irradiation, with possible detrimental effects on cladding stress state and orientation of hydride precipitates in high-burnup fuel rods [305]. Further tests and analyses are needed on this issue.

Finally, it should be remarked that the current database of RIA simulation tests on pre-irradiated fuel rods contains eight tests on undoped UO_2 fuel with atypically large grains, and that the measured transient fission gas release was very low in all but one of these tests. It is therefore reasonable to assume that dopants that significantly increase the grain size of UO_2 fuel will reduce transient FGR in RIAs, but this hypothesis should be confirmed by additional RIA simulation tests on pre-irradiated doped fuel.

6.2.3 LOCA simulation tests

To the authors best knowledge, results from integral LOCA simulation tests on UO_2 fuel with additives are currently unavailable in the open literature. However, tests of this kind are being conducted as part of the fourth phase of the Studsvik Cladding Integrity Project (SCIP-IV), which is an international research project that is operated by Studsvik Nuclear

AB under the auspices of the OECD Nuclear Energy Agency (NEA) [306]. The testing is aimed at investigating fine fragmentation of high-burnup "non-standard" fuel materials under typical LWR LOCA conditions. The materials under study are UO_2 large-grain fuels with and without additives, (U,Gd)O_2 burnable absorber fuels and (U,Pu)O_2 mixed oxide (MOX) fuels. The objective is to investigate the fragmentation behavior of these fuels under light water reactor LOCA conditions and to compare it with that of standard undoped UO_2, which has been studied in earlier phases of SCIP [306].

6.3 Computer simulations and models

The tests and demonstration programs reviewed in sections 6.1-6.2 have two main objectives. The first one is to demonstrate the feasibility of new fuel materials by verifying their adequate performance under normal and off-normal operating conditions. The second objective is to produce data that are required for formulation and validation of models, which are used in computer programs for design and safety analyses. Various computer programs are applied to a wide range of operating conditions, from normal reactor operation to design basis accidents, and they should be validated against data produced under prototypical conditions. This poses a particular problem for the design basis accident (LOCA and RIA) conditions, for which very specific testing facilities are needed [275, 276]. Moreover, models and supporting data are required for the entire lifespan of the fuel, including intermediate and long-term storage of discharged fuel. An example of requirements placed on fuel behavioral models for design and safety analyses by regulatory authorities is given in [307].

In the following, we present a brief review of open literature publications on computer simulations and computer models for additive UO_2 fuels. The primary objective is to illustrate the overall maturity of models and computer programs for different kinds of fuel, and secondary, to help identify suitable candidates among various behavioral models for each type of fuel. The reviewed studies differ significantly with regard to scope, depth and rigour. Many are simple feasibility studies, in which the effects of a single notable material property of the additive fuel, e.g. thermal conductivity, on a few fuel performance parameters, e.g. the peak fuel temperature and enthalpy, are calculated for postulated operating conditions. Hence, the scope of the analysis is limited. The effects of fuel additives are in many cases considered only for a subset of the fuel properties, and the effects of additives on particularly complex phenomena, such as creep, fission gas release and gas induced fuel swelling, are usually not modeled at all. With regard to output from these analyses, we note that more than a few fuel performance parameters have to be considered for assessing the merits and demerits of candidate fuels. More precisely, performance metrics have been proposed, by which candidate fuels can be assessed relative to one another and to standard UO_2 in a systematic way [308, 309]. These metrics generally include a wide range of fuel performance attributes that cover the entire lifespan of the fuel, as well as different postulated operating, transient and accident conditions.

It is also common that simulations and computational studies on additive UO_2 fuels are presented without comparing the calculated results with experimental data. The results are usually compared only with results calculated for undoped UO_2 fuel, which serves as a reference for illustrating the pros and cons of the additive fuels. The lack of model-data comparisons is understandable, considering the shortage of experimental data on additive

UO_2 fuels in the open literature. However, this makes it difficult to assess the accuracy of the applied models.

In sections 6.3.1-6.3.4 below, we briefly present and discuss computational studies on different types of additive UO_2 fuels for light water reactors. An overview of the reviewed studies is given in tables 20 - 22, which summarize published simulations pertaining to normal reactor operation, transients, and design basis accidents. As indicated in these summary tables, the studies cover different types of fuel pellet materials, different fuel and reactor designs, and different aspects of the fuel behavior. More precisely, the tables include studies on reactor physics (neutronics), thermal-mechanics, and fission gas behavior of various types of additive UO_2 fuel. Some studies include not only non-standard fuel pellet materials, but also novel cladding tube materials, such as SiC-SiC composites and FeCrAl alloys. These cladding materials are not considered here. Moreover, computational studies on some non-UO_2 fuel materials not covered in this report (UN and U_3Si_2) may be found in a 2018 literature survey by Zhou and Zhou [165].

6.3.1 Burnable absorber UO_2 fuel

As mentioned in section 6.1.1, gadolinium bearing fuel has been used commercially since the 1970s, and computational models for this type of fuel are mature and adequately validated against experimental data [23]. For example, in a 1992 paper, Massih and co-workers [80] presented a set of models for (U,Gd)O_2 BWR fuel that were implemented in the STAV fuel rod performance program and validated against experimental data. The set comprised a microburnup model for calculating the radial power distribution in the fuel pellets and its evolution with time as the gadolinia is burnt, and models for the reduction in thermal conductivity and fission gas diffusivity caused by the gadolinia. The models were compared with results from separate effect tests, as well as data from post-irradiation examinations of commercial BWR fuel rods. Figure 82 reproduces calculated radial power distributions for 8×8 BWR UO_2 fuel with 3.95 wt% gadolinia, presented in [80]. The figure illustrates the significant change from an initially edge-peaked to a more uniform power distribution that takes place early in life as the gadolinia is burnt. The transition is usually completed at fairly low fuel burnup (<8 MWd/kgU). At higher burnup, the most noticeable effect of gadolinia is the reduction in fuel thermal conductivity.

Another early example of fuel performance models for (U,Gd)O_2 is the work of Billaux et al. [310], who presented models introduced in the COMETHE III-L program and their validation against data from two high burnup 17×17 PWR fuel rods charged with 3 wt% Gd_2O_3. More precisely, a microburnup model for calculating the radial power distribution in the (U,Gd)O_2 fuel pellets and a model for the reduction in thermal conductivity were introduced in COMETHE, and calculated results for fuel fission gas release, microstructure and deformation were successfully validated against data from post-irradiation examinations. In addition, specific features in the behavior observed for the (U,Gd)O_2 fuel were discussed in light of observations for UO_2 fuel of similar design and in similar operating conditions. It should be remarked that the investigated fuel had exceptionally high enrichment of ^{235}U (8.25 %) and were operated under challenging conditions in the BR3 test reactor, Mol, Belgium.

Computational analyses of (U,Gd)O_2 PWR fuel with the FAST fuel rod analysis program

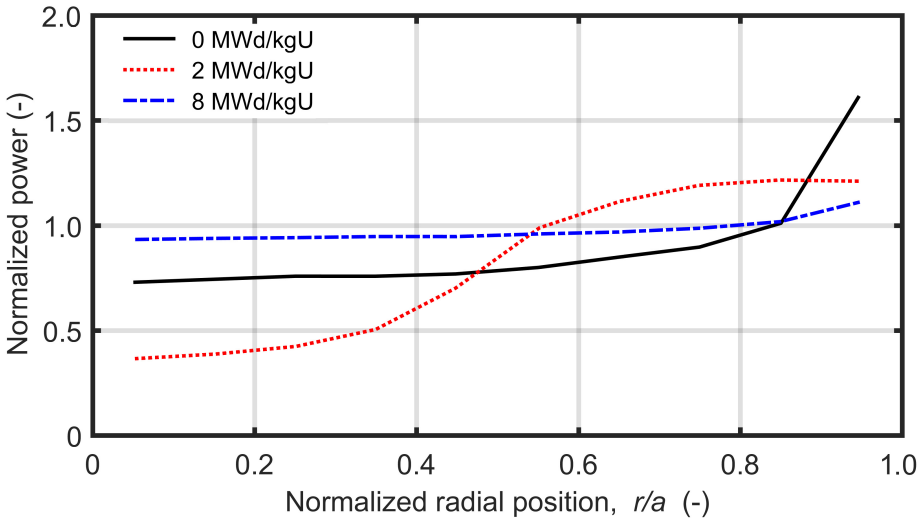

Figure 82: Calculated change in radial power distribution with burnup for UO_2 fuel with 3.95 wt% gadolinia, presented in [80]. The example pertains to 8×8 BWR fuel with 3.17 wt% ^{235}U and a pellet radius (a) of 5.22 mm.

have recently been presented by Richmond and Geelhood [311]. More precisely, they simulated UO_2 and (U,Gd)O_2 fuel rods from the IFA-681 experiment in Halden [312] with FAST, and compared calculated and measured fuel centerline temperature and fission gas release for the test rods. The considered rods were irradiated to a burnup of about 45 MWd/kgOxide under steady-state operating conditions in the Halden reactor. In addition, Richmond and Geelhood also simulated ramp test on UO_2 and (U,Gd)O_2 fuel rods with FAST and compared calculated versus measured transient fission gas release during the ramp [311].

The FAST (Fuel Analysis Steady-State and Transient) computer program [313] is a recent merger of the well-known FRAPCON (used for steady-state analysis) and FRAPTRAN (used for transient analysis) programs [188, 314]. These programs have been utilized by the United Stated Nuclear Regulatory Commission (US NRC) over more than 20 years for independent analyses of vendor fuel rod analysis models and methods that are used for evaluating the performance of LWR fuel relative to various safety analysis design limits. FAST, FRAPCON and FRAPTRAN share the same models and correlations for fundamental material properties. The only UO_2 pellet additive that the programs have explicit models for is gadolinia, since the addition of Gd_2O_3 has a significant impact on the fuel pellet radial power profile and thermal conductivity. In a recent thesis, Mattos [315, 316] applied FRAPCON to PWR UO_2 fuel with hypothetical concentrations of gadolinia from 2 to 7 wt% to study the impact of Gd_2O_3 on the thermal-mechanical behavior of a fuel rod up to a burnup of about 60 MWd/kgU. Comparisons were made with calculated results for undoped UO_2 fuel, but not with measured data.

6.3.2 Chromia/alumina doped UO_2 fuel

The thermal-mechanical behavior of chromia and chromia+alumina doped UO_2 has been modeled and simulated with the BISON fuel rod performance program [317], which is developed by Idaho National Laboratory (INL). As of today, BISON is probably the best

equipped independent fuel performance program for modeling this kind of additive fuel: fuel vendors like Framatome and Westinghouse that provide commercial chromia and chromia+alumina doped UO_2 fuels have their own programs [284, 307], but models in these computational tools are proprietary.

In 2018, Che et al. [318] used BISON for simulating chromia and chromia+alumina doped UO_2 under normal reactor operation (IFA-677 experiment on PWR fuel in Halden), transients (Framatome power ramp tests on PWR and BWR fuel in OSIRIS and Halden), and design basis accidents (postulated PWR large-break LOCA). Except for the LOCA, calculated results were compared with measured data. For the simulated normal operating conditions, the agreement between calculated and measured fuel temperature and FGR was overall satisfactory [318]. For the simulated power transients, the calculated transient FGR was in reasonable agreement with experimental data. The simulated hypothetical LOCA suggested that fuel rods with Cr_2O_3-doped UO_2 exhibit lower transient FGR, and consequently, reduced cladding ballooning, delayed fuel rod rupture, and less radioactive gas release upon fuel rod failure, compared to fuel rods with standard UO_2.

In the 2018 BISON analyses by Che et al., only two specific properties of the chromia and chromia+alumina doped fuel were considered in the calculations: the average grain size was increased to values reported for the modeled materials, and the intragranular fission gas diffusivity was increased by a factor 3 on an ad hoc basis. In later analyses of chromia and chromia+alumina doped UO_2 fuel with BISON [282, 319], the intragranular fission gas diffusivity has been modified based on atomistic calculations [245]. These modifications are presented and discussed in section 4.3.2. Also, the maximum densification of chromia and chromia+alumina doped fuel has been reduced in the BISON model, in comparison with the densification of standard UO_2 fuel [319]. Comparisons of calculated and measured fuel centerline temperature and fission gas release for test rods with chromia and chromia+alumina doped UO_2 fuel in the Halden IFA-677 and IFA-716 [44, 286] experiments show that BISON reproduces these parameters quite well. It should be remarked that no comparisons of calculated versus measured deformations have yet been made: development of specific creep and fracture models for chromia-doped UO_2 fuel is ongoing at INL [282].

Moreover, Richmond and Geelhood [311] have presented computational analyses of chromia and chromia+alumina doped PWR UO_2 fuel with the FAST fuel rod analysis program and compared the calculated results with measured in-core data for these kinds of fuel from the same Halden instrumented fuel assemblies (IFAs) as mentioned above. Although FAST lacks specific models for other UO_2 additives than gadolinia, Richmond and Geelhood concluded that the program provides reasonable predictions of fuel centerline temperatures for the investigated chromia and chromia+alumina doped fuels. More precisely, differences between calculated and measured temperatures were within uncertainty ranges previously established for undoped UO_2 fuel [311].

Very few simulations of the transient behavior of chromia or chromia+alumina doped UO_2 fuel have been reported in open literature. However, Zhou et al. [297] have reported from simulations of a single power ramp test and a few "bump tests" on Westinghouse 10×10 BWR fuel rods charged with ADOPT^{TM} pellets (see section 6.2.1) with the STAV fuel performance program. Details on the specific models used for the doped fuel are scarce in this publication, but it seems that only the fuel densification model differed from that of undoped UO_2 fuel [297]. Calculated post-test fission gas release and cladding tube

deformations were compared with measured data. Based on this comparison, the authors concluded that specific models for gaseous swelling, creep and fission gas diffusivity for ADOPT^{TM} fuel pellets were warranted [297].

6.3.3 Enhanced conductivity UO_2 fuel

An early computational study on UO_2-BeO fuel is due to McCoy and Mays [320], who compared the neutronic and thermal performance of doped fuels with either 4 or 9.6 vol% BeO with that of undoped UO_2. The comparison was made such that the doped fuel gave the same infinite neutron-multiplication factor, k_∞, at end of life and provided the same energy extraction per fuel assembly over its lifetime. The considered fuel was of 15×15 PWR design. Neutronic calculations with CASMO-3 indicated that, for fuel with 4 vol% BeO, only a small increase in enrichment was required to maintain the k_∞ at end of life. The smallness of the change was attributed to the neutron-multiplication reaction of Be with fast neutrons and the moderating effect of BeO. Moreover, the COPERNIC fuel rod performance program was adapted to compare the thermal performance of BeO-doped with undoped UO_2 fuel. The analysis was simplistic, since it was done merely by hypothetically increasing the fuel thermal conductivity by 0, 5, 10 or 50 % in order to simulate the effect of various concentrations of BeO. Other thermophysical properties of the fuel were assumed independent of BeO, and so were the mechanical properties and properties related to fission gas behavior. A challenging fuel rod operating history was simulated, including three Condition I transients and one Condition II transient. The calculations showed a significant improvement in thermal performance, as evidenced by reduced fuel temperature, internal rod pressure and fission gas release, even with modest (5-10 %) increases in thermal conductivity [320].

The neutronic performance of UO_2-BeO fuel in a VVER was studied by use of the SVL computer program by Kovalishin and co-workers [321]. They compared the performance of UO_2 fuel with 0, 3 and 5 wt% BeO at typical VVER operating conditions, accounting for the differences in fuel thermal conductivity, and hence, in fuel temperature. They studied the evolution in fuel assembly neutron multiplication factor from beginning of life to an assembly burnup of 40 MWd/kgU. They reported that the multiplication factor increased with increasing BeO content over the entire burnup range and concluded that the addition of BeO affects the neutron multiplication factor of the fuel assembly mainly by substantially decreasing the fuel temperature. They also stated that the reduced temperature of the BeO fuel is beneficial from a safety point of view, but that it leads to a decrease in resonance neutron capture by ^{238}U, and accordingly, in breeding of fissile ^{239}Pu. This effect can necessitate a shorter operating cycle, unless it is compensated for by higher fuel enrichment in ^{235}U.

Similar analyses of UO_2-BeO fuel have been published by researchers at the Texas A&M University, USA [322–324]. They used DRAGON and CRONOS for studying the neutronic performance of UO_2 fuel doped with either 5 or 10 vol% BeO in a 17×17 PWR fuel design. The doped fuel was simulated by enhancing its thermal conductivity, based on measurements on fresh (unirradiated) UO_2-BeO fuel. Similar to the results of Kovalishin and co-workers, their analysis showed that the enrichment of the UO_2-BeO fuel must be increased to maintain a cycle length equivalent to that for UO_2 fuel.

Zhang and co-workers [325] studied the neutronic performance of 17×17 PWR UO_2 fuel with additions of up to 30 vol% BeO, using the SERPENT depletion code. They reported that, by increasing the fraction of BeO in the fuel, more penalty on reactivity is caused by extra neutron capture. On the other hand, the increasing moderating effect of BeO increases the reactivity. Hence, these two opposite effects compete with each other to decide the final impact the cycle length. Moreover, a reactivity perturbation analysis showed that adding BeO in the fuel leads to less negative reactivity coefficients for moderator temperature and void fraction. These calculated results raise concerns for BeO fuel designs with regard to reactor core stability.

An early computational study on the neutronic performance of UO_2-SiC fuel is due to Wang [326], who used CASMO-3 for analyzing the effect of 0-15 vol% SiC added to UO_2 in a 15×15 PWR fuel assembly. More precisely, he reported the effect of various concentrations of SiC on infinite neutron-multiplication factor, k_∞, doppler coefficient and moderator temperature coefficient for equivalent fuel burnups from 0 to 60 MWd/kgU. Comparisons were made with undoped UO_2 fuel. The effect of SiC on reducing the fuel temperature was not fully accounted for in these comparisons: it was hypothetically assumed that all UO_2-SiC fuel, irrespective of SiC concentration, had 200 K lower temperature than undoped UO_2. Wang found that there is a reactivity penalty at the end of life, since the non-fissile SiC replaces UO_2. The neutronic calculations showed that k_∞ of UO_2 with 5, 10 and 15 vol% SiC was about 2.4, 4.9 and 7.6 % less than k_∞ of UO_2 fuel at a burnup of 60 MWd/kgU. The calculation also showed that, in UO_2 with up to 15 vol% SiC additives, the Doppler and moderator temperature coefficients remain negative.

The thermal effects of 10 or 15 vol% SiC added to UO_2 were superficially studied in computations with FRAPCON by Gomes and Silva [327], who used the Hasselman-Johnson model (see section 3.3.5) for estimating the thermal conductivity of these fuel materials. They also modified the heat capacity of the doped fuel, which was calculated from the heat capacities of the constituents by interpolation in weight fractions. Other properties of the fuel material were, however, assumed to be identical to those of undoped UO_2. They studied fuel centerline temperatures and fission gas release versus time for a high-power PWR fuel rod and compared calculated results for undoped UO_2 with those obtained for the two blends of UO_2-SiC. The results indicated that fuel centerline temperatures were reduced by 200-300 K at LHGRs of about 30-35 kW/m as a result of the SiC addition, thereby reducing also thermal fission gas release.

Researchers at the City University of Hong Kong, China, have modeled the thermal- mechanical behavior of various types of enhanced conductivity UO_2 fuel by use of a specifically developed in-house fuel performance program, named CAMPUS [273, 328–331]. The program is built upon the COMSOL Multiphysics finite-element platform and utilizes a two-dimensional axisymmetric geometrical representation of a single fuel pellet enclosed in the cladding tube. It is described in [331], where it is also benchmarked against more established fuel performance programs (FRAPCON, BISON) for the case of standard undoped UO_2 fuel. CAMPUS has been used for analyzing the thermal-mechanical behavior of UO_2-BeO fuel [328–330] and UO_2-SiC fuel [273]. In all these analyses, a similar approach was adopted for modeling the thermal-mechanical properties of the doped UO_2 materials:

- The thermal conductivity was defined as a function of dopant concentration, either by use of data from thermal conductivity experiments on doped fuel (see section 3.3) or

from the conductivities of the constituents by use of the Hasselman-Johnson effective thermal conductivity model (see section 3.3.5);

- The heat capacity was calculated from the heat capacities of the constituents by interpolation in weight fractions;
- Other fundamental thermal-mechanical properties (density, elastic properties, thermal expansion) were calculated from the properties of the constituents by interpolation in volume fractions;
- Effects of dopant on more complex phenomena, such as fuel pellet creep, densification, swelling and fission gas behavior, were not explicitly modeled. However, indirect effects on these phenomena, caused by the reduced fuel temperature, were captured.

The computational analyses were restricted to normal operating conditions. Comparisons were made between calculated results for undoped UO_2 fuel and calculated results for various concentrations of the dopant under study, but no comparisons were made to experimental data. A typical example of the analyses is given in figure 83, which shows the calculated centerline and surface temperatures of UO_2-SiC fuel pellets versus time under hypothetical PWR operating conditions. More precisely, the LHGR was assumed to rise linearly over three hours when the fuel was taken into operation (figure 83a) and then remain constant at 20 kW/m for four years (figure 83b). The calculated fuel centerline temperature drops with increasing BeO concentration, whereas the opposite is true for the pellet surface temperature.

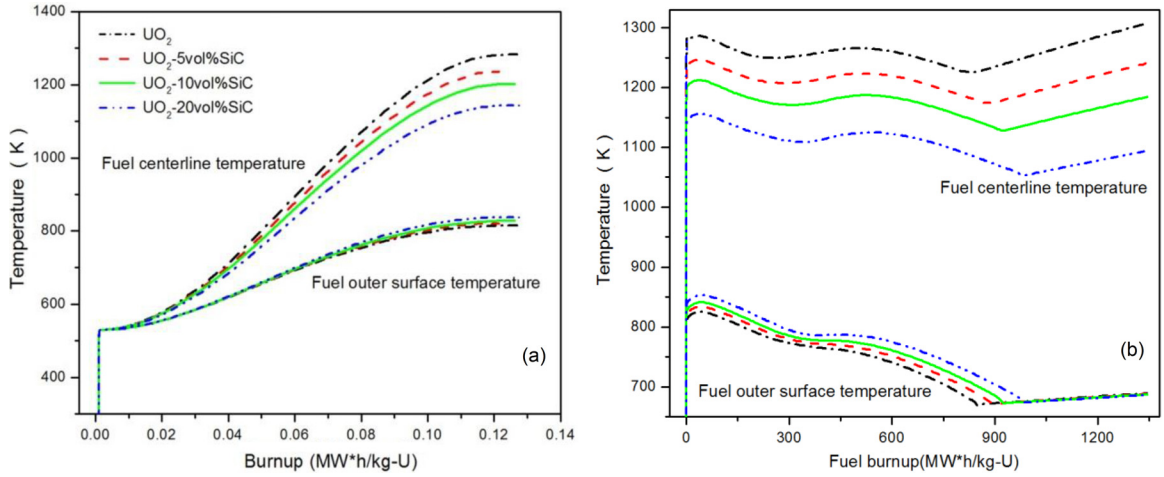

Figure 83: Centerline and surface temperatures of UO_2 fuel pellets with different additions of SiC, calculated with the CAMPUS fuel performance program [331].

Considering the limitations in applied models for the additive UO_2 fuel materials and the lack of validation against measured data, the modeling in [273, 328–331] must be viewed merely as exploratory assessments of the impact of various additives to improve UO_2 fuel performance by enhancing its thermal conductivity. The applied material properties were based on very limited composite material property data, extrapolated from unirradiated samples or interpolated in single component properties. Further work, in particular comparisons with experimental measurements from irradiated fuel samples, is required to refine and eventually validate the models.

The aforementioned approach for estimating the properties of enhanced conductivity UO_2 fuel has also been used in a computational study that addressed the thermal performance of BeO and SiC doped UO_2 under power-cooling mismatch (PCM) transients in a PWR, leading to departure from nucleate boiling (DNB) and overheating of the fuel [332]. The study was carried out with the COBRA-EN program, which is intended for thermal-hydraulic analyses of fuel assembly sub-channels. A 5×5 subchannel of a typical 17×17 PWR fuel assembly was modeled under four different postulated transient scenarios, all leading to DNB: the scenarios were based on tests used in an international benchmark activity [333]. The four transient scenarios were simulated for undoped UO_2, as well as for fuel with 10 and 20 vol% addition of either BeO or SiC. In addition, other cladding materials than Zircaloy were studied [332]. Calculated results for different combinations of fuel and cladding materials were presented in terms of thermal safety margins for fuel pellet and cladding. For Zircaloy cladding, this margin was defined as the margin between the calculated peak cladding temperature and 1200°C. For other materials, the margin was defined as the difference between the melting temperature of the fuel/cladding material and its calculated peak temperature. As expected, the fuel pellet thermal safety margins were significantly improved by addition of BeO or SiC. However, the thermal safety margins calculated for Zircaloy cladding were slightly reduced by these additives [332].

A key incentive for introducing enhanced conductivity UO_2 fuel is that the reduced fuel temperature afforded by this kind of fuel under normal reactor operation may mitigate the consequences of a loss-of-coolant accident: the lower fuel temperature before the accident leads to less stored heat that has to be removed by the emergency core cooling system (ECCS) in the course of the accident. Consequently, there are several computational studies on the potential benefits of BeO, SiC and other high-conductivity additives on the fuel behavior under postulated LOCAs in the open literature; see table 22. The following general comments should be made on these studies:

- As mentioned in section 6.2.3, results from LOCA simulation tests and experiments on doped UO_2 are currently unavailable in the open literature, which means that no model-data comparisons are made in the studies. At best, comparisons are made between the calculated LOCA performance of doped versus undoped UO_2 fuel;
- Fundamental thermo-physical properties of the doped fuel are typically estimated by use of the Hasselman-Johnson effective thermal conductivity model and by calculating the effective heat capacity from the capacities of the constituents by interpolation in weight fractions. These estimates are usually based on the properties of unirradiated materials and have no support for irradiated materials. Effects of the dopant on other material properties than fuel thermal conductivity, heat capacity and enthalpy are in most cases neglected;
- Calculated peak temperatures for fuel and cladding are usually the primary output reported from the analyses. Hence, possible effects of the additive on fuel pellet deformation or fission gas release under the accident are not addressed.

As a typical example, computational studies on the LOCA performance of PWR UO_2 fuel with 10 vol% BeO have been conducted at Purdue University, USA [187, 334]. Different LOCA scenarios were analyzed using different computer programs, but similar models were used for estimating the thermo-physical properties of the UO_2-10vol%BeO fuel in the programs. In [334], two scenarios of a PWR small-break (SB) LOCA were analyzed with

the RELAP5-MOD3.3 program: one scenario with reactor scram and water injection and another without scram and water injection. For the first scenario, the calculated fuel rod temperatures were initially lower for the UO_2-BeO fuel and reached the asymptotic state earlier than for the undoped UO_2 fuel. For the scenario without scram and water injection, the calculated fuel rod centerline temperatures were about 320 K lower for UO_2-BeO than for undoped UO_2 fuel [334]. In [187], four rather hypothetical LOCA scenarios, based on the MT-1 LOCA simulation test on undoped UO_2 fuel in the National Research Universal (NRU) reactor [335], were analyzed with the FRAPTRAN computer program. Apart from the beneficial reduction in pre-LOCA fuel temperature and stored energy afforded by the UO_2-BeO fuel, the analyses suggested that the addition of BeO gives rise to other advantages, e.g. reduction in rod internal gas pressure during the LOCA, and hence, to reduced risk for cladding ballooning and burst.

The behavior of UO_2 PWR fuel with additions of 10, 20 and 30 vol% BeO under postulated large-break and small-break LOCA has been studied by use of the RELAP5-MOD3.4 program by Yu et al. [336]. The focus of their study was reactor system simulations of various LOCA scenarios in a Chinese Pressurized Water Reactor (CPR1000), considering the specific thermal-hydraulic behavior of various candidate designs for accident tolerant fuel. For this reason, the analyses included not only UO_2-BeO fuel pellets, but also FeCrAl and SiC/SiC (SiC matrix reinforced with SiC fibers) composite cladding materials [336].

There are also a few computational studies on the performance of enhanced conductivity UO_2 fuel under reactivity initiated accidents; see table 22. Firstly, Chen and co-workers carried out thermal-hydraulic analyses of a PWR core under a postulated control rod ejection accident (CREA), occurring at hot full power (HFP) reactor conditions [337]. The analyses, which were done with the COBRA-EN program, were aimed to study the thermal-hydraulic behavior of various candidates for accident tolerant fuel under these accident conditions. Although the focus was on the propensity for film boiling and overheating of various cladding materials (Zircaloy, FeCrAl, SiC/SiC composites), the analyses were carried out with these cladding materials in combination with undoped UO_2 as well as UO_2 doped with different volume fractions of BeO and SiC. The different combinations of fuel and cladding materials were ranked with regard to calculated peak fuel and cladding temperatures, duration of film boiling phase, and the axial length of the fuel assemblies that experienced film boiling and overheating. The analyses were rather superficial, since the only fuel pellet properties that were modified with regard to the BeO/SiC additives were thermal conductivity (Hasselman-Johnson model) and heat capacity (interpolation in weight fractions). The calculated results suggest that, in comparison with Zircaloy, FeCrAl and SiC/SiC composite claddings have a higher propensity for film boiling and overheating during the considered RIA scenario, but that enhanced conductivity fuel pellets may alleviate this heat transfer deterioration [337]. A very similar study, dealing with the aforementioned cladding materials in combination with uranium nitride and uranium silicide fuel pellets, have been published by the same research group [338].

Secondly, He and colleagues [339] used an extended version of the FRAPTRAN program [188] for analyzing the behavior of PWR UO_2-BeO fuel under postulated RIA conditions. More precisely, they used conditions taken from the CIP0-1 RIA simulation test on a high-burnup UO_2 fuel rod in the CABRI test reactor, Cadarache, France [340], and applied the conditions to hypothetical fuel rods charged with UO_2 fuel doped with 5 or 10 vol% BeO. The postulated RIA, which was representative for a CREA occurring at hot zero power

(HZP) PWR conditions, was supposed to take place either at beginning of life or at a rod average burnup around 60 MWd/kgU. The steady-state operation of the fuel rods to this burnup was modelled with an extended version of the FRAPCON program [314]. The applied versions of FRAPCON and FRAPTRAN included material property models for UO_2-BeO fuel that were claimed to be validated against data from the Halden IFA-716 experiment [44, 281, 287]; see section 6.1.3. Unfortunately, the paper by He and colleagues [339] does not provide much information, either on the models used or on the results obtained.

6.3.4 UO_2 fuel with other dopants

In a 2013 study, Lee et al. [341] used the MARK-KS program for simulating the behavior of UO_2 fuel with additions of 1, 5 and 10 vol% graphene under a postulated large-break LOCA in an OPR-1000. The MARK-KS is a Korean analysis tool, combining RELAP5-MOD3.2 with COBRA TF. In the analyses, the Maxwell model (see section 3.3.5) was used for estimating the effect of graphene on fuel thermal conductivity: models for other properties of the fuel were not changed from their standard UO_2 versions. Hence, the analyses were rather superficial. In addition to the study of graphene as an additive to UO_2, Lee and co-workers also analyzed the impact of different cladding materials in combination with the doped fuel. More precisely, calculations were repeated for Zircaloy, ZIRLO and SiC cladding. Unfortunately, the thermal conductivity models used for these materials in the analyses are questionable.

Table 20: Computational studies on the performance of additive UO_2 fuels under normal LWR operation.

Type of additive	Additive concentration	Fuel rod design	Aspect(s) studied*	Computer program(s) used	Comparison with UO_2?	Validation against data?	Literature source(s)
Gd_2O_3	2-9 wt%	BWR, 8×8	N,T,G	PHOENIX,POLCA,STAV	Yes	Yes	[80]
	3.0 wt%	PWR, 17×17	T,G	COMETHE	Yes	Yes	[310]
	2.0,8.0 wt%	PWR	T,G	FAST	Yes	Yes	[311]
	2-7 wt%	PWR, 16×16	T,G	FRAPCON	Yes	No	[315, 316]
Cr_2O_3	2.0,8.0 wt%	PWR	T,G	FAST	Yes	Yes	[311]
	0.05-0.09 wt%	PWR	T,G	BISON	No	Yes	[318]
	0.05-0.16 wt%	PWR	T,G	BISON	No	Yes	[319]
	0.05-0.09 wt%	PWR	T,G	BISON	No	Yes	[282]
BeO	4.0,9.6 vol%	PWR, 15×15	N,T	CASMO-3,COPERNIC	Yes	No	[320]
	8.0,13.4 vol%	VVER	N	SVL	Yes	No	[321]
	5.0,10.0 vol%	PWR, 17×17	N	DRAGON,CRONOS	Yes	No	[322–324]
	0-30 vol%	PWR, 17×17	N	SERPENT	Yes	No	[325]
	2-36 vol%	PWR	T,G	CAMPUS	Yes	No	[328–330]
	10 vol%	PWR 17×17	T,M,G	FRAPCON	Yes	No	[342]
	10 vol%	PWR 17×17	T	FRAPCON	Yes	No	[343]
	10 vol%	PWR 17×17	T,G	FRAPCON	Yes	No	[344]
	5,10 vol%	PWR 17×17	T,M,G	FRAPCON	Yes	No	[339]
SiC	5-15 vol%	PWR, 15×15	N	CASMO-3	Yes	No	[326]
	10,15 vol%	PWR, 17×17	T,G	FRAPCON	Yes	No	[327]
	5-20 vol%	PWR	T,M,G	CAMPUS	Yes	No	[273]

* N: Neutronic behavior; T: Thermal behavior; M: Mechanical behavior; G: Fission gas behavior.

Table 21: Computational studies on the performance of additive UO_2 fuels under transients.

Type of additive	Additive concentration	Fuel rod design	Type of transient(s)	Aspect(s) studied*	Computer program(s) used	Comparison with UO_2?	Validation against data?	Literature source
Gd_2O_3	5.0 wt%	PWR, 17×17	Power ramp	G	FAST	No	Yes	[311]
Cr_2O_3	0.1 wt%	BWR, 10×10	Power ramp	M,G	STAV7.3	Yes	Yes	[297]
	0.16 wt%	PWR,BWR	Power ramp	M,G	BISON	Yes	Yes	[318]
BeO	4.0,9.6 vol%	PWR, 15×15	Overpower transients	N,T	CASMO-3,COPERNIC	Yes	No	[320]
	10,20 vol%	PWR, 17×17	PCM transients	T	COBRA-EN	Yes	No	[332]
SiC	10,20 vol%	PWR, 17×17	PCM transients	T	COBRA-EN	Yes	No	[332]

* N: Neutronic behavior; T: Thermal behavior; M: Mechanical behavior; G: Fission gas behavior.

Table 22: Computational studies on the performance of additive UO_2 fuels under design basis accidents.

Type of additive	Additive concentration	Fuel rod design	Type of accident(s)	Aspect(s) studied*	Computer program(s) used	Comparison with UO_2?	Validation against data?	Literature source
Cr_2O_3	0.16 wt%	PWR	LB LOCA	M,G	BISON	Yes	No	[318]
BeO	10 vol%	PWR	SB LOCA	T,G	RELAP5	Yes	No	[334]
	10 vol%	PWR	LOCA	T,G	FRAPTRAN	Yes	No	[187]
	10 vol%	PWR 16×16	LOCA	T,M	FRAPTRAN	Yes	No	[344]
	10,20,30 vol%	PWR	SB+LB LOCA	T	RELAP5	Yes	No	[336]
	10,20,30 vol%	PWR 17×17	RIA (HFP)	T	COBRA-EN	Yes	No	[337]
	5,10 vol%	PWR 17×17	RIA (HZP)	T,M	FRAPTRAN	Yes	No	[339]
SiC	10,20,30 vol%	PWR 17×17	RIA (HFP)	T	COBRA-EN	Yes	No	[337]
Graphene	1,5,10 vol%	PWR 16×16	LB LOCA	T	MARK-KS	Yes	No	[341]

* N: Neutronic behavior; T: Thermal behavior; M: Mechanical behavior; G: Fission gas behavior.

7 Summary and conclusions

In this report, we have reviewed the effects of various additives on UO_2 fuel behavior. Three categories of UO_2 fuel with additives for light water reactors (LWRs) were discussed: (i) Standard UO_2 fuel containing a small amount of metal oxide (≤ 0.2 wt%) to improve fuel mechanical performance, (ii) UO_2 with burnable absorber, such as Gd_2O_3, where an additive is used to control reactor power early during irradiation when fuel reactivity is high, (iii) composite UO_2 fuel mixed with a high-thermal conductivity material to enhance the effective thermal conductivity of pure UO_2, thereby improving its performance, i.e. reduce fuel temperature for the same power density.

Additives of the first category are introduced in UO_2 during fabrication of fuel pellets to enlarge fuel grain size, reduce fuel porosity and enhance fuel plasticity. These changes emanate from redistribution of point defects and generation of new ones in the UO_2 polycrystalline lattice. Doping of UO_2 with an additive would modify thermophysical properties, fission gas diffusion and release in and from fuel, high temperature creep of UO_2 and fuel densification during irradiation.

Among the thermophysical properties, the heat capacity and the thermal conductivity are most influenced by additives, however, for small concentrations (≤ 0.2 wt%) of dopants, for example Cr_2O_3 and Al_2O_3, the effects would be negligible. For certain dopants, such as MgO and the burnable absorber Gd_2O_3, where high concentrations (few wt%) are used in UO_2, the effects are non-negligible. MgO enhances thermal conductivity, while Gd_2O_3 reduces that quantity as a function of temperature. Also, for UO_2 doped with these additives, measured data and appropriate correlations as a function of dopant concentration are available, which are summarized in this report (section 3 and Appendix A). However, for the important dopants Cr_2O_3 and Al_2O_3, such data and correlations, which would depend on the dopant concentration, have not been reported in the literature. For these trivalent oxides, generically designated as M_2O_3, one may utilize the thermophysical quantities of Gd_2O_3-doped UO_2, with consideration given to the mass difference between the trivalent ions, as first approximations to the thermophysical properties of the doped fuel.

We have also reviewed data and models for thermal conductivity enhanced composite UO_2 reported in the literature. The additives for this category of fuel comprise BeO, SiC, synthetic diamonds or carbon-base substances. Virtually all the data, generated by experiments, and models reported in the literature for this kind of fuel are applicable to temperatures expected during normal LWR operation. That is, temperatures that fuel may experience during transients or off-normal conditions are not covered in these experiments.

Fission product gas retention and release in and from the fuel, and also gaseous fuel swelling, get affected by additives, namely (i) by the larger grain size, which extends the diffusion path to fuel grain boundaries, and (ii) by the change in fission gas diffusivity, caused by restructuring of point defects in the fuel. In general, oxides that simulate hypostoichiometry UO_{2-x}, e.g. by doping with Gd_2O_3 or Y_2O_3, reduce the cation (U) diffusion coefficient through increased trapping. In contrast, those that simulate hyperstoichiometry UO_{2+x}, e.g. by doping with Nb_2O_5, enhance the cation diffusion coefficient and show less pronounced trapping, thereby resulting in higher xenon release.

There is dearth of data on gas diffusivity in doped UO_2 fuels in the literature. Yet, there

are some data available regarding the effect of additives Al_2O_3, Cr_2O_3, SiO_2, TiO_2, MgO, and Nb_2O_5 on thermal diffusivity of ^{133}Xe in UO_2, obtained by means of a post-irradiation annealing technique [11, 50]. We have compared xenon diffusivities in these materials with each other and with that of undoped UO_2 as a function of temperature. The literature data indicate that xenon diffusivity in (slightly hyperstoichiometric Al_2O_3 and slightly hypostoichiometric MgO)-doped UO_2 is close to that in undoped UO_2; whereas the diffusivities in (Cr_2O_3, SiO_2, TiO_2 or Nb_2O_5)-doped are different from that in undoped UO_2. In particular, based on the limited available data, the xenon diffusivity (temperature range $\approx$ 1200 to 1900 K) in Nb_2O_5-doped UO_2 is consistently higher than in undoped UO_2; whereas in a slightly hyperstoichiometric Cr_2O_3-doped UO_2, the Xe diffusivity is close to or slightly higher than that in UO_2 above 1500 K and somewhat lower than that in UO_2 below 1500 K; see figure 46. Hence, appropriate Arrhenius-type relations for fission gas diffusivity (cf. table 12) should be considered, when such fuels are analyzed with a fuel rod modeling computer program.

We have made sample computations on fission gas release and intergranular gaseous swelling, using the aforementioned diffusivities with varying grain sizes as input to a standard model (section 4.2), to illustrate the effect of these parameters on gas release and swelling as a function of irradiation time under isothermal conditions. The results of our computations of thermal fission gas release versus irradiation time at temperatures 1600-2000 K, for Cr_2O_3-, Al_2O_3-, and Nb_2O_5-doped and "pure" UO_2 fuels indicated that among these, the Nb_2O_5-doped UO_2 has the largest FGR, while the Al_2O_3-doped the lowest. The relative gas release from the Cr_2O_3-doped sample depends on the temperature, e.g., at 1600 K, its release is in the order of that from "pure" UO_2, while at 2000 K, it is close to that from Nb_2O_5-doped samples. The gas release rate, as expected, was predicted to be inversely dependent on the fuel grain size, while it is roughly proportional to the square root of gas diffusivity in the fuel.

Regarding fuel gaseous swelling, our computations showed that among the aforementioned four fuel types, the Cr_2O_3-doped sample has the highest swelling rate, while the Nb_2O_5-doped sample has the lowest. It is the combination of gas diffusion, grain boundary saturation and grain size, which yields this behavior. It was observed that the larger is the grain size, the smaller is the swelling rate and the saturation value for the swelling.

The thermal creep rate of doped UO_2 was assessed in section 5. Fuel additives used in normal UO_2 fuel usually enhance the thermal creep rate of UO_2. The creep rate depends on the applied stress, temperature, grain size, and the O/U ratio [47]. The main feature of the creep rate versus stress curves is the separation between a region, in which the strain rate is linearly dependent on the applied stress, and one manifested by a power law creep, i.e. $\dot{\epsilon} \propto \sigma^n$, for which the stress exponent varies from $n \approx 4$ to $n \approx 6$. The former region is typical for diffusional creep, with a grain size rate dependence $\propto d_g^{-2}$, whereas the latter one is consistent with the dislocation climb creep, and is regarded to be independent of grain size. The transition stress from one region to another is considered to be temperature independent and may vary with grain size [47].

The limited published data show that there exist considerable variations in creep rate among additive UO_2 fuels. Measurements made on Nb_2O_5-doped UO_2 at a uniaxial stress around 20 MPa indicates that creep occurs by Nabarro-Herring diffusion with a $\propto d_g^{-2}$ dependent creep rate. It is observed that Nb_2O_5 addition causes a dramatic increase in the steady-state creep, as long as the niobium ion is kept in the Nb^{5+} valence state [248]. Similarly, Cr_2O_3

and Al_2O_3 dopants (up to 0.1 wt%) both enhance the thermal creep rate of UO_2 [250]. The creep tests made on these materials at temperatures 1620-1920 K and stress levels 40-65 MPa show that the creep rate may follow a dislocation climb mechanism.

In-reactor irradiation of Cr_2O_3-doped UO_2 fuel under normal BWR operation to exposures 30.5-33.5 MWd/kgU shows that the chromia-doped UO_2 fuel in-reactor volume increase is appreciably larger than that of undoped UO_2; see section 6.1.2. After the pre-irradiated rods were subjected to power ramps in a test reactor, the chromia-doped fuel exhibited less fission gas release than the undoped UO_2. However, the cladding diameter increase caused by pellet-cladding mechanical interaction was larger in the former than the latter. Also, rod axial length measurements, after long BWR exposures, indicate appreciably larger growth of chromia bearing rods than pure UO_2 rods [17, 283, 285]. The difference in fuel volume change, rod growth, and the cladding diametral increase under power ramps, partly can be due to the lower in-reactor densification of Cr_2O_3-doped UO_2 relative to pure UO_2 fuel. Suchlike fuel behavior has also been observed in a PWR [19]. Although significant operating experience has been accumulated for fuels doped with chromia, chromia+alumina and alumino-silicate, there are currently very few tests that address the performance of these materials under design basis accident conditions; see section 6.2.

With regard to modeling, the properties of UO_2 doped with chromia, alumina or alumino-silicate seem not too different from those of standard undoped UO_2 fuel, and existing analyses suggest that the behavior is fairly well reproduced by models for standard UO_2 merely by considering the larger grain size of the doped materials. To reproduce the behavior of UO_2 doped with chromia, chromia+alumina or alumino-silicate with higher fidelity, specific models are needed first and foremost for thermal fission gas release and high-temperature creep. Regarding burnable absorber (U,Gd)O_2 fuel, there exists an extensive database, and computational models for this type of fuel are generally mature and adequately validated against experimental data.

Over the past few years, a significant number of computational analyses on the neutronic and thermal-mechanical performance of enhanced conductivity UO_2 fuel materials have been published; see tables 20 - 22 in section 6.3. The UO_2 additives of primary interest are BeO and SiC. The models used for the properties of the enhanced conductivity fuel materials in these analyses are usually simple: they are typically based on very limited composite material property data, extrapolated from unirradiated samples, or interpolated in single component properties. Moreover, the effects of BeO or SiC are in many cases considered only for a subset of the material properties, and the possible effects of these additives on particularly complex phenomena, such as creep, fission gas release and gas induced fuel swelling, are usually not modeled at all. Considering these limitations in applied material models and the lack of validation against measured data, the modeling must be viewed merely as exploratory assessments of the impact of various additives to improve UO_2 fuel performance by enhancing its thermal conductivity. Extensive testing and qualification programs for these enhanced conductivity UO_2 fuels are needed to produce useful data for formulation and validation of fundamental behavioral models for these materials.

Acknowledgements. The work was sponsored by the Swedish Safety Authority (SSM) through grant DNR SSM2018-4298.

Notes

[1]*Frenkel defects* are vacancies and interstitials of the same species in equilibrium. For example in UO_2, one finds oxygen vacancies and oxygen interstitials in pairs. *Schottky defects* are only vacancies, e.g. when two oppositely charged ions leave their normal lattice positions forming two vacancies in the lattice structure [129].

[2]The oxygen partial pressure p_{O_2} is usually expressed in atmosphere (1 atm = 0.101 MPa) or in units of MPa divided by 0.101 MPa, $R = 8.314$ Jmol^{-1}K^{-1}, and T in kelvin.

[3]The name polaron is used for an electronic carrier with its associated distortion and polarization field. Charge carriers in solid oxides interact with the ion vibrations. The corresponding electron-phonon interaction controls the transport properties of the materials [129]. As electron travels through the conduction band of an ionic crystal it will generate a polarization cloud that will change its effective mass. The resulting quasi-particle is called a polaron. It is the behavior of the polarons rather than bare electrons that will determine the observed transport properties such as mobility, conductivity [156]

[4]In UO_{2+x}, the so-called Willis type cluster has the (2:2:2) configuration and consists of two oxygen interstitial atoms along <110> identified as $0'$, two oxygen interstitial atoms along <111> identified as $0''$, and two vacancies in the oxygen sublattice [345]; for a recent assessment see [346].

[5]Critical temperature, critical phenomena and phase transitions are central and active subjects in condensed matter physics; among introductory textbooks and reviews, we mention [347–349].

[6]In more detail, $\sigma = (a^3\omega_D/k_B v^3)^{1/2}$, where a^3 is the atomic volume, ω_D the Debye frequency, and v the phonon velocity.

[7]More accurately, Booth's short time approximation for post-irradiation annealing condition would result in $F(t) \approx \frac{6}{a_e}\sqrt{Dt/\pi} - 3Dt/a_e^2$, which is valid for $F \leq 0.9$ [220].

[8]BET device is used in surface area measurements of powder or batch samples and pore size and pore size distribution. The device determines needed gas quantity to cover the sample surface with a molecular layer and calculates surface area using Brunauer, Emmett and Teller (BET) theory [350].

[9] In the gaseous swelling model, for the grain boundary gas saturation, the Van der Waals equation of state is used rather than the ideal gas equation of state, as it is assumed in fission gas release computations for convenience. Moreover, an external pressure of 1 MPa is used in the VdW equation of state, rather than $P_{ext} = 0$, see [239].

[10]Here, the total unperturbed fission gas diffusivity for undoped UO_2 is expressed as

$$D = D_1 + D_2 + D_3,$$

where $D_1 = C_1 e^{-Q_1/T}$, $D_2 = C_2\sqrt{\dot{F}}e^{-Q_2/T}$, and $D_3 = C_3\dot{F}$ represent the intrinsic, irradiation-enhanced, and athermal contributions to fission gas diffusivity, respectively [231], with T being the temperature, $\dot{F}$ the fission rate per unit volume, and the other parameters constants.

[11]Shutdown Margin is defined as the amount of reactivity by which a full reactor core is subcritical at its present condition assuming all full-length control blades or rod cluster assemblies (shutdown and control) are fully inserted [351].

[12]Yield strength or yield stress, also called flow stress, is a stress level related to the onset of irreversible plastic deformation of solid materials [352].

[13]From the longitudinal velocity v_L and shear velocity v_S, Young's modulus and Poisson's ratio are:

$$E = \frac{v_L^2\rho(1+\nu)(1-2\nu)}{1-\nu}, \quad \nu = \frac{1-2(v_S/v_L)^2}{2-2(v_S/v_L)^2},$$

where E is Young's modulus, ν is Poisson's ratio, and ρ is the density of the pellet [352].

[14]Water-water energetic reactor. Pressure water reactor design originally developed in the Soviet Union.

Appendix A Thermophysical correlations

The correlations for thermophysical properties listed here are the enthalpy, the heat capacity (specific heat), the coefficient of thermal expansion, and the thermal conductivity. No such correlations or data have been published in the literature for the commonly utilized doped UO_2 fuels, such as dopants Cr_2O_3 or Al_2O_3-Cr_2O_3, as a function of temperature and dopant concentration, except for the widely used burnable absorber dopant Gd_2O_3. All the listed correlations below pertain to unirradiated fuels.

Enthalpy The $(U_{1-y},M_y)O_2$ enthalpy (J/mol) relative to the enthalpy at room temperature is given by [136]

$$\Delta H = H(T) - H(298.15), \tag{A.1}$$

where

$$H(T) = aT + \frac{b}{2}T^2 + \frac{c}{T} + \sqrt{2}\Delta H_f \exp\Big(\frac{\Delta S_f T - \Delta H_f}{2RT}\Big), \tag{A.2}$$

$$a = 79.8 \tag{A.3}$$
$$b = 0.1263y^2 - 0.0073y + 0.0061 \tag{A.4}$$
$$c = (1.68 - 1.48y) \times 10^6 \tag{A.5}$$

and

$$\Delta H_f = (-73880y^3 + 10190y^2 - 612.13y + 310) \times 10^3 \tag{A.6}$$
$$\Delta S_f = 61.969 - 45.56y \tag{A.7}$$

where ΔS_f, ΔH_f are the entropy and enthalpy of formation per Frenkel pair, T is temperature in kelvin and $R = 8.3145$ J/molK.

Heat capacity The corresponding expression for the heat capacity at constant pressure, $C_p = (\partial H/\partial T)_P$, is

$$C_p(T) = a + bT - \frac{c}{T^2} + \Delta C_p, \tag{A.8}$$

where

$$\Delta C_p = \frac{(\Delta H_f)^2}{\sqrt{2}RT^2} \exp\Big(\frac{\Delta S_f T - \Delta H_f}{2RT}\Big). \tag{A.9}$$

Thermal expansion The linear thermal expansion for $(U,Gd)O_2$ fuel is [136]

$$\begin{aligned} L(T)/L(273) = {} & 0.99866 + 7.2512 \times 10^{-6}T + (2.0463 \times 10^{-13}g^2 \\ & +3.4846 \times 10^{-11}g + 2.0653 \times 10^{-9})T^2, \end{aligned} \tag{A.10}$$

where $L(T)$ and $L(273)$ are the lengths at temperature T and 273 K, respectively, and g is wt% Gd_2O_3 in UO_2. The plots of thermal expansion versus temperature are shown in figure A1 for up to 0.5 wt% dopant concentration.

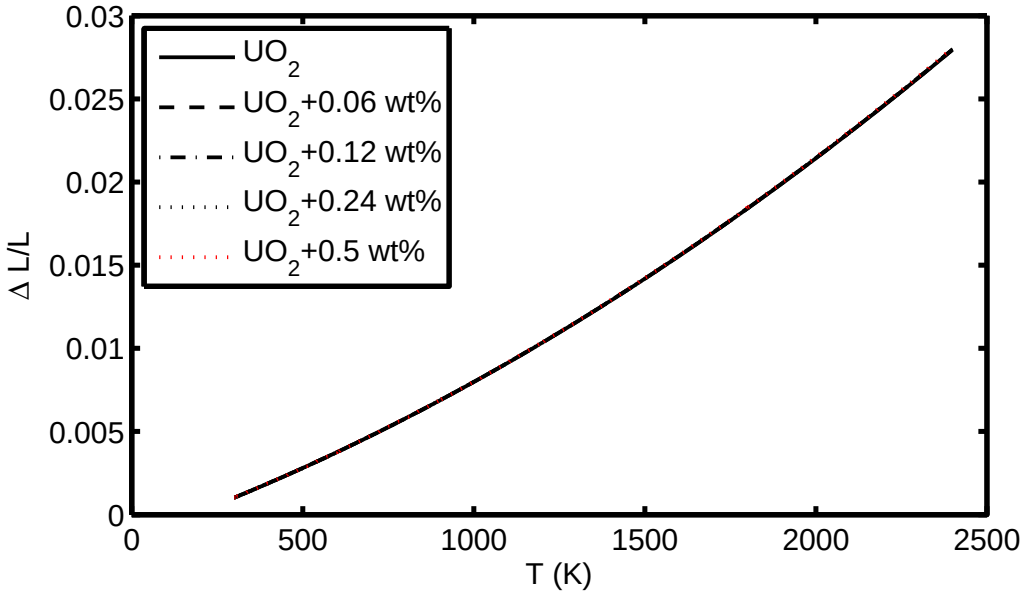

Figure A1: Calculated relative thermal expansion, $\Delta L/L \equiv [L(T) - L(273)]/L(273)$ according to eq. (A.10).

Thermal conductivity The thermal conductivity of (95% TD) fuel, from [145, 152], in the temperature range 300-2800 K is

$$\lambda = \frac{\lambda_0}{w}\arctan(w) + \frac{6600}{\bar{T}^{3/2}}\exp(-16.35/\bar{T}), \quad \text{(A.11)}$$

$$\lambda_0 = \frac{1}{2.45\times10^{-2} + 2.56\times10^{-4}T}, \quad \text{(A.12)}$$

$$w = 3.31\exp(-7.61\times10^{-4}T)\sqrt{x\lambda_0}, \quad \text{(A.13)}$$

$$\bar{T} \equiv T/1000; \quad \text{(A.14)}$$

where λ is in W/mK, the temperature T in K, λ_0 is the thermal conductivity for point defect free UO_2, w is the phonon scattering parameter by the impurities, and x is the Gd_2O_3 content (mole fraction). The first term in (A.11) represents the contribution from phonons (λ_p) and the second term that of electrons (λ_e). To adjust for fuel porosity, one may use the Maxwell-Eucken correction factor given by $\lambda = \lambda_{100}(1-P)/(1+\beta P)$, where λ_{100} is the thermal conductivity of fully (100%) dense material, P the fractional porosity, and $\beta = 0.5$ a constant.

The phonon thermal conductivity of Mg-UO_2 ($Mg_yU_{1-y}O_{2-y}$) fuel based on the work of Fujino et al. [166] has the form

$$\lambda_p = \frac{1}{A + BT}, \quad \text{(A.15)}$$

$$A = 2.268\times10^{-2} + 0.46047y - 2.6933y^2, \quad \text{(A.16)}$$

$$B = 2.32\times10^{-4} - 2.2\times10^{-4}y. \quad \text{(A.17)}$$

where λ_p is in W/mK, the temperature T in K and y is the Mg atom fraction in UO_2. The undoped UO_2 thermal conductivity pertains to that of 96%TD unirradiated fuel. The measurements were made from 473 to 1673 K [166].

Appendix B Thermal diffusivity versus thermal conductivity

Thermal diffusivity D_{th} can be defined through the classical heat equation:

$$\frac{\partial T}{\partial t} = D_{\mathrm{th}} \nabla^2 T, \tag{B.1}$$

where the dimension unit of D_{th} is the square of length divided by time or $[\mathrm{L}^2/\mathrm{T}]$. The thermal conductivity λ, on the other hand, is defined by the Fourier equation, which relates the heat flux J_h to temperature gradient, viz.

$$J_h = -\lambda \nabla T, \tag{B.2}$$

where λ has the dimension unit $[\frac{\mathrm{LM}}{\mathrm{T}^3\Theta}]$. Conservation of energy (heat balance) gives

$$\nabla \cdot J_h = -\frac{\partial H}{\partial t}, \tag{B.3}$$

where H stands for the total energy or enthalpy of the system, with its time derivative expressed as an integral over mass elements dm

$$\frac{\partial H}{\partial t} = \frac{d}{dt} \int_M c_p T dm = \int_M c_p \frac{\partial T}{\partial t} dm, \tag{B.4}$$

where c_p is the specific heat (at constant pressure) per unit mass. Writing the mass element in terms of the volume element as $dm = \rho d^3 r$, where ρ is the mass density, leads to

$$\int_M c_p \frac{\partial T}{\partial t} dm = \int_V \rho c_p \frac{\partial T}{\partial t} d^3 r. \tag{B.5}$$

The enthalpy can change by conduction through the surface (area element $d\mathbf{A}$) with the heat flux vector J_h, hence

$$\int_V \rho c_p \frac{\partial T}{\partial t} d^3 r = -\int J_h \cdot d\mathbf{A}. \tag{B.6}$$

Using the divergence theorem on the right-hand side of (B.6)

$$\int_V \rho c_p \frac{\partial T}{\partial t} d^3 r = -\int_V \nabla \cdot J_h d^3 r, \tag{B.7}$$

or the equivalent differential form

$$\rho c_p \frac{\partial T}{\partial t} = -\nabla \cdot J_h. \tag{B.8}$$

Substituting equations (B.1) and (B.2) in (B.8) yields $\rho c_p D_{\mathrm{th}} \nabla^2 T = \lambda \nabla^2 T$, or

$$\lambda = \rho c_p D_{\mathrm{th}}. \tag{B.9}$$

Appendix C Thermal boundary conductance

Thermal conductivity of a composite solid is affected, not only by the embracing particle concentration, size and distribution, but also, by the interphase thermal boundary conductance in the bulk. Indeed, the interfacial thermal conductance, also called the Kapitza conductance, is a crucial parameter that affects the heat flow within the bulk [196].

Two models are traditionally used to calculate the thermal boundary conductance, namely, the acoustic mismatch model (AMM) and the diffuse mismatch model (DMM). In these models and calculations, the phonon dispersion relationship, i.e. the phonon frequency versus phonon wave vector, is usually approximated by a linear relationship or the Debye model; see e.g. [127, 138]. This is accurate for wave vectors close to the Brillouin zone center, but deviates significantly for wave vectors near the zone edges. The acoustic mismatch model posits a perfect interface, and treats phonons as plane waves and the materials as continua (no lattice), i.e. the phonons specularly reflect or refract through the interface in the AMM. For phonons with wavelengths much longer than typical interatomic spacings, the continuum approximation might be expected to be accurate. However, studies have shown that the AMM breaks down for high frequency phonons, which can be produced at high temperatures and get scattered diffusely by a rough interface [196].

The simplest description deducible from the AMM is that each material can be assigned an acoustic impedance Z equal to the product of the mass density and the phonon velocity, $Z_i = \rho_i c_i$. The formula for the transmission probability from side $i = 1$ to side 2, for a phonon with normal incidence, may read [196]

$$\mathcal{T}_{1\to 2} = \frac{4Z_2 Z_1}{(Z_1 + Z_2)^2}. \tag{C.1}$$

Furthermore, the number of phonons of energy $\hbar\omega$ incident on a small area dA of the interface per unit time at angle of incident between θ_1 and $\theta_1 + d\theta_1$ will be

$$\frac{1}{2} c_1 N_1(\omega) \cos\theta_1 d\theta_1 dA d\omega, \tag{C.2}$$

where c_1 is the group velocity of the longitudinal phonons in the first medium and $N_1(\omega)d\omega$ is the number of phonons of energy lying between $\hbar\omega$ and $\hbar(\omega + d\omega)$ per unit volume of the first medium. The value of $N_1(\omega)$ is given by the number of degrees of freedom of the lattice lying between ω and $\omega + d\omega$ and by the Bose-Einstein energy distribution:

$$N_{1,j}(\omega)d\omega = \frac{\omega^2 d\omega}{2\pi^2 c_{1,j}^3 \big(\exp[\hbar\omega/k_B T] - 1\big)}, \tag{C.3}$$

where $c_{1,j}$ denotes the phonon propagation velocity in side 1 with mode j, ω the phonon angular frequency, k_B the Boltzmann constant and $\hbar$ is the reduced Planck constant.

In order now to compute the heat transfer coefficient across the boundary, additional assumptions are made: Solids are assumed to be *isotropic Debye solids*, with the generalization that the longitudinal and transverse speeds of sound are different. Then, for frequencies below the Debye cutoff frequency, ω_D, the thermal boundary conduction h_c is [196]

$$h_c = \frac{1}{2} \sum_j c_{1,j} \Gamma_{1,j} \int_0^{\omega_D} \hbar\omega \frac{dN_{1,j}}{dT} d\omega, \tag{C.4}$$

where ω_D is the Debye frequency and

$$\Gamma_{1,j} = \int_0^{\pi/2} \mathcal{T}_{1\to 2}(\theta, j) \cos\theta \sin\theta d\theta. \tag{C.5}$$

Inserting equation (C.3) in (C.4) and simplifying, we can write

$$h_c = \frac{\omega_D^3}{4\pi^2} \sum_j c_{1,j}^{-2} \Gamma_{1,j} k_B \Big(\frac{T}{\Theta_D}\Big)^3 \int_0^{\Theta_D/T} \xi^4 \frac{e^\xi}{(e^\xi - 1)^2} d\xi, \tag{C.6}$$

with $\xi = \hbar\omega/k_B T$ and $\Theta_D = \hbar\omega_D/k_B$ is the Debye temperature. Recall now that in the Debye theory, the specific heat of a solid is expressed as [138]

$$C_V = 9nk_B \Big(\frac{T}{\Theta_D}\Big)^3 \int_0^{\Theta_D/T} \xi^4 \frac{e^\xi}{(e^\xi - 1)^2} d\xi, \tag{C.7}$$

where n is the number of ions in the crystal per unit volume. Hence,

$$h_c = \frac{\omega_D^3}{36\pi^2 n} \sum_j c_{1,j}^{-2} \Gamma_{1,j} C_V. \tag{C.8}$$

Assuming that $\mathcal{T}_{1\to 2}$ is angle invariant, putting equation (C.1) in (C.8) and averaging

$$h_c \approx \frac{\omega_D^3}{18\pi^2 n} c_1^{-2} \frac{\rho_1 c_1 \rho_2 c_2}{(\rho_1 c_1 + \rho_2 c_2)^2} C_V. \tag{C.9}$$

In the literature, however, authors often use the formula [115, 165, 353]

$$h_c \approx \frac{1}{2} \rho_1 c_1^3 c_2^{-2} \frac{\rho_1 c_1 \rho_2 c_2}{(\rho_1 c_1 + \rho_2 c_2)^2} C_1, \tag{C.10}$$

for computation when using the AMM. Here the subscripts 1 and 2 refer to matrix and particle (inclusion), respectively. Furthermore, the phonon velocities v_1 and v_2 may be estimated by the three phonon wave speeds (two transverse and one longitudinal) [354]

$$\frac{1}{v_{i,l}^2} + \frac{2}{v_{i,t}^2} = \frac{3}{v_i^2}, \qquad i = 1, 2. \tag{C.11}$$

where subscripts l and t denote the longitudinal and transverse components of phonon velocities. Note that in equation (C.10), C_1 is the specific heat of the matrix.

Let us compute h_c according to formulae (C.10)-(C.11) as a function of temperature for the UO_2-SiC system. The UO_2 longitudinal and transverse phonon velocities are 5552.7 and 2841.8 m/s [355], respectively, and those of SiC are 11800 and 7600 m/s [356], respectively. The phonon velocities of UO_2 and SiC, according to equation (C.11), are 3272.8 and 8470.9 m/s, respectively. The density and the specific heat of UO_2 as a function of temperature can be computed from relations given in [169] or [197]. The SiC density at room temperature is $\rho_{\mathrm{SiC}} = 3200$ kg/m^3 [173]. This quantity as a function of temperature can be estimated from $\rho_{\mathrm{SiC}} = 3200[1 - 3\alpha(T)(T - 298)]$, where $\alpha(T)$ is the coefficient of thermal expansion [173] and T is temperature in kelvin. Below are the computed values for the UO_2 specific heat and h_c at several temperatures (cf. [115]):

Quantity	Unit	$T = 373$ K	$T = 573$ K	$T = 1173$ K
C_p(UO_2)	J/kgK	258.20	304.66	314.20
h_c(UO_2-SiC)	W/m^{2}K	1.69×10^8	1.98×10^8	2.02×10^8
h_c(UO_2-BeO)	W/m^{2}K	1.95×10^8	2.28×10^8	2.32×10^8

In this table, we have also listed the computed values of h_c for UO_2-BeO. The BeO longitudinal and transverse phonon velocities are taken to be 10222 and 7033 m/s [268], respectively. The phonon velocity of BeO according to equation (C.11) is 7745.6 m/s. The BeO density at room temperature is $\rho_{\mathrm{BeO}} = 2870$ kg/m^3 and the coefficient of thermal expansion $\alpha(T)$ is calculated from the expression given in [204].

The diffuse mismatch model, which is more applicable at higher (above room) temperatures, assumes complete diffuse scattering at the interface. The transmission probability is then related to the phonon density of states on both sides of the interface. Diffuse scattering becomes important at higher temperatures, e.g. at reactor fuel operating temperatures, and for non-perfect interfaces. In DMM within the Debye theory the transmission probability or coefficient is expressed as [196]

$$\mathcal{T}_{1\to 2} = \frac{\sum_j c_{2,j}^{-2}}{\sum_j c_{1,j}^{-2} + \sum_j c_{2,j}^{-2}}. \tag{C.12}$$

Assuming that $\mathcal{T}_{1\to 2}$ is angle invariant, putting equation (C.12) in (C.8) and averaging

$$h_c = \frac{\omega_D^3}{36\pi^2 n} \sum_j \frac{c_{1,j}^{-2} c_{2,j}^{-2}}{c_{1,j}^{-2} + c_{2,j}^{-2}} C_V. \tag{C.13}$$

Here, C_V and ω_D are the specific heat and the Debye frequency of the base material (UO_2). We note that for UO_2, $\Theta_D \approx 395$ K [355]; hence, $\omega_D = (k_B/\hbar)\Theta_D \approx 5.17\times 10^{13}$ Hz.

Experiments, however, indicate that the DMM with Debye approximation does not fully capture all the thermal transport mechanisms occurring at the interfaces [196, 357]. Hence, for quantitative analysis of thermal boundary conductance at high temperatures, modeling beyond the Debye theory is necessary [358–360]. In a recent article, Zhu et al. [195] have computed the thermal boundary conductance of UO_2-BeO by DMM, based on full band phonon dispersion using density functional theory (DFT). Thereafter, they compute the effective thermal conductivity of the composite using the Hasselman and Johnson (HJ) formula alluded in section 3.3.5, which they compare with measurements.

Zhu et al.'s computations indicate that, when the temperature is greater than 70 K, both AMM and DMM based on acoustic phonon modes and Debye approximation yield an order of magnitude larger thermal resistance than that based on full band DFT computations [195]. This is because the optical mode phonons in UO_2 get activated at temperatures beyond 70 K and become the main carriers of heat through the interface. In addition, for UO_2 containing dispersed BeO, the HJ model for a matrix with a random distribution of spherical dispersions was used. They found that the results of the HJ model with the DMM based DFT computations can fit experimental data well; indicating that the vibrational mismatch between UO_2 and BeO considered by DMM is the main mechanism for attenuating the heat flux through UO_2/dispersed BeO interface. For UO_2 containing continuous BeO, however, they found that using the interface thermal conductance computed by DMM and DFT overestimates the thermal conductivities compared with the experimental data; indicating that DMM is not applicable to the interface between UO_2 and continuous BeO [195].

Appendix D Fission gas release equations

The mole of gas in the intergranular gas bubbles per unit area of grain boundary at time t, $N_{gb}(t)$, which considers the influence of irradiation-induced re-solution of gas atoms has been derived in a number of publications in the past [232, 234, 239]. Here, the resulting equations used in the computations of section 4.2 are outlined as follows: For $\tau/a^2 \leq 1/\pi^2$:

$$N_{gb}(\tau) = \frac{2\beta_e}{h_1}\Big(\tau + \frac{1}{h_2 h_3} - \frac{h_2 \exp(h_3^2\tau)\mathrm{erfc}(h_3\tau^{1/2}) + h_3 \exp(h_2^2\tau)\mathrm{erfc}(-h_2\tau^{1/2})}{h_2 h_3 (h_2 + h_3)}\Big) + O(\tau^{\infty}), \tag{D.1}$$

where

$$h_1 = \frac{\lambda\nu(t)}{D(t)}, \tag{D.2}$$

$$\beta_e = \frac{\beta(t)}{D(t)}, \tag{D.3}$$

$$h_2 = -\frac{h_1}{2} + \sqrt{\frac{h_1^2}{4} + \frac{h_1}{a}}, \tag{D.4}$$

$$h_3 = \frac{h_1}{2} + \sqrt{\frac{h_1^2}{4} + \frac{h_1}{a}}, \tag{D.5}$$

$$\tau(t) = \int_0^t D(s)ds. \tag{D.6}$$

Here, the ratios h_1 and β_e are assumed to be time-independent, a is the grain radius, ν is the gas atom re-solution rate (frequency) off the intergranular gas bubbles, λ is the corresponding re-solution distance back into the grain, D is the effective fission gas diffusion coefficient in the fuel matrix, and β is the fission gas production rate per unit volume.

For late times, $\tau/a^2 > 1/\pi^2$:

$$N_{gb}(\tau) = \frac{2\beta_e a}{3 + h_1 a}\Big(\tau - \frac{a^2}{5(3 + h_1 a)}\Big) + \sum_{m=1}^{\infty} \frac{4\beta_e a^3 e^{-(u_m/a)^2\tau}}{u_m^2[u_m^2 + a h_1(3 + a h_1)]} \tag{D.7}$$

where

$$u_m = \arctan\Big(\frac{a h_1 u_m}{u_m^2 + a h_1}\Big) + m\pi. \tag{D.8}$$

The model assumes that thermal fission gas release occurs when $N_{gb} = N_{gs}$, where N_{gs} is the grain boundary fission gas concentration upon saturation, which is calculated from an ideal gas equation of state

$$N_{gs} = \frac{8.72 \times 10^{-9}}{T}\Big(\frac{2\gamma}{r_f} + P_{ext}\Big), \tag{D.9}$$

Table D1: Input values to the model parameters used for fission gas release and gaseous swelling computations.

Parameter	Unit	Definition
$\beta = 0.3\dot{F}_m$	mol m^{-3}s^{-1}	Fission gas production rate
$\dot{F}_m = 5.189 \times 10^{-14} q_v$	mol m^{-3}s^{-1}	Fission rate density (molar)
$\dot{F} = N_A \dot{F}_m$	m^{-3}s^{-1}	Fission rate density
$N_A = 6.022 \times 10^{23}$	mol^{-1}	Avogadro constant
$q_v = q_l / 4\pi r_{\mathrm{p}}^2$	W m^{-3}	Power density
$q_l = 27000$	W m^{-1}	Linear power density
$r_{\mathrm{p}} = 4.24$	mm	Fuel pellet radius
$\rho_{\mathrm{T}} = 10.96$	g cm^{-3}	Fuel theoretical density
$P_{\mathrm{ext}} = 0$ or 1*	MPa	External pressure
$2\gamma / r_f = 2.4$	MPa	Gas bubble surface tension to radius ratio
$\nu\lambda = 5.7 \times 10^{-8}\beta$	ms^{-1}	Re-solution rate

*See end-note 9.

where N_{gs} is in mole/m^2, T is the absolute temperature, γ is the surface tension of gas bubble, r_f is the projected radius of grain boundary bubble at saturation, P_{ext} is the external pressure, see e.g. [167, 234] for more details. The fractional fission gas release from fuel is calculated according to

$$F_{gr}(t) = \frac{3}{2a}\Big(\frac{\max\big(N_{gb}(t) - N_{gs}, 0\big)}{\int_0^t \beta(s)s}\Big). \tag{D.10}$$

References

[1] J. A. Turnbull. The effect of grain size on the swelling and gas release properties of UO_2 during irradiation. *J. Nucl. Mater.*, 50:62–68, 1974.

[2] H. Matzke. On the effect of TiO_2 additions on sintering of UO_2. *J. Nucl. Mater.*, 20:328–331, 1966.

[3] I. Amato, R. L. Columbo, and A. P. Balzari. Grain growth in pure and titania-doped uranium dioxide. *J. Nucl. Mater.*, 18:252–260, 1966.

[4] J. B. Ainscough, F. Rigby, and S. C. Osborn. The effect of titania on grain growth and densification of sintered UO_2. *J. Nucl. Mater.*, 52:191–203, 1974.

[5] K. Une, S. Kashibe, and K. Ito. Fission gas behavior during postirradiation annealing of large grained UO_2 fuels irradiated to 23 GWd/t. *J. Nucl. Sci. Techn.*, 30:221–231, 1993.

[6] J. C. Killeen. The effect of additives on the irradiation behaviour of UO_2. *J. Nucl. Mater.*, 58:39–46, 1975.

[7] J. B. Ainscough, F. Rigby, and S. A. Morrow. Effect of oxygen potential on the thermal creep of niobia-doped UO_2. *J. Amer. Ceram. Soc.*, 64:315–318, 1981.

[8] H. Assmann, W. Dörr, G. Gradel, G. Maier, and M. Peehs. Doping UO_2 with niobia - beneficial or not? *J. Nucl. Mater.*, 98:216–220, 1981.

[9] K. W. Song, S. H. Kim, and S. H. Na et al. Effects of Nb_2O_5 addition on grain growth and densification in UO_2 pellets under reducing and/or oxidizing atmospheres. *J. Nucl. Mater.*, 209:280–285, 1994.

[10] J. C. Killeen. The measurement of the electron-to-hole mobility in UO_2 and its effect on thermal conductivity. *J. Nucl. Mater.*, 92:136–140, 1980.

[11] S. Kashibe and K. Une. Effect of additives (Cr_2O_3, Al_2O_3, SiO_2, MgO) on diffusion release of Xe-133 from UO_2 fuel. *J. Nucl. Mater.*, 254:234–242, 1998.

[12] T. Fujino, N. Sato, and K. Fukuda. Changes of thermodynamic properties of UO_2 fuel doped with magnesium and other metals. In *1997 Internat. Topical Meeting on Light Water Reactor Fuel Performance*, pages 565–575, Portland, Oregon, 2-6 March 1997. American Nuclear Society.

[13] T. Fujino, N. Sato, and K. Yamada et al. Post-irradiation examinations of high burnup Mg-doped UO_2. In *Internat. Topical Meeting on Light Water Fuel Performance*, pages 641–651, Park City, Utah, 2000. American Nuclear Society.

[14] T. Matsuda, Y. Yuasa, S. Kobayashi, and M. Toba. Characteristics of fuel pellets with additive of Al and Si. In *Advances in Fuel Pellet Technology for Improved Performance*, IAEA-TECDOC-1036, International Atomic Energy Agency, Vienna, Austria, 1998.

[15] J. Matsunaga, Y. Takagawa, and K. Kusagaya et al. Fundamentals of GNF Al-Si-O additive fuel. In *Proc. of Top Fuel 2009*, pages 767–772, Paris, France, 6-10 September, 2009.

[16] K. Une, M. Hirai, and K. Nogita et al. Rim structure formation and high burnup fuel behavior of large-grained UO_2 fuels. *J. Nucl. Mater.*, 278:54–63, 2000.

[17] J. Arborelius, K. Backman, and L. Hallstadius et al. Advanced doped UO_2 pellets in LWR applications. *J. Nucl. Sci. Techn.*, 43:967–976, 2006. Also in Proceedings of Water Reactor Fuel Performance Meeting, 2-6 October, 2006, Kyoto, Japan.

[18] C. Delafoy, P. Blanpain, and C. Maury. Advanced UO_2 fuel with improved PCI resistance and fission gas retention capability. In *Proceedings of the ANS/ENS Top Fuel 2003 Meeting*. European Nuclear Society, 16-19 March 2003.

[19] C. Delafoy and P. Dewes. AREVA NP new UO_2 fuel development and qualification for LWRs applications. In *Top Fuel 2006*, pages 487–491, Salamanca, Spain, 22-26 October 2006. European Nuclear Society.

[20] B. E. Ingleby and K. Hand. Fabrication and performance of large-grained UO_2-MgO fuel. In I. J. Hastings, editor, *Fission Product Behavior in Ceramic Nuclear Fuel*, volume 17 of *Advances in Ceramics*, pages 57–72. The American Ceramic Society, Columbus, Ohio, 1986.

[21] J. C. Killeen. Fission gas release during post irradiation annealing of large grain size fuels from Hinkley Point B. In *Water Reactor Fuel Element Modelling at High burnup and Experimental Support*, IAEA-TECDOC-957, pages 467–479, International Atomic Energy Agency, Vienna, Austria, 1994.

[22] H. Matzke. Gas release mechanism in UO_2 - a critical review. *Radiation Effects*, 53:219–242, 1980.

[23] IAEA. Characteristics and use of urania-gadolinia fuels. Technical Report IAEA-TECDOC-844, IAEA, Vienna, Austria, 1995.

[24] L. V. Corsetti, S. C. Hatfield, and A. Jansson. Recent advances in PWR fuel design at ABB-CE. In *International Topical Meeting on LWR Fuel Performance*, pages 113–121, Avignon, France, April 21-24 1991. European Nuclear Society.

[25] H. S. Kim, Y. K. Yoon, and M. S. Yang. Thermodynamic study on the $(U_{1-y},Er_y)O_{2\pm x}$ solid solutions. *J. Nucl. Mater.*, 209:286–293, 1994.

[26] F. Franceschini and B. Petrović. Fuel with advanced burnable absorbers design for the IRIS reactor core: Combined erbia and IFBA. *Ann. Nucl. Energy*, 36(8):1201–1207, 2009.

[27] M. A. Abu Sondos, V. M. Demin, and V. I. Savander. The effect of burnable absorbers (Gd and Eu) on the neutronphysical characteristics of fuel assemblies of VVER-1000 reactors. In *Journal of Physics: Conference Series*, volume 1189, page 012003. IOP Publishing, 2019.

[28] J. A. Lange. *Handbook of Chemistry*. McGraw-Hill, New York, 1979.

[29] V. Peres, L. Bourgeois, and P. Dehaudt. Grain growth and Ostwald ripening in chromia-doped uranium dioxide. *J. de Physique IV*, 3:1477–1480, 1993.

[30] T. Cardinaels, J. Hertog, and B. Vos et al. Dopant solubility and lattice contraction in gadolinia and gadolinia-chromia doped UO_2 fuels. *J. Nucl. Mater.*, 424:289–306, 2012.

[31] S. C. Middleburgh, R. W. Grimes, and K. H. Desai et al. Swelling due to fission products and additives dissolved within the uranium dioxide lattice. *J. Nucl. Mater.*, 427:359–363, 2012.

[32] S. Nishigaki and K Maekawa. Fabrication of BeO-UO_2-Be fuel pellets. *J. Nucl. Mater.*, 14:453–458, 1964.

[33] S. Ishimoto, M. Hirai, K. Ito, and Y. Korei. Thermal conductivity of UO_2-BeO pellet. *J. Nucl. Sci. Techn.*, 33:134–140, 1996. See also references therein.

[34] K. H. Sarma, J. Fourcade, S. G. Lee, and A. A. Solomon. New processing methods to produce silicon carbide and beryllium oxide inert matrix and enhanced thermal conductivity oxide fuels. *J. Nucl. Mater.*, 352:324–333, 2006.

[35] James Tulenko. Development of innovative accident tolerant high thermal conductivity UO_2-diamond composite fuel pellets. Technical Report Project 12-4037, US-DOE & Univ. of Florida, 2016.

[36] A. R. Massih. Effects of additives on uranium dioxide fuel behavior. Research report 2014:21, Swedish Radiation Safety Authority (SSM), Stockholm, Sweden, 2014.

[37] J. D. B. Lambert and R. Strain. Oxide fuels. In R. W. Cahn, P. Haasen, and E. J. Kramer, editors, *Nuclear Materials*, volume 10A of *Material Science and Technology*, chapter 7. VCH, Weinheim, Germany, 1994. Volume editor B.R.T. Frost.

[38] K. C. Radford and J. M. Pope. UO_2 fuel pellet microstructure modification through impurity additions. *J. Nucl. Mater.*, 116:305–313, 1983.

[39] S. Valin, L. Cailot, and Ph. Dehaudt et al. Synthesis of the results obtained on the advanced UO_2 microstructures irradiated in the TANOX device. In *Advanced Fuel Pellet Materials and Fuel Rod Design for Water Cooled Reactors*, IAEA-TECDOC-1416, International Atomic Energy Agency, Vienna, Austria, 2003.

[40] C. Delafoy, P. Dewes, and T. Miles. AREVA Cr_2O_3-doped fuel development for BWRs. In *Proceedings of the 2007 International LWR Fuel Performance Meeting*, pages 1–7, San Francisco, California, October 2007. American Nuclear Society.

[41] L. Bourgeois, Ph. Dehaudt, C. Lemaignan, and A. Hammou. Factors governing microstructure development of Cr_2O_3-doped UO_2 during sintering. *J. Nucl. Mater.*, 297:313–326, 2001.

[42] A. Leenaers, L. de Tollenaere, C. Delafoy, and S. Van den Berghe. On the solubility of chromium sesquioxide in uranium dioxide fuel. *J. Nucl. Mater.*, 317:62–68, 2003.

[43] T. Cardinaels, K. Govers, and B. Vos et al. Chromia doped UO_2 fuel: Investigation of the lattice parameter. *J. Nucl. Mater.*, 424:252–260, 2012.

[44] O. Brémond. IFA-716.1 fission gas release mechanisms. Report HWR-1008, Institutt for Energiteknikk, Halden, Norway, 2011.

[45] R. J. M. Konings, T. Wiss, and C. Guéneau. Nuclear fuels. In L. R. Morss, N. M. Edelstein, and J. Fuger, editors, *The Chemistry of the Actinide and Transactinide Elements*, volume 6, chapter 34. Springer, Dordrecht, The Netherlands, 2011.

[46] R. E. Latta and R. E. Fryxell. Determination of solidus-liquidus temperatures in the UO_{2+x} system ($-0.50 < x < 0.20$). *J. Nucl. Mater.*, 35:195–210, 1970.

[47] D. R. Olander. *Fundamental Aspects of Nuclear Reactor Fuel Elements*. National Technology Information Services, Springfield, Virginia, 1976.

[48] X. Y. Liu, D. A. Andersson, and B. P. Uberuaga. First-principle DFT modeling of nuclear fuel materials. *J. Mater. Sci.*, 47:7367–7384, 2012.

[49] T. Matsui and K. Naito. Electrical conductivity measurement and thermogravimetric study of pure and niobium-doped uranium dioxide. *J. Nucl. Mater.*, 136:59–68, 1985.

[50] K. Une, I. Tanabe, and M. Oguma. Effects of additives and the oxygen potential on the fission gas diffusion in UO_2 fuel. *J. Nucl. Mater.*, 150:93–99, 1987.

[51] T. Yao, S. M. Scott, G. Xin, and J. Lian. TiO_2 doped UO_2 fuels sintered by spark plasma sintering. *J. Nucl. Mater.*, 469:251–261, 2016.

[52] T. Fujino, S. Nakama, N. Sato, K. Yamada, K. Fukuda, H. Serizawa, and T. Shiratori. Solubility of magnesium in uranium dioxide. *J. Nucl. Mater.*, 246:150–157, 1997.

[53] J. Tateno, T. Fujino, and H. Tagawa. Thermodynamics of $Mg_yU_{1-y}O_{2+x}$ by EMF measurements: II Properties at low magnesium concentrations. *J. Solid State Chem.*, 30:265–273, 1979.

[54] T. Fujino and N. Sato. Analyses of the oxygen potential of the solid solutions $M_yU_{1-y}O_{2+x}$ (M = M^{3+} and M^{3+}) by statistics of defects and defect complexes. *J. Nucl. Mater.*, 189:103–115, 1992.

[55] S. M. Lang, F. P. Knudsen, C. L. Fillmore, and R. S. Roth. High-temperature reactions of uranium dioxide with various metal oxides. Technical Report Circular 568, National Bureau of Standards, 1956. Publisher: US Depatment of Commerce.

[56] M. Sugisaki, K. Hirashima, S. Yoshihara, and Y. Oishi. Phase equilibrium of UO_{2+x}–MgO system. *J. Nucl. Sci. and Techn.*, 10:387–389, 1973.

[57] T. C. Chawla, M. G. Chasanov, D. R. Pedersen, L. Baker Jr, and J. D. Bingle. Thermophysical properties of MgO, UO_2, their eutectic solution and slurry of liquid-solid mixtures, concrete, sodium, stainless steel and debris beds for use in molten pool penetration of MgO substrate. *Nucl. Eng. Design*, 80:65–77, 1984.

[58] K. W. Kang, J. H. Yang, J. H. Kim, Y. W. Rhee, D. J. Kim, K. S. Kim, and K. W. Song. Effects of MnO-Al_2O_3 on the grain growth and high-temperature deformation strain of UO_2 fuel pellets. *J. Nucl. Sci. Techn.*, 47(3):304–307, 2010.

[59] T. S. Jung, S. J. Lee, Y. S. Na, and K. Y. Lim. Study on manufacturing technology of MnO-Al_2O_3 doped UO_2 pellets for remedy of PCI failure. In *Proceedings of the 2017 Water Reactor Fuel Performance Meeting*, Jeju Island, Korea, 2017.

[60] Jang-Soo Oh et al. Development of additives doped UO_2 pellet for PCI remedy. In *Proceedings of the 2017 Water Reactor Fuel Performance Meeting*, Jeju Island, Korea, 2017.

[61] A. R. Massih and L. O. Jernkvist. Effect of additives on self-diffusion and creep of UO_2. *Comput. Mater. Sci.*, 110:152–162, 2015.

[62] M. Hong, B. P. Uberuaga, D. A. Andersson, C. R. Stanek, S. R. Phillpot, and S. B. Sinnott. Role of electronic effects on the incorporation of Cr at a $\Sigma 5$ grain boundary in UO_2. *Comput. Mater. Sci.*, 78:29–33, 2013.

[63] K. W. Song, K. S. Kim, K. W. Kang, and Y. H. Jung. Effects of Nb_2O_5 and oxygen potential on sintering behavior of UO_2 fuel pellets. *J. Korean Nucl. Soc.*, 31:335–343, 1999.

[64] Ch. Riglet-Martial, Ph. Martin, D. Testemale, C. Sabathier-Devals, G. Carlot, P. Matheron, X. Iltis, U. Pasquet, C. Valot, et al. Thermodynamics of chromium in UO_2 fuel: A solubility model. *J. Nucl. Mater.*, 447:63–72, 2014.

[65] E. Curti and D. A. Kulik. Oxygen potential calculations for conventional and Cr-doped UO_2 fuels based on solid solution thermodynamics. *J. Nucl. Mater.*, 534, 2020. Paper ID 152140.

[66] M. W. D. Cooper, C. R. Stanek, and D. A. Andersson. Calculate parameters controlling grain growth in doped UO_2. Technical Report LA-UR-18-25549, Los Alamos National Laboratory, New Mexico, USA, 2018. See also Acta Mater. 150 (2018) 403-404.

[67] D. R. Costa, F. J. Ezequiel, R. Gonzaga, and S. H. Bernardelli. Individual influence of Al_2O_3 and Nb_2O_5 on grain growth of UO_2 sintered pellets manufactured at INB. In *2013 International Nuclear Atlantic Conference - INAC 2013*, November 24-29, 2013. Recife, PE, Brazil.

[68] M. Sun, J. Stackhouse, and P. M. Kowalski. The +2 oxidation state of Cr incorporated into the crystal lattice of UO_2. *Commun. Mater.*, 1:1–8, 2020.

[69] C. E. Sanders and J. C. Wagner. Study of the effect of integral burnable absorbers for PWR burnup credit. Technical Report ORNL/TM-2000/321, Oak Ridge National Laboratory, Tennessee, USA, 2002. Also as USNRC report NUREG/CR-6760.

[70] J. C. Wagner and C. E Sanders. Investigation of the effect of fixed absorbers on the reactivity of PWR spent nuclear fuel for burnup credit. *Nucl. Techn.*, 139:91–126, 2002.

[71] M. Loveckỳ, J. Závorka, J. Jiřičková, and R. Škoda. Increasing efficiency of nuclear fuel using burnable absorbers. *Prog. Nucl. Energy*, 118:103077, 2020.

[72] V. Barchevtsev, V. Artisyuk, and H. Ninokata. Concept of erbium doped uranium oxide fuel cycle in light water reactors. *J. Nucl. Sci. Techn.*, 39:506–513, 2002.

[73] A. A. Galahom. Investigation of different burnable absorbers effects on the neutronic characteristics of PWR assembly. *Ann. Nucl. Energy*, 94:22–31, 2016.

[74] A.M. Fedosov. RBMK uranium-erbium fuel. *Atomic Energy*, 124:221–226, 2018.

[75] A. A. Galahom. Study of the possibility of using europium and pyrex alloy as burnable absorber in PWR. *Ann. Nucl. Energy*, 110:1127–1133, 2017.

[76] M. Asou and J. Porta. Prospects of poisoning reactor cores of the future. *Nucl. Eng. Design*, 168:261–270, 1997.

[77] T. Wada, K. Noro, and K. Tsukui. Behaviour of UO_2-Gd_2O_3 fuel. In *Nuclear Fuel Performance*, pages 63–1. Thomas Telford Publishing, London, UK, 1973.

[78] L. W. Newman, C. T. Rombough, and T. A. Thornton. Development and demonstration of an advanced extended-burnup fuel-assembly design incorporating urania-gadolinia. Second semi-annual progress report, october 1981-march 1982. Technical report, Babcock and Wilcox Co., Lynchburg, VA, USA, 1982. Also as US-DOE report DOE/ET/34212-36.

[79] H. Assmann, W. Doerr, and M. Peehs. Oxide fuels with controlled microstructure. *J. Amer. Ceram. Soc.*, 67(9):631–636, 1984.

[80] A. R. Massih, S. Persson, and Z. Weiss. Modelling of (U,Gd)O_2 fuel behaviour in boiling water reactors. *J. Nucl. Mater.*, 188:323–330, 1992.

[81] L. Hälldahl and S. Eriksson. Characterization of homogeneity in (U,Gd)O_2-pellets. *J. Nucl. Mater.*, 153:66–70, 1988.

[82] R. J. Beals, J. H. Handwerk, and B. J. Wrona. Behavior of urania–rare-earth oxides at high temperatures. *J. Amer. Ceram. Soc.*, 52(11):578–581, 1969.

[83] Ki Won Kang, Jae Ho Yang, Jong Hun Kim, Young Woo Rhee, Dong Joo Kim, Keon Sik Kim, and Kun Woo Song. The solidus and liquidus temperatures of UO_2-Gd_2O_3 and UO_2-Eu_2O_3 fuels. *Thermochimica acta*, 455(1-2):134–137, 2007.

[84] J. W. McMurray, D. Shin, B. W. Slone, and T. M. Besmann. Thermochemical modeling of the $UO_{1-y}Gd_yO_{2\pm x}$ phase. *J. Nucl. Mater.*, 443(1-3):588–595, 2013.

[85] J. W. McMurray, D. Shin, B. W. Slone, and T. M. Besmann. Thermodynamic reassessment of U–Gd–O system. *J. Nucl. Mater.*, 452(1-3):397–406, 2014.

[86] K. Une and M. Oguma. Thermodynamic properties of nonstoichiometric urania-gadolinia solid solutions in the temperature range 700-1100°C. *J. Nucl. Mater.*, 110:215–222, 1982.

[87] K. Une and M. Oguma. Oxygen potential of (U,Gd)$O_{2\pm x}$ solid solutions in the temperature range 1000-1500°C. *J. Nucl. Mater.*, 115:84–90, 1983.

[88] K. Une and M. Oguma. Oxygen potential of $U_{0.96}Gd_{0.04}O_2$ (UO_2-3wt% Gd_2O_3) solid solution. *J. Nucl. Mater.*, 131:88–91, 1985.

[89] T. B. Lindemer and A. L. Sutton. Study of nonstoichiometry of $U_{1-z}Gd_zO_{2\pm x}$. *J. Amer. Ceram. Soc.*, 71:553–561, 1988.

[90] K. Park and D. R. Olander. Defect model for oxygen potentials of gadolinium- and europium-doped urania. *J. Nucl. Mater.*, 187:89–96, 1992.

[91] H. S. Kim, Y. K. Yoon, and M. S. Yang. Defect structures of (U_{1-y},Er_y)$O_{2\pm x}$ solid solutions. *J. Nucl. Mater.*, 226:206–215, 1995.

[92] S-H. Won Kang, J-D. Yi, H. Yoo, S-H. Kim, and Y. W. Lee. The solidus and liquidus temperatures of UO_2-Gd_2O_3 and UO_2-Eu_2O_3 fuels. *J. Phys. Chem. Solids*, 63:773–780, 2002.

[93] B. T. M. Willis. The defect structure of hyper-stoichiometric uranium dioxide. *Acta Crystallographica Section A: Crystal Physics, Diffraction, Theoretical and General Crystallography*, 34(1):88–90, 1978.

[94] A. V. Fedotov, E. N. Mikheev, A. V. Lysikov, and V. V. Novikov. Theoretical and experimental density of (U,Gd)O_2 and (U,Er)O_2. *Atomic Energy*, 113:429–434, 2013.

[95] M. Durazzo, A. C. Freitas, A. E. S. Sansone, N. A. M. Ferreira, E. F. Urano de Carvalho, H. G. Riella, and R. M. Leal Neto. Sintering behavior of UO_2-Er_2O_3 mixed fuel. *J. Nucl. Mater.*, 510:603–612, 2018.

[96] M. Durazzo, A. M. Saliba-Silva, E. F. Urano De Carvalho, and H. G. Riella. Sintering behavior of UO_2-Gd_2O_3 fuel: Pore formation mechanism. *J. Nucl. Mater.*, 433:334–340, 2013.

[97] L. N. Grossman, J. E. Lewis, and D. M. Rooney. The system UO_2-Eu_2O_3 at high temperatures. *J. Nucl. Mater.*, 21:302–309, 1967.

[98] Rykijanto Tanamas. *Das System Uranoxid-Europiumoxid-Sauerstoff*. PhD thesis, Ges. f. Kernforschung mbH, 1974.

[99] U. Berndt, R. Tanamas, and C. Keller. The ternary UO_2-UO_3-$EuO_{1.5}$(EuO) system and investigation of Eu(II)-actinide(IV)-perovskites. *J. Solid State Chem.*, 17:113–120, 1976.

[100] T. Fujino. Thermodynamics of fluorite type solid solutions containing plutonium, lanthanide elements or alkaline earth metals in uranium dioxide host lattices. *J. Nucl. Mater.*, 154:14–24, 1988.

[101] T. Fujino, K. Ouchi, Y. Mozumi, R. Ueda, and H. Tagawa. Composition and oxygen potential of cubic fluorite–type solid solution $Eu_yU_{1-y}O_{2+x}$ ($x \gtreqless 0$) and rhombohedral Eu_6UO_{12+x}($x < 0$). *J. Nucl. Mater.*, 174:92–101, 1990.

[102] T. Fujino, N. Sato, and K. Yamada. A refined analysis of oxygen potential of $M_yU_{1-y}O_{2+x}$ (M = M^{3+} and M^{3+}) by lattice statistics based on the grand partition function and the Flory methods. *J. Nucl. Mater.*, 223:6–19, 1995.

[103] T. Fujino, N. Sato, K. Yamada, S. Nakama, K. Fukuda, H. Serizawa, and T. Shiratori. Oxygen potential of solid solution $Eu_yU_{1-y}O_{2+x}$. *J. Nucl. Mater.*, 265:154–160, 1999.

[104] T. Fujino, N. Sato, K. Yamada, et al. Thermodynamics of the UO_2 solid solution with magnesium and europium oxides. *J. Nucl. Mater.*, 297:332–340, 2001.

[105] T. Fujino, N. Sato, K. Yamada, et al. Oxygen potential and defect structure of the solid solution, Mg–Gd–UO_2. *J. Nucl. Mater.*, 289:270–280, 2001.

[106] G. A. Slack. Nonmetallic crystals with high thermal conductivity. *J. Phys. Chem. Solids*, 34:321–335, 1973.

[107] L. F. Epstein and W. H. Howland. Binary mixtures of UO_2 and other oxides. *J. Amer. Ceram. Soc.*, 36:334–335, 1953.

[108] A. Solomon, S. Revankar, and J. K. McCoy. Enhanced thermal conductivity oxide fuels. Report DOE/SF/22613, Purdue University School of Nuclear Engineering, 2006.

[109] S. Yeo, E. Mckenna, R. Baney, G. Subhash, and J. Tulenko. Enhanced thermal conductivity of uranium dioxide–silicon carbide composite fuel pellets prepared by Spark Plasma Sintering (SPS). *J. Nucl. Mater.*, 433:66–73, 2013.

[110] H. Assmann, W. Dörr, and M. Peehs. Control of UO_2 microstructure by oxidative sintering. *J. Nucl. Mater.*, 140:1–6, 1986.

[111] Z. A. Munir, U. Anselmi-Tamburini, and M. Ohyanagi. The effect of electric field and pressure on the synthesis and consolidation of materials: A review of the spark plasma sintering method. *J. Mater. Sci.*, 41:763–777, 2006.

[112] L. Ge, G. Subhash, R. H. Baney, and J. S. Tulenko. Influence of processing parameters on thermal conductivity of uranium dioxide pellets prepared by spark plasma sintering. *J. Euro. Ceram. Soc.*, 34:1791–1801, 2014.

[113] H. Chevrel, P. Dehaudt, B. Francois, and J. F. Baumard. Influence of surface phenomena during sintering of overstoichiometric uranium dioxide UO_{2+x}. *J. Nucl. Mater.*, 189:175–182, 1992.

[114] Sunghwan Yeo. *UO*2*-SiC Composite Reactor Fuels With Enhanced Thermal And Mechanical Poperties Prepared By Spark Plasma Sintering*. PhD thesis, University of Florida, Fl, USA, 2013.

[115] S. Yeo, R. Baney, G. Subhash, and J. Tulenko. The influence of SiC particle size and volume fraction on the thermal conductivity of spark plasma sintered UO_2–SiC composites. *J. Nucl. Mater.*, 442:245–252, 2013.

[116] Z. Chen, G. Subhash, and J. S. Tulenko. Spark plasma sintering of diamond-reinforced uranium dioxide composite fuel pellets. *Nucl. Eng. Des.*, 294:52–59, 2015.

[117] Zhichao Chen. *Densification evolution and properties evaluation of UO_2-based composites prepared by spark plasma sintering (SPS)*. PhD thesis, University of Florida, 2015.

[118] T. Ironman, J. Tulenko, and G. Subhash. Exploration of viability of spark plasma sintering for commercial fabrication of nuclear fuel pellets. *Nucl. Techn.*, 200:144–158, 2017.

[119] G. Subhash. Development of innovative high-thermal conductivity UO_2 ceramic composite fuel pellets with carbon nano-tubes using spark plasma sintering. Report Project 10-917, Battelle Energy Alliance, LLC, 2014.

[120] H. Ma, H. Wang, P. C. Burns, B. K. McNamara, E. C. Buck, and C. Na. Synthesis and preservation of graphene-supported uranium dioxide nanocrystals. *J. Nucl. Mater.*, 475:113–122, 2016.

[121] T. Yao, G. Xin, S. M. Scott, B. Gong, and J. Lian. Thermally-conductive and mechanically-robust graphene nanoplatelet reinforced UO_2 composite nuclear fuels. *Scientific Reports*, 8:2987, 2018.

[122] B. Li, Z. Yang, Z. Wang, Q. Huang, X. Liu, B. Yan, L. Cheng, T. Shi, D. Zhang, M. Wu, et al. Graphite flakes-UO_2 fuel pellets with excellent thermal conductivity in radial direction. *J. Nucl. Mater.*, page 152639, 2020.

[123] E. S. Toberer, L. L. Baranowski, and C. Dames. Advances in thermal conductivity. *Annual Review of Materials Research*, 42:179–209, 2012.

[124] E. Muller, T. Lambert, and N. L'Hullier et al. Thermal behavior of advanced UO_2 fuel at high burnup. In *Proceedings of the 2007 International LWR Fuel Performance Meeting*, pages 40–46, San Francisco, California, October 2007. American Nuclear Society.

[125] G. J. Hyland and R. W. Ohse. The heat capacity and enthalpy of condensed UO_2: A critical review and assessment. *J. Nucl. Mater.*, 140:149–170, 1986.

[126] C. Ronchi and G. J. Hyland. Analysis of recent measurements of the heat capacity of uranium dioxide. *J. Alloys & Compounds*, 213/214:159–168, 1994.

[127] C. Kittel. *Solid State Physics*. John Wiley & Sons, New York, seventh edition, 1996. Chapter 5.

[128] N. H. March, D. D. Richardson, and M. P. Tosi. Correlations of the superionic transition temperature and the Frenkel energy of fluorite crystals. *Solid State Commun.*, 35:903–905, 1980.

[129] W. Hayes and A. M. Stoneham. *Defects and Defect Processes in Nonmetallic Solids*. John Wiley & Sons, New York, 1985. Chapter 3; Dover reprint 2004.

[130] K. Clausen, W. Hayes, J. E. Macdonald, and R. Osborn. Observations of oxygen Frenkel disorder in uranium dioxide above 2000 K by use of neutron-scattering techniques. *Phys. Rev. Lett.*, 52:1238–1241, 1984.

[131] K. Clausen, M. A. Hackett, and W. Hayes et al. Coherent diffuse neutron-scattering from UO_2 and ThO_2 at temperatures above 2000 K. *Physica B*, 156/157:103–106, 1989.

[132] R. Szwarc. The defect contribution to the excess enthalpy of uranium dioxide calculation of the Frenkel energy. *J. Phys. Chem. Solids*, 30:705–711, 1969.

[133] T. Matsui, Y. Arita, and K. Naito. High temperature heat capacities and electrical conductivities of UO_2 doped with yttrium and simulated fission products. *J. Nucl. Mater.*, 188:205–209, 1992.

[134] K. Naito. High temperature heat capacities of UO_2 and doped UO_2. *J. Nucl. Mater.*, 189:30–35, 1989.

[135] H. Inaba, K. Naito, and M. Oguma. Heat capacity measurements of $U_{1-y}Gd_yO_2$ ($0.00 \leq y \leq 0.142$) from 310 to 1577 K. *J. Nucl. Mater.*, 149:341–348, 1987.

[136] IAEA. Thermophysical properties database of materials for light water reactors and heavy water reactors. Technical Report IAEA-TECDOC-1496, IAEA, Vienna, Austria, 2006.

[137] K. Une. Thermal expansion of UO_2-Gd_2O_3 fuel pellets. *J. Nucl. Sci. Techn.*, 23:84–86, 1986.

[138] N. W. Ashcroft and N. D. Mermin. *Solid State Physics*. Harcourt College Publishers, New York, 1976. Chapter 25.

[139] T. Yamashita, N. Nitani, T. Tsuji, and T. Kato. Thermal expansion of neptunium-uranium mixed oxides. *J. Nucl. Mater.*, 247:90–93, 1997.

[140] T. Ivanova, K. Gesheva, A. Cziraki, A. Szekeres, and E. Vlaikova. Structural transformations and their relation to the optoelectronic properties of chromium oxide thin films. *Journal of Physics: Conference Series*, 113:012030, 2008.

[141] P. G. Klemens. Thermal resistance due to point defects at high temperatures. *Phys. Rev.*, 119:507–509, 1960.

[142] B. Abeles. Lattice thermal conductivity of disordered semiconductor alloys at high temperatures. *Phys. Rev.*, 131:1906–1911, 1963.

[143] J. M. Casado, J. H. Harding, and G. J. Hyland. Small-polaron hopping in Mott-insulating UO_2. *J. Phys.: Condens. Matter*, 6:4685–4698, 1994.

[144] Q. Yin and S. Y. Savrasov. Origin of low thermal conductivity in nuclear fuels. *Phys. Rev. Lett.*, 100:225504, 2008.

[145] C. Ronchi, M. Sheindlin, M. Musella, and G. J. Hyland. Thermal conductivity of uranium dioxide up to 2900 K from simultaneous measurement of the heat capacity and thermal diffusiviy. *J. Appl. Phys.*, 85:776–789, 1999.

[146] R. A. Young. Model for electronic contribution to the thermal and transport properties of ThO_2, UO_2 and PuO_2 in solid and liquid phases. *J. Nucl. Mater.*, 87:283–296, 1979.

[147] S. Fukushima, T. Ohmichi, A. Maeda, and H. Watanabe. The effect of gadolinium content on the thermal conductivity of near-stoichiometric (U,Gd)O_2 solid solutions. *J. Nucl. Mater.*, 105:201–210, 1982.

[148] M. Peehs, W. Dörr, G. Gradel, and G. Maier. Zur Wärmeleitfähigkeit und Plastizität von UO_2 mit Gd-Zusätzen. *J. Nucl. Mater.*, 106:221–230, 1982.

[149] M. Hirai. Thermal diffusivity of UO_2-Gd_2O_3 pellets. *J. Nucl. Mater.*, 173:247–254, 1990.

[150] M. Hirai and S. Ishimoto. Thermal diffusivities and thermal conductivities of UO_2-Gd_2O_3. *J. Nucl. Sci. Techn.*, 28:995–1000, 1991. See also references therein.

[151] M. Amaya, K. Une, and M. Hirai. Heat capacity measurements of $U_{1-y}Gd_yO_2$ ($y = 0 - 0.27$) from 325 to 1673 K. *J. Nucl. Sci. Techn.*, 41:108–115, 2004.

[152] S. Ishimoto, M. Hirai, K. Ito, and Y. Korei. Effects of soluble fission products on thermal conductivities of nuclear fuel pellets. *J. Nucl. Sci. Techn.*, 31:796–802, 1994.

[153] M. Amaya and M. Hirai. The effects of oxidation on the thermal conductivity of (U, M)O_2 pellets (M=Gd and/or simulated soluble FPs). *J. Nucl. Mater.*, 246:158–164, 1997.

[154] K. Minato, T. Shiratori, H. Serizawa, K. Hayashi, K. Une, K. Nogita, M. Hirai, and M. Amaya. Thermal conductivities of irradiated UO_2 and (U,Gd)O_2. *J. Nucl. Mater.*, 288:57–65, 2001.

[155] M. Amaya, M. Hirai, H. Sakurai, K. Ito, M. Sasaki, T. Nomata, K. Kamimura, and R. Iwasaki. Thermal conductivities of irradiated UO_2 and (U,Gd)O_2 pellets. *J. Nucl. Mater.*, 300:57–64, 2002.

[156] A. R. Massih. Electronic transport in pure and doped UO_2. *J. Nucl. Mater.*, 497:166–182, 2017.

[157] M. J. Qin, S. C. Middleburgh, M. W. D. Cooper, M. J. D. Rushton, M. Puide, E. Y. Kuo, R. W. Grimes, and G. R. Lumpkin. Thermal conductivity variation in uranium dioxide with gadolinia additions. *J. Nucl. Mater.*, 540:152258, 2020.

[158] Si-Hyung Kim, Han-Soo Kim, Young-Woo Lee, Dong-Seong Sohn, and Dong-Soo Suhr. Thermal expansion of near stoichiometric (U,Er)O_2 solid solutions. *Materials Letters*, 60:1480–1483, 2006.

[159] Si-Hyung Kim, Yeon-Gu Kim, Han-Soo Kim, Sang-Ho Na, Young-Woo Lee, and Dong-Soo Suhr. Thermal conductivity of near-stoichiometric (U,Er)O_2 solid solutions. *J. Nucl. Mater.*, 342:119–124, 2005.

[160] S. Yamanaka, K. Kurosaki, M. Katayama, J. Adachi, M. Uno, T. Kuroishi, and M. Yamasaki. Thermal and mechanical properties of (U,Er)O_2. *J. Nucl. Mater.*, 389:115–118, 2009.

[161] H. Xiao, C. Long, X. Wang, H. Chen, S. Fan, C. Yu, and G. Liu. Microstructure and thermophysical properties of Er_2O_3-doped UO_2 ceramic pellets. *J. Nucl. Mater.*, page 152109, 2020.

[162] T. Matsui, T. Kawase, and K. Naito. Heat capacities and electrical conductivities of ($U_{1-y}Eu_y$)O_2 ($y = 0.044$ and 0.090) from 300 to 1550 K. *J. Nucl. Mater.*, 186:254–258, 1992.

[163] R. V. Krishnan, G. Jogeswararao, G. Panneerselvam, M. P. Antony, and K. Ananthasivan. Solid solubility and thermal expansion studies of uranium–europium mixed oxides. *J. Nucl. Mater.*, 465:719–723, 2015.

[164] R V. Krishnan, R. Babu, A. Senapati, G. Jogeswararao, and K. Ananthasivan. Thermophysical properties of uranium–europium mixed oxides. *J. Advan. Ceram.*, 4:253–259, 2015.

[165] Wei Zhou and Wenzhong Zhou. Enhanced thermalconductivity accident tolerant fuels for improved reactor safety: A comprehensive review. *Ann. Nucl. Energy*, 119:66–86, 2018.

[166] T. Fujino, T. Shiratori, N. Sato, and K. Fukuda et al. Post-irradiation examination of high burnup Mg doped UO_2 in comparison with undoped UO_2, Mg-Nb doped UO_2 and Ti doped UO_2. *J. Nucl. Mater.*, 297:176–205, 2001.

[167] L. O. Jernkvist and A. R. Massih. Models for fuel rod behaviour at high burn-up. Technical Report 2005:41, Swedish Nuclear Power Inspectorate (SKI), Stockholm, Sweden, 2005. Available at: www.ssm.se.

[168] I. Shamanin, A. Karengin, A. Karengin, I. Novoselov, A. Poberezhnikov, and E. Alyukov. Plasmachemical synthesis and the assessment of the thermal conductiv-

ity of fuel compounds UO_2–MgO. In *AIP Conference Proceedings*, volume 2101, page 020017. AIP Publishing LLC, 2019.

[169] J. K. Fink. Thermophysical properties of uranium dioxide. *J. Nucl. Mater.*, 279:1–18, 2000.

[170] R. Latta, S. T. Revankar, and A. A. Solomon. Modeling and measurement of thermal properties of ceramic composite fuel for light water reactors. *Heat Transfer Eng.*, 28:357–365, 2008.

[171] B. Li, Z. Yang, J. Jia, et al. High temperature thermal physical performance of BeO/UO_2 composites prepared by spark plasma sintering (SPS). *Scripta Mater.*, 142:70–73, 2018.

[172] R. A. Verrall, M. D. Vlajic, and V. D. Krstic. Silicon carbide as an inert-matrix for a thermal reactor fuel. *J. Nucl. Mater.*, 274:54–60, 1999.

[173] L. L. Snead, T. Nozawa, Y. Katoh, T-S. Byun, S. Kondo, and D. A. Petti. Handbook of SiC properties for fuel performance modeling. *J. Nucl. Mater.*, 371:329–377, 2007.

[174] B. Li, Z. Yang, J. Jia, P. Zhang, et al. High temperature thermal physical performance of SiC/UO_2 composites up to 1600°C. *Ceram. Int.*, 44:10069–10077, 2018.

[175] R. R. Reeber and K. Wang. Thermal expansion, molar volume and specific heat of diamond from 0 to 3000 K. *J. Electronic Materials*, 25:63–67, 1996.

[176] E. Pop, V. Varshney, and A. K. Roy. Thermal properties of graphene: Fundamentals and applications. *MRS Bulletin*, 37:1273–1281, 2012.

[177] James Clerk Maxwell. *A treatise on electricity and magnetism*, volume 1. Oxford: Clarendon Press, 3rd edition, 1904.

[178] D. P. H. Hasselman and L. F. Johnson. Effective thermal conductivity of composites with interfacial thermal barrier resistance. *J. Compos. Mater.*, 21(6):508–515, 1987.

[179] R. L. Hamilton and O. K. Crosser. Thermal conductivity of heterogeneous two-component systems. *Indust. & Engin. Chem. Fundamentals*, 1(3):187–191, 1962.

[180] K. von Lichtenecker. Der elektrische Leitungswiderstand künstlicher und natürlicher Aggregate. *Physikalische Zeitschrift*, 25(8):169–181, 1924.

[181] H. Hatta and M. Taya. Effective thermal conductivity of a misoriented short fiber composite. *J. Appl. Phys.*, 58(7):2478–2486, 1985.

[182] H. Hatta and M. Taya. Equivalent inclusion method for steady state heat conduction in composites. *Int. J. Eng. Sci.*, 24(7):1159–1172, 1986.

[183] F. Badry, R. Brito, M. G. Abdoelatef, S. McDeavitt, and K. Ahmed. An experimentally validated mesoscale model of thermal conductivity of a UO_2 and BeO composite nuclear fuel. *JOM*, 71:4829–4838, 2019.

[184] B. Schulz. On the effective thermal diffusivity of macroscopic heterogeneous two phase materials. In *Thermal Conductivity 18*, pages 33–42. Springer, 1985.

[185] C. G. Morrison, W. Ji, and P. Blejwas. Feasibility study of solid matrix fuels for space power reactors. In *Proceedings of Conference on Nuclear and Emerging Technologies for Space (NETS 2015)*, Albuquerque, New Mexico, USA, 23-26 February 2015.

[186] K. Y. Spencer, L. Sudderth, R. A. Brito, J. A. Evans, C. S. Hart, A. Hu, A. Jati, K. Stern, and S. M. McDeavitt. Sensitivity study for accident tolerant fuels: Property comparisons and behavior simulations in a simplified PWR to enable ATF development and design. *Nucl. Eng. Design*, 309:197–212, 2016.

[187] D. Chandramouli and S. T. Revankar. Development of thermal models and analysis of UO_2-BeO fuel during a loss of coolant accident. *Int. J. Nucl. Energy*, 2014:751070, 2014.

[188] K. J. Geelhood, W. G. Luscher, J. M. Cuta, and I. E. Porter. FRAPTRAN-2.0: A computer code for the transient analysis of oxide fuel rods. Report PNNL-19400, Vol.1 Rev2, Pacific Northwest National Laboratory, Richland, WA, USA, 2016.

[189] I. Shamanin, A. Karengin, I. Novoselov, A. Karengin, E. Alyukov, A. Poberezhnikov, R. Babaev, and O. Mendoza. Plasmachemical synthesis and evaluation of the thermal conductivity of metal-oxide compounds for prospective nuclear fuel. In *Journal of Physics: Conference Series*, volume 1145, page 012057. IOP Publishing, 2019.

[190] C-W. Nan, R. Birringer, D. R. Clarke, and H. Gleiter. Effective thermal conductivity of particulate composites with interfacial thermal resistance. *J. Appl. Phys.*, 81(10):6692–6699, 1997.

[191] C. B. Garcia, R. A. Brito, L. H. Ortega, J. P. Malone, and S. M. McDeavitt. Manufacture of a UO_2-based nuclear fuel with improved thermal conductivity with the addition of BeO. *Metall. Mater. Trans. E*, 4:70–76, 2017.

[192] F. Badry and K. Ahmed. A new model for the effective thermal conductivity of polycrystalline solids. *AIP Advances*, 10(10):105021, 2020.

[193] D. S. Li, H. Garmestani, and J. Schwartz. Modeling thermal conductivity in UO_2 with BeO additions as a function of microstructure. *J. Nucl. Mater.*, 392:22–27, 2009.

[194] F. W. Hilty and M. R. Tonks. Development and application of a microstructure dependent thermal resistor model for UO_2 reactor fuel with high thermal conductivity additives. *J. Nucl. Mater.*, 540:152334, 2020.

[195] X. Zhu, R. Gao, H. Gong, T. Liu, D-Y. Lin, and H. Song. UO_2/BeO interfacial thermal resistance and its effect on fuel thermal conductivity. *Ann. Nucl. Energy*, 154:108102, 2021. arXiv preprint arXiv:2006.11705.

[196] E. T. Swartz and R. O. Pohl. Thermal boundary resistance. *Rev. Mod. Phys.*, 61:605, 1989.

[197] J. J. Carbajo, G. L. Yoder, S. G. Popov, and V. K. Ivanov. A review of the thermophysical properties of MOX and UO_2 fuels. *J. Nucl. Mater.*, 299(3):181–198, 2001.

[198] D. G. Martin. The thermal expansion of solid and (U, Pu) mixed oxides - a review and recommendations. *J. Nucl. Mater.*, 152:94–101, 1988.

[199] W. G. Luscher, K. J. Geelhood, and I. E. Porter. Material property correlations: Comparisons between FRAPCON-4.0, FRAPTRAN-2.0, and MATPRO. Technical Report PNNL-19417 Rev. 2, Pacific Northwest National Lab., Richland, WA (United States), 2015.

[200] A. C. Victor and T. B. Douglas. Thermodynamic properties of magnesium oxide and beryllium oxide from 298 to 1,200 K. *Journal of Research of the National Bureau of Standards. Section A, Physics and Chemistry*, 67:325, 1963.

[201] H. Kleykamp. Selection of materials as diluents for burning of plutonium fuels in nuclear reactors. *J. Nucl. Mater.*, 275:1–11, 1999.

[202] A. M. Hofmeister. Thermal diffusivity and thermal conductivity of single-crystal MgO and Al_2O_3 and related compounds as a function of temperature. *Physics and Chemistry of Minerals*, 41:361–371, 2014.

[203] T. J. Ahrens. *Mineral physics & crystallography: A handbook of physical constants*, volume 2. American Geophysical Union, 1995.

[204] IAEA. Thermophysical properties of materials for nuclear engineering: A tutorial and collection of data. Technical Report IAEA-THPH, IAEA, Vienna, Austria, 2008.

[205] L. Wei, P. K. Kuo, R. L. Thomas, T. R. Anthony, and W. F. Banholzer. Thermal conductivity of isotopically modified single crystal diamond. *Phys. Rev. Lett.*, 70:3764, 1993.

[206] A. C. Victor. Heat capacity of diamond at high temperatures. *J. Chem. Phys.*, 36:1903–1911, 1962.

[207] J. R. Olson, R. O. Pohl, J. W. Vandersande, A. Zoltan, T. R. Anthony, and W. F. Banholzer. Thermal conductivity of diamond between 170 and 1200 K and the isotope effect. *Phys. Rev. B*, 47:14850, 1993.

[208] C. H. Xu, C. Z. Wang, C. T. Chan, and K. M. Ho. Theory of the thermal expansion of Si and diamond. *Phys. Rev. B*, 43:5024–5027, 1991.

[209] N. S. Rasor and J. D. McClelland. Thermal properties of graphite, molybdenum and tantalum to their destruction temperatures. *J. Phys. Chem. Solids*, 15:17–26, 1960.

[210] A. T. D. Butland and R. J. Maddison. The specific heat of graphite: an evaluation of measurements. *J. Nucl. Mater.*, 49(1):45–56, 1973.

[211] A. A. Balandin. Thermal properties of graphene and nanostructured carbon materials. *Nature Materials*, 10:569–581, 2011.

[212] D. L. Nika, S. Ghosh, E. P. Pokatilov, and A. A. Balandin. Lattice thermal conductivity of graphene flakes: Comparison with bulk graphite. *Appl. Phys. Lett.*, 94:203103, 2009.

[213] D. L Nika and A. A. Balandin. Phonons and thermal transport in graphene and graphene-based materials. *Rep. Prog. Phys.*, 80:036502, 2017.

[214] W. D. Swank, F. I. Valentin, M. Kawaji, and D. M. McEligot. Thermal conductivity of G-348 isostatic graphite. *Nucl. Techn.*, 199:103–109, 2017.

[215] G. Fugallo, A. Cepellotti, L. Paulatto, M. Lazzeri, N. Marzari, and F. Mauri. Thermal conductivity of graphene and graphite: collective excitations and mean free paths. *Nano Letters*, 14:6109–6114, 2014.

[216] A. I. Savvatimskiy. Measurements of the melting point of graphite and the properties of liquid carbon (a review for 1963–2003). *Carbon*, 43:1115–1142, 2005.

[217] Yu. D. Fomin and V. V. Brazhkin. Comparative study of melting of graphite and graphene. *Carbon*, 157:767–778, 2020.

[218] R. W. Grimes and C. R. A. Caltlow. The stability of fission products in uranium oxide. *Phil. Trans. R. Soc. Lon.*, 335:609–634, 1990.

[219] M. O. Tucker. Grain boundary porosity and gas release in irradiated UO_2. *Radaition Effects*, 53:251–256, 1980.

[220] K. Lassmann and H. Benk. Numerical algorithms for intragranular fission gas release. *J. Nucl. Mater.*, 280:127–135, 2000.

[221] INSAG. Defence in depth in nuclear safety. Technical Report INSAG-10, IAEA, Vienna, Austria, 1996. A report by the International Safety Advisory Group.

[222] W. Miekeley and F. W. Felix. Effect of stoichiometry on diffusion of xenon in UO_2. *J. Nucl. Mater.*, 42:297–306, 1972.

[223] K. Shiba. Fission iodine and xenon release from the UO_2-U_3O_8 system with emphasis on radiation damage. *J. Nucl. Mater.*, 57:271–279, 1975.

[224] C.R.A. Catlow. Theory of fission gas migration in UO_2. *Radiation Effects*, 53:127–132, 1980.

[225] H. Matzke. Diffusion in doped UO_2. *Nucl. Appl.*, 2:131–137, 1966.

[226] G. Long, W. P. Stanaway, and D. Davies. Experiments relating to the mechanism of the diffusion of xenon-133 in uranium dioxide. Technical Report AERE-M-1251, AERE Harwell, Didcot, U.K., 1964.

[227] R. D. MacDonald. The effect of TiO_2 and Nb_2O_5 additions on the irradiation behaviour of sintered UO_2. Technical Report AECL-1810, Atomic Energy of Canada Ltd., Chalk River, Ontario, Canada, 1963.

[228] J. C. Killeen. Fission gas release and swelling in UO_2 doped with Cr_2O_3. *J. Nucl. Mater.*, 88:177–184, 1980.

[229] D. Davies and G. Long. The emission of xenon-133 from lightly irradiated uranium dioxide spheroids and powders. Technical Report AERE-R-4347, AERE Harwell, Didcot, U.K., 1963.

[230] A. H. Booth. A method of calculating gas diffusion from UO_2 fuel and its application to the X-2-f test. Technical Report AECL 496 CRDC-721, Atomic Energy of Canada Limited, 1957.

[231] J. A. Turnbull, C. A. Friskney, J. R. Findlay, F. A. Johnson, and A. J. Walter. The diffusion coefficient of gaseous and volatile species during irradiation of uranium dioxide. *J. Nucl. Mater.*, 107:168–184, 1982.

[232] K. Forsberg and A. R. Massih. Diffusion theory of fission gas migration in irradiated nuclear fuel. *J. Nucl. Mater.*, 135:140–148, 1985.

[233] M. V. Speight. A calculation on the migration of fission gas in material exhibiting precipitation and re-solution of gas atoms under irradiation. *Nuclear Science and Engineering*, 37:180–185, 1969.

[234] K. Forsberg, A. R. Massih, and K. Andersson. A calculation of fission gas migration in nuclear fuel with re-solution effect. In *Transactions of the Enlarged Halden Programme Group Meeting on Fuel Performance Experiments and Analysis, Sanderstolen, Norway, 2-7 March, 1986*. OECD Halden Reactor Project, 1986. Halden Project Report HPR-330.

[235] J. Spino, J. Rest, W. Goll, and C. T. Walker. Matrix swelling rate and cavity volume balance of UO_2 fuels at high burnup. *J. Nucl. Mater.*, 346:131–144, 2005.

[236] G. L. Reynolds and G. H. Bannister. Examination of neutron-irradiated UO_2 using the scanning electron microscope. *J. Mater. Sci.*, 5:84–85, 1970.

[237] W. Beeré and G. I. Reynolds. The morphology and growth rate of interlinked porosity in irradiated UO_2. *J. Nucl. Mater.*, 47:51–57, 1973.

[238] J. A. Turnbull and M. O. Tucker. Swelling in UO_2 under conditions of gas release. *Phil. Mag.*, 30:47–63, 1974.

[239] A. R. Massih and K. Forsberg. Calculation of grain boundary gaseous swelling in UO_2. *J. Nucl. Mater.*, 377:406–408, 2008.

[240] P. T. Sawbridge, C. Baker, R. M. Cornell, K. W. Jones, D. Reed, and J.B. Ainscough. The irradiation performance of magnesia-doped UO_2 fuel. *J. Nucl. Mater.*, 95:119–128, 1980.

[241] M. Hirai, J. H. Davies, and R. Williamson. Diffusivities of fission gas species in UO_2 and (U,Gd)O_2 nuclear fuels during irradiation. *J. Nucl. Mater.*, 226:238–251, 1995.

[242] R. J. Ball and R. W. Grimes. Diffusion of Xe in UO_2. *J. Chem. Soc. Faraday Trans.*, 86:1257–1261, 1990.

[243] A. B. Lidiard. Self-diffusion of uranium in UO_2. *J. Nucl. Mater.*, 19:106–108, 1966.

[244] M. J. Norgett and A. B. Lidiard. The migration of inert gases in ionic crystals. *Phil. Mag.*, 18:1193–1210, 1968.

[245] M. W. D. Cooper, G. Pastore, Y. Che, C. Matthews, et al. Fission gas diffusion and release for Cr_2O_3-doped UO_2: From the atomic to the engineering scale. *J. Nucl. Mater.*, 545, 2021. Paper 152590.

[246] S. O. Andersson, E. Patrakka, L. Hydén, H. Pettersson, and B. Grapengiesser. The Finnish-Swedish high burnup fuel evaluation programme. In *Improvements in Water Reactor Fuel Technology and Utilization*, STI/PUB/721, pages 281–289, Stockholm,

Sweden, 15-19 September 1986. International Atomic Energy Agency, Vienna, Austria. Published: 1987.

[247] Ingvar Matsson and Björn Grapengiesser. Developments in gamma scanning irradiated nuclear fuel. *Applied Radiation and Isotopes*, 48:1289–1298, 1997.

[248] P. T. Sawbridge, G. L. Reynolds, and B. Burton. The creep of UO_2 fuel doped with Nb_2O_5. *J. Nucl. Mater.*, 97:300–308, 1981.

[249] C. Duguay, A. Mocellin, P. Dehaudt, and G. Fantozzi. High temperature compression tests performed on doped fuels. *Key Engineering Materials*, 132-136:579–582, 1997.

[250] C. Dugay, A. Mocellin, P. Dehaudt, and M. Sladkoff. High temperature mechanical tests performed on doped fuels. In *Advances in Fuel Pellet Technology for Improved Performance*, IAEA-TECDOC-1036, pages 409–419, International Atomic Energy Agency, Vienna, Austria, 1998.

[251] T. G. Langdon. Creep mechanisms in stoichiometric uranium dioxide. *J. Nucl. Mater.*, 38:88–92, 1971.

[252] T. G. Langdon. Deformation of polycrystalline materials at high temperatures. In N. Hansen, A. Horsewell, T. Leffers, and H. Lilholt, editors, *Deformation of polycrystals: Mechanisms and microstructures*, pages 45–54, Risø National Laboratory, Roskilde, Denmark, 14-18 September 1981.

[253] T. G. Langdon. The physics of superplastic deformation. *Mater. Sci. Eng. A*, 137:1–11, 1991.

[254] C. Nonon, J. C. Menard, and S. Lansiart et al. PCI behaviour of chromium oxide doped fuel. In *International Seminar on Pellet-Clad Interaction in Water Reactor Fuels*, Aix-en-Provence, France, 9-11 March 2004. OECD Nuclear Energy Agency, Paris, France. Report NEA No. 6004 (2005).

[255] H. Matzke. On uranium self-diffusion in UO_2 and UO_{2+x}. *J. Nucl. Mater.*, 30:26–35, 1969.

[256] J. Wright, C. Anghel, S. Middleburgh, and M. Limbäck. Towards an increased understanding of fuel pellet and cladding features enhancing the PCI resistance of LWR fuel. In *Proceedings of the NEA Workshop on PCI in Water-Cooled Reactors*, pages 307–316, Lucca, Italy, 22-24 June, 2016. OECD Nuclear Energy Agency, Paris, France. Report NEA/CSNI/R(2018)9.

[257] K. Forsberg, L. O. Jernkvist, and A. R. Massih. Modeling oxygen redistribution in UO_{2+x} fuel pellet. *J. Nucl. Mater.*, 528:151829, 2020.

[258] Y. W. Rhee, K. W. Kang, and K. S. Kim et al. Effect of SiO_2-CaO-Cr_2O_3 on the creep property of uranium dioxide. *Nucl. Eng. & Techn.*, 37:287–292, 2005.

[259] C. Delafoy and I. Arimescu. Developments in fuel design and manufacturing in order to enhance the PCI performance of AREVA NP fuel. In *Proceedings of the NEA Workshop on PCI in Water-Cooled Reactors*, pages 294–305, Lucca, Italy, 22-24 June, 2016. OECD Nuclear Energy Agency, Paris, France. Report NEA/CSNI/R(2018)9.

[260] A. A. Solomon, J. L. Routbort, and J. C. Voglewede. Fission-induced creep of UO_2 and its significance to fuel-element performance. Technical Report ANL-7857, Argonne National Laboratory, Argonne, IL (United States), 1971.

[261] A. R. Massih. Models for MOX fuel behaviour. Technical Report 2006:10, Swedish Nuclear Power Inspectorate (SKI), Stockholm, Sweden, 2006. Available at: www.ssm.se.

[262] R. Hill. The elastic behaviour of a crystalline aggregate. *Proc. Phys. Soc. London. Section A*, 65(5):349, 1952.

[263] R. Hill. Elastic properties of reinforced solids: some theoretical principles. *J. Mech Phys. Solids*, 11:357–372, 1963.

[264] R. A. Wolfe and S. F. Kaufman. Mechanical properties of oxide fuels. Report WAPD-TM-587, Bettis Atomic Power, Pittsburgh, PA, USA, 1967.

[265] A. R. Hall. Elastic moduli and internal friction of some uranium ceramics. *J. Nucl. Mater.*, 37:314–323, 1970.

[266] D. L. Hagrman and G. A. Reymann. MATPRO-Version 11: A handbook of materials properties for use in the analysis of light water reactor fuel rod behavior. Report NUREG/CR-0497,TREE-1280, Idaho National Engineering Lab., Idaho Falls, ID, USA, 1979.

[267] R. G. Munro. Elastic moduli data for polycrystalline oxide ceramics. Report NISTIR 6853, National Institute of Standards and Technology, Gaithersburg, MD, USA, 2002.

[268] A. L. Ivanovskii, I. R. Shein, Yu. N. Makurin, V. S. Kiiko, and M. A. Gorbunova. Electronic structure and properties of beryllium oxide. *Inorganic Materials*, 45(3):223, 2009.

[269] S. Lakel, F. Elhamra, and K. Almi. Structural phase transition, electronic, and mechanical properties of beryllium oxide: Temperature and pressure-induced effects. *physica status solidi (b)*, 255:1700524, 2018.

[270] K. K. Phani, D. Sanyal, and A. K. Sengupta. Estimation of elastic properties of nuclear fuel material using longitudinal ultrasonic velocity–a new approach. *J. Nucl. Mater.*, 366:129–136, 2007.

[271] Z. Hashin and S. Shtrikman. A variational approach to the theory of the elastic behaviour of multiphase materials. *J. Mech. Phys. Solids*, 11:127–140, 1963.

[272] Z. Hashin and S. Shtrikman. A variational approach to the theory of the elastic behaviour of polycrystals. *J. Mech. Phys. Solids*, 10:343–352, 1962.

[273] R. Liu, W. Zhou, A. Prudil, and P. K. Chan. Multiphysics modeling of UO_2-SiC composite fuel performance with enhanced thermal and mechanical properties. *Applied Thermal Engineering*, 107:86–100, 2016.

[274] Z. Chen, G. Subhash, and J. S. Tulenko. Raman spectroscopic investigation of graphitization of diamond during spark plasma sintering of UO_2-diamond composite nuclear fuel. *J. Nucl. Mater.*, 475:1–5, 2016.

[275] Nuclear fuel behaviour in loss-of-coolant (LOCA) conditions. Report NEA No. 6846, OECD Nuclear Energy Agency, Paris, France, 2009.

[276] Nuclear fuel behaviour under reactivity initiated accident (RIA) conditions. Report NEA No. 6847, OECD Nuclear Energy Agency, Paris, France, 2010.

[277] K. Hesketh, G. Rossiter, R. Largenton, and M. Puide. Burnable poison-doped fuel. In R. J. M. Konings and R. E. Stoller, editors, *Comprehensive Nuclear Materials (2nd ed.)*, volume 2, chapter 2.04, pages 106–124. Elsevier, 2020.

[278] A. M. Fedosov. RBMK uranium-erbium fuel. *Atomic Energy*, 124:221–226, 2018.

[279] V. N. Shevaldin, G. P. Negrivoda, B. A. Vorontsov, et al. Experience with uranium-erbium fuel at the Ignalinsk Atomic Power Plant. *Atomic Energy*, 85:517–522, 1998.

[280] V. Remeikis, J. Grineviciute, G. Duškesas, L. Juodis, R. Plukienė, and A. Plukis. Review of modeling experience during operation and decommissioning of RBMK-1500 reactors. I. Safety improvement studies during operation. *Nucl. Eng. Design*, 2021. In press.

[281] B. Baurens and K. Fuglesang. In-pile results from the fission gas release mechanisms study in IFA-716 after final unloading. Report HWR-1161, Institutt for Energiteknikk, Halden, Norway, 2016.

[282] K. A. Gamble, G. Pastore, and M. W. D. Cooper. BISON development and validation for priority LWR-ATF concepts. Report INL/EXT-20-59969 Rev0, Idaho National Laboratory, Idaho Falls, ID, USA, 2020.

[283] K. Backman, L. Hallstadius, and G. Rönnberg. Westinghouse advanced doped pellet: Characteristics and irradiation behaviour. In *Advanced Fuel Pellet Materials and Fuel Rod Design for Water Cooled Reactors*, IAEA-TECDOC-1654, pages 117–126, International Atomic Energy Agency, Vienna, Austria, 2009.

[284] L. H. Hallman et al. Westinghouse advanced doped pellet technology (ADOPT^{TM}) fuel. Report WCAP-18482-NP, Rev. 0, Westinghouse Electric Company, Cranberry Township, PA, USA, 2020. US NRC ADAMS accession nr: ML20132A014.

[285] G. Zhou, A. R. Massih, and L. Hallstadius et al. Fuel performance experience, analysis and modeling: Deformations, fission gas release and pellet-clad interaction. In *Proceedings of the 2007 International LWR Fuel Performance Meeting*, pages 143–152, San Francisco, California, October 2007. American Nuclear Society.

[286] R. Josek. The high initial rating test IFA-677.1: Final report on in-pile results. Report HWR-872, Institutt for Energiteknikk, Halden, Norway, 2008.

[287] B. Volkov, T. Tverberg, and M. McGrath. Experimental investigations of additives on irradiation performances of oxide fuel. In *2014 Water Reactor Fuel Performance Meeting*, Sendai, Japan, September 14-17 2014. Atomic Energy Society of Japan. Paper no. 100141.

[288] Y. Russin, Y. Shakhvorostov, and M. McGrath et al. Innovative fuel development in ULBA (Khazakhstan) and testing in the Halden reactor. In *Proceedings of the 2011 Water Reactor Fuel Performance Meeting*, Chengdu, China, 11-14 September 2011.

[289] S. Koike and B. Volkov. Progress report on the irradiation of VVER large grain and Gd-doped fuel in IFA-676.1. Report HWR-1007, Institutt for Energiteknikk, Halden, Norway, 2011.

[290] D. A. Chulkin, V. I. Kuznetsov, A. V. Krupkin, and V. V. Novikov. FGR modeling of large grained fuel during transients by START-3A. In *Proc. 2013 TopFuel Conference*, pages 211–218, Charlotte, NC, USA, 15-19 September 2013.

[291] J. H. Davies, S. Vaidyanathan, and R. A. Rand. Modified fuel for high burn-up. In *Proceedings of Top Fuel '99: International Topical Meeting*, pages 385–395, Avignon, France, 13-15 September, 1999. SFEN/ENS.

[292] B. Cox. Pellet-cladding interaction PCI failures of zirconium alloy fuel cladding - A review. *J. Nucl. Mater.*, 172(3):249–292, 1990.

[293] J. S. Armijo and Z. Abdullahi. Pellet-cladding interaction fuel failures during anticipated operational occurrences in boiling water reactors. Report, US NRC Advisory Committee on Reactor Safeguards, Rockville, MD, USA, 2009. US NRC ADAMS accession nr: ML093500677.

[294] J. S. Armijo and Z. Abdullahi. Pellet-cladding interaction fuel failures during anticipated operational occurrences in pressurized water reactors. Report, US NRC Advisory Committee on Reactor Safeguards, Rockville, MD, USA, 2014. US NRC ADAMS accession nr: ML14107A179.

[295] Ch. Riglet-Martial, J. Sercombe, J. Lamontagne, J. Noirot, I. Roure, T. Blay, and L. Desgranges. Experimental evidence of oxygen thermo-migration in PWR UO_2 fuels during power ramps using in-situ oxido-reduction indicators. *J. Nucl. Mater.*, 480:32–39, 2016.

[296] P. Konarski, J. Sercombe, C. Riglet-Martial, L. Noirot, I. Zacharie-Aubrun, K. Hanifi, M. Fregonèse´, and P. Chantrenne. 3D simulation of a power ramp including fuel thermochemistry and oxygen thermodiffusion. *J. Nucl. Mater.*, 519:104–120, 2019.

[297] G. Zhou, J. Arborelius, and L. Hallstadius et al. Westinghouse advanced UO_2 fuel behaviors during power transient. In *2005 Water Reactor Fuel Performance Meeting*, pages 147–156, Kyoto, Japan, October 2-6 2005. Atomic Energy Society of Japan.

[298] J. Wright, C. Anghel, S. Middleburgh, and M. Limbäck. Fuel hardware considerations for BWR PCI mitigation. In *Proc. 2016 TopFuel Conference*, pages 87–96, Boise, ID, USA, 11-15 September 2016.

[299] J. Matsunaga, K. Une, and K. Kusagaya. Chemical trap effect of aluminosilicate additive fuel. In *Proc. 2010 LWR Fuel Performance/TopFuel/WRFP Meeting*, pages 571–576, Orlando, FL, USA, 26-29 September, 2010.

[300] T. Mihara, Y. Udagawa, M. Amaya, Y. Tanigushi, and K. Kakiuchi. Behavior of LWR fuels with additives under recativity initiated accident conditions. In *Proceedings of Top Fuel 2019: Light Water Reactor Fuel Performance Conference*, pages 544–550, Seattle, WA, USA, 22-26 September 2019. American Nuclear Society.

[301] S. Shiozawa, S. Saito, T. Fujishiro, Y. Kondo, S. Abeta, M. Takeda, H. Ikehata, H. Fujimoto, and Y. Komano. Study on the behavior of Gd_2O_3 fuel rod failure

under a reactivity initiated accident. Report JAERI-M-88-084, Japan Atomic Energy Research Institute, Tokyo, Japan, 1988.

[302] K. Yanagisawa. Behavior of Nb_2O_5 doped UO_2 fuel in reactivity initiated accident conditions. *J. Nucl. Sci. Techn.*, 28(5):459–471, 1991.

[303] K. Yanagisawa. Behavior of Nb_2O_5 doped unpressurized UO_2 fuel under transient. *J. Nucl. Sci. Techn.*, 32(2):111–117, 1995.

[304] K. Yanagisawa, T. Fujishiro, A. Negrini, and F. Franco. Behavior of PCI-resistant additive fuel for BWR under reactivity initiated accident conditions. *J. Nucl. Sci. Techn.*, 27(1):56–67, 1990.

[305] Y. Udagawa, T. Mihara, Y. Taniguchi, K. Kakiuchi, and M. Amaya. The effect of base irradiation on failure behaviors of UO_2 and chromia-alumina additive fuels under simulated reactivity-initiated accidents: A comparative analysis with FEMAXI-8. *Ann. Nucl. Energy*, 139, 2020. Paper ID 107268.

[306] H. U. Zwicky. SCIP-IV technical description. Report STUDSVIK/N-18/027, Studsvik Nuclear AB, Nyköping, Sweden, 2018.

[307] G. A. Peters. Incorporation of chromia-doped fuel properties in AREVA approved methods. Report ANP-10340NP-A, Rev. 0, Framatome Inc., Lynchburg, VA, USA, 2018. US NRC ADAMS accession nr: ML18171A119.

[308] S. M. Bragg-Sitton, M. Todosow, R. Montgomery, C. R. Stanek, R. Montgomery, and W. J. Carmack. Metrics for the technical performance evaluation of light water reactor accident-tolerant fuel. *Nucl. Techn.*, 195(2):111–123, 2016.

[309] State-of-the-art report on light water reactor accident-tolerant fuels. Report NEA No. 7317, OECD Nuclear Energy Agency, Paris, France, 2018.

[310] M. Billaux, P. Blanpain, and D. Boulanger. Evaluation of the thermomechanical properties of high burnup gadolinia fuel. In *International Topical Meeting on LWR Fuel Performance*, pages 356–363, Williamsburg, VA, USA, April 17-20 1988. American Nuclear Society.

[311] D. J. Richmond and K. J. Geelhood. Expanded assessment of FAST for power ramp cases with short hold times and advanced UO_2 fuel with various dopants. In *Proceedings of Top Fuel 2018: Reactor Fuel Performance Meeting 2018*, Prague, Czech Republic, 30 September - 04 October 2018. European Nuclear Society. Paper A0116.

[312] F. Khattout. The gadolinia fuel test IFA-681: Overview of in-pile measurements from beginning of irradiation to unloading. Report HWR-1038, Institutt for Energiteknikk, Halden, Norway, 2013.

[313] I. E. Porter, K. J. Geelhood, D. V. Colameco, E. E. Torres, W. G. Luscher, L. Kyriazidis, and C. E. Goodson. FAST-1.0: A computer code for thermal-mechanical nuclear fuel analysis under steady-state and transients. Report PNNL-29720, Pacific Northwest National Laboratory, Richland, WA, USA, 2020.

[314] K. J. Geelhood, W. G. Luscher, P. A. Raynaud, and I. E. Porter. FRAPCON-4.0: A computer code for the calculation of steady-state, thermal-mechanical behavior of

oxide fuel rods for high burnup. Report PNNL-19418, Vol.1 Rev.2, Pacific Northwest National Laboratory, Richland, WA, USA, 2015.

[315] C. E. Mattos, A. T. E. Silva, I. C. Martins, and E. F. Urano de Carvalho. Study of models for high burnup behaviour of uranium-7%gadolinium fuel rods for pressurized light water reactors. In *2018 European Research Reactor Conference (RRFM 2018)*, Munich, Germany, 11-15 March 2018.

[316] C. E. Mattos. *Study of models for high burnup behaviour of uranium-7%gadolinium fuel rods for pressurized light water reactors*. Doctoral thesis, Nuclear and Energy Research Institute (IPEN/CNEN-SP), Sao Paulo, Brazil, 2018. (In Portuguese).

[317] R. L. Williamson, J. D. Hales, and S. R. Novascone et al. Multidimensional multiphysics simulation of nuclear fuel behavior. *J. Nucl. Mater.*, 423:149–163, 2012.

[318] Y. Che, G. Pastore, J. Hales, and K. Shirvan. Modeling of Cr_2O_3-doped UO_2 as a near-term accident tolerant fuel for LWRs using the BISON code. *Nucl. Eng. Design*, 337:271–278, 2018.

[319] K. A Gamble, G. Pastore, D. Andersson, and M. Cooper. ATF material model development and validation for priority fuel concepts. Report CASL-U-2019-1870-000 Rev0, Idaho National Laboratory, Idaho Falls, ID, USA, 2019.

[320] K. McCoy and C. Mays. Enhanced thermal conductivity oxide nuclear fuels by cosintering with BeO: II. Fuel performance and neutronics. *J. Nucl. Mater.*, 375:157–167, 2008.

[321] A. A. Kovalishin, V. N. Prosyolkov, V. D. Sidorenko, and Y. V. Stogov. On the possibility of using uranium-beryllium oxide fuel in a VVER reactor. *Physics of Atomic Nuclei*, 77(14):1661–1663, 2014.

[322] S. M. McDeavitt, C. Garcia, J. C. Ragusa, J. Smith, and J. Malone. Evaluation of high thermal conductivity oxide nuclear fuel concept containing beryllium. In *Proc. 2010 LWR Fuel Performance/TopFuel/WRFP Meeting*, pages 621–625, Orlando, FL, USA, 26-29 September, 2010.

[323] J. R. Smith. Enhanced thermal conductivity UO_2-BeO nuclear fuel: Neutronic performance studies and economic analyses. Master thesis, Texas A&M University, College station, TX, USA, 2012.

[324] S. M. McDeavitt, C. Garcia, J. C. Ragusa, J. Smith, and J. Malone. Behavior assessments for UO_2-BeO enhanced conductivity fuel in a PWR. In *Proc. 2013 TopFuel Conference*, pages 1161–1166, Charlotte, NC, USA, 15-19 September 2013.

[325] Q. Zhang, X. Wang, Y. Zhang, X. Chi, L. Liang, K. Zhuang, and C. Wang. Neutronic analysis for potential accident tolerant fuel UO_2-BeO in the light water reactor. *Ann. Nucl. Energy*, 127:278–292, 2019.

[326] J. Wang. *Developing a high thermal conductivity nuclear fuel with silicon carbide additives*. Doctoral thesis, University of Florida, Gainesville, FL, USA, 2008.

[327] D. S. Gomes and A. T. Silva. Performance analysis of UO_2-SiC fuel under normal conditions. In *Proc. 2019 International Nuclear Atlantic Conference (INAC 2019)*, pages 5056–5069, Santos, SP, Brazil, 21-25 October, 2019.

[328] R. Liu, W. Zhou, P. Shen, A. Prudil, and P. K. Chan. Fully coupled multiphysics modeling of enhanced thermal conductivity UO_2-BeO fuel performance in a light water reactor. *Nucl. Eng. Design*, 295:511–523, 2015.

[329] R. Liu, A. Prudil, W. Zhou, and P. K. Chan. Multiphysics coupled modeling of light water reactor fuel performance. *Progress in Nuclear Energy*, 91:38–48, 2016.

[330] Wei Zhou and Wenzhong Zhou. Thermophysical and mechanical analyses of UO_2-36.4 vol% BeO fuel pellets with zircaloy, SiC, and FeCrAl claddings. *Metals*, 8(1):65, 2018.

[331] R. Liu. *CAMPUS: A fully coupled multiphysics modeling approach for light water reactor fuel performance*. Doctoral thesis, Hong Kong City University, Hong Kong, China, 2016.

[332] J. Cai, Z. Chen, S. He, and R. Liu. Research on thermal behaviors of several accident tolerant fuels based on 5×5 bundle subchannel model. *Ann. Nucl. Energy*, 133:9–20, 2019.

[333] A. Rubin, A. Schoedel, and M. Avramova et al. OECD/NRC benchmark based on NUPEC PWR sub-channel and bundle test (PSBT). Report NEA/NSC/DOC(2012)1, OECD Nuclear Energy Agency, Paris, France, 2012.

[334] S. T. Revankar, W. Zhou, and D. Chandramouli. Thermal performance UO_2-BeO fuel during a loss of coolant accident. *Int. J. Nucl. Energy Sci. Eng.*, 5:1–8, 2015.

[335] G. E. Russcher, R. K. Marshall, and G. M. Hesson et al. LOCA simulation in the NRU reactor: Materials Test - 1. Report NUREG/CR-2152, US Nuclear Regulatory Commission, Washington, DC, USA, 1981.

[336] H. Yu, Z. Chen, and J. Cai. Accident tolerant fuel thermal hydraulic behaviors evaluation during loss of coolant accident in CPR1000. *Ann. Nucl. Energy*, 139, 2020. Paper 107273.

[337] Z. Chen, J. Cai, R. Liu, and Y. Wang. Preliminary thermal hydraulic analysis of various accident tolerant fuels and claddings for control rod ejection accidents in LWRs. *Nucl. Eng. Design*, 331:282–294, 2018.

[338] S. He, J. Cai, Z. Chen, and R. Liu. Thermal hydraulic analysis of accident tolerant fuels for reactivity-initiated-accident in PWR with different coolant channel geometries. *Nucl. Eng. Design*, 351:131–142, 2019.

[339] Y. He, Y. Wu, S. Wang, B. Qui, and G. Su. Analysis of UO_2-BeO fuel performance during normal conditions and RIA. In *Proc. 26th International Conference on Nuclear Engineering (ICONE-26)*, volume 9, London, UK, 22-26 July 2018. Paper 82076.

[340] Reactivity-initiated accident (RIA) fuel codes benchmark Phase III - Uncertainty and sensitivity anayses. Report NEA/CSNI/R(2020)10, OECD Nuclear Energy Agency, Paris, France, 2020. (In press).

[341] S. W. Lee, H. T. Kim, and I. C. Bang. Performance evaluation of UO_2/graphene composite fuel and SiC cladding during LBLOCA using MARS-KS. *Nucl. Eng. Design*, 257:139–145, 2013.

[342] Y. Sukjai. Silicon carbide performance as cladding for advanced uranium and thorium fuels for light water reactors. Master thesis, Massachusetts Institute of Technology, Cambridge, MA, USA, 2014.

[343] D. S. Gomes, Y. Abe, R. O. R. Muniz, and C. Giovedi. Analysis of UO_2-BeO fuel under transient using fuel performance code. In *Proc. 2017 International Nuclear Atlantic Conference (INAC 2017)*, Belo Horizonte, MG, Brazil, 22-27 October, 2017.

[344] D. S. Gomes, A. Abe, A. T. Silva, R. O. R. Muniz, C. Giovedi, and M. R. Martins. Assessment of high conductivity ceramic fuel concept under normal and accident conditions. In *Modelling of Fuel Behaviour in Design Basis Accidents and Design Extension Conditions: Proceedings of a Technical Meeting*, IAEA-TECDOC-1913, pages 95–101, Shenzhen, China, 13-16 May 2019. IAEA, Vienna, Austria.

[345] B. T. M. Willis. Crystallographic studies of anion-excess uranium oxides. *J. Chem. Soc. Faraday Trans.*, 83:1073–1081, 1987.

[346] J. Wang, R. C. Ewing, and U. Becker. Average structure and local configuration of excess oxygen in UO_{2+x}. *Scientific Reports*, 4:4216, 2014.

[347] H. E. Stanley. *Introduction to Phase Transitions and Critical Phenommena*. Oxford University Press, Oxford, U.K., 1971.

[348] H. E. Stanley. Scaling, univarsility, and renormalizations: three pillars of modern critical phenomena. *Rev. Mod. Phys.*, 71:S358–S666, 1999.

[349] H. Nishimori and G. Ortiz. *Elements of Phase Transitions and Critical Phenommena*. Oxford University Press, Oxford, U.K., 2011.

[350] S. Brunauer, P. H. Emmett, and E. Teller. Adsorption of gases in multimolecular layers. *J. Am. Chem. Soc.*, 60:309–319, 1938.

[351] Y. Shaposhnik, E. Shwageraus, and E. Elias. Shutdown margin for high conversion BWRs operating in Th-^{233}U fuel cycle. *Nucl. Eng. Design*, 276:162–177, 2014.

[352] J. Lemaitre and J. L. Chaboche. *Mechanics of Solid Materials*. Cambridge University Press, Cambridge, U.K., 1990.

[353] Y. Liu, C. Hu, W. Feng, J. Men, L. Cheng, and L. Zhang. Microstructure and properties of diamond/SiC composites prepared by tape-casting and chemical vapor infiltration process. *J. Eur. Ceram. Soc.*, 34:3489–3498, 2014.

[354] L. W. Da Silva and M. Kaviany. Micro-thermoelectric cooler: interfacial effects on thermal and electrical transport. *Int. J. Heat & Mass Transfer*, 47:2417–2435, 2004.

[355] B-T. Wang, P. Zhang, R. Lizárraga, I. Di Marco, and O. Eriksson. Phonon spectrum, thermodynamic properties, and pressure-temperature phase diagram of uranium dioxide. *Phys. Rev. B*, 88:104107, 2013.

[356] P. Riou, C. Denoual, and C. E. Cottenot. Visualization of the damage evolution in impacted silicon carbide ceramics. *Int. J. Impact Engin.*, 21:225–235, 1998.

[357] R. J. Stevens, A. N. Smith, and P. M. Norris. Measurement of thermal boundary conductance of a series of metal-dielectric interfaces by the transient thermoreflectance technique. *J. Heat Transfer*, 127:315–322, 2005.

[358] P. Reddy, K. Castelino, and A. Majumdar. Diffuse mismatch model of thermal boundary conductance using exact phonon dispersion. *Appl. Phys. Lett.*, 87(21):211908, 2005.

[359] R. J. Stevens, L. V. Zhigilei, and P. M. Norris. Effects of temperature and disorder on thermal boundary conductance at solid–solid interfaces: Nonequilibrium molecular dynamics simulations. *Int. J. Heat & Mass Transfer*, 50:3977–3989, 2007.

[360] J. Larroque, P. Dollfus, and J. Saint-Martin. Phonon transmission at Si/Ge and polytypic Ge interfaces using full-band mismatch based models. *J. Appl. Phys.*, 123:025702, 2018.

The Swedish Radiation Safety Authority has a comprehensive responsibility to ensure that society is safe from the effects of radiation. The Authority works from the effects of radiation. The Authority works to achieve radiation safety in a number of areas: nuclear power, medical care as well as commercial products and services. The Authority also works to achieve protection from natural radiation an to increase the level of ratiation safety internationally.

The Swedish Radiation Safety Authority works proactively and presentively to protect people and the environment from the harmful effects of radiation, now and in the future.
The Authority issues regulations and supervises compliance, while also supporting research, providing training and information, and issuing advice. Often, activities involving radiation require licences issued by the Authority. The Swedish Radiation Safety Authority maintains emergency preparedness around the clock with the aim of limiting the aftermath of radiation accidents and the unintentional spreading of radioactive substances. The Authority participates in international co-operation in order to promote radiation safety and finances projects aiming to raise the level of radiation safety in certain Eastern European countries.

The Authority reports to the Ministry of the Environment and has around 300 employees with competencies in the fields of engineering, natural and behavioral sciences, law, economics and communications. We have recieved quality, environmental and working environment certification.

Publikationer utgivna av Strålsäkerhetsmyndigheten kan laddas ned via stralsäkerhetsmyndigheten.se eller beställas genom att skicka e-post till registrator@ssm.se om du vill ha broschyren i alternativt format, som punktskrift eller daisy.

Strålsäkerhetsmyndigheten
Swedish Radiation Safety Authority
SE-171 16 Stockholm
Phone: 08-799 40 00
Web: ssm.se
E-mail: registrator@ssm.se

E-print AB, 2021